Material Forming Processes

Mathematical and Mechanical Engineering Set

coordinated by
Abdelkhalak El Hami

Volume 1

Material Forming Processes

Simulation, Drawing, Hydroforming and Additive Manufacturing

Bouchaib Radi
Abdelkhalak El Hami

iSTE WILEY

First published 2016 in Great Britain and the United States by ISTE Ltd and John Wiley & Sons, Inc.

Apart from any fair dealing for the purposes of research or private study, or criticism or review, as permitted under the Copyright, Designs and Patents Act 1988, this publication may only be reproduced, stored or transmitted, in any form or by any means, with the prior permission in writing of the publishers, or in the case of reprographic reproduction in accordance with the terms and licenses issued by the CLA. Enquiries concerning reproduction outside these terms should be sent to the publishers at the undermentioned address:

ISTE Ltd
27-37 St George's Road
London SW19 4EU
UK

www.iste.co.uk

John Wiley & Sons, Inc.
111 River Street
Hoboken, NJ 07030
USA

www.wiley.com

© ISTE Ltd 2016
The rights of Bouchaib Radi and Abdelkhalak El Hami to be identified as the authors of this work have been asserted by them in accordance with the Copyright, Designs and Patents Act 1988.

Library of Congress Control Number: 2016945874

British Library Cataloguing-in-Publication Data
A CIP record for this book is available from the British Library
ISBN 978-1-84821-947-2

Contents

Preface xi

Chapter 1. Forming Processes 1

1.1. Introduction 1
1.2. Different processes 1
1.2.1. Smelting 2
1.2.2. Machining 3
1.2.3. Powder metallurgy 5
1.3. Hot and cold forming 6
1.3.1. Influence of the static parameters 9
1.3.2. Hydroforming 12
1.3.3. The limitations of the process 13
1.3.4. Deep drawing 14
1.4. Experimental characterization 14
1.5. Forming criteria 16
1.5.1. Influence of the structure of sheet metal 18
1.5.2. Physical strain mechanisms 20
1.5.3. Different criteria 21

Chapter 2. Contact and Large Deformation Mechanics 23

2.1. Introduction 23
2.2. Large transformation kinematics 23
2.2.1. Kinematics of the problem in spatial coordinates 24
2.3. Transformation gradient 25
2.4. Strain measurements 26
2.4.1. Polar decomposition of $\mathbb{F}$ 26

2.4.2. Strain rate tensor 27
2.4.3. Canonical decomposition of $\mathbb{F}$ 28
2.4.4. Kinematics of the problem in convective coordinates 28
2.4.5. Transformation tensor 29
2.4.6. Strain rate measures 32
2.4.7. Strain tensor 35
2.5. Constitutive relations 36
2.5.1. Large elastoplastic transformations 38
2.5.2. Kinematic decomposition of the transformation 41
2.6. Incremental behavioral problem 42
2.6.1. Stress incrementation 42
2.6.2. Strain incrementation 44
2.6.3. Solution of the behavior problem 46
2.7. Definition of the P.V.W. in major transformations 49
2.7.1. Equilibrium equations 49
2.7.2. Definition of the P.V.W. 50
2.7.3. Incremental formulation 51
2.8. Contact kinematics 52
2.8.1. Definition of the problem and notations 52
2.8.2. Contact formulation 53
2.8.3. Formulation of the friction problem 53
2.8.4. Friction laws 54
2.8.5. Coulomb's law 54
2.8.6. Tresca's law 55

Chapter 3. Stamping 57

3.1. Introduction 57
3.2. Forming limit curve 59
3.3. Stamping modeling: incremental problem 60
3.3.1. Modeling of sheet metal 61
3.3.2. Spatial discretization: finite elements method 62
3.3.3. Choice of sheet metal and finite element approximation . . 63
3.4. Modeling tools 64
3.4.1. Tool surface meshing into simple geometry elements 64
3.4.2. Analytical representation of tools 65
3.4.3. Bezier patches 65
3.5. Stamping numerical processing 72
3.5.1. Problem statement 73
3.5.2. The augmented Lagrangian method 75
3.6. Numerical simulations 79
3.6.1. Sollac test 81

Chapter 4. Hydroforming 83

4.1. Introduction 83
4.2. Hydroforming 85
4.2.1. Tube hydroforming 85
4.2.2. Sheet metal hydroforming 86
4.3. Plastic instabilities in hydroforming 87
4.3.1. Tube buckling 88
4.3.2. Wrinkling 90
4.3.3. Necking 91
4.3.4. Springback 92
4.4. Forming limit curve 92
4.5. Material characterization for hydroforming 94
4.5.1. Tensile testing 95
4.5.2. Bulge testing 95
4.6. Analytical modeling of a inflation test 97
4.6.1. Hill48 criterion in planar stresses 97
4.7. Numerical simulation 100
4.8. Mechanical characteristic of tube behavior 101

Chapter 5. Additive Manufacturing 105

5.1. Introduction 105
5.2. RP and stratoconception 107
5.3. Additive manufacturing definitions 109
5.4. Principle 113
5.4.1. Principle of powder bed laser sintering/melting 114
5.4.2. Principle of laser sintering/melting by projecting powder 116
5.5. Additive manufacturing in the IT-based development process 117
5.5.1. Concept “from the object to the object” 117
5.5.2. Key element of the IT development process 118

Chapter 6. Optimization and Reliability in Forming 121

6.1. Introduction 121
6.2. Different approaches to optimization processes 122
6.2.1. Limitations of the deterministic approaches 124
6.3. Characterization of forming processes by objective functions 125
6.4. Deterministic and probabilistic optimization of a T-shaped tube 126
6.4.1. Problem description 126

6.4.2. Choice of the objective function and definition of the stresses 127
6.4.3. Choice of the uncertain parameters 128
6.4.4. Choice of the objective function and the stresses 130
6.4.5. Deterministic formulation of the optimization problem . . . 132
6.4.6. Probabilistic formulation of the optimization problem 133
6.4.7. Optima sensitivity to uncertainties 140
6.5. Deterministic and optimization-based reliability of a tube with two expansion regions 142
6.5.1. Problem description 142
6.5.2. Deterministic and reliabilist formulation of the optimization problem 147
6.6. Optimization-based reliability of circular sheet metal hydroforming 150
6.6.1. Problem description 150
6.6.2. Construction of the objective function and of the stresses 151
6.6.3. Effects diagram 151
6.6.4. Deterministic solution of the optimization problem 155
6.6.5. Reliabilist solution of the optimization problem 157
6.6.6. Effect of uncertainties on the optimal variables 159
6.7. Deterministic and robust optimization of a square plate 160
6.7.1. Robust resolution of the optimization problem 166
6.8. Optimization of thin sheet metal 168

Chapter 7. Application of Metamodels to Hydroforming 171

7.1. Introduction 171
7.2. Sources of uncertainty in forming 172
7.3. Failure criteria 173
7.3.1. Failure criteria for necking 174
7.3.2. Failure criteria for wrinkling 174
7.4. Evaluation strategy of the probability of failure 175
7.4.1. Finite element model and choice of uncertainty parameters 176
7.4.2. Identification of failure modes and definition of boundary states 180
7.4.3. Identification of elements and critical areas 181
7.5. Critical strains probabilistic characterization 185
7.5.1. Choice of numerical experimental design 186
7.5.2. Construction of metamodels 186
7.5.3. Validation and statistical analysis of metamodels 187

7.5.4. Fitting of distributions 187
7.6. Necking and wrinkling probabilistic study 193
7.7. Effects of the correlations on the probability of failure 196
7.7.1. Spatial estimation of the probability of failures 197

Chapter 8. Parameters Identification in Metal Forming 199

8.1. Introduction 199
8.2. Identification methods 199
8.2.1. Validation test 200
8.3. Welded tube hydroforming 203
8.3.1. Thin sheet metal hydroforming 205

Appendices 213

Appendix 1. Optimization in Mechanics 215

Appendix 2. Reliability in Mechanics 223

Appendix 3. Metamodels 233

Bibliography 243

Index 253

Preface

In the current economical climate, the automotive, aviation, aerospace, defense, etc., industries have established the following priority: improve the quality and the reliability of products while reducing production costs. To achieve this goal, the industry strives to modernize its work tools in order to minimize the duration of design cycles and improve manufacturing processes.

The field of metal forming (stamping, thin sheet metal deep-drawing, tubes and plates hydroforming, forging of solid materials, cutting, composite draping, foundry, etc.) is the subject of much research and of different courses destined to engineers and academics (as part of masters and doctoral schools). This interest is due to the increasing demands from different industrial sectors for graduates with experience in these disciplines.

In different industries (automotive, aeronautics, etc.), metal forming constitutes, in the course of the entire manufacturing processes, a decisive phase in the overall quality and cost of the final product. A vehicle is first judged on its design.

Currently, numerical simulations of forming processes are being used almost systematically in the development of industrial products. The studies, based on the modeling of physical phenomena involved in the manufacturing or the utilization of industrial products or infrastructures, answer the growing need to:

– decrease the duration of the product development cycle;

– optimize product development procedures;

– improve the productivity in design and manufacturing phases;

– improve product quality and process reliability;

– optimize testing and reducing its costs;

– simulate non-reproducible complex phenomena by means of trials.

The use of digital educational tools maintains a strong relationship with the training and research strategy (http://mediamef.insa-rouen.fr/).

This book presents the various methods for forming used in the industry: stamping, hydroforming and additive manufacturing and proposes a modeling of the latter by providing the theoretical and numerical advances for each process involving large deformation mechanics on the basis of large transformations. It presents the various techniques relative to the optimization and calculation of the reliability of different processes.

Acknowledgments

We wish to thank everyone who has directly or indirectly contributed to this book, in particular the engineering students and the PhD students of the INSA Rouen that we worked with in recent years.

Bouchaïb RADI
Abdelkhalak EL HAMI
June 2016

1

Forming Processes

1.1. Introduction

The field of metal forming comprises a wide range of semifinished and finished products. Each requirement of the acquisition criteria is defined, justifying the use of various forming processes. A number of recurring characteristics can be observed in the desired shapes. The latter should respond with the best dimensional precision possible and the most suitable surface condition for its usage. The final product must meet material health conditions for usage properties with the least possible continuity defects. There is, therefore, an interest in what the most appropriate macro- and microstructures are.

1.2. Different processes

Metallic materials offer a rich range of independent or combined forming methods. Among the large families, the following processes are identified:

– smelting;

– machining;

– powder metallurgy;

– hot or cold plastic strain forming.

Each of these processes present characteristics of optimal quality, variable depending on the material being used, on the dimensions and on the desired accuracy, on the metallurgical quality, on the final cost and on the quantity. The choice is oriented according to specific criteria:

Material Forming Processes: Simulation, Drawing, Hydroforming and Additive Manufacturing, First Edition. Bouchaib Radi and Abdelkhalak El Hami.
© ISTE Ltd 2016. Published by ISTE Ltd and John Wiley & Sons, Inc.

– the abilities of the material in relation to the different processes (particular attention should be given to the difference between a foundry alloy and alloys deemed “wrought”) regarding the form and the dimension of the product;

– the defined metallurgical health (limitation of defects such as cracks, porosities and chemical segregations);

– the usage properties of the product in the mechanical field;

– the desired surface condition (in terms of cleanliness, roughness, of residual stresses, etc.).

1.2.1. *Smelting*

The metal or the alloy is melted inside a crucible and then it is poured into a specific mold inside which it will solidify when cooled down. Complex forms can be obtained often linked with a minimum of induced thickness. Large variations of the latter involve consequences on the development of the final properties. Casting workpieces are produced from simple and often fairly cheap traditional techniques. This results in obtaining monobloc parts whose quality and mechanical properties are lower than those of wrought products (products having undergone hot hammering in order to obtain the desired properties often in a compulsory direction). There are numerous and very varied molding techniques depending on shape, quantities and on the quality requirements:

– The mold is made up of sand and inside it a cavity can be found that will represent the resulting piece. The first operation consists of building a pattern generating the shape of the desired casting by integrating the machining allowances and the useful drafts. The pattern represents the mold cavity left in the sand when the mold is closed. The mold is opened to extract the pattern therefrom and closed to the molten metal. When solidification is achieved after slow cooling, the mold is broken in order to retrieve the final product. One casting is thus obtained per mold.

– The mold is in metal and thus is reusable. The cooling proves to be much faster than the sand casting process. The pattern is obtained by machining the mass and with respect to the hollow parts, they can be achieved with eventually destructible cores.

– Die-casting integrates a metal mold but the filling of the pattern is ensured by means of a piston that pushes the liquid at high speed in a short period of time (a few $1/10$ of a second). A slight overpressure can be maintained in the

mold, which has the effect of properly feeding the pattern, while avoiding the design of a hot-top to perform this function. The mechanization of the process is total. On the other hand, the tools undergo very significant repeated efforts, which reduces their life expectancy ($20,000$–$50,000$ parts depending on the nature of the cast alloy).

– Centrifugal casting concerns all so-called revolution parts. The fundamental difference lies at the level of the introduction of liquid material, which is carried out along an axis around which the mold revolves. The centrifugal force promotes uniform filling. The structural composition is finer and full.

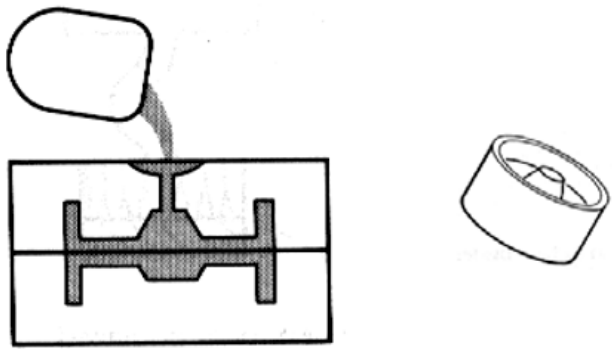

Figure 1.1. *Gravity die casting accompanied by the obtained casting*

1.2.2. *Machining*

Machining is a material removal operation making use of a cutting tool. This process allows for highly accurate complex forms and a controlled surface finishing. Different processes are identified and classified into two large categories. The first involves chip formation, which mainly includes turning, milling, grinding and drilling. The second does not involve chip formation and designates flow-turning, electrical discharge machining, shearing and waterjet cutting. From a structural point of view, machining only alters a superficial layer of the material, which therefore causes a hardening of the surface. As a result, we can observe the creation of a residual sublayer stress field, causing significant heating in the superficial layer. Ease of machining is linked to the

physical contact of the tool-workpiece pair during machining. It depends not only on the mechanical behavior of the material (resistance, consolidation and malleability of the machined material) but also on its thermal behavior. A low resistance is recommended, which means a sufficient malleability, however this facilitates chip breaking. It can also be noted that a good thermal conductivity most often facilitates the machining. As a result of adding cold or hot particles, the cutting conditions can be improved (controlled inclusions of low melting point lead or even sulfides, etc.). These latter facilitate the fragmentation of the chip:

– *Chip formation*: Machining takes place following optimized cutting conditions, which consider the geometry of the cutting tool, the cutting fluid and the dimension of the non-deformed chip. It is formed following primary shearing of the metal when making contact with the cutting edge of the tool and following a secondary shear when in contact with the external edge of the tool. This effort zone undergoes superficial strain hardening and heating. In addition, the chip is subjected to the same efforts coupled to the tool on its external edge. Futhermore, the cutting speed V_c plays a paramount role and is thus expressed:

$$V_c = \frac{n.\pi.d}{1000}$$

with V_c expressed in m/min, rotational speed in rpm and tool diameter for milling.

– *The machined surface*: It is defined by a heated and hard-tempered underlying superficial area. The microstructure can therefore be modified (constituents or phase change) or even undergo local strain hardening by cold working. Often, there remains a significant local residual stress field. Moreover, microcracks can be observed.

– *The chip*: When the material is fragile, it quickly becomes fragmented into lemels (for example some smeltings). In the event that it is ductile and slightly consolidates. However, when this consolidation occurs as a result of the hardening phenomenon, it easily fragments. On the other hand, a few obstacles to chip formation may surge notably due to heating and pressure. A galling phenomenon can be observed between tool and chip forming a build-up edge. It is defined by lemel stuck to the tool. Thus, the maximal temperature is variable according to the cutting speed and the hardness of the tool. The stress and strain field induced by the cutting enforces an increase in the temperature of the metal.

As a result to the cutting conditions, the tool is subjected to the following observations:

– adhesive wear;

– abrasive wear;

– damage due to atomic diffusion or to oxidation;

– damage due to thermal fatigue;

– irreversible deformation (creeping).

1.2.3. *Powder metallurgy*

This process consists of obtaining a final piece adapted to special needs by means of compression and sintering. From the agglomeration of very fine powders, a compacted object is produced with a form very close to that desired. Then, we control the cohesion of the powder with a thermal sintering process. Different applications can be identified, used in specific categories of workpieces:

– in cases where the production of controlled fine-porosity metal products with complicated forms is sought after;

– in pieces composed of refractory metals presenting a good resistance to heat;

– in alloys that cannot be obtained by smelting, notably tungsten or some magnetic materials such as soft magnetic metal ferrite composites. As an example, we can therefore cite cermets composed of “coarse” ceramics particles distributed in a metal matrix. In the field of cutting tools, we come accross cobalt matrix-based indexable lathe tools;

– in friction materials of which brake pads or clutch discs are made of;

– in electrical contact materials of which we can cite as an example silver- or copper-based contacts.

This technique is often used when some materials are hardly fusible or seldom deformable by plastic deformation. We then obtain products with improved microstructure, finer and more homogeneous than that observed by smelting as some nickel-based superalloys. It is also popular as an alternative with other forming processes to reduce production costs. As a matter of fact, metal losses and machining operations can be significantly optimized because it allows engineers to manufacture complexly shaped pieces with precise

dimensions using a single method. The latter is a very common method in the development of multiple products in mineral materials such as oxides, carbides and refractory products. It mainly enables the control of the porosity of the developed products. Two categories can be contrasted:

– weak microporous parts;

– massive parts with almost no porosity providing good mechanical properties as well as good ductility.

The process is defined as follows:

– *Powder production*: The shape and the grain size can vary between 1 and $1,000$ μm and are obtained by means of mechanical techniques involving the grinding of hard metals such as molybdenum (Mo) and chromium (Cr). The production can originate from a liquid phase by atomization of aluminum or copper. In addition, the process of atomization is defined by a drying operation that consists of transforming a liquid pulverized in the form of droplets in reaction with a hot gas into powder. It is operational in all processing industries of the material, particularly in the agrifood and the chemistry sectors. Its design is dependent on the properties of the product to be obtained and the characteristics of the drying gas as well as on the specifications of the powder.

– *Powder compaction*: This operation is compulsory to reduce the porosity. The latter is measured by the ratio $\delta = \frac{(V_a - V_r)}{V_a}$ where V_a is the apparent volume of the powder and V_r its actual material volume. The compaction is given by the following relation $\gamma = \frac{V_r}{V_a}$ and the expansion is $\frac{1}{\gamma}$. Powder forming is achieved by cold, hot and isostatic compression.

– *Powder sintering*: This step consists of forming while respecting the continuity of the solid. It is a process activated by solid-state atomic diffusion at a temperature ranging from 60 to 80% of that of fusion for a variable period according to the material under study. This energy is activated between the contact surfaces of the grains of powder and the shape of the pores is deformed until it is completely reduced.

As a whole, the process must be highly controlled due to the permanent risk of oxidation.

1.3. Hot and cold forming

Liquid casting, hot open-die forging and cold sheet metal forming have been documented as early as $5,000$ B.C. These are often relatively simple methods based on the use of molds, a hammering tool and a base. During the

first centuries of the Christian era, wire drawing by means of perforated plates and primitive machining using chisels were discovered. During the Renaissance, rolling dominated the industry because of its high productivity and its great versatility. Over the last century, the sector has been in full expansion, with an acceleration in the development of processes since 1940. As a matter of fact, the Germans invented cold forging (extrusion) of steels for the manufacture of weapons. Since 1945, machining has improved considerably and other processes such as electrical discharge machining or waterjet cutting have been invented. We would like to point out the discovery of hot melt spinning of copper alloys by the Frenchman Séjournet.

Forming ability is intrinsically linked to structural evolution, whether under the effect of thermomechanical processing or not, according to its three-dimensional plastic behavior. The latter is subjected to deformation speeds and imposed temperatures. It can be observed that compression efforts associated with the reduction of gradients of strain rate facilitate deformation without necking nor rupture. The literature discusses three major phenomena that have to be avoided:

– ductility generalized to fracture in mismatch with the targeted deformation amplitude. Deformation involving several steps separated by annealing is thus advocated;

– incompatible necking ductility with respect to localized deformation;

– sensitivity to strain rate inconsistent with the field of practiced speeds. Under optimal forming conditions, it is possible to take action on this field by decreasing the average rate or by lubricating the solicited surfaces with the aim to reduce the rate gradients between the edges and the center of the desired shape. Among these methods, we cite the following:

- *forming by plastic deformation*: this operation relies on hot or cold work in the plastic region of the metal. It allows that the product be obtained without metal loss in large productivity. There is a certain interest for very long parts or with a very small thickness. Plasticity is therefore an important property. Following a stress state, the plasticity criterion whose critical value is defined by the plastic flow constraint is verified. It is assumed at first that the volume remains invariant. It is applicable on the majority of metal alloys and implements numerous processes. In the case of massive products, the work is carried out by means of direct action of the pressure (open-die forging, discharge, stamping, forging, sheet rolling, wiring or extrusion). Through the indirect action of the pressure, we obtain traction-type processes such as wire-drawing and cold-drawing;

- *typical operational chain for the forming of steel*: it is particularly long and complex for the manufacture of steel for common use. It begins by obtaining a semifinished product by continuous casting at a relatively low speed and a relatively large section. These conditions are required by the exhaust speed of heat and the productivity rate. Then, a decrease in the transversal dimensions can be observed that is caused by rolling. It is defined as a continuous cycle of strong productivity. A first hot pass is necessary, then a cold one aiming for thinner products;

- *hot forming*: the recognized high quality of hot forming lies surely in its ability to endure very large deformations as a result of reduced efforts. On the other hand, it should be noted that the final dimensions remain inaccurate and the state of the surface is often altered (oxidation, decarburization, etc.). It is advised to carry out blasting as a finalizing solution. Overall, the metal does not present a good mechanical resistance with hot casting but this gives it a very significant malleability. We refer to hot forming when the temperature rises above 0.5 Tf (melting point). We are interested in the behavior of the material during and between the stages of plastic deformation by recrystallization or restoration. These individual or conjugate phenomena strongly decrease the hardening and the yield stress value decreasing according to the temperature. On the other hand, the yield stress becomes an increasing function with the plastic strain rate;

- *cold forming*: we refer to cold forming when the ambient working temperature is comprised between 0.15 Tf (melting temperature) and 0.3 Tf. We retain a structure that only works in the field of plastic deformation. This phenomenon is characterized by hardening by increasing the material yield stress. On the other hand, a decrease in ductility can be seen that is defined by its ability to endure plastic deformation without damage;

- *warm deformation*: an intermediate area is observable that is called warm deformation. In theory, this relates to taking advantage of hot forming (lower yield stress) and those of cold forming in order to harden the product by strain hardening. The method commonly used is by forging. This method is seldom used due to the big problems in formulating the necessary tools and lubricants, notably for all fairly ductile materials, but it is suitable for high-speed steels. It is possible to obtain forms and thicknesses for very varied products making use of forming techniques that often result in different characteristics. They differ by the tools being used and the strain and the rate fields associated with the operated directions as well as their amplitude (compression, traction, etc.). They are also limited each in their respective fields of productivity. Some examples include:

- *rolling*: this process is characterized by passing between the rolling mill cylinders in reverse rotation of the production of the flat (sheet) or long product (profiled). Rolling is qualified as discontinuous when it is effected through a single cage at a time or continuous through a number of several cages. The result is a product in the form of more or less thick sheets or of strips packaged in coils. The desired deformation is obtained after several passes and intermediate annealings (beams, rails, etc.);

- *forging*: this process is defined from a billet that is compressed by the pilon hammer or by hydraulic or mechanical presses. The forging is known as "open-die" when the deformation slopes are not subjected to any pressure. Forging can be done by dieing or stamping. A blank is compressed in a mold. In addition, die forging is recognized for the family of light alloys;

- *spinning and extrusion*: these two operating procedures, consisting of slow compression through a die, allow for reducing the cross-section of long products and giving them the desired final shape. In the case of high speeds, it is referred to as wire drawing since the aim is to obtain a calibrated wire in the coil form. This is the result of a pass through a suite of lubricated dies;

- *stamping*: it is advisable for complex workpieces with non-developable surfaces. The principle consists of a shaping punch penetrating a blank held in position, which will give the final form with the counter form called forming die. The efforts are often very important and can alter the structure; it is the reason why intermediate annealings are common practice. There are several forming areas determined by the orientation of the deformations, that is the expansion, the restraint or the extension. We can also observe the limits of the process according to the material used that can lead to necking (a phenomenon observed before the fracturing of a structure at the point where the value of the yield strength permissible by the material is reached) or fracture [CHE 08b].

1.3.1. *Influence of the static parameters*

1.3.1.1. *Stress level*

At least one stress level is imposed by the yield strength of the material under consideration. The latter evolves according to the hardening by means of work hardening directly linked with the deformation. There is a strain hardening exponent determined by tensile testing for each material. It follows a behavioral law for the generalized stress (Pa) that appears as a significant

factor notably for cold forming. We thus obtain, in three-dimensional plasticity without necking nor rupture at a given temperature:

$$\bar{\sigma} = k\bar{\varepsilon}^n \dot{\bar{\varepsilon}}^m \qquad [1.1]$$

where $\bar{\varepsilon}$ is the generalized strain, $\dot{\bar{\varepsilon}}$ is the generalized strain rate (in s^{-1}), m is the strain rate sensitivity coefficient and n is the work hardening coefficient.

1.3.1.2. *Stress triaxiality*

Stress triaxiality conditions the "confinement" of the material and delays the appearance and the multiplication of internal or surface microruptures. It is identifiable by means of the ratio $\frac{\sigma_m}{\sigma_{eq}}$ of the hydrostatic component $\sigma_m = \frac{(\sigma_1+\sigma_2+\sigma_3)}{3}$ (directly interfering on the elastic change of the volume) to the equivalent Von Mises stress (σ_{eq}) responsible for the change in shape.

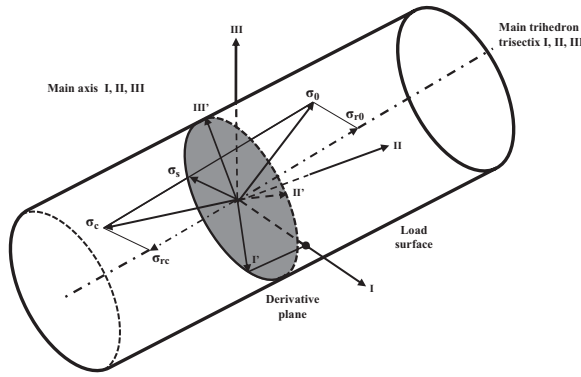

Figure 1.2. *Space of the principal stresses in the Von Mises cylinder with the state decomposition of depressive (σ_D) and compressive stress (σ_C) accompanied by its deviatoric (σ_S) and spherical components (σ_{TD} and σ_{TC})*

In the case of massive or long products, the formability limit increases with decreasing positive values as those of the uniaxial tension to the negative values of those spinning or forging. These latter, respectively, characterize the depressive mechanical state and the compressive mechanical state. Concerning the deformations, triaxiality can be estimated by a tensile test in which the two dimensions of the cross-section of a flat test piece are measured. The observed deformations are therefore inferred as well as the anisotropy coefficient $r(\varepsilon_1, \alpha) = \frac{\varepsilon_2}{\varepsilon_3}$ for a longitudinal stress ε_1 observing an

angle with the rolling direction. An average anisotropy coefficient r^* is specified for the flat products containing all of the directions α. The sheets are usually anisotropic, and we thus estimate the average coefficient by:

$$r^* = \frac{r(0^\circ) + 2r(45^\circ) + r(90^\circ)}{4} \qquad [1.2]$$

We obtain the following consequences:

– *consequences in rolling*: a single phase of plane strain is observed because the width of a sheet is not modified with this manufacturing process. The work hardening coefficient n plays an important role since it drives the effort of cold rolling. This may result in a deformation of the rolling mills. In contrast, in hot rolling the coefficient n is small;

– *consequences in stamping*: in this specific case, we are considering the field of planar stresses outside folding. The charges and the strains have very complex trajectories:

- it is possible to form in the region "in expansion", that is ε_2 comprised between 0 and ε_1 and σ_2 is located between σ_1 and $\frac{\sigma_1}{2}$,

- in "extension", the region spreads for ϵ_2 comprised between 0 and $-\frac{\epsilon_1}{2}$ for the strains and concerning that of the stresses, it positions itself for ϵ_2 comprised between $\sigma_1/2$ and 0,

- in the "restraint" area, ϵ_2 can be observed ranging between $-\varepsilon_1/2$ and $-\varepsilon_1$ and so as σ_2 be located between 0 and $-\sigma_1$,

- testing can be performed to determine the restraint with a limit deep-drawing ratio, increasing with n. Also, there is a biaxial test ($\varepsilon_1 = \varepsilon_2$) characterizing the expansion.

This coefficient n varies mostly according to the microstructure but little with the texture. It is observed that a high value of n improves the deformations by expansion. A high coefficient r^* depending on the texture for most metallic materials helps toward restraint deformations. Thus, when a high value of the two previous regions is combined, we can speak of optimum conditions for expansion forming.

– *consequences of strain rate*: local plastic strain rates are in direct relation to the strain modes and the usual operating parameters of machines. The strain is expressed by the following relation: $\frac{d\varepsilon}{dt}$ in s^{-1}. When the rate is high, it can be seen that the thermodynamic and the inertial efforts must be taken into

account. The yield stress varies according to the plastic strain rate following a power relation:

$$\sigma = C(\frac{d\varepsilon}{dt})^m \qquad [1.3]$$

where C is the plastic flow stress (Pa.s^{-1}).

1.3.2. *Hydroforming*

The signatory countries of the Kyoto protocol for the reduction of greenhouse gas emissions and the agreements of the COP(21) in Paris in 2015 have prompted the automotive industry to review their methods and their production technologies with the objective of meeting these new environmental standards. A decrease in fuel consumption can immediately lead to a reduction in the emission of gaseous pollutants. It is estimated that there is a 15% gain in consumption when the mass of the vehicle is reduced by 25%. The appearance of these new requirements has resulted in the development of new lighter grades in motor structures. As such aluminum alloys already make up the structural parts of several vehicles. Moreover, new grades of steel with high elastic yields offer a better specific weight resistance ratio than that of conventional steel.

In the spirit of reducing weight, an idea is being developed concerning a method which consists of the reduction of the number of elementary parts. As a result, we can note a decrease in primary material being used, of welding seam, or even of blank. Concretely, deep drawing finds its limitations in the production of complex forms in one single part. As a result, the hydroforming process proves to be indispensable with regard to quality as an alternative technology. This relatively new method makes both use of diverse and varied technologies. However, these are based on the same principle, that is to say that a liquid under pressure is injected for the forming of a primary piece that can be a tube, a blank or a preform. The hydroforming process is characterized by pressurizing a liquid that pushes the material, with a homogeneous distribution, called tool or die. This equipment is mounted on a hydraulic press specifically equipped with an injection system to ensure the closing in order to avoid any risks of leakage from the liquid. The tubes or the sheets are plastically deformed until obtaining the final piece. When comparing with deep drawing or die forging processes, there is no use of punches or intermediate forms. Four main variants can be noted in the implementation:

– *fixed-die hydroforming*: in this case, the pressurization of the fluid itself enables obtaining the final form;

– *mobile-die hydroforming*: this is the most commonly employed and the most technical process. The strain is assisted by the action of cylinders at the ends of the workpiece in constant relation with the internal pressure that acts simultaneously. There is therefore interest in this process and we will describe the main stages of the full forming cycle;

– *low-pressure hydroforming*: we refer to low-pressure expansion when it does not exceed $1,000$ bars;

– *high-pressure hydroforming*: we refer to high-pressure expansion when it does exceed $1,000$ bars. A thinning phenomenon can be observed in the thickness of the wall enduring the tension. High-tonnage presses are used for shutdown forces that can reach more than $10,000$ tonnes according to the surface projected of the workpiece to obtain.

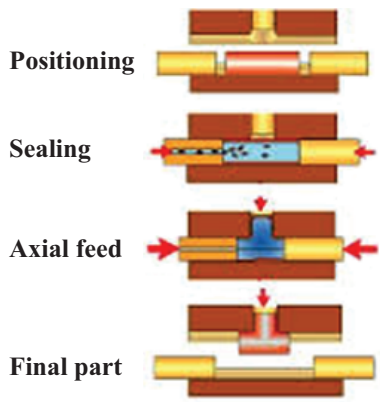

Figure 1.3. *Hydroforming principle*

1.3.3. *The limitations of the process*

We can identify two disadvantages in this process:

– *pleating effect known as "wrinkle"*: it occurs when the axial force is too high relative to the internal pressure. It can be eliminated by increasing the internal pressure;

– *buckling*: occurs when the axial force is too high for the length of the tube that is not supported or when changes in the geometry of parts are not symmetrical after the tube have reached plastic deformation or when the variations in friction states result in unbalanced deformation.

1.3.4. *Deep drawing*

Deep drawing is a sheet metal forming process in which a sheet metal blank is radially drawn in a forming mold by the mechanical action of a punch. This is therefore a form transformation process with retention material. The process is considered to be "deep" when the depth of the drawn part exceeds its diameter. This is achieved by redrawing the piece through a series of dies.

The flange region (sheet metal in the shoulder region of the die) undergoes a radial drawing stress and a tangential compression stress due to the material retention property. These compressive stresses cause flange wrinkles (first-order wrinkles). Wrinkles can be avoided by using a blank holder, whose function is to facilitate the controlled material flow within the radius of the sheet metal [MOR 10].

The total tensile load is composed of the ideal load and forming an additional component to compensate for frictions in the contact regions of the flange area and the bending forces as well as the inflexible forces at the level of the die radius. The forming load is transferred from the punch radius through the wall of the workpiece drawn in the deformation region.

In the wall of the drawn workpiece, in contact with the punch, the circumferential deformation is equal to zero by which the plane strain state is reached. In fact, most of the time the stress condition is only brought forward. Due to the tensile forces acting in the wall of the part, the thinning of the wall is important and results in an uneven thickness such that the wall thickness is the lowest where the wall of the part loses contact with the punch.

1.4. Experimental characterization

The most widespread development process of sheet metal is rolling. Due to its nature, this process provides a strong orientation according to the rolling direction to the grains constituting the material. The end results are rolled sheets characterized by fiber patterns at the microscopic scale and a texture, that is to say preferential crystallographic orientations.

The study of the behavior of these sheets is most often addressed within the context of an elastic–plastic approach for most of the processes of sheet-metal forming. The elastic–plastic theory itself comprises two different approaches describing each on a physical scale of the behavior: the first is called phenomenological approach (or macroscopic) and the second is called microscopic approach (or micro–macro model). The two approaches have the objective of describing the evolution of the stress and the strain state during a succession of deformations.

Within a phenomenological approach, the elastic–plastic behavior of the material is described by an envelope called initial charge surface. Defined in the stress space, this closed surface defines the elastic limit and the beginning of the plastic flow of the material for the different configurations of possible loading, it is a generalization of the uniaxial elastic limit. We introduce in the phenomenological approach the concept of the plasticity criterion that is nothing more than a mathematical description of the form of the initial charge surface. This criterion can be isotropic (von Mises, Tresca, Hosford criterion) or anisotropic. In addition, the Hill48 criterion [HIL 50] describes both general anisotropy and orthotropic anisotropy particular to rolled sheet metal. There are other anisotropic criteria [HOS 79, BAR 05] that contribute to the description of the orthotropic anisotropy and that differ among themselves by their form (quadratic or non-quadratic functional), the stress hypothesis in use (plane stress, 3D stress), the shear stress being taken into account or not, as well as by the number of parameters utilized in these criteria.

Once the shape of the initial charge surface is described by the plasticity criterion, the phenomenological approach introduces a work-hardening model for describing the evolution of the shape, size and position of the initial charge surface during the deformation. Although isotropic work hardening results in the expansion of the charge surface without any distortion of its form, anisotropic work hardening, such as kinematic hardening, describes the displacement of the charge surface without distortion, in the stress space [KOS 94]. Since the strain-hardening model is supposed to describe the update of the initial charge surface during charging, and that the latter is formed by a number of different stress states, this update thus has to be carried out for each of the stress states to a same value of an internal variable; this variable can be either work hardening [KOS 94], or the equivalent plastic work-hardening strain [KUR 00].

After the definition of the charge surface and the type of work hardening, the third hypothesis upon which the phenomenological approach relies is relative to the description of the plastic flow, which is the description of the

relationship, on the one hand, between the strain rate tensor, the stress rate tensor and the stress tensor. This is then referred to as the associated plastic flow rule when the plasticity criterion is considered as being the plastic potential, and to the non-associated flow rule if a second function other than the plasticity criterion is considered (most often the chosen function is of the same mathematical form as the plasticity criterion).

In contrast, within a microscopic approach, the macroscopic quantities such as the stress tensor and the strain tensor are typically deducted from the numerical modeling of the behavior of the grains constituting the material. Although this approach is becoming more consistent and is getting closer to the physics of plastic strains, it has a limited utilization due to the need for storage and the significant memory size as well as a prohibitive computational time. The phenomenological approach is more widespread because of its convenience, its relative ease of implementation, its speed but also often because of the sufficient accuracy of its results. Futhermore, the two approaches can be complementary to the extent where the microscopic study enables for understanding the mechanisms of plastic deformation and validating phenomenological models.

1.5. Forming criteria

The function of these criteria is to judge the capacity of a sheet to endure the different possible strains during forming:

– *Conventional criteria*: These are the fastest and the cheapest to implement because they mainly consist of simple tests on the blank that tend to reproduce as much as possible the strains occurring in pressing. We mainly use the following tests:

– Rockwell hardness (HRB index);

– stress–strain (yield point Re);

– tensile strength Rm;

– elongation at break A (%);

– Erichsen's deep-drawing (index IE).

This type of criterion provides only a single element and therefore only provides a low accuracy in the study of the blank. Nevertheless, by only considering these tests, it is possible to bring forward a number of essential characteristics of the metal. The metal has to exhibit a very high fracture

toughness in order to resist uniaxial tensile strength, a low yield point (because in the plastic field, despite being the lowest possible to avoid fractures, the exercised strains have nonetheless to be above the yield point), significant elongations and low resistance to the tangential compression in the blank holder (that is a good capacity to restraint).

– *Combined criteria*: They are not merely accepting separate parameters but make use of combinations of conventional factors. We thus find criteria such as Re/Rm, Rm-Re, (Rm-Re)*A, etc. They contribute with higher accuracy to the characterization of forming but require a larger number of experiments and materials.

– *Rational criteria*: These are the most difficult and the most expensive to determine but they are the ones that offer the best judgment to the forming of sheet metal. Two can be found: the strain-hardening n and the anisotropy r coefficients.

The strain-hardening coefficient n is linked to the consolidation of the material. Note that strain-hardening increases fracture toughness as well as the yield strength that gets closer to fracture toughness. If two sheets having the same value of n but different elasticity coefficient k are formed, they will behave in a similar manner despite of the different forming forces. Thus, this criterion can determine the capacity of a sheet to be implemented. It is obtained from the rational stress–strain curve connecting the relation $\sigma = \frac{F}{S}$ to the rational strain $\varepsilon = \ln(\frac{S}{S_0})$ (where σ is the stress, F is the applied force and S is the actual cross-section).

In the general case, it uses two successive formulas of the form:

$$\sigma = \sigma_0 + k.\varepsilon_0 \quad \text{or} \quad \sigma = k(\varepsilon_0 + \varepsilon)^n \qquad [1.4]$$

In the simplest case, the work-hardening coefficient n is also equal to the rational elongation at the end of the uniform distributed elongation ε_u at the maximum of the charge elongation curve. When $\frac{dF}{dl} = 0$, the derivation of $\sigma = k\varepsilon_0$ leads to $\varepsilon_u = n$.

It is therefore shown that this criterion is justified to characterize sheet metal forming, but it should be accompanied by a criterion characterizing the biaxial stress instability, that is to say the appearance of necking.

The plastic strain anisotropy r of sheet metal plays an important role in characterizing a sheet. The extent of this criterion has been highlighted by

means of the strain analysis of the blank on the blank holder (restraint) in the walls of a cup or at the poles of the drawn (expansion).

Due to the preferential orientation of the crystals, the plate does not have the same mechanical properties according to the direction under consideration. It also results in a loss in the equilibrium of the strains between the width and the thickness during a uniaxial strain–stress test. It is on this point that we have decided to base the second deep-drawing criterion:

$$r = \frac{\ln(\omega/\omega_0)}{\ln(e/e_0)} \qquad [1.5]$$

with (ω) the width and (e) the thickness.

Figure 1.4 shows the variation of the anisotropy coefficient r in the sheet-metal blank with a value of the angle between the tensile test direction and the rolling direction. These curves represent the three possible cases in the case of low-carbon steel for forming:

– curve (1) in Figure 1.4 corresponds to the general case, that is to say, where r reaches a minimum. This is characterized by a drawn with 4 ears at $0°$ and $90°$;

– curve (2) in Figure 1.4 represents the case in which r reaches a maximum, that is to say, where the sheet presents two $45°$ ears;

– curve (3) in Figure 1.4 represents the case in which r increases between $0°$ and $90°$. In the latter case, the sheet presents two ears at $90°$.

This criterion, if high, would therefore indicate a strong resistance to thinning from the sheet metal and a large ability to deform before necking.

1.5.1. *Influence of the structure of sheet metal*

Thin sheets are polycrystalline aggregates. Their forming, as well as all of their characteristics, depends to a large extent on these aggregates:

– *Influence of the grain size*: Grain size is one of the most important parameters. Actually, it has an effect on the yield point and on the tensile strength which are (conventional) criteria of drawability. It should be added that, in the case of low-carbon steel, it is possible to relate the drawing coefficient to the size of the grains as follows and it should be recalled that if d (average grain size) increases, a change in structure occurs causing an increase

in r. It is however necessary to note that if the grains are too significant, a surface defect appears. It is called "orange peel" and it is characterized rise by a blurred and undulating surface.

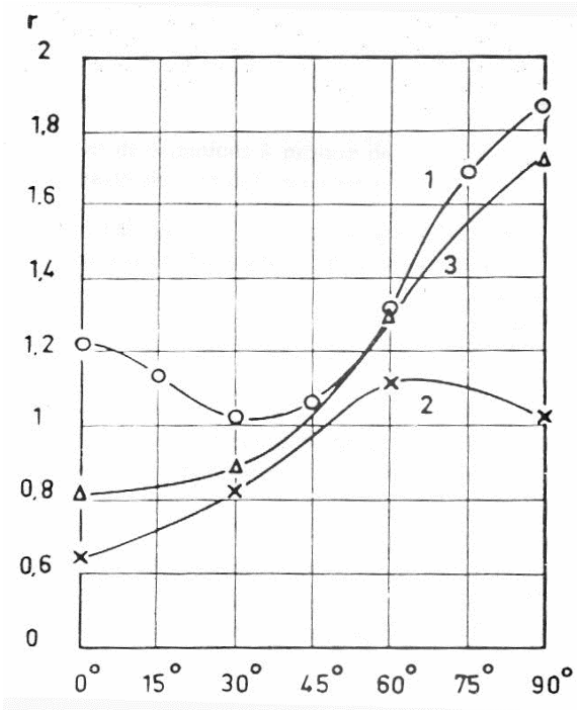

Figure 1.4. *Variation of r according to the rolling direction*

– *Influence of the crystallographic structure*: As mentioned previously, the crystallographic orientation is a non-negligible parameter. It occurs not only at the work-hardening level but also on the characteristics Re, Rm, A, etc. Work hardening of sheet metal occurring during annealing or rolling is responsible for the crystallographic direction of the grains and therefore for the preferential tensile directions or other similar tests.

– *Springback*: When the punch withdraws after forming, the piecework thus formed part is no longer subject to the retention force. A shrinkage of the material then occurs due to the elastic deformation of the primitive blank and resulting from residual stress after forming. This is then referred to as springback. It manifests itself in bent workpieces, cylindrical workpieces (inner diameter of the piece greater than the diameter of the punch) and in slightly deformed large dimension workpieces. This phenomenon is easily

verifiable by means of a controlled stress–strain test. Indeed, if the test is stopped before the fracturing of the test piece and the stress is sufficient to exceed the yield point, the length of the test piece will be greater than its initial length but less than that obtained at the end of the test. The test piece undergoes a springback corresponding to the strain it suffered prior to its yield. In order to obtain a piece of dimensions corresponding to the expectations, it is thus important to take this phenomenon into consideration. To mitigate this phenomenon, it is common use to resort to some artifacts such as coining, bottom bending or extended maintaining of the punch. This phenomenon is so significant that the yield point of the material is itself increased (case of stainless steels compared to mild steels);

– *Other influential elements*: The presence of alloy elements in solid solution in ferrite increases the yield, tensile strength and reduces the elongation. These elements may have a significant indirect influence by modifying the conditions of the recrystallization and grain growth, in the texture, during annealing. Similarly, the second phase particles are of great importance in the ability of a sheet to be deep-drawn. This influence depends on their size and distribution. Thus, fine particles will likely impair the drawability (an increase in Re and Rm and a decrease in A and n) and clusters of non-negligible size may result in tearing or fractures.

1.5.2. *Physical strain mechanisms*

The observed macroscopic behavior is actually the result of local deformations on a microscopic scale. This microscopic aspect is fundamental for the physical understanding of phenomena:

– *elastic strains*: correspond to variations of interatomic spaces and reversible movements of dislocations. These strains are essentially instantly reversible; the initial configuration is recovered after discharge;

– *viscous deformations*: correspond to the undergoing deformation while the charge is constant; there is no more equilibrium. Time and strain rates play an important role in the laws of behavior of a viscous material. When this phenomenon is favored by thermal activation, it is referred to as creep flow;

– *permanent strains*: correspond to irreversible movements of dislocations. These displacements occur when the crystallographic planes slip (plane of greater atoms density). In practice, these movements do not alter the crystal structure and the volume remains unchanged; it is referred to as plastic incompressibility;

– *strain hardening*: this phenomenon corresponds to an increase in the number of bottlenecks in the dislocations motion. It counteracts the increase in the number of dislocations and modifies the threshold beyond which the deformations are no longer reversible;

– *restoration*: this phenomenon corresponds to a recrystallization by regrouping opposite sign dislocations. It occurs over time and is favored by thermal activation;

– *conventional yield strength*: unlike the yield strength Re, the conventional yield strength is defined as the yield obtained when the strain reaches 0.2% of the initial length. However, the yield strength is the stress delimiting the elastic limits of the other limit regions and defines the range of validity of Hooke's law.

1.5.3. *Different criteria*

The determination of a criterion is particularly delicate. There is unfortunately no universal criterion that integrates all the experimental results. Even if it was possible to determine such a criterion, it is feared that the cost of preparation and the utilization costs would not be admissible at the industrial level. Indeed, the determination of the various yield points associated with the different tests makes use of more or less sophisticated testing machines that can prove expensive. Moreover, it is preferable to use criteria that only involve one or two trials and that are simpler to implement. We are then fully aware that we are losing some accuracy, but this loss has to be relativized with regard to the uncertainties of the experimental measurements of the yield points, or when determining the characteristic quantities of the law of behavior:

– *Von Mises criterion*: This criterion is based on the last observation regarding the isotropic compression and the strain energy. As there is no limit, it is necessary that this criterion allows quantifying the strain energy that is not depending on the isotropic compression. Based on the results obtained by the experiment, namely that we modify the volume without modifying the form, it can be shown that the stress tensor as the strain tensor is purely spherical. The deviatoric parts are non-existing. The idea associated with the Von Mises criterion is therefore to limit the deviatoric elastic strain energy, that is to say that obtained from deviatoric tensors. According to the principal stresses, we obtain:

$$(\sigma_1 - \sigma_2)^2 + (\sigma_1 - \sigma_3)^2 + (\sigma_3 - \sigma_1)^2 \leq 2\sigma_e^2 \qquad [1.6]$$

Depending of the form of the stress tensor, the Von Mises criterion will assume different notations. In the general case, it is written in the following manner:

$$\sigma_{eq} = \sqrt{\frac{1}{2}\left[(\sigma_{11}-\sigma_{22})^2+(\sigma_{22}-\sigma_{33})^2+(\sigma_{33}-\sigma_{11})^2+6\left(\sigma_{12}^2+\sigma_{13}^2+\sigma_{23}^2\right)\right]} \quad [1.7]$$

The equivalent strain must naturally be smaller than the plastic flow stress to remain in the elastic limits of the material.

– *Tresca's criterion*: This criterion is based on a limitation of shear at one point. It amounts in fact to limiting the radius of the largest of Mohr's circles and due to this fact it is particularly well suited to shear stresses such as beam torsion. Its expression is simply given in main stresses ordered by the formula:

$$\frac{\sigma_1-\sigma_3}{2} \leq \tau_e \quad [1.8]$$

Such as for the Von Mises criterion, we are confronted with a simple criterion to define and to implement but that does not consider taking into account the complexity of the different test results. In particular, as for the previous criterion, it can be observed that there is no limitation to isotropic tensile stress, which contradicts the experimental results.

2

Contact and Large Deformation Mechanics

2.1. Introduction

Generally, the problems with forming consist of large transformation problems. In this chapter, we present the formulations adopted. A formulation in convective coordinates is used to denote the mechanical equations of the problem. It is shown that this type of formalism facilitates the notation of large transformation and large deformation equations.

Based on the basic notions of continuum kinematics in large transformations, the solution of behavioral and structural equilibrium problems can be obtained with an incremental notation.

In the concept of large transformations, both configurations, actual and "reference", are not confused. This chapter discusses the choice of the strain tensors and the deformations to be used in order to have a coherent formulation that respects the principles of physics, such as material indifference. We present a rigorous notation of the expression of the stress tensor defined from the current configuration according to the stress tensor defined from the reference configuration and the increment of the stresses.

2.2. Large transformation kinematics

There are two different ways to describe the kinematics of a solid subjected to large transformations. This solid occupies at the instant t_0, before

Material Forming Processes: Simulation, Drawing, Hydroforming and Additive Manufacturing, First Edition. Bouchaib Radi and Abdelkhalak El Hami.
© ISTE Ltd 2016. Published by ISTE Ltd and John Wiley & Sons, Inc.

transformation, a configuration C_0, and at the current instant t it occupies a configuration C_t.

The first method, which is also the most widely used, consists of providing each of these configurations with a system of spatial coordinates. These systems are chosen to be Cartesian, and both configurations can be represented in the same reference frame, which is usually orthonormal. The coordinates defined in C_0 are called Lagrangian coordinates and those defined in C_t Eulerian coordinates. The equations and the problem variables can be denoted in one or the other configuration. This is thus referred to as Lagrangian or Eulerian formalism.

The second method considers that all the quantities are expressed, relative to a material referential system that evolves in time, in a curvilinear coordinate system called material or convective coordinates. This formalism is well adapted to the kinematics of large transformations.

2.2.1. *Kinematics of the problem in spatial coordinates*

To describe the motion of a solid that occupies a domain Ω_0 at instant t_0 and a domain Ω at instant t, X denotes the Lagrangian coordinate system, x the Eulerian coordinate system and an application denoted ϕ is introduced such that $\phi(\vec{X}) = \vec{x}$, which is assumed to be differentiable with respect to X. This application connects the Lagrangian coordinate system X to the Eulerian system x. The vector $\vec{x}$ position of a point M at instant t is the image (or the transform) of the vector $\vec{X}$ position of M at instant t_0.

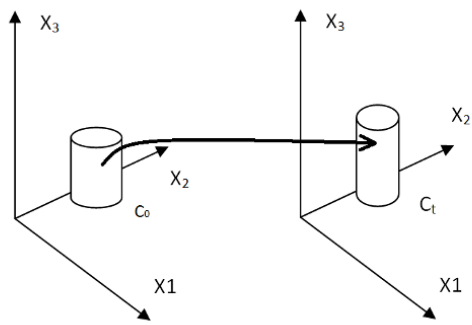

Figure 2.1. *Deformation of a solid, spatial coordinates*

Let $\vec{x}$ be the position vector of a point M at instant t. $\vec{x} = \varphi(\vec{X}, t)$ is also written as: $x_i = \varphi_i(X_j, t)$ with X_j the Lagrangian variables. If we write the equations of the problem in C_0, this is referred to as a Lagrangian description and x_i are the Eulerian variables. When writing the equations of the problem in C_t, this is referred to as a Eulerian description.

2.3. Transformation gradient

It is the tangent linear application that allows moving from C_0 to C_t; it is defined by:

$$d\vec{x} = \mathbb{F}(X, t)d\vec{X} \qquad [2.1]$$

$\mathbb{F}$ is the gradient tensor of the transformation: $X \to x = \varphi(X, t)$

$$(2.1) \Longleftrightarrow dx_i = \frac{\partial \varphi_i(X, t)}{\partial X_j} dX_j \qquad [2.2]$$

We denote $F_{ij}(X, t) = \frac{\partial \varphi_j(X,t)}{\partial X_j}$.

This application allows the transformation laws of volume and surface to be established. In effect, if we denote $J = \det\mathbb{F}$, dV and dS the volume and surface elements at instant t, dV_0 and dS_0 the volume and surface elements at instant t_0, $\vec{n_0}$ the unit normal of dS_0, we get: $dV = JdV_0$ and $\vec{n}dS = J\mathbb{F}^{-1}\vec{n_0}dS_0$.

Let $\vec{u}$ be the displacement vector between C_0 and C_t, defined by:

$$\vec{x} = \varphi(\vec{X}) = \vec{X} + \vec{u}(X) \qquad [2.3]$$

the tensor $\mathbb{F}$ is expressed with respect to $\vec{u}$ in the following manner:

$$\mathbb{F} = \mathbb{I} + \mathbb{H}(X, t) \qquad [2.4]$$

with $H_{ij} = \frac{\partial u_i}{\partial X_j}$ and $\mathbb{I}$ the identity tensor.

2.4. Strain measurements

The variation of the scalar product of two elementary vectors between C_0 and C_t makes it possible to calculate the variations of the angles and the lengths and therefore to characterize the change in form of the solid.

Let $d\vec{X}$ and $\delta\vec{X}$ be two material vectors defined in C_0, $d\vec{x}$ and $\delta\vec{x}$ two material vectors defined in C_t. We obtain:

$$(d\vec{x}, \delta\vec{x}) = dx_i \delta x_i = F_{ij} dX_j F_{ik} \delta X_k = (\overrightarrow{dX}, \mathbb{C}\overrightarrow{\delta X}) \quad [2.5]$$

with $C_{ik} = F_{ij}F_{ik}$, or even $\mathbb{C} = \mathbb{F}^T\mathbb{F}$, where $\mathbb{F}$ denotes the transpose of $\mathbb{F}$.

$\mathbb{C}$ is called the expansion tensor or the right Cauchy–Green tensor. It allows the deformations to be described in the reference configuration C_0:

$$(\overrightarrow{dX}, \overrightarrow{\delta X}) = (\overrightarrow{dx}, \mathbb{B}^{-1}\overrightarrow{\delta x}) \quad [2.6]$$

where $\mathbb{B} = \mathbb{F}\mathbb{F}^T$ is the left Cauchy–Green tensor. It is used to describe the strains in the configuration C_t.

To measure the strains suffered by the solid between C_0 and C_t, we introduce:

– the Green–Lagrange strain tensor defined on C_0 and denoted $\mathbb{E}$;

– the Euler–Almansi strain tensor defined on C_t and denoted $\mathbb{A}$, these two tensors are defined by:

$$(\overrightarrow{dx}, \overrightarrow{\delta x}) - (\overrightarrow{dX}, \overrightarrow{\delta X}) = 2(\overrightarrow{dX}, \mathbb{E}\overrightarrow{\delta X}) = 2(\overrightarrow{dx}, \mathbb{A}\overrightarrow{\delta x}) \quad [2.7]$$

It can be derived that: $\mathbb{E} = \frac{1}{2}(\mathbb{C} - \mathbb{I})$; $\mathbb{A} = \frac{1}{2}(\mathbb{I} - \mathbb{B}^{-1})$

NOTE 2.1.– $\mathbb{A} = \mathbb{F}^{-1T}\mathbb{E}\mathbb{F}^{-1}$ and if $\mathbb{F} = \mathbb{I}$, we obtain $\mathbb{E} = \mathbb{A} = \mathbb{O}$

2.4.1. *Polar decomposition of* $\mathbb{F}$

Given a tensor $\mathbb{F}$ defined as positive, there exists $\mathbb{V}$, $\mathbb{U}$, $\mathbb{R}$, which are unique such that:

$$\mathbb{F} = \mathbb{V}\mathbb{R} = \mathbb{R}\mathbb{U}. \quad [2.8]$$

$\mathbb{R}$ is an orthogonal tensor called the rotation tensor. $\mathbb{V}$ and $\mathbb{U}$ are the pure left and right strain tensors, respectively. They are both symmetric positive definite. It can be observed that $\mathbb{C} = \mathbb{F}^T\mathbb{F} = \mathbb{U}^2$ and $\mathbb{B} = \mathbb{F}\mathbb{F}^T = \mathbb{V}^2$.

Tensors $\mathbb{C}$ and $\mathbb{U}$ describe the strain in C_0, $\mathbb{B}$ and $\mathbb{V}$ in C_t. They also make it possible to define a more general family of strain tensors, denoted e_α and $\hat{e}_\alpha$, by:

$$e_\alpha = \frac{1}{\alpha}(\mathbb{U}^\alpha - \mathbb{I}), \quad \hat{e}_\alpha = \tfrac{1}{\alpha}(\mathbb{V}^\alpha - \mathbb{I}), \quad \text{for } \alpha \neq 0, \qquad [2.9]$$

$$e_0 = \log(\mathbb{U}), \qquad \hat{e}_0 = \log(\mathbb{V}), \qquad \text{for } \alpha = 0 \qquad [2.10]$$

Tensors $\mathbb{E}$ and $\mathbb{A}$ are, respectively, e_2 and $\hat{e}_2$.

NOTE 2.2.– With the small perturbation hypothesis (S.P.H.), we obtain:

$$e_\alpha = \hat{e}_\alpha = \mathbb{I}, \ \mathbb{B} = \mathbb{C} = \mathbb{I} + 2\varepsilon \qquad [2.11]$$

with $\varepsilon = \frac{1}{2}(\mathbb{H} + \mathbb{H}^T)$, and $\mathbb{R} = \mathbb{I} + \mathbb{W} = 1 + \frac{1}{2}(\mathbb{H} - \mathbb{H}^T)$.

2.4.2. *Strain rate tensor*

We introduce the rate vector $\overrightarrow{V}$, derived with respect to the time of $\vec{x} = \varphi(\vec{X}, t)$. That is, $\vec{V} = \frac{\partial \vec{x}}{\partial t} = \frac{\partial \varphi(\vec{X},t)}{\partial t}$.

If we define the tensor $\mathbb{L}$ by:

$$\dot{\overrightarrow{dx}} = \dot{\mathbb{F}}d\vec{X} = \dot{\mathbb{F}}\mathbb{F}^{-1}d\vec{x} = \mathbb{L}d\vec{x}, \qquad [2.12]$$

with $\dot{\mathbb{F}} = \frac{\partial \mathbb{F}(\vec{X},t)}{\partial t}$, we obtain:

$$\nabla_X \vec{V} = \frac{\partial \vec{V}}{\partial X} = \dot{\mathbb{F}} \text{ and } \nabla_X \vec{V} = \frac{\partial \vec{V}}{\partial X} = \nabla_X \vec{V}\mathbb{F}^{-1} = \dot{\mathbb{F}}\mathbb{F}^{-1} \Rightarrow \mathbb{L} = \nabla_X \vec{V}.$$

$\mathbb{L}$ is called the strain rate tensor.

2.4.3. *Canonical decomposition of* $\mathbb{F}$

The tensor $\mathbb{L}$ is written as:

$$\mathbb{L} = \mathbb{L}^S + \mathbb{L}^A \qquad [2.13]$$

where

$$\mathbb{L}^S = \frac{1}{2}(\mathbb{L} + \mathbb{L}^T), \qquad [2.14]$$

and

$$\mathbb{L}^A = \frac{1}{2}(\mathbb{L} - \mathbb{L}^T) \qquad [2.15]$$

$\mathbb{D}$ is the strain rate tensor, it is a Eulerian measure of the strain rate. $\mathbb{W}$ is the rotation rate tensor, it is a Eulerian measure of the rotation rate.

NOTE 2.3.– By definition of $\mathbb{D}$ and $\mathbb{E}$, it yields:

$$\frac{\partial \mathbb{E}}{\partial t} = \dot{\mathbb{E}} = \mathbb{F}^T \mathbb{D} \mathbb{F} \qquad [2.16]$$

$\dot{\mathbb{E}}$ is a Lagrangian measure of the strain rate.

2.4.4. *Kinematics of the problem in convective coordinates*

DEFINITION 2.1 (Material basis).– *We call the natural basis in M the vector system:*

$$g_\alpha = \frac{\partial OM}{\partial X^i} \qquad [2.17]$$

Let M_0 be the position of a point at instant t_0, and M that at instant t. Let $\alpha = 1, 2, 3$. At instant t_0, we have:

$$\overrightarrow{dM_0} = \frac{\partial \overrightarrow{OM}_0}{\partial X^\alpha} dX^\alpha = g^0_\alpha dX^\alpha \qquad [2.18]$$

We denote its dual g_0^α defined by:

$$(g_0^\beta, g_\alpha^0) = \delta_\alpha^\beta \quad (\delta_i^j \text{ represents the Kroenecker symbol}) \qquad [2.19]$$

At instant t, we have:

$$\overrightarrow{dM} = \frac{\partial \overrightarrow{OM}}{\partial X^\alpha} dX^\alpha = g_\alpha dX^\alpha \qquad [2.20]$$

2.4.5. *Transformation tensor*

DEFINITION 2.2.– *The bijective application that associates with any point M_0 of Ω_0 the point M_t of Ω_t is called the transformation and it is denoted as $f_{0,t}$:*

$$f_{0,t} : \Omega_0 \to \Omega_t$$
$$M_0 \mapsto f_{0,t}(M_0) = M_t$$

Let $\overrightarrow{dM_0}$ be a material vector defined at instant t_0, which is transformed into $\overrightarrow{dM}$ at instant t. The gradient tensor of the transformation denoted as $\mathbb{F}$ is verified by definition: $\overrightarrow{dM} = \mathbb{F}\overrightarrow{dM_0}$.

NOTE 2.4.– If a system of Cartesian coordinates x_i is defined relative to a basis $\vec{e}_i$ such that a material vector $\overrightarrow{dX}$ is written, $\overrightarrow{dX} = dx^i \vec{e}_i$, it yields:

$$\overrightarrow{dX} = dx^i \vec{e}_i = dX^\alpha g_\alpha = \frac{\partial x^i}{\partial X^\alpha} dX^\alpha \vec{e}_i = F_\alpha^i dX^\alpha \vec{e}_i \Leftrightarrow g_\alpha = F_\alpha^i \vec{e}_i \qquad [2.21]$$

F_α^i is the transition matrix from $\vec{e}_i$ to g_α; it is also the representative of $\mathbb{F}$ in the basis $\vec{e}_i \otimes g_0^\alpha$. It then yields: $\mathbb{F} = F_\alpha^i \vec{e}_i \otimes g_0^\alpha$.

On the other hand, we have $\delta_\alpha^\delta = F_\alpha^i \vec{e}_i g^\delta$; by multiplying this expression by $\vec{e}^j$ (with $\vec{e}^j \vec{e}_i =)\delta_i^j$), we obtain:

$$\delta_\alpha^\delta \vec{e}^j = F_\alpha^i g^\delta \delta_i^j = F_\alpha^j g^\delta = F_\alpha^j g^\alpha \delta_\alpha^\delta, \qquad [2.22]$$

Then, $\vec{e}^j = F_\alpha^j g^\alpha$.

These equations allow moving from a notation in convective coordinates to a notation in spatial coordinates. It is obvious that the two notations are equivalent.

2.4.5.1. *Convective transport*

Convective transport expresses the correspondence between the initial and current positions of the material elements.

DEFINITION 2.3 (Contravariant convective transport).– *We say that* $V' = V^{\alpha} g_{\alpha}$ *is obtained by contravariant convective transport of* V *if* $V = V^{\alpha} g^0_{\alpha}$.

Similarly, a tensor $\mathbb{M}' = M^{ij} \overrightarrow{e_i} \otimes \overrightarrow{e_j}$ is obtained by contravariant convective transport of a tensor of $\mathbb{M}$ if $\mathbb{M} = M^{ij} g^0_{\alpha} \otimes g^0_{\beta}$.

The contravariant convective transport is denoted Φ^c such that $\Phi^c(\mathbb{M}) = \mathbb{M}'$. The inverse transport is noted Ψ^c, and we have $\Psi^c(\mathbb{M}') = \mathbb{M}$.

DEFINITION 2.4 (Covariant convective transport).– *A tensor* $\mathbb{M}' = \mathbb{M}_{\alpha\beta} g^{\alpha} \otimes g^{\beta}$ *is obtained by covariant convective transport of a tensor* $\mathbb{M}$ *if the latter is written as:* $\mathbb{M} = M_{\alpha\beta} g^{\alpha}_0 \otimes g^{\beta}_0$.

The covariant convective transport is denoted Φ^*_c such that: $\Phi^*_c(\mathbb{M}) = \mathbb{M}'$. The inverse transport is noted Ψ^*_c, and we have $\Psi^*_c(\mathbb{M}') = \mathbb{M}$.

2.4.5.2. *Convective derivatives*

The convective derivative is obtained by simple derivation with respect to time. It consists of considering a Lagrangian description and then of returning to a Eulerian description to obtain the desired Eulerian form, using a particular derivative, within a Eulerian description.

DEFINITION 2.5 (Contravariant convective derivative).–

– The contravariant convective derivative of a tensor $\mathbb{M} = M^{\alpha\beta} g_{\alpha} \otimes g_{\beta}$ *is written as:*

$$D^c \mathbb{M} = \Phi^c \left(\frac{d\Psi^c(\mathbb{M})}{dt} \right) = \frac{dM^{\alpha\beta}}{dt} g_{\alpha} \otimes g_{\beta} \qquad [2.23]$$

– The contravariant convective derivative of a vector $V = V^{\alpha} g_{\alpha}$ *is written as:*

$$D^c V = \frac{dV^{\alpha}}{dt} g_{\alpha} \qquad [2.24]$$

DEFINITION 2.6 (Covariant convective derivative).– *The covariant convective derivative of a tensor* $\mathbb{M} = \mathbb{M}_{\alpha\beta} g^{\alpha} \otimes g^{\beta}$ *is defined by:*

$$D_c\mathbb{M} = \Phi_c^* \left(\frac{d\Psi_c^* (\mathbb{M})}{dt} \right) = \frac{dM_{\alpha\beta}}{dt} g^{\alpha} \otimes g^{\beta}$$

2.4.5.3. *Strain tensor*

Let $\overrightarrow{dM_0}$ a material vector defined in the initial configuration and $\overrightarrow{dX}$ its transformed in the current configuration (at instant t); as a result, we get:

$$\overrightarrow{dX}^2 - \overrightarrow{dX^0}^2 = \left(g_{\alpha\beta} - g^0_{\alpha\beta} \right) dX^{\alpha} dX^{\beta} \qquad [2.25]$$

with: $g_{\alpha\beta} = g^{\alpha}.g^{\beta}$ and $g^0_{\alpha\beta} = g^0_{\alpha}.g^0_{\beta}$.

We thus obtain the definition of the strain material tensor:

$$e_{\alpha\beta} = \frac{1}{2} \left(g_{\alpha\beta} - g^0_{\alpha\beta} \right)$$

in the case where g^0_{α} coincides with the Cartesian basis e^0_{α}, we obtain: $e_{\alpha\beta} = \frac{1}{2}(g_{\alpha\beta} - \delta_{\alpha\beta})$.

Based on $e_{\alpha\beta}$, we write all the strain measures that have already been previously introduced. In effect, it can be shown that:

– the Green–Lagrange tensor is written as:

$$\mathbb{E} = e_{\alpha\beta} g_0^{\alpha} \otimes g_0^{\beta}$$

– and the Euler–Almansi tensor is written as:

$$\mathbb{A} = e_{\alpha\beta} g^{\alpha} \otimes g^{\beta}.$$

$\mathbb{A}$ is therefore obtained by covariant convective transport $\mathbb{E}$. We write: $\mathbb{A} = \Phi_c^*(\mathbb{E})$. Similarly, we have: $\mathbb{E} = \Psi_c^*(\mathbb{A})$ and it can be easily verified that:

$$\mathbb{E} = \mathbb{F}^T \mathbb{A} \mathbb{F}, \qquad \mathbb{A} = (\mathbb{F}^{-1})^T \mathbb{A} \mathbb{F}^{-1}.$$

Reconsidering the case where the initial frame of reference is orthonormal (g_α^0 coincides with a Cartesian coordinate system), we obtain $g_\alpha^0 = g_0^\alpha = e_i^0 = e_0^i$,

$$\mathbb{E} = \frac{1}{2} g_{\alpha\beta} g_0^\alpha \otimes g_0^\beta - \frac{1}{2} \delta_{\alpha\beta} g_\alpha^0 \otimes g_\beta^0, \qquad [2.26]$$

$\delta_{\alpha\beta} g_\alpha^0 \otimes g_\beta^0 = \mathbb{I}$, the identity tensor, and it has been previously shown that $g_{\alpha\beta} g_0^\alpha \otimes g_0^\beta = \mathbb{F}^T \mathbb{F}$, then:

$$\mathbb{E} = \frac{1}{2} (\mathbb{F}^T \mathbb{F} - \mathbb{I}). \qquad [2.27]$$

We thus recover the expression of the Green–Lagrange tensor.

2.4.6. *Strain rate measures*

The rate of the material strain tensor, expressed in the current configuration, is:

$$\dot{e}_{\alpha\beta} g^\alpha \otimes g^\beta = \frac{1}{2} \dot{g}_{\alpha\beta} g^\alpha \otimes g^\beta \qquad [2.28]$$

The covariant convective derivative of $\mathbb{A}$ is written as:

$$D_c \mathbb{A} = \Phi_c^* \left(\frac{d\Psi_c^* (\mathbb{A})}{dt} \right) = \frac{de_{\alpha\beta}}{dt} g^\alpha \otimes g^\beta = \Phi_c^* \left(\frac{d\mathbb{E}}{dt} \right) \qquad [2.29]$$

The covariant convective derivative of $\mathbb{A}$ is thus obtained by covariant convective transport of $\frac{d\mathbb{E}}{dt}$.

2.4.6.1. *Convective derivation and Cristoffel symbols*

The objective of the Cristoffel symbols is to establish the link between two natural coordinate systems that are infinitely close.

Convective derivative of a vector

Given that $u = u^\beta g_\beta$ is a vector, we have:

$$du = \frac{\partial u}{\partial X^\alpha} dX^\alpha = \frac{\partial u^\beta}{\partial X^\alpha} dX^\alpha g_\beta + u^\beta \frac{\partial g_\beta}{\partial X^\alpha} dX^\alpha \qquad [2.30]$$

$$= u_{,\alpha}\, dX^\alpha = u^\beta{}_{,\alpha}\, dX^\alpha g_\beta + u^\beta g_{\beta\alpha} dX^\alpha$$

$$= u^\beta{}_{,\alpha}\, dX^\alpha g_\beta + u^\beta \Gamma^\gamma_{\alpha\beta} dX^\alpha g_\gamma \qquad [2.31]$$

with: $g_{\beta,\alpha} = \Gamma^\gamma_{\alpha\beta} g_\gamma$ where $\Gamma^\gamma_{\alpha\beta}$ are the Cristoffel coefficients and $u_{,\alpha}$ represents the partial derivative of u with respect to α.

$$[2.30] \Leftrightarrow du = \left(u^{,\beta}_{,\alpha} + u^\gamma \Gamma^\gamma_{\alpha\beta} \right) dX^\alpha g_\beta$$

$$\Leftrightarrow u_{,\alpha} = u^\beta \mid_\alpha g_\beta.$$

with: $u^\beta \mid_\alpha = u^\beta{}_{,\alpha} + u^\gamma \Gamma^\gamma_{\alpha\beta}$, the convective derivative of u is the mixed representative (once covariant and once contravariant) of the tensor ∇u.

Similarly, we obtain:

$$u_\beta \mid_\alpha = u_{\beta,\alpha} - u^\gamma \Gamma^\beta_{\alpha\gamma}.$$

which is the twice-covariant representative of ∇u.

Convective derivative of a tensor

Following a similar method, we can calculate the convective derivative denoted by $\sigma^{\alpha\beta} \mid_\gamma$ of a tensor σ that is written as:

$$\sigma = \sigma^{\alpha\beta} g_\alpha \otimes g_\beta \qquad [2.32]$$

It yields:

$$\sigma^{\alpha\beta} \mid_\gamma = \sigma^{\alpha\beta}_{,\gamma} + \sigma^{\delta\beta} \Gamma^\alpha_{\delta\gamma} + \sigma^{\alpha\delta} \Gamma^\beta_{\delta\gamma} \qquad [2.33]$$

2.4.6.2. *Calculation of the strain rate*

Let $\overrightarrow{v} = V^{\alpha} g_{\alpha}$ be the rate vector of the displacement defined by $\overrightarrow{v} = \frac{\overrightarrow{dX}}{dt}$. It is shown that for any material vector $\overrightarrow{dX}$:

$$\nabla \overrightarrow{v} \overrightarrow{dX} = \dot{\mathbb{F}} \mathbb{F}^{-1} \overrightarrow{dX} = \mathbb{L} \overrightarrow{dX}. \qquad [2.34]$$

The tensor $\mathbb{L}^s$, the symmetric part of $\mathbb{L}$, verifies:

$$\dot{g}_{\alpha\beta} = 2(\mathbb{L}^s g_{\alpha}, g_{\beta}),$$

and denoting: $\mathbb{D} = \mathbb{L}^s = \nabla \overrightarrow{v^s}$, we obtain the Eulerian tensor expression of the strain rates:

$$\mathbb{D} = \frac{1}{2} \dot{g}_{\alpha\beta} g^{\alpha} \otimes g^{\beta}. \qquad [2.35]$$

It can be verified that:

$$\mathbb{D} = D_c \mathbb{A} = \Phi_c^* \left(\frac{d\mathbb{E}}{dt} \right).$$

The strain rate Euler tensor $\mathbb{D}$ is obtained by covariant convective transport $\frac{d\mathbb{E}}{dt}$.

2.4.6.3. *Calculation of the strain tensor according to the displacement*

Let $\overrightarrow{u} = u^i g_i$ be the displacement vector between C_0 and C_t, it yields:

$$\overrightarrow{X} = \overrightarrow{X^0} + \overrightarrow{u} \Leftrightarrow \overrightarrow{dX} = \mathbb{F} \overrightarrow{dX^0} = \overrightarrow{dX^0} + \overrightarrow{du}. \qquad [2.36]$$

The strain tensor according to the displacement is:

$$e_{il} = \frac{1}{2} \left(u_k \mid_i u^k \mid_l + u_i \mid_l + u_l \mid_i \right) \quad i, k, l = 1, 2, 3$$

2.4.7. *Strain tensor*

If dS^0 denotes the area element defined in the reference configuration C_0, $\overrightarrow{n^0}dS^0$ is the corresponding elementary area vector $\overrightarrow{n^0}$ representing the unit normal to dS^0. Let $\vec{n}dS$ be the transform of $\overrightarrow{n^0}dS^0$ in the current configuration, $\vec{n}$ being the unit normal to dS, we obtain:

$$\vec{n}dS = J(\mathbb{F}^{-1})\overrightarrow{n^0}dS^0 \Leftrightarrow \overrightarrow{n^0}dS^0 = J^{-1}\mathbb{F}^T\vec{n}dS, \quad J = \det\mathbb{F}$$

Given that df is the force exerted on an element of area $\vec{n}dS$, it is written in the configuration C_t.

DEFINITION 2.7 (Cauchy stress tensor).– *The Cauchy stress tensor U is defined by:*

$$\overrightarrow{df} = \sigma\overrightarrow{n}dS$$

If df is expressed relative to the reference configuration, the first Piola–Kirchhoff tensor is obtained:

$$df = \mathbb{T}\overrightarrow{n^0}dS^0$$

hence: $\sigma = J^{-1}\mathbb{T}\mathbb{F}^T$.

Given that df^0 is the stress exerted on an element of area $\overrightarrow{n^0}dS^0$, it is written in the current configuration C_0. The second Piola–Kirchhoff tensor $\mathbb{S}$ is defined by:

$$\begin{aligned} df^0 &= \mathbb{S}\overrightarrow{n^0}dS^0 \\ &= \mathbb{F}^{-1}df = \mathbb{F}^{-1}\sigma\overrightarrow{n}dS \\ &= \mathbb{F}^{-1}\sigma J\mathbb{F}^{-1}\overrightarrow{n^0}dS^0 \end{aligned}$$

hence:

$$\mathbb{S} = J\mathbb{F}^{-1}\sigma(\mathbb{F}^{-1})^T$$

$$\sigma = J^{-1}\mathbb{F}\mathbb{S}\mathbb{F}^T$$

The Kirchhoff tensor is defined by:

$$\tau = J\sigma = \mathbb{F}\mathbb{S}\mathbb{F}^T = \mathbb{T}\mathbb{F}^T \qquad [2.37]$$

If the reference configuration coincides with the current configuration, we obtain:

$$\mathbb{F} = 1,\ J = 1 \Rightarrow \tau = \sigma = \mathbb{S} = \mathbb{T}.$$

2.5. Constitutive relations

The notation of a large strain elastic–plastic behavior model is based, on the one hand, on the kinematic decomposition of the transformation (partly elastic reversible and partly plastic irreversible) and, on the other hand, on the independence of the plastic behavior and the velocity of the motion.

We designate by kinematic decomposition the decomposition of the strain into a reversible elastic part and an irreversible plastic part. This decomposition, trivial in S.P.H., becomes complicated when taking the large strains into account.

In general, to write an elastic–plastic behavior law, the following approach is followed:

1) Choose a decomposition of the total deformation, in S.P.H.:

$$\varepsilon = \varepsilon^e + \varepsilon^p$$

where ε^e is the elastic strain and ε^p is the plastic strain (see Figure 2.2).

2) Define a plasticity criterion, in S.P.H.: $f(\sigma, \alpha) = 0$ where σ is the stress and α is the internal variable and f is the plasticity threshold function.

3) Define a relation between the stresses and the elastic strains or between the stress rate and the elastic strain rate,

in S.P.H.: $\sigma = \mathbb{A}\varepsilon^e$
or even: $\dot{\sigma} = \mathbb{A}\dot{\varepsilon^e}$

$\mathbb{A}$ is a fourth-order tensor that depends or not on σ and α.

4) Write an evolution (or flow) law for the plastic part of the strain,

$$\dot{\varepsilon}^P = \dot{\lambda} h(\sigma, \alpha)$$

5) Write an evolution law for α,

$$\dot{\alpha}^P = \dot{\lambda} l(\sigma, \alpha)$$

$\mathbb{A}$, f, h and l define the model material, and $\dot{\lambda}$ is a plastic multiplier.

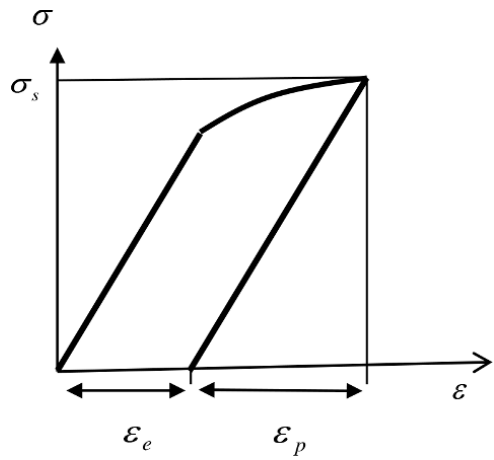

Figure 2.2. *Illustration of the strain decompositions*

In the following, we will mention a few model materials, beginning with the simplest case:

1) Isotropic linear elastic case

The behavior of the material is defined by:

$$\sigma = \mathbb{A}\varepsilon^e$$

$\mathbb{A}$ is Hooke's stiffness tensor.

2) Von Mises perfect plasticity

Let σ^s be the yield strength of the material (constant), if the stress deviator is denoted by σ^D, the equivalent stress $\overline{\sigma}$ is written as:

$$\overline{\sigma} = \sqrt{\frac{3}{2}\sigma^D : \sigma^D}$$

Futhermore, the equivalent cumulated strain is given by:

$$\overline{\varepsilon^p} = \int_0^t \dot{\overline{\varepsilon^p}} dt$$

with

$$\dot{\overline{\varepsilon}}^p = \sqrt{\frac{3}{2}\dot{\varepsilon}^p : \dot{\varepsilon}^p}.$$

The plasticity threshold function is:

$$f(\sigma) \quad = \overline{\sigma} - \sigma_s \leq 0 \qquad [2.38]$$

$$\dot{\varepsilon}^p \quad = \dot{\lambda}\frac{\partial f}{\partial \sigma} = \dot{\lambda}\frac{3}{2}\frac{\sigma^D}{\overline{\sigma}} \qquad [2.39]$$

This corresponds to a case of associated plasticity, f and h are identical.

3) Case of isotropic strain hardening

The model is of the same type as previously except that the threshold surface is no longer assumed to be constant, $\sigma_s = \sigma_s(\overline{\varepsilon}^p)$.

Other models can be cited, kinematic strain hardening, whether isotropic or not, etc. We are only going to consider isotropic strain hardening in this study.

2.5.1. *Large elastoplastic transformations*

Similarly to the kinematic study, the definition of two different configurations is necessary to describe the large transformations. The stresses and the strains can be defined on one or the other of the configurations; this is no longer referred to as a stress or strain tensor, but as a multitude of tensors following the notation and the configuration of the chosen reference. Two types of formalism can then be distinguished:

– Lagrangian, relative to a fixed initial configuration (before transformation);

– Eulerian, relative to a deformed configuration (after deformation).

The choice between the two notations constitutes the first difficulty of the large strains. The second point that has to be solved is that of the decomposition of the partly elastic and plastic transformation. The third point concerns the concept of objectivity in the behavior law, which should be absolutely independent of the coordinate system of observation.

Before discussing the notation problem of the behavior laws, we begin by studying the notion of objectivity and its consequences on the notation of such laws.

2.5.1.1. *Objectivity and objective derivatives*

The objectivity of the quantities can be used to distinguish between the quantities that are basically the same for all observers (the density, for example) and others have different values according to the observer (rate vector, for example).

The objectivity principle expresses the fact that the behavior of the material does not depend on the chosen reference frame. As a result, any quantity involved in the notation of such a law must obey the rules of changing reference frames.

Let X be a coordinate system defined in a frame $\mathcal{R}$ and $\overrightarrow{X}$ a given vector, $\overrightarrow{C}(t)$ a vector and $\mathbb{Q}(t)$ any orthogonal tensor. A new referential $\mathcal{R}'$ is defined in which the new coordinate system is denoted X'. The vector $\overrightarrow{X}'$, the image of $\overrightarrow{X}$ in $\mathcal{R}'$, is written as:

$$\overrightarrow{X}' = \mathbb{Q}(t)\overrightarrow{X} + \overrightarrow{C}(t)$$

It is easy to verify that any vector $\overrightarrow{V}$ in $\mathcal{R}$ is transformed into a vector $\overrightarrow{V}'$ in $\mathcal{R}'$ according to the relation:

$$\overrightarrow{V}' = Q\overrightarrow{V}$$

The tensor $\mathbb{F}$ is transformed into $\mathbb{F}'$ such that:

$$\overrightarrow{dX'} = \mathbb{F}'\overrightarrow{dX}^0 \Rightarrow \overrightarrow{dX'} = \mathbb{Q}\overrightarrow{dX} = \mathbb{Q}\mathbb{F}\overrightarrow{dX}^0 = \mathbb{F}'\overrightarrow{dX}^0$$
$$\Rightarrow \mathbb{Q}\mathbb{F} = \mathbb{F}'$$

Any tensor variable $\mathbb{M}$ expressed in $\mathcal{R}$ must therefore be transformed in $\mathcal{R}'$ into $\mathbb{M}'$ by the relation:

$$\mathbb{M}' = \mathbb{Q}\mathbb{M}\mathbb{Q}^T \qquad [2.40]$$

It can be verified that any strain or stress Lagrangian measure is invariant when changing frames of reference.

$$\mathbb{C} = \mathbb{F}'^T\mathbb{F}'$$
$$= \mathbb{F}^T\mathbb{F} \Rightarrow U' = U$$
$$\mathbb{E}' = \mathbb{E}\,; \mathbb{S}' = \mathbb{S}$$

which is not the case when considering Eulerian tensors, in effect,

$$\mathbb{B}' = \mathbb{Q}\mathbb{B}\mathbb{Q}^T\,; \quad \mathbb{V}' = \mathbb{Q}\mathbb{V}\mathbb{Q}^T \qquad \mathbb{A}' = \mathbb{Q}\mathbb{A}\mathbb{Q}^T$$

With regard to the stress tensors, we have:

$$g'_\alpha = \mathbb{F}' g_\alpha$$

which gives:

$$\sigma' = \mathbb{Q}\sigma\mathbb{Q}^T \quad \text{and} \quad \tau' = \mathbb{Q}\tau\mathbb{Q}^T.$$

The tensor $\mathbb{R}$ obtained by polar decomposition of $\mathbb{F}$ is transformed into $\mathbb{R}' = \mathbb{Q}\mathbb{R}$.

To summarize, a tensor is objective if it is:

– either defined on the initial configuration (Lagrangian tensor);

– or transformed according to [2.40] by a change in coordinate system.

The tensor $\mathbb{L}$ is written $\mathbb{L} = \dot{\mathbb{F}}\mathbb{F}^{-1}$ when changing the frame of reference, it is transformed into:

$$\mathbb{L}' = \mathbb{Q}\mathbb{L}\mathbb{Q}^T + \Omega \quad \text{with } \Omega = \dot{\mathbb{Q}}\mathbb{Q}^T$$

which gives:

$$\mathbb{D}' = \mathbb{Q}\mathbb{D}\mathbb{Q}^T \quad \text{and} \quad \mathbb{W}' = \mathbb{Q}\mathbb{W}\mathbb{Q}^T + \Omega$$

similarly:

$$\sigma' = \mathbb{Q}\sigma\mathbb{Q}^T \Leftrightarrow \sigma = \mathbb{Q}\sigma'\mathbb{Q}^T$$

A constitutive law must connect the objective quantities, which eliminates the conventional time derivatives of tensors. We have already introduced a type of derivative known as a convective that verifies:

$$D_c\sigma' = \mathbb{Q}D_c\sigma\mathbb{Q}^T.$$

This is the type of derivative that we are going to utilize. There are other types of objective derivatives that all rely on the notion of differentiating the tensor in a reference frame related, one way or another, to the material.

2.5.2. *Kinematic decomposition of the transformation*

Kinematic decomposition of the transformation designates a multiplicative decomposition of $\mathbb{F}$, which allows writing the strain rate tensor $\mathbb{D}$ in the form:

$$\mathbb{D} = \mathbb{D}^e + \mathbb{D}^p \qquad [2.41]$$

The decompositions found in the literature are of the type:

– material with relaxed configuration, obtained by elastic charging, which gives:

$$\mathbb{F} = \mathbb{F}^e\mathbb{F}^p \Rightarrow \mathbb{L} = \dot{\mathbb{F}}^e\mathbb{F}^{e^{-1}} + \mathbb{F}^e\dot{\mathbb{F}}^p\mathbb{F}^p\mathbb{F}^{e^{-1}}.$$

Under the hypothesis of small elastic deformations, we obtain a a notation of the type of [2.41];

– material with relaxed intermediary configuration:

$$\mathbb{L} = \overline{\mathbb{F}}^p\mathbb{V}^e$$

$\mathbb{V}^e$ being the pure elastic strain,

$$\overline{\mathbb{F}}^p = \mathbb{F}^p\mathbb{R}^p$$

Under the hypothesis of small elastic deformations, $\mathbb{F}^e = \mathbb{1} + \varepsilon^e$ where $\|\varepsilon^e\| \ll 1$, a notation of the type of [3.15] is used, with $\mathbb{D}^e = \varepsilon^{eJ}$, the Jauman derivative of the plastic deformation;

– Gelin [GEL 92] proposes the following type of decomposition:

$$\mathbb{A} = \mathbb{A}^e + \mathbb{A}^P$$

which makes it possible to have

$$D_c\mathbb{A} = \overline{\mathbb{A}} = \mathbb{D} = D_c\mathbb{A}^e + D_c\mathbb{A}^p = \mathbb{D}^e + \mathbb{D}^p.$$

with this notation, the case where $\mathbb{F}^p = \mathbb{I}$ gives $\mathbb{D} = \mathbb{D}^e = D_c\mathbb{A}^e$ without any confusion.

2.6. Incremental behavioral problem

In an incremental process (see Figure 2.3); starting from an initial configuration C_0, it is assumed that the configuration at instant t denoted C_t is known, we are looking for the configuration $C_{t'}$ at instant $t' = t + \Delta t$.

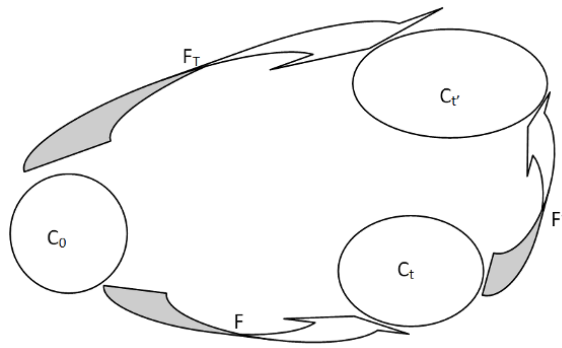

Figure 2.3. *Decomposition of the transformation*

$\mathbb{F}$ denotes the gradient of the transformation between C_0 and C_t, $\mathbb{F}'$ that between C_0 and C_t and $\mathbb{F}_T$ between C_0 and C'_t. The corresponding determinants are denoted: $J = \det(\mathbb{F})$; $J' = \det(\mathbb{F}')$ and $J_T = \det(\mathbb{F}_T)$.

2.6.1. *Stress incrementation*

A few useful relations:

$$\mathbb{S} = \mathbb{S}^{\alpha\beta} g^0_\alpha \otimes \overrightarrow{g^0_\beta} \Rightarrow D^c_\tau = \tau^c = \dot{\mathbb{S}}^{\alpha\beta} g_\alpha \otimes g_\beta$$

$$\dot{\mathbb{S}} = \dot{\mathbb{S}}^{\alpha\beta} g^0_\alpha \otimes g^0_\beta$$

$$= \mathbb{F}^{-1} \tau^c \mathbb{F}^{-1^T}$$

$$\dot{\tau} = \tau^c + \mathbb{L}\tau + \tau \mathbb{L}^T$$

$$\sigma^c = -J^{-1} \tau tr\mathbb{D} + J^{-1} \tau^c, \qquad [2.42]$$

It can be noted that $g_\alpha = \mathbb{F} g^0_\beta$ and $g'_\alpha = \mathbb{F}' g_\beta = \mathbb{F}_T g^0_\beta$. We start by writing, at any instant and in any configuration, the corresponding stress tensor:

at instant t:	at instant $t\prime$:
$\mathbb{S} = \mathbb{S}^{\alpha\beta} g_\alpha^0 \otimes g_\beta^0$	$\mathbb{S}' = \mathbb{S}'^{\alpha\beta} g_\alpha^0 \otimes g_\beta^0$
$\tau = \mathbb{S}^{\alpha\beta} g_\alpha \otimes g_\beta$	$\tau' = S'^{\alpha\beta} g'_\alpha \otimes g'_\beta$
$\tau^c = \dot{\mathbb{S}}^{\alpha\beta} g_\alpha \otimes \overrightarrow{g_\beta}$	$\tau'^c = \dot{\mathbb{S}}'^{\alpha\beta} g'_\alpha \otimes g'_\beta$

If it is assumed that $t' - t = \Delta t \ll 1$, $\dot{S}'^{\alpha\beta}$ can be approximated by:

$$\dot{S}'^{\alpha\beta} \approx \frac{S'^{\alpha\beta} - S^{\alpha\beta}}{\Delta t} = \frac{\Delta S'^{\alpha\beta}}{\Delta t}$$

Thus, it can be written as:

$$\mathbb{S}' = S'^{\alpha\beta} g_\alpha^0 \otimes g_\beta^0 = (S^{\alpha\beta} + \Delta S'^{\alpha\beta}) g_\alpha^0 \otimes g_\beta^0 = \mathbb{S} + \Delta\mathbb{S}' \qquad [2.43]$$

with $\Delta\mathbb{S}' = \Delta S'^{\alpha\beta} g_\alpha^0 \otimes g_\beta^0$.

It gives:

$$\tau' = (S^{\alpha\beta} + \Delta S'^{\alpha\beta}) g'_\alpha \otimes g'_\beta$$

and

$$\tau'^c = \dot{S}^{\alpha\beta} g'_\alpha \otimes g'_\beta = \frac{\Delta S'^{\alpha\beta}}{\Delta t} e'_\alpha \otimes e'_\beta \qquad [2.44]$$

It yields:

$$\tau' = \mathbb{F}^T \mathbb{S} \mathbb{F}_T^T + \Delta t \tau'^c = \mathbb{F}' \tau \mathbb{F}'^T + \Delta t . \tau'^c \qquad [2.45]$$

or even

$$\tau'^{\alpha\beta} = S^{\alpha\beta} + \Delta t . \tau'^{c\alpha\beta} \qquad [2.46]$$

in the following $\Delta t . \tau'^c$ will be denoted $\Delta\tau'$.

The principle of virtual work (P.V.W.) is expressed according to the Kirchhoff stress tensor. We define and we show that:

$$\sigma' = \frac{1}{C}(J'^{-1}\mathbb{F}'\sigma\mathbb{F}'^{T} + \Delta t.\sigma'^{c}) \qquad [2.47]$$

Still under the hypothesis: $\Delta t \ll 1$, it can be written as:

$$\Delta t\sigma'^{c} \approx (\sigma'^{\alpha\beta} - \sigma^{\alpha\beta})g'_{\alpha} \otimes g'_{\beta} = \Delta\sigma'^{\alpha\beta}g'_{\alpha} \otimes g'_{\beta} \qquad [2.48]$$

It gives:

$$\sigma'^{\alpha\beta} = \frac{1}{C}(J'^{-1}\sigma^{\alpha\beta} + \Delta\sigma'^{\alpha\beta}). \qquad [2.49]$$

It is assumed that $C \approx 1$ and $J' \approx 1$, which amounts to assuming that the variation of the volume is infinitesimal. At this time, we have:

$$\sigma'^{\alpha\beta} = \sigma^{\alpha\beta} + \Delta\sigma'^{\alpha\beta}. \qquad [2.50]$$

The use of σ in an incremental formulation in this form must be considered with caution since it constitutes as a matter of fact another source of error that comes to add up to the rest of the approximations.

However, if we only ignore the term $\Delta t\,\mathrm{tr}\,\mathbb{D}\prime$ in front of 1 (under the plastic incompressibility hypothesis and given that $\Delta t \ll 1$) while keeping J', it yields:

$$\sigma'^{\alpha\beta} = (J'^{-1}\sigma^{\alpha\beta} + \Delta\sigma'^{\alpha\beta}) \qquad [2.51]$$

2.6.2. *Strain incrementation*

Similarly, we have:

at instant t	at instant t'
$\mathbb{A} = e_{\alpha\beta}g^{\alpha} \otimes g^{\beta}$,	$\mathbb{A}' = e'_{\alpha\beta}g'^{\alpha} \otimes g'^{\beta}$
$\mathbb{E} = e_{\alpha\beta}g_0^{\alpha} \otimes g_0^{\beta}$	$\mathbb{E}' = e'_{\alpha\beta}g_0^{\alpha} \otimes g_0^{\beta}$

$$\begin{array}{cc} \mathbb{A}_c = \dot{e}_{\alpha\beta} g^\alpha \otimes g^\beta = \mathbb{D} & \mathbb{A}'_c = \dot{e'}_{\alpha\beta} g'^\alpha \otimes g'^\beta = \mathbb{D}' \\ \dot{\mathbb{E}} = \dot{e}_{\alpha\beta} g_0^\alpha \otimes g_0^\beta & \dot{\mathbb{E}}' = \dot{e'}_{\alpha\beta} g_0^\alpha \otimes g_0^\beta \\ \dot{e}_{\alpha\beta} = \dot{g}_{\alpha\beta} & \dot{e'}_{\alpha\beta} = \dot{g}'_{\alpha\beta} \end{array}$$

We further note that:

$$\begin{aligned} g^\alpha &= \mathbb{F}^{-1T} g_0^\alpha \\ g'^\alpha &= \mathbb{F}'^{-1T} g^\alpha \\ &= \mathbb{F}_T^{-1T} g_0^\alpha \end{aligned}$$

The derivative of ${e'}_{\alpha\beta}$ with respect to time is approximated by:

$$\dot{e'}_{\alpha\beta} \approx \frac{e'_{\alpha\beta} - e_{\alpha\beta}}{\Delta t} = \frac{\Delta e'_{\alpha\beta}}{\Delta t} \qquad [2.52]$$

with $\Delta e'_{\alpha\beta} = g'_{\alpha\beta} - g_{\alpha\beta}$.

$\Delta e'_{\alpha\beta}$ can be expressed according to Δu, the displacement increment between t and t'. With this approximation, we obtain:

$$\Delta t \mathbb{D}' = \Delta t \mathbb{A}'_c = \Delta e'_{\alpha\beta} g'^\alpha \otimes g'^\beta \qquad [2.53]$$

or also: $\Delta t D'_{\alpha\beta} = \Delta e'_{\alpha\beta}$.

NOTE 2.5.– If a behavior law is available such as $\tau'^c = H^{ep}\mathbb{D}'$, where H^{ep} is an elastoplastic operator, multiplying each member by Δt we have:

$$\Delta t \tau'^c = H^{ep} \delta t . \mathbb{D}',$$

which gives in index-based notation:

$$\Delta {S'}^{\alpha\beta} = H^{ep} \Delta e'_{\alpha\beta}$$

$\Delta e'_{\alpha\beta}$ is calculated with respect to u, the displacement increment between t and t'. Once $\Delta S^{\alpha\beta}$ is obtained, knowing τ and $\mathbb{A}$, it is possible using [2.46] and [2.52] to calculate τ' and $\mathbb{A}'$.

The equations that have just been developed allow us to have either a total Lagrangian formulation using the strain $(\mathbb{E}, \mathbb{E}' \ldots)$ and the stress Lagrangian

measures $(\mathbb{S}, \mathbb{S}' \ldots)$, that is to say a Eulerian formulation using the strain $(\mathbb{A}', \mathbb{D}' \ldots)$ and stress Eulerian measures $(\tau, \sigma \ldots)$.

NOTE 2.6.–

1) The kinematic decomposition valid in S.P.H. is only valid in large deformations if a number of precautions is taken. The definition of the elastic and plastic strain rates is not as clear as in the S.P.H.. The classical stress derivative with respect to time, if we choose a velocity notation, must be replaced by an objective derivative in order to guarantee the principle of material indifference. The convective derivative that has been introduced answers this last question.

2) The convective derivative is used instead of the classical stress derivative with respect to time, if we choose a notation in velocity.

A rigid body motion does not generate any strain since $\mathbb{D}' = \mathbb{O}$.

3) It is assumed that $e'_{\alpha\beta}(\widetilde{t})$ is a continuous differentiable function and a continuous derivative of the time variable $\widetilde{t}$, and we define $e'_{\alpha\beta}(\widetilde{t} = t) = e_{\alpha\beta}$ and $e'_{\alpha\beta}(\widetilde{t} = t') = e'_{\alpha\beta}$. Because it is assumed that $\Delta t \ll 1$, it gives:

$$\dot{e}_{\alpha\beta} = \dot{e'}_{\alpha\beta} = \dot{g'}_{\alpha\beta}. \qquad [2.54]$$

In effect:

$$\dot{e}'_{\alpha\beta}(t') = \lim_{t \to t'} \frac{e'_{\alpha\beta}(t') - e'_{\alpha\beta}(t)}{t - t'} \approx \frac{e_{\alpha\beta} - e'_{\alpha\beta}}{-\Delta t} = \frac{e'_{\alpha\beta} - e_{\alpha\beta}}{\Delta t} \qquad [2.55]$$

and

$$\dot{e}'_{\alpha\beta}(t) = \lim_{t' \to t} \frac{e'_{\alpha\beta}(t') - e'_{\alpha\beta}(t)}{t' - t} \approx \frac{e'_{\alpha\beta} - e_{\alpha\beta}}{\Delta t} \qquad [2.56]$$

2.6.3. *Solution of the behavior problem*

2.6.3.1. *Elastic case*

The behavior law in terms of velocity is written as:

$$\tau'^{c} = \mathbb{H}^e \mathbb{D}'$$

with $\mathbb{H}^e$ being the Hooke operator and $\mathbb{D}' = \mathbb{D}'^e$; this is equivalent to

$$\Delta t.\tau'^{c} = \mathbb{H}^e \Delta t \mathbb{D}'^{e} \qquad [2.57]$$

which gives in index-based notation:

$$\Delta \mathbb{S}^{'\alpha\beta} = (H^e)^{\alpha\beta\gamma\delta} \Delta e'_{\gamma\delta}. \quad [2.58]$$

Therefore, knowing the displacement increment between t and t', we obtain $\Delta e'_{\gamma\delta}$ and this notation makes it possible to obtain the corresponding stress increment.

2.6.3.2. *Elastoplastic case*

In order to solve this problem, we consider the configuration $C_{t'}$. We are thus working on the basis of g'_α and all quantities being used are defined on this basis.

To make the notation more understandable, each tensor representative in the basis ${g'}_\alpha$ is replaced by the tensor itself. Thus, the matrix ${\mathbb{S}'}^{\alpha\beta}$ is denoted τ', $\Delta{\mathbb{S}'}^{\alpha\beta}$ is denoted $\Delta\tau'$, and by abuse of notation $\mathbb{S}^{\alpha\beta}$ is written τ ($\mathbb{S}^{\alpha\beta}$ are the components of τ in the base $g_\alpha \otimes g_\beta$ and not in $g'_\alpha \otimes g'_\beta$). Finally, $\Delta e'_{\gamma\delta}$ will be denoted $\Delta e' = \mathbb{D}'\Delta t = (\mathbb{D}'^e + \mathbb{D}'^p)\Delta t = \Delta e'^e + \Delta e'^p$.

The elastoplastic model that is adopted is Von Mises's with isotropic strain hardening; it is written as:

$$\Delta e' = \Delta e'^e + \Delta e'^p \quad [2.59]$$

$$f(\tau', \overline{\varepsilon'}^p) = \frac{1}{2}[\tau' \mathbb{M} \tau' - \sigma_s^2(\overline{\varepsilon'}^p)] \quad [2.60]$$

where:

– f is the Von Mises threshold function at instant t' in quadratic form,

– $\overline{\varepsilon'}^p$ is the equivalent plastic deformation at instant t' defined by:

$$\dot{\overline{\varepsilon'}}^p = \sqrt{\frac{2}{3}\dot{e}'^p : \dot{e}'^p} = -\dot{\lambda}\frac{\partial f}{\partial \sigma_s} \quad [2.61]$$

– $\mathbb{M}$ is a fourth-order tensor,

– σ^s is the yield strength according to $\overline{\varepsilon}^p$.

Considering a flow law of the following type:

$$\dot{e}'^p = \dot{\lambda}\frac{\partial f(\tau, \overline{\varepsilon}^p)}{\partial \tau}. \quad [2.62]$$

Knowing that:

$$\int_t^{t'} \dot{e'}^p(\tau)d\tau = e'^p(t') - e'^p(t) = \Delta e'^p \qquad [2.63]$$

if we intend to integrate [2.62], according to the following numerical scheme:

$$\int_t^{t'} \dot{e'}^p(\tau)d\tau = \Delta\lambda \left[(1-\eta)\frac{\partial f}{\partial \tau}(\tau) + \eta\frac{\partial f}{\partial \tau}(\tau')\right] \qquad [2.64]$$

Solving the behavior problem amounts to solving the following system of equations:

$$\begin{cases} \Delta e' = (H^e)^{-1}\Delta\tau' + \Delta e'^p \\ \Delta e'^p = \Delta\lambda\left[(1-\eta)\frac{\partial f}{\partial \tau}(\tau) + \eta\frac{\partial f}{\partial \tau}(\tau')\right] \\ \tau'\mathbb{M}\tau' - \sigma_s^2(\overline{\varepsilon'}^p) = 0 \end{cases} \qquad [2.65]$$

If we replace f by its expression and if, to show the stress increment, τ' is replaced by $(\tau + \Delta\tau')$, the system becomes:

$$\begin{cases} \Delta e' - (H^e)^{-1}\Delta\tau' - \Delta e'^p & = 0 \\ \Delta e'^p - \Delta\lambda\mathbb{M}(\tau + \eta\Delta\tau') & = 0 \\ (\tau + \Delta\tau')\mathbb{M}(\tau + \Delta\tau') - \sigma_s^2(\overline{\varepsilon'}^p) & = 0 \end{cases} \qquad [2.66]$$

We thus get three equations and four unknowns: $\Delta e'^p$, $\Delta\tau'$, $\Delta\lambda$ and $\overline{\varepsilon'}^p$. To solve this problem, we must either add another equation to bring forward $\overline{\varepsilon'}^p$ explicitly according to the other variables, or linearize the third equation to eliminate the fourth unknown.

One method to obtain the fourth equation would be by means of integrating $\dot{\overline{\varepsilon'}}^p$ with the numerical scheme already used to integrate $\dot{e}'^p$:

$$\dot{\overline{\varepsilon'}}^p = \dot{\lambda}\sigma_s(\overline{\varepsilon}^p) \Rightarrow \Delta\overline{\varepsilon'}^p = \Delta\lambda[(1-\eta)\sigma_s(\overline{\varepsilon}^p) + \eta\sigma_s(\overline{\varepsilon'}^p)]$$

with $\overline{\varepsilon'}^p = \overline{\varepsilon}^p + \Delta\overline{\varepsilon'}^p$.

The system used to solve this becomes:

$$\begin{cases} \Delta e' - H^{e-1}\Delta\tau' - \Delta e'^p & = 0 \\ \Delta e'^p - \Delta\lambda\mathbb{M}(\tau + \eta\Delta\tau') & = 0 \\ (\tau + \Delta\tau')\mathbb{M}(\tau + \Delta\tau') - \sigma_s^2(\overline{\varepsilon'}^p) & = 0 \\ \Delta\overline{\varepsilon'}^p - \Delta\lambda[(1-\eta)\sigma_s(\overline{\varepsilon}^p) + \eta\sigma_s(\overline{\varepsilon}^p + \Delta\overline{\varepsilon'}^p)] & = 0 \end{cases} \qquad [2.67]$$

This system is solved with an iterative Newton-based method.

The second method that consists of linearizing $\sigma_s^2(\overline{\varepsilon'^p})$ makes it possible to solve the first system of three equations with a Newton-type method. It yields an expression of the term $\dfrac{\partial \sigma_s^2(\overline{\varepsilon'^p})}{\partial \overline{\varepsilon}^p}$, linear of $\Delta e'^p$, which allows us to obtain the expression of the tangent Newton matrix.

2.7. Definition of the P.V.W. in major transformations

2.7.1. *Equilibrium equations*

The definition of the equilibrium equations of the continuum occupying at instant t a domain Ω (respectively, at instant t_0 a domain Ω_0) requires the use of a stress tensor having a physical meaning. Only σ and $\mathbb{T}$ meet this condition. The expression of the equilibrium according to $\mathbb{S}$ or to τ is obtained using the transformation formulas of section 2.4.7. Using the Cauchy tensor σ, the fundamental principle of mechanics, reflected by the conservation of the quantity of motion, is written as:

$$\frac{d}{dt}\int_\Omega \rho v d\Omega = \int_{\partial\Omega} \sigma \overrightarrow{n} \Gamma + \int_\Omega \rho f d\Omega \qquad [2.68]$$

where v is the velocity vector du of the motion of the solid; ρ is its density, f is the volume stresses and $\vec{n}$ is normal to the surface $\partial\Omega$.

The mass conservation and Green's formula allow us to obtain:

$$\frac{d}{dt}\int_\Omega \rho v d\Omega = \int_\Omega \rho \frac{d\nu}{dt} d\Omega \qquad [2.69]$$

$$\frac{d}{dt}\int_{\partial\Omega} \sigma \overrightarrow{n}\, d\Gamma = \int_\Omega \mathrm{div}\sigma d\Omega \qquad [2.70]$$

Without density stress and ignoring the stress of the accelerations, we obtain:

$$\int_\Omega \mathrm{div}\sigma d\Omega = 0 \qquad [2.71]$$

which yields the equilibrium equations of the continuum:

$$\mathrm{div}\sigma = 0 \qquad [2.72]$$

that is also written as:

$$\sigma^{ij} \mid_j = 0 \qquad [2.73]$$

with $\sigma^{ij} n_j = T^i$, where T^i is the density of the surface stress.

2.7.2. *Definition of the P.V.W.*

Let V^{ad} be the set of the virtual velocity vectors kinematically admissible. By multiplying [2.72] by a vector $v \in V^{ad}$ and integrating over the whole of Ω, we obtain:

$$\int_\Omega \text{div}\sigma.v d\Omega = 0 \quad \forall v \in V^{ad} \qquad [2.74]$$

$$\Leftrightarrow \int_\Omega \sigma \nabla v d\Omega - \int_\Omega \text{div}(\sigma v) d\Omega = 0 \quad \forall v \in V^{ad} \qquad [2.75]$$

$$\Leftrightarrow \int_\Omega \sigma \nabla v d\Omega = \int_{\partial\Omega} \sigma \overrightarrow{n} v d\Gamma \quad \forall v \in V^{ad} \qquad [2.76]$$

which is written according to the components relative to a basis g^i and its dual basis g_i:

$$\int_\Omega \sigma^{ij} v_i \mid_j d\Omega = \int_{\partial\Omega_F} \sigma^{ij} n_j v_i d\Gamma \qquad [2.77]$$

It is assumed that $\partial\Omega = \partial\Omega_U \cup \Omega_F$ and $\sigma^{ij} n_j = 0$ sure $\partial\Omega_U$, $\sigma^{ij} n_j = T^i$ over $\partial\Omega_F$. We then obtain:

$$\int_\Omega \sigma^{ij} v_i|_j \, d\Omega = \int_{\partial\Omega_F} T^i v_i d\Gamma \quad \forall v \in V^{ad} \qquad [2.78]$$

$$\Leftrightarrow \int_\Omega \sigma^{ij} D_{ij} \, d\Omega = \int_{\partial\Omega_F} T^i v_i \, d\Gamma \quad \forall v \in V^{ad} \qquad [2.79]$$

$$\Leftrightarrow \int_\Omega \sigma : \mathbb{D} \, d\Omega = \int_{\partial\Omega_F} T v \, d\Gamma \quad \forall v \in V^{ad} \qquad [2.80]$$

NOTE 2.7.– Knowing that $J = \det(\mathbb{F})$, where $\mathbb{F}$ is the transformation gradient between t_0 and t, and according to [2.87] the transformation laws of volume

and surface, the P.V.W. expressed according to the Kirchhoff tensor is denoted as:

$$\int_{\Omega_0} \nu \colon D d\Omega_0 = \int_{\partial\Omega_F} T\nu d\Gamma = \int_{\partial\Omega_{0F}} T_0 \nu d\Gamma_0 \quad \forall \nu \in V^{ad} \qquad [2.81]$$

and knowing that $\sigma = J^{-1}\mathbb{F}\mathbb{S}\mathbb{F}^T$, we obtain a Lagrangian notation of the P.V.W. making use of $\mathbb{S}$ and $\mathbb{E}$.

2.7.3. *Incremental formulation*

The equilibrium problem will not be solved in terms of stress and strain rate, but in terms of increment or increase in the strains and stresses.

As has already been detailed in the previous section, at instant t_0 there is a configuration C_0 and it is supposed that we have reached, at instant t, a configuration C_t where the equilibrium is satisfied (equation [2.80] is verified). We are looking for a configuration C_t with $t' = t + \Delta t$ ($\Delta t \ll 1$) that is at equilibrium. This is expressed as:

$$\int_{\Omega'} \sigma' \colon \mathbb{D}' \, d\Omega' = \int_{\partial\Omega'_F} T' \nu' \, d\Gamma' \quad \forall v' \in V^{ad}$$

$$\int_{\Omega'} \sigma'^{ij} \nu'_i \mid_j \, d\Omega' = \int_{\partial\Omega'_F} T'^i \nu'_i \, d\Gamma' \quad \forall v' \in V^{ad} \qquad [2.82]$$

When resorting to a discretization of this equation, the use of an iterative algorithm such as Newton–Raphson's to solve it allows at each iteration that an estimate of the displacement increment be available. With this displacement increment, the problem of the behavior is solved, which provides the corresponding stress and strain increment.

NOTE 2.8.– The notion of incremental formulation states that: knowing σ^{ij} are the components of σ at instant t and knowing Δu is the displacement increment, $\Delta\sigma^{ij}$ is calculated, which is the necessary stress increment to obtain σ'. It is recalled that in the case of the Cauchy tensor the calculation of σ'^{ij} based on σ^{ij} is carried out according to two methods:

– either we solve the problem making use of the Kirchhoff tensor τ, and at this time the calculation of the components of τ' is given by:

$$\tau'^{ij} = \tau^{ij} + \Delta\tau'^{ij} \qquad [2.83]$$

we can deduce thereof:

$$\sigma'^{ij} = J_T^{-1}(\tau^{ij} + \Delta\tau'^{ij}) \qquad [2.84]$$

where $J_T = \det\mathbb{F}_T$ and $\mathbb{F}_T = \mathbb{F}'\mathbb{F}$ represents the gradient of the total transformation between t_0 and t';

– or a behavior law is employed that connects the Cauchy tensor to the strain rate; τ has to be replaced by σ in the solution of the behavioral problem and once $\Delta\sigma'^{ij}$ is obtained, σ'^{ij} is calculated by:

$$\sigma'^{ij} = J'^{-1}\sigma^{ij} + \Delta\sigma'^{ij}. \qquad [2.85]$$

2.8. Contact kinematics

One of the major problems in the forming simulation is the contact between sheet metal and the deep-drawing tools, for example. In effect, many technical problems involve contact between two or more components. In these problems, a normal force on the contact surfaces is exerted on both bodies when they touch each other. If there is friction between the surfaces, the shear forces can be created resisting the tangential motion (sliding) of the bodies.

2.8.1. *Definition of the problem and notations*

Let us take two solids that may come into contact by friction.

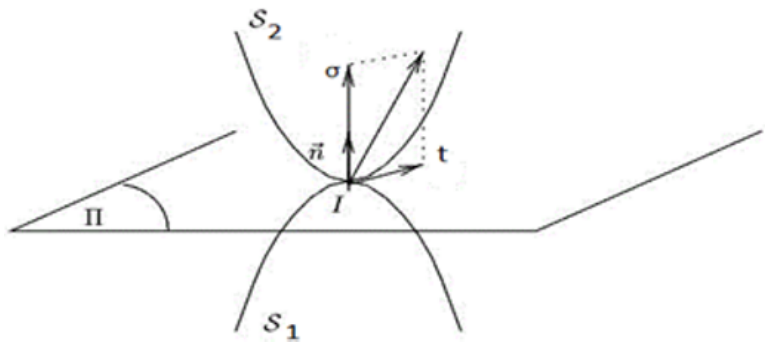

Figure 2.4. *Two solids in contact*

Let $\vec{n}$ be the outbound normal to the surface of one of the solids in contact, $\vec{u}_n = u.\vec{n}$ the displacement following this normal, g the backlash between two

solids and $p = \sigma_n.\vec{n}.\vec{n}$ the pressure (contact strain density) exerted by one of the surfaces on the other and $\overrightarrow{\sigma_t} = \sigma.\vec{n} - p.\vec{n}$ the shear.

More precisely, for two solids (S_1) and (S_2) in contact, the contact area is either a point, a line or even a surface. The direction of the shear force is then, in the contact area, a vector t located in the tangent plane (t_1, t_2) indicated in Figure 2.4.

2.8.2. *Contact formulation*

During the process of forming, the boundary conditions relative to the contact and the friction change. From a geometrical point of view, this implies that the nodes of the sheet metal move according to the movement of the punch: whether in contact or not. In the contact area, a local orthonormal reference frame (n, t_1, t_2) is defined in each node, where n is the normal external to the surface and (t_1, t_2) represents the tangent plane to the surface.

The displacement and the reaction are written in accordance with the local reference configuration as follows:

$$\left\{\begin{array}{rcl} u_n & = & u.n \\ u_t & = & u - (u_n.n) \end{array}\right. \qquad \left\{\begin{array}{rcl} r_n & = & r.n \\ r_t & = & r - (r_n.n) \end{array}\right. \qquad [2.86]$$

and the unilateral conditions written in the Γ_c part of the boundary are:

$$u_n \leq 0, \quad r_n \leq 0 \qquad u_n.r_n = 0 \qquad [2.87]$$

2.8.3. *Formulation of the friction problem*

Depending on whether these solids slide against each other, this is referred to as sliding (dynamic friction) or adherence, as long as there is no motion (static friction or striction). In both cases, the reciprocal actions exerted between these solids comprise:

– a normal component σ_n that presses one against the other;

– a tangential component T which opposes, or tends to oppose, the sliding.

The ratio between the strain T and the reaction of the solid (S_2) defines the adherence coefficient.

2.8.4. *Friction laws*

The chosen friction criteria are of the form: $g(r) \leq 0$ where $g(r)$ is a convex function. The non-slip domain is defined by the interior of the convex. Two friction criteria of the $g(r) \leq 0$ form are particularly used: the Tresca criterion and the Coulomb criterion.

The first works on friction were carried out by Leonard da Vinci at the beginning of the 16th Century. The first value of the proportionality coefficient between the friction force and the weight of the body. Amontons and then Coulomb would continue the studies of Leonard of Vinci and develop them. Coulomb is mainly responsible for presenting the first laws of friction.

The law of friction derived from Coulomb's model is the oldest and the most utilized in contact problems with friction. This law integrates the concept of threshold and is characterized by the contact pressure.

2.8.5. *Coulomb's law*

The reaction $\overrightarrow{R}$ at the contact point can be divided into a normal force F^n and a tangential force (or friction force) F^t:

$$\vec{R} = F^n.\vec{n} + F^t.\vec{t}. \qquad [2.88]$$

Historically, Amontons proposed a proportionality law between the normal force F_n and the friction force F_t. Any law respecting this proportionality is called Coulomb's friction law.

Coulomb's law is exposed in the following manner:

If $U^n = 0$ and $F^n < 0$ (contact condition), then the tangential force F^t is equal to the product of the normal force F^n by the friction coefficient ν_f.

$$|F^t| \leq \nu_f \|F^n\| \qquad [2.89]$$

with:

– if $|F^t| < \nu_f||F^n||$, then $V_{\text{slid}} = 0$ (adherence region);

– if$|F^t| = \nu_f||F^n||$, then $A \geq 0$ such that $V_{\text{slip}} = -AF^t$ (slip region);

with ν_f the Coulomb friction coefficient and V_{slip} the relative slip velocity between the two bodies in contact.

Coulomb's law can be represented graphically in the form of a cone commonly called Coulomb's cone (see Figure 2.5).

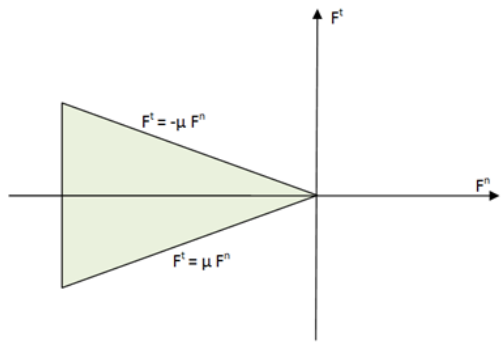

Figure 2.5. *Representation of Coulomb's cone*

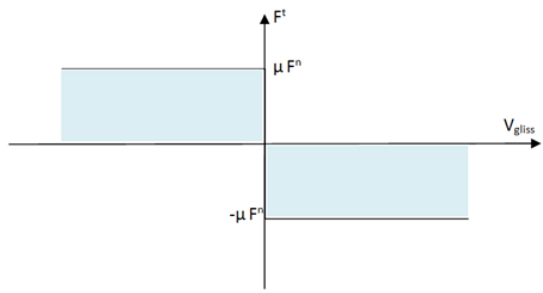

Figure 2.6. *Coulomb's law*

In the literature, numerous experimental results and empirical formulae involve the variation of the friction coefficient according to the slip velocity.

2.8.6. *Tresca's law*

Another model employed in modeling the friction, utilized when the normal forces are significant (for example for the simulation of material forming), is called Tresca's law. Unlike Coulomb's law, which is expressed in

terms of forces (or stresses), Tresca's law is expressed in stresses only in the following manner:

if $U^n = 0$ and $F^n < 0$ (contact condition), then:

$$\|\sigma_t\| \leq \|\sigma_{\max}\| \qquad [2.90]$$

with:

– if $||\sigma_t|| < ||\sigma_{\max}||$, then $V_{\text{slip}} = 0$ (adherence);

– if $||\sigma_t|| = ||\sigma_{\max}||$, there is then $A \geq 0$ such that: $V_{\text{slip}} = -A\sigma_t$ (slip);

with $\sigma_{\max}$ Tresca's threshold, σ_t the tangential stress and V_{slip} the relative tangential velocity between the two bodies in contact.

Figure 2.7 corresponds to the graphical representation of this law.

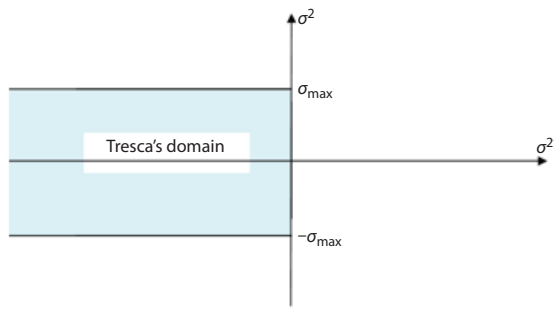

Figure 2.7. *Graphical representation of Tresca's law*

3

Stamping

3.1. Introduction

In the current economical context, the motor industry community have established as their priority the following objectives: improve product quality, minimize production costs and time to market.

To achieve these goals, the industry strives to modernize their working tools in order to minimize the duration of design cycles and improve manufacturing processes.

In the industry, deep-drawing of metal sheet constitutes, during the manufacturing process, a crucial phase with respect to the quality and the cost of the final product. A vehicle is first judged according to its external appearance.

Figure 3.1 presents the two main deformation modes encountered in deep-drawing. Case (a) corresponds to expansion deep-drawing using a punch, where the sheet metal is fixed in a blank holder. Case (b) corresponds to deep-drawing with shrinkage of the metal sliding under the blank-holder and without expansion on the head of the punch.

When faced with a difficult piece to shape, the stamper is always faced with the dilemma:

– utilization of a high blank-holder force (BHF) to avoid wrinkles at the risk of fracture (example (3.1a));

– choice of a lower BHF incurring the possibility of the presence of wrinkles (example (3.1b)).

Material Forming Processes: Simulation, Drawing, Hydroforming and Additive Manufacturing, First Edition. Bouchaib Radi and Abdelkhalak El Hami.
© ISTE Ltd 2016. Published by ISTE Ltd and John Wiley & Sons, Inc.

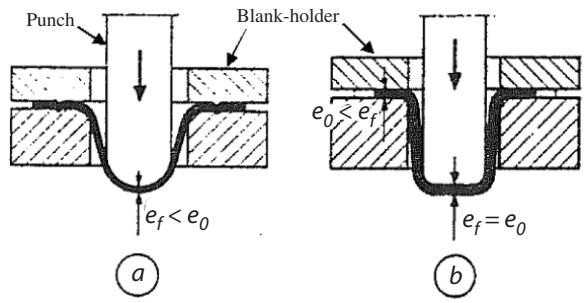

Figure 3.1. *Main deformation modes by deep-drawing, blank thickness at the initial state, e_f, blank thickness. a) Stretching, and b) shrinkage*

For a given die and circular punch, the larger the blank, the more metal there is to swage. This naturally increases the forces at the level of the blank-holder the risks of fracture, the circumferential compression, and the risks of wrinkling.

There are two limits for adjusting the BHF [COL 02]. To determine them, the severity of deep-drawing a flat-bottom bowl is experimentally studied, the objective being to study the ability of the metal to shrink and not its ability to expand (Figure 3.1(b)). The test is analyzed using the deep-drawing ratio defined as: β is equal to the diameter of the blank/diameter of the punch.

The test begins with small diameters blanks and a low BHF. Wrinkles appear on the flange. The force is gradually increased until the wrinkles disappear. On the following blanks, the BHF increases until the moment where, under the effect of the increasingly high resistance forces, the drawn part breaks or undergoes a process of necking. The gap existing between BHFfol and BHFfra is called adjustment latitude of the BHF. The larger the latitude for a given tooling and a given blank size, the better the ability of the metal to undergo shrinkage. The acceptable range of BHF decreases and may eventually become equal to zero. This state is reached when the force necessary to remove wrinkles becomes equal to the force necessary to break the workpiece. The deep-drawing limit ratio is then reached.

Due to the decrease in the thicknesses, drawn parts often reach the limit defining the success of the operation, compared to risks such as necking followed by fracture. The next section focuses on the forming limit curves (FLCs) that make it possible to predict the success of deep-drawing.

3.2. Forming limit curve

Regarding the quantitative prediction of the success of deep-drawing in thin sheet metal, we rely on the concept of FLC, which came into existence in 1965 through the works of Keeler [KEE 65] and was completed in 1968 by Goodwin [GOO 68].

Based on the FLC, the deep-drawing industrialist can understand the nature of the deformation modes in different areas of the workpiece. The FLCs are plotted in $\frac{\varepsilon_1}{\varepsilon_2}$ diagrams where:

– ε_1 is the maximal principal strain (with greater algebraic value, it then determines the main strain direction) in the y-axis;

– ε_2 is the minimal principal strain in the x-axis.

FLC have great interest for deep-drawers, because the plane $(\varepsilon_1, \varepsilon_2)$ is split into two domains:

– the domain located above the curve, which corresponds to the fracturing of the drawn parts;

– the area located underneath, which corresponds to the success of the deep-drawing.

Theoretically, four conditions must be satisfied to plot a FLC:

1) plane stresses state (no stresses in the thickness);

2) negligible thickness shear;

3) direct trajectories;

4) no bending.

The FLCs do not systematically give perfectly relevant indications. In fact, their shape and their level, for a given material, depend greatly on the conditions of their acquisition. These occur on at least four levels: the thickness of the sheet, the means used to deform it, the tools used to measure the deformations and the method employed to estimate the appearance of localized necking.

To build an FLC, it is therefore necessary to carry out tests allowing different deformation modes to be obtained from direct trajectory. In addition, it is essential for each test to be able to measure the deformations, in order to represent each test in the forming limit diagram $(\varepsilon_1, \varepsilon_2)$.

The purpose of evaluating the values of the strains for the FLCs is to be able to follow the changes in the value of components of the plane tensor of the deformation of material points over time. In the case where the area of interest would have undergone multiple deformations (several-pass deep-drawing, for example), the measure must be performed continuously during testing, and not only at the final state. To this end, a marking related to the sheet is applied before forming and its deformations are then measured. For this, it is necessary to first ensure that the properties of the material are not modified when marking. It is also necessary that the marking entirely covers the area under study [LAC 69].

In addition, the marking on the blank must withstand a minimum level of aggression due to the manipulations when in contact with the tool, it should not disrupt the friction conditions too much and it should not be a source of local damage to the metal. The solutions currently in use for marking the networks are classified in two large families that depend on the method of measure being employed [ARR 81, COL 02]: grid marking or random marking. Figure 3.2 gives an example of an FLC.

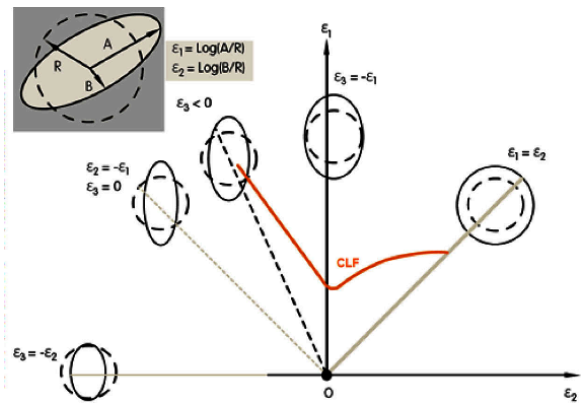

Figure 3.2. *Example of a forming limit curve*

3.3. Stamping modeling: incremental problem

Although the description of the stamping process is an easy task, its implementation remains a delicate operation and difficult to control. During the development of a finished workpiece, the dialog between consultancy firms, planning and manufacturing departments is somewhat prolonged. After

having been defined, a piece undergoes several modifications, before becoming feasible while respecting the requirements of the consultants.

During this dialogue, numerical modelling constitutes an alternative that can meet the objectives mentioned above. In effect, it can be used as a tool to assist in the design, further reducing the number of expensive feasibility tests.

The fast-paced development in the field of modeling is linked to the progress of information technology. The latter has allowed the development of very sophisticated numerical methods, such as the finite element method that requires, especially in nonlinear applications, fast computers with a sufficiently large memory capacity.

The numerical simulation of sheet metal stamping comprises several difficulties:

– representation of the tools, due to the complexity of the geometric shapes;

– formulation of the problem that leads to equations requiring high-performance approximation and resolution methods. If the modeling of sheet metal by the method of the finite element seems obvious, the choice of the finite element is much less;

– modeling the behavior of sheet metal that undergoes large transformations and large elastic–plastic deformation during deep-drawing;

– modeling friction contact between the sheet metal and the tools;

– the size of the numerical problems to solve requires the use of high performance methods and numerical algorithms in order to reduce the calculation time to a reasonable level.

Therefore, different skills are required to achieve a satisfactory result. This is the perspective that this chapter follows.

3.3.1. *Modeling of sheet metal*

Being a thin product, sheet metal is represented by its average parameterized surface and by X^{α}, a convective coordinate system. It is likened to a membrane in which the mechanical quantities of thickness do not vary. Flexural stress is ignored and we assume the plane stress hypothesis, $\sigma^{i3} = 0$ for $i = 1, 2, 3$.

Let $M^0(X^\alpha)$ be the position of any point of the membrane at the initial instant t_0 and $M(X^\alpha)$ that at instant t. The material basis was defined at instant t_0 by:

$$g_\alpha^0 = \frac{\partial M^0}{\partial X^\alpha}$$

and at instant t by:

$$g_\alpha = \frac{\partial M}{\partial X^\alpha}$$

g_0^α and g^α being the respective dual basis. The vector g_3 is chosen as being normalized and orthogonal to the tangent plane M:

$$g_3 = \frac{e_1 \wedge e_2}{\| g_1 \wedge g_2 \|} = g^3$$

which gives

$$g_{33} = g^{33} = 1, \quad g_{\alpha 3} = g_{3\alpha} = g^{3\alpha} = g^{\alpha 3} = 0.$$

and taking into account the previous assumptions, equation [2.82] becomes:

$$\int_{\Omega'} \sigma'^{\alpha\beta} \nu'_\alpha \,|_\beta \, d\Omega' = \int_{\partial\Omega'_F} T'^i \nu'_i d\Gamma' \quad \forall \nu' \in V^{ad} \qquad [3.1]$$

with $d\Omega = h(X^\alpha) d\Gamma$.

The kinematics of the problem, as it has been presented, do not allow calculating $\Delta e'_{33}$. It is thus not yet possible to mention the variation of thickness. However, it can be shown that the plane stress hypothesis and the plastic incompressibility make it possible to obtain the expression $\Delta e'_{33}$, and therefore to calculate the thickness variation h.

3.3.2. *Spatial discretization: finite elements method*

Equation [3.1] is discretized by the finite element method. It uses two isoparametric membrane elements, a quadrangle $Q4$ and a triangle $T3$.

Ψ^n denotes the interpolation functions, the convective coordinates in each element are interpolated by:

$$X^\alpha = X_n^\alpha \Psi^n(X^1, X^2)$$

with $\Psi^n(X^1, X^2) = \Psi^n(\mathcal{F}(\zeta^1, \zeta^2))$ where ζ^α are the local coordinates of the element and $\mathcal{F}$ is the transformation that enables shifting from the basic element to the real element.

This notation allows the expression of the displacement field u (or velocity field v) and its derivative, with respect to the displacement in each node, of the functions Ψ and their derivatives with respect to X^α. Following a similar method, we can calculate the g_α.

Equation [3.1] is calculated in each finite element; $v_\alpha \mid_\beta$ is replaced by its interpolated form. By integrating over the whole domain Ω, we have to solve a problem that is represented in the form:

$$\text{Res}(\delta u) = 0 = F_{int}(\Delta u) - F_{est}(\Delta u) \qquad [3.2]$$

where $\text{Res}(\delta u)$ is a vector of dimension, N is the total number of degrees of freedoms (D.O.F), $F_{int}(\Delta u)$ represents the internal stresses and $F_{ext}(\Delta u)$ represents the external stresses.

NOTE 3.1.–

1) For reasons of numerical processing, it is further assumed than the vector $\text{Res}(\delta u)$ constitutes the gradient of a functional energy of the structure, whose expression is not necessarily known.

2) The vector $\text{Res}(\delta u)$ constitutes the gradient of a functional energy of the structure. In deep-drawing modeling, the conditions of unilateral contact with friction will be the ones that will generate external stresses.

3.3.3. *Choice of sheet metal and finite element approximation*

As in all numerical approximation methods, the hypotheses assumed during the modeling of a problem and the chosen discretization determine the accuracy of the solution and the allocated calculation time. In the finite element method, such hypotheses influence the choice of the basic functions of the element. The more these assumptions are simplified, the less rich the element, which limits the size of the problem regarding the accuracy of the solution.

The approximation of sheet metal using an adopted membrane is not necessarily the best choice. However, having three D.O.F. per node allows for the reduction of the size of the problem to solve. On the other hand,

neglecting the flexural stiffness, numerical problems emerge whenever the sheet is locally flat. This is expressed either by a singular tangent stiffness matrix or a strongly ill-conditioned matrix.

We can modelize sheet metal with a shell, using discrete Kirchhoff theory (D.K.T) elements. These are sufficiently rich and performing elements, and have only 6 D.O.F. per node.

3.4. Modeling tools

The process of deep-drawing consists of deforming sheet metal (called blank in the deep-drawing industry) by means of tools including:

– a punch that has the shape of the desired part, which constitutes the male tool;

– a die cavity of the same shape as the tool, which constitutes the female tool;

– a blank-holder that allows specific boundary conditions to be imposed to the sheet;

– a casing that connects the die cavity and the blank-holder.

Tooling modeling, assumed to be perfectly rigid, constitutes a delicate and important task in the numerical modeling of deep-drawing; there are three methods for modeling a tool, which will obviously be represented by its active surface. We present the advantages and the limitations of each method.

3.4.1. *Tool surface meshing into simple geometry elements*

To overcome the difficulty that exists in the complexity of the modelled surfaces, one approach consists of meshing these surfaces by triangular or quadrangular finite elements. Furthermore, finite element designates a purely geometrical surface element.

This model presents two disadvantages:

– the modeling of complicated surfaces is a delicate task, which is difficult to achieve;

– the non-regularity of the meshed surface generates numerical issues in solving the contact problem, in particular the cycling problems state that sometimes the algorithm cannot convergence.

3.4.2. *Analytical representation of tools*

This method is used in the simulation of academic deep-drawing cases. The validation of calculation software has required that simple geometry examples be processed. This allows the analysis of the experimental results, knowing that this operation is virtually impossible to achieve when it comes to an industrial case. The examples of the tooling under consideration consist of an o-ring forming die, a crown-shaped blank-holder and a punch that is either spherical or conical with a flat base. With this type of tooling, in which the first method is easy to use, an analytical representation of the surfaces has been chosen. This is a very easy task to perform.

This method has the following advantages:

– the surfaces obtained are regular;

– the method requires an insignificant memory size. In fact, only a few parameters have to be stored (rays, etc.), unlike the first method that requires that the coordinates of all vertices of the elements be stored, as well as their connectivity;

– the tooling is very easy to manage.

The limitation of this method lies in the fact that an industrial surface does not admit any analytical representation.

3.4.3. *Bezier patches*

The geometry of the tooling for deep-drawing is very complicated. Since there is no accurate or approximated analytical representation (a map) of the surfaces of tools, approximation methods for surfaces have imposed themselves. Inspired by the deep-drawer's profession, which uses a very unique method to manage curves (which are only sections of surfaces), Bezier has implemented an approximation method well suited to this profession. This method has been extended to the case of surfaces.

3.4.3.1. *Curve polynomial approximation*

Given a curve $\mathcal{C}$, it is possible to approach the coordinates of a point belonging to this curve by:

$$x(\upsilon) = \alpha_i \upsilon^i$$
$$y(\upsilon) = \beta_i \upsilon^i \quad i = 0, \ldots, N$$
$$z(\upsilon) = \gamma_i \upsilon^i$$

where a parameter $\upsilon \in [0, 1]$ has been introduced.

υ^i denotes υ to the power i, N is the polynomial degree, α_i, β_i and γ_i its coefficients verifying:

$x(0) = \alpha_0$; $y(0) = \beta_0$; $z(0) = \gamma_0$, the coordinates of the origin of the curve,

$x(1) = \alpha_1$; $y(1) = \beta_1$; $z(1) = \gamma_1$, the coordinates of the end of the curve,

and if $P(\upsilon)$ denotes the coordinate vector from any point of the curve, we get:

$$P(\upsilon) = \begin{bmatrix} x(\upsilon) \\ y(\upsilon) \\ z(\upsilon) \end{bmatrix}$$

which can be expressed in the form:

$$P(\upsilon) = b_i \upsilon^i \quad i = 1, \ldots, N, \; b_i = [\alpha_i, \beta_i, \gamma_i]$$

This equation perfectly defines the curve parametrized by υ.

3.4.3.2. *Surface polynomial approximation*

Starting from the fact that a surface can be obtained by varying the points of a curve in a well-defined domain, each point of this curve will describe a curve belonging to the surface. The first curve is the so-called generatrix curve that may be approximated by a polynomial of degree N; each curve is created by the motion of the generatrix and can be approximated by a polynomial of degree M. Both curves described by the extreme points of the generatrix are called directrix curves. These curves are parameterized by a variable $\varpi \in [0, 1]$. For $\varpi = 0$, we find the initial generatrix, and for $\varpi = 1$, we get the final generatrix.

The generated surface S is parametrized by υ and ϖ. A point belonging to the surface is denoted $P(\upsilon, \varpi)$, it is expressed by:

$$P(\upsilon, \varpi) = B_{ij}\upsilon^{(i)}\varpi^{(j)} \quad i = 1, \ldots, N, \text{ and } j = 1, \ldots, M \qquad [3.3]$$

This representation allows, from a given set of points, the definition of any surface that approximates the actual surfaces of the tool. The coefficients b_i and B_{ij} are calculated from the coordinates of the points collected on the actual surface. This allows all relevant information at each point of the surface to be obtained (the tangent plane and the normal to the surface at a point, etc.).

However, such a representation cannot be of any help to deep-drawing technicians who are accustomed to their own working methods. This has resulted in creating an approximation method called polygonal approximation, which is more similar to a graphical concept than to a mathematical concept.

3.4.3.3. *Curve polygonal approximation*

Given a curve S and a set of points P_i; $i = 1, \ldots, N+1$ where P_1 and P_{N+1} belong to the curve (see Figure 3.3). If $G_i = OP_i = P_i$ denotes a vector set, for all $\upsilon \in [0, 1]$, a point $P(\upsilon)$ can be written:

$$P(\upsilon) = \gamma_i G_i, \qquad [3.4]$$

the coefficients must verify the Cauchy condition:

$$\sum_{i=1}^{N+1} \gamma_i = 1 \qquad [3.5]$$

(in order to see the necessity of this condition, it is sufficient to take all components following x of G_i equal to 1).

One way to obtain these coefficients consists of developing the Bernstein polynomial:

$$((1 - \upsilon) + \upsilon)^N = 1 = (1 - \upsilon)^N + \cdots + \upsilon^N, \qquad [3.6]$$

which gives:

$$P(\upsilon) = (1-\upsilon)^N G_1 + \cdots + \upsilon^N G_{N+1}$$
$$= \mathcal{B}_i$$

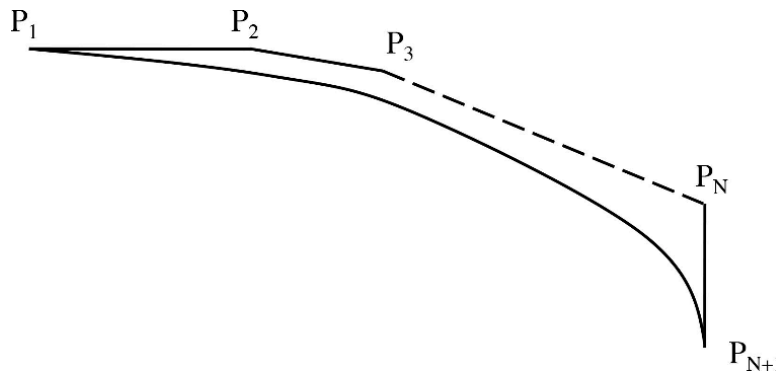

Figure 3.3. $N+1$ *class curve*

For $N = 3$,

$$P(\upsilon) = (1-\upsilon)^3 P_1 + 3\upsilon(1-\upsilon)^2 P_2 + 3\upsilon^2(1-\upsilon)P_3 + \upsilon^3 P_4. \quad [3.7]$$

Developing this equation, by factorizing the υ with equal powers, yields:

$$P(\upsilon) = P_1\upsilon^0 + 3(P_2 - P_1)\upsilon^1 + (3P_1 - 6P_2 + 3P_3)\upsilon^2$$
$$+ (-P_1 + 3P_2 - 3P_3 + P_4)\upsilon^3 \quad [3.8]$$
$$= b_i \upsilon^i,$$

NOTE 3.2.–

1) The reasoning taken for $N = 3$ is generalized for any N.

2) If we denote $a_i = P_{i+1} - P_i$, and if $\|a_i\| = 1$, the fundamental Bezier curve is found again.

3) The points P_i are called the control points of the polygon.

4) A curve represented by a polynomial of degree N will be represented by a polygon with $N+1$ control points, called a $N+1$-class curve.

5) The polynomial and the polygonal notations are equivalent, therefore knowing P_i is tantamount to knowing the b_is, and vice versa.

Highlighting such equivalence allows the computational scientist to manipulate the polynomial form and to manage the information on the geometric entity that he needs, as it allows the technician to manipulate the control points to modify the geometry of its curve.

3.4.3.4. *Polygonal approximation of a curve*

The reasoning followed in the case of curves is generalized to the surfaces and a point $P(\upsilon, \varpi) \in S$ is written:

$$P(\upsilon, \varpi) = [\varpi]^T [M_2] [P] [M_1] [\upsilon],$$

with

– $[\upsilon]^T = \left[1 \, \upsilon \ldots \upsilon^M\right]$;

– $[\varpi]^T = \left[1 \, \varpi \quad \varpi^N\right]$;

– $[P]$ is the $((M+1) \times (N+1))$ matrix that contains the coordinates of the control points, P_{ij} is the jth control point of the curve i;

– $[M_1]$ and $[M_2]$ are two transition matrices;

– $M+1$ the number of control points of the generatrix curve;

– $N+1$ the number of control points of the directrix curves.

Taking the case of a curve and considering only one 4-class curve $(N=3)$, in polynomial notation, we get:

$$P(\upsilon) = b_i \upsilon^i \quad i = 0, \ldots, 3$$

In order to bring the expression of $[M1]$, forward, equation [3.8] is put in matrix form:

$$P(\upsilon) = \begin{bmatrix} P_1 & P_2 & P_3 & P_4 \end{bmatrix} \begin{bmatrix} 1 & -3 & 3 & -1 \\ 0 & 3 & -6 & 3 \\ 0 & 0 & 3 & -3 \\ 0 & 0 & 0 & 1 \end{bmatrix} \begin{bmatrix} 1 \\ \upsilon \\ \upsilon^2 \\ \upsilon^3 \end{bmatrix}$$

$$= \begin{bmatrix} b_0 & b_1 & b_2 & b_3 \end{bmatrix} \begin{bmatrix} 1 \\ \upsilon \\ \upsilon^2 \\ \upsilon^3 \end{bmatrix}$$

$$= [P_i]\,[M_1]\,[\upsilon]$$

$[P_i]$ is a row of matrix $[P]$.

This notation is generalized to curves of class N. If a surface is described by M N-class directrix curves (or alternatively N M-class generatrix curve), the ith generatrix curve is represented by a polynomial $P_i(\upsilon)$ such that (see Figure 3.4):

$$P_i(\upsilon) = [P_i]\,[M_1]\,[\upsilon] \qquad [3.9]$$

with: $[P_i] = \begin{bmatrix} P_{i1} & P_{i2} & \dots & P_{iM} \end{bmatrix}$, $[\Upsilon]^T = \begin{bmatrix} 1 & \upsilon & \dots & \upsilon^M \end{bmatrix}$ and $[M_1]$ is a $M \times M$ matrix.

$P_i(\upsilon)$ is the point that describes the generatrix i when υ describes the interval $[0, 1]$. It is possible to write N equations of this type, which represent the N generatrixes curves. After assembling the N equations, the following condensed notation is obtained:

$$[P\,(\upsilon)] = [P]\,[M_1]\,[\upsilon] \qquad [3.10]$$

with: $[P\,(\upsilon)]^T = \begin{bmatrix} P_1\,(\upsilon) & P_2\,(\upsilon) & \dots & P_N(\nu) \end{bmatrix}$ and

$$[P] = \begin{bmatrix} P_{11} & P_{12} & \cdots & P_{1M} \\ P_{21} & P_{22} & \cdots & P_{2M} \\ \vdots & \vdots & \vdots & \vdots \\ P_{N1} & P_{N2} & \cdots & P_{NM} \end{bmatrix} \qquad [3.11]$$

For a given υ, points $P_i(\upsilon)$, $i = 1 \dots N$, which belong to the generatrixes i, may constitute the poles of a directrix curve belonging to the surface S. It is possible to choose υ in such a manner that $P_i(\upsilon)$ be the poles of the given directrix j.

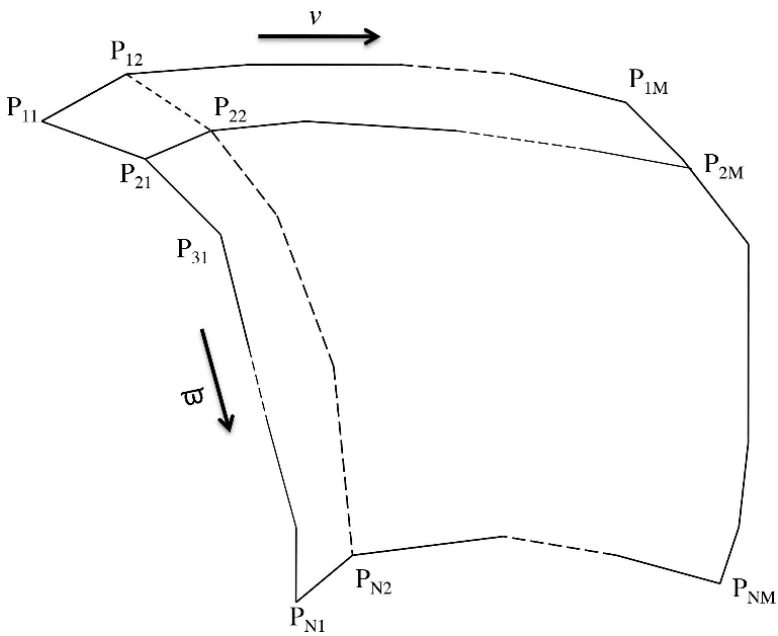

Figure 3.4. *Surface with N M-class generatrixes*

Thus for a given (any) $\upsilon = \upsilon^0$, all generatrixes can be described with a parameter ϖ describing the interval $[0, 1]$. This is written in polynomial form as:

$$P(\upsilon = \upsilon^0, \varpi) = b_i' \varpi^1, \quad i = 0, \ldots, N$$

In polygonal form, a point describing a generatrix takes the form:

$$P(\upsilon = \upsilon^0, \varpi) = [\overline{\omega}]^T [M_2] [P(\nu)]$$

where $[\varpi]^T = \begin{bmatrix} 1 & \varpi & \ldots & \varpi^N \end{bmatrix}$ and $[M_2]$ is an $N \times N$ matrix.

By replacing $[P(\upsilon)] = \begin{bmatrix} P_1(\upsilon) & \ldots & P_N(\upsilon) \end{bmatrix}$ with its expression [3.9] for the case of any υ (the value of υ^0 has been taken randomly at the beginning), we get:

$$P(\upsilon, \varpi) = [\varpi]^T [M_2] [P] [M_1] [\upsilon].$$

Thus, when the two parameters (υ, ϖ) describes $[0,1] \times [0,1]$, the point $P(\upsilon, \varpi)$ describes the entire surface S.

According to [3.11], the matrix B components $[B_{ij}]$ can be identified (the formulae for shifting from one notation to another) by:

$$[B] = [M_2]\,[P]\,[M_1]\,,$$
$$[B_{ij}] = [M_2]_{ik}\,[P]_{kl}\,[M_1]_{lj}$$

It is possible to derive that the two polynomial and the polygonal approximations are equivalent. The above equations constitute the formulae for changing from one notation to the other.

NOTE 3.3.–

1) The approximate surface S, represented in polygonal form, is called a Bezier patch.

2) A deep-drawing tool is represented by several patches.

3) In CAD, a patch is defined by its control points. A shift from polygon to polynomial is therefore necessary in order to manage the patch in calculation software.

4) Some techniques such as the computation of the intersection of a straight line or a plane with a patch, and the computation of the orthogonal projection of a point on a patch, are necessary for processing the contact problem. Without going into details, it should be noted that the calculation of the orthogonal projection of a point on a patch requires the application of successive approximations.

3.5. Stamping numerical processing

The problem of the contact between different solids is quasi-existent in several industrial applications. It may be the cause of certain peculiarities in the design of the product and sometimes in the structure. In fact, the phenomenon of contact can be a frequent cause of the fracture of the structure. The implementation of the material is an industrial example where unilateral contact with friction is present throughout the process. The study of this contact determines the geometrical form of the deformed metal and provides the stresses on the contact surface. Several methods have been proposed in recent years for the solution of the problem of contact between thin sheet metal and a punch. The majority of these methods are based on the

finite element approximation [CHA 98, LI 97, RAD 98, REF 98, BAB 00]. In reality, the validity of the solution found depends on the choice of the design parameters. Nonetheless, several tests show that the latter are known only in an approximate manner, while they must follow a statistical distribution.

The modeling of forming processes (rolling, forging, deep drawing, etc.) of mechanical parts presents numerous difficulties. These originate from multiple mechanical nonlinearities such as:

– material nonlinearities due to the law of the material's behavior. Most often, this law can be expressed in the form of first-order nonlinear differential equations;

– geometric nonlinearities that emerge when large displacements, large rotations and large deformations appear;

– the nonlinearities in the development of the boundary conditions. This type of nonlinearity appears particularly in problems of contact and friction between solids. These phenomena are described by inequalities and projection operators.

It should be noted that these three nonlinearities are often intrinsically linked to one another. For instance, the nonlinear behavior of metals such as plasticity is due to large deformations. Naturally, if one of these three linearities appears in a mechanical problem, a nonlinear processing procedure must be employed. As a result, numerical difficulties occur at several levels, in particular when:

– solving the nonlinear equations of equilibrium (global level);

– integrating the laws of behavior (local level);

– solving the nonlinear equations of contact and friction coupled with the equilibrium equations (global or local level).

There are numerous laws of friction occurring during forming processes; however, Coulomb's friction law remains the most used due to the simplicity of its implementation and to the fact that it is generally suitable for metal/metal friction. Consequently, we make use of this law in this chapter.

3.5.1. *Problem statement*

It is assumed that a deformable solid (thin sheet metal) occupies an open bounded subset Ω^t of $\mathbb{R}^3$ with a regular border Γ^t at instant t and the open

and bounded subset Ω^0 at instant t_0. Furthermore, it is subject to the volume force f, to the surface stress g applied to the portion Γ_g, a displacement is imposed on the portion Γ_u and the contact reaction t_c on the portion Γ_c (Γ_c is an unknown of the problem). It is assumed that $\Gamma_g \cap \Gamma_u \cap \Gamma_c = \emptyset$.

Let M be a point in the domain, it has coordinates (x, t) in the current configuration C_t and (X, t) in the initial configuration C_0. In the context of a quasi-static evolutive formulation, the equation of motion in the local coordinate system of point M in the current configuration is given by:

$$(E)\begin{cases} \text{div}\sigma + f = 0 & \text{on } \Omega^t \\ u = \bar{u} & \text{on } \Gamma_u^t \\ \sigma.n = g & \text{on } \Gamma_g^t \\ \sigma.n = t_c & \text{on } \Gamma_c^t \end{cases} \qquad [3.12]$$

where σ is the Cauchy stress tensor and Γ_c^t is the candidate contact area. In our working context, the displacement imposed is equal to zero.

However, in the initial configuration C_0, the equation of motion item M is:

$$(E_0)\begin{cases} divT + f = 0 & in \ \Omega^0 \\ u = \bar{u_0} & \text{on } \Gamma_u^0 \\ T.n = g & \text{on } \Gamma_g^0 \\ T.n = t_c & \text{on } \Gamma_c^0 \end{cases} \qquad [3.13]$$

where T is the first Piola–Kirchhoff stress tensor and f_0 is the external volume force applied to the initial configuration.

To solve the mechanical problem under large elastoplastic deformations, the equations relative to the behavior of the material must be integrated during loading generated by the deformation of the structure. The numerical method used to solve this problem must respect the indifference of the material [10].

By taking conditions [2.87] into account, the principle of virtual work provides the weak form of the problem (E):

$$\int_{\Omega^t} \sigma : \nabla^s v d\Omega - \int_{\Omega^t} f v d\Omega - \int_{\Gamma_g^t} g v d\Gamma - \int_{\Gamma_c^t} t_c v d\Gamma = 0 \qquad [3.14]$$

which is valid for any v with $v = u$ on Γ_u^t satisfying the condition $v.n \leq 0$ on Γ_c^t. Similarly, a weak formulation of the problem can be obtained (E_0).

Despite its elementary form, we use the classic Coulomb's law as the friction law. According to Duvaut [DUV 72], this law of friction can be written in the form:

$$\left\{ \begin{array}{lcll} \|r_t\| & \leq & \nu_f |r_n| & \\ \|r_t\| & < & \nu_f |r_n| & \Rightarrow \quad \dot{u_t} = 0 \\ \|r_t\| & = & \nu_f |r_n| & \Rightarrow \quad \exists \alpha \geq 0 \quad \dot{u_t} = -\alpha r_t \end{array} \right. \qquad [3.15]$$

where ν_f is the Coulomb friction coefficient.

NOTE 3.4.– Other laws of friction can be used such as that proposed by Oden and Pires [ODE 83]. Our numerical experiences have shown that similar results are obtained by making use of a local [3.15] or non-local [RAD 94] law. In [BUC 99], we can find a stochastic model relative to the non-local law.

Within the context of the approximation by finite elements, the Ahmed-type shell finite element (3D degenerate) is employed, taking into account the transverse distortion by means of joint interpolation. This type of finite element has been developed by Garner and Lochegnies [GEL 92] in the case of quadrilateral elements and by Boisse *et al.* [BOI 94] for triangular elements. These elements are isoparametric with linear interpolation. To avoid the locking problem associated with plastic incompressibility, we use mixed interpolation.

3.5.2. *The augmented Lagrangian method*

The deep-drawing process introduces various nonlinearities: geometric with large kinematic behavior and elastoplastic deformation. Taking the contact friction into consideration introduces more nonlinearities: the contact area is *a priori* unknown, the nonlinear term introduced in the weak form of the problem(E): $\int_{\Gamma_c^t} t_c v d\Gamma$ and the nature of Coulomb's friction law.

Without the term relative to the contact condition, equation [3.14] is nonlinear and can be solved by means of the Newton–Raphson method. The presence of the new term resulting from the frictional contact makes the direct utilization of this method impossible (discontinuity and non-differentiability) without prior processing.

To show the implicit form of this problem, the next variational formulation is given by:

$$\int_{\Omega^t} \sigma : \nabla^s v d\Omega - \int_{\Omega^t} f v d\Omega - \int_{\Gamma_g^t} g v d\Gamma - \int_{\Gamma_c^t} (\sigma_n N + \sigma_t) v d\Gamma \quad [3.16]$$

$$\begin{cases} \sigma_n \geq 0, & u_n(s_n - \sigma_n) \geq 0, \quad \forall s_n \geq 0 \\ \sigma_t \in C(\sigma_n), & u_t(s_t - \sigma_t) \geq 0, \quad \forall s_t \in C(\sigma_n), \end{cases} \quad [3.17]$$

where $C(\sigma_n) = \{s_t,\ s_t.n = 0,\ \|s_t\| \leq \nu_f |\sigma_n|\}$.

The dependency between the Coulomb cone $C(r_n)$ ($s_t \in C(\sigma_n)$) and the solution of the problem can be clearly seen. Incidentally, unilateral contact is a special case of stress problems and can be solved:

– either with a direct method; in this case, it is necessary to build a complicated projection operator and eliminate the possibility of using certain known algorithms such as the Newton algorithm;

– or with one of the penalty methods;

– or even by reducing the problem for finding saddle points using a dual method. This approach makes it possible to solve the problem by employing a very simple projection operator, while retaining the possibility of using Newton-based algorithms.

To solve the friction problem, it is shown that it can be reduced to a problem of finding saddle points. The approach proposed by Simo and Larsen (2D) [SIM 92] is extended to solve the problem of metal forming: contact between thin sheet metal and a punch (3D with elastoplastic behavior). The augmented Lagrangian approach relative to the contact problem with friction is based on the following weak form of the equilibrium equation:

$$G^*(u, \delta u) = G(u, \delta u) + \int_{\Gamma_c} (r_n \delta u + r_t.\delta u_t) d\Gamma^c \quad [3.18]$$

Taking into account the contact condition [2.87], the permissible displacement must satisfy the condition $\delta u.n \geq 0$ along the contact zone Γ_c. The nonlinear equation [3.18] must be solved at each time step, but it cannot be directly solved, therefore the reactions r_t and r_n are considered as known through an iterative process and the Newton–Raphson method is employed.

With the purpose of using a prediction-correction scheme, Coulomb's friction law is introduced in the form:

$$\Phi(r_n, r_t) = \|r_t\| - \nu_f |r_n| \leq 0 \quad [3.19]$$

$$\dot{u}_t = -\varsigma \frac{\partial \Phi}{\partial r_t} \quad [3.20]$$

$$\varsigma \geq 0 \quad [3.21]$$

$$\varsigma \Phi = 0 \quad [3.22]$$

It can be clearly seen that [3.19–3.22] is equivalent to the expression [3.15]. The quantities r_n and r_t are computed as the sum of a penalty and a Lagrange multiplier:

$$r_n = \lambda_n + \epsilon_n u_n. \quad [3.23]$$

Equation [3.20] is regularized taking this sum into account as follows:

$$\dot{u}_t - \varsigma \frac{\partial \Phi}{\partial r_t} = \frac{1}{\varepsilon_t}(r_t - \lambda_t) \quad [3.24]$$

The computation of contact and friction is carried out within the iterative process of the solution of the equilibrium equation. They are integrated between the instant t_k and t_{k+1}. By utilizing an Euler implicit method combined with a prediction-correction method, we get the following algorithm:

For the contact:

$$r_n^{k+1} = \lambda_n^{old} + \varepsilon_n u_n^k \quad [3.25]$$

where λ_n^{old} is the Lagrange multiplier obtained during the previous equilibrium state.

For the friction:

The analogy with the plasticity model is used to calculate the tangential reaction. During the current iteration, the tangential reaction is calculated as follows:

$$r_t^{k+1} = \lambda_t^k + (r_t^0)^k \quad [3.26]$$

where $(r_t^0)^k$ is the penalized part, it is given in this form:

$$(r_t^0)^k = r_t^k + \Delta\lambda_t^k + \varepsilon_t \Delta u_t^k \quad [3.27]$$

At this level, the verification of the Coulomb model is carried out:

– if $\Phi(r_n^{k+1}, r_t^{k+1}) \leq 0$ then the friction law is verified and $\lambda_t^{k+1} = r_t^{k+1}$,

– otherwise, the correction of the reaction r_t^{k+1} is achieved as follows:

$$r_t^{k+1} = \nu_f r_n^{k+1} \frac{(r_t^0)^k}{\left\|(r_t^0)^k\right\|} \quad [3.28]$$

and the equilibrium equation is solved by using the reactions r_t^{k+1} and r_t^{k+1}.

The updated value of $\Delta\lambda_t^{k+1}$ is given by:

$$\Delta\lambda_t^{k+1} = \Delta\lambda_t + \epsilon_t \left(\Delta u_t - \Delta\varsigma \frac{(r_t^0)^k}{\left\|(r_t^0)^k\right\|} \right) \quad [3.29]$$

where:

$$\Delta\lambda_t = \lambda_t^{k+1} - \lambda_t^k, \quad [3.30]$$

$$\Delta u_t = u_t^{k+1} - u_t^k, \quad [3.31]$$

$$r_t^0 = r_t^k + \Delta\lambda_t + \epsilon_t \Delta u_t, \quad [3.32]$$

and $\Delta\varsigma$ is relative to the consistency condition, which is written in the form:

$$\Delta\varsigma = \begin{cases} 0, & \text{if } \Phi^0 \leq 0 \\ \dfrac{\Phi^0}{\epsilon_t}, & \text{otherwise} \end{cases} \quad [3.33]$$

with $\Phi^0 = \Phi(r_t^0, r_n)$.

When the equilibrium state is obtained, the test relative to the contact condition is performed. If this condition is true, then the iterative process is stopped and the algorithm skips to the following increment.

– otherwise, the Lagrange multiplier λ_n is reupdated as follows:

$$\lambda_n^{new} = \lambda_n^{old} + \varepsilon_n u_n^{equi} \qquad [3.34]$$

The iterative process continues until the contact condition is verified.

The equilibrium equation is completely solved before reupdating the Lagrange multipliers (λ_n and λ_t). With this strategy, the contact condition is respected and the global system obtained is symmetrical.

NOTE 3.5.–

1) The convergence test only takes the contact condition into account, whereas the tangential reaction is built on the basis of Coulomb's law.

2) The advantage of this method is that it does not need large penalty parameters ε_n and ε_t to verify the condition of contact with friction. Such parameters must increase the problem of conditioning of the system.

3) It is difficult to find the slipping direction in the three-dimensional case when the slip direction is unknown. Despite this, good results can be achieved by employing regularization [3.24].

3.6. Numerical simulations

The method of the augmented Lagrangian proposed in the previous section is applied to solve a reference test proposed by Lee *et al*. [LEE 90]. The punch is hemispheric, the mesh is imposed and the deformable solid closed on the external part, as illustrated in Figure 3.5. The friction coefficient is equal to 0.3 and the behavior of the material is supposed to be elastoplastic with isotropic hardening.

Figure 3.5 compares the results of our approach and the results given by Lee *et al*. [LEE 90]. This figure shows the strong agreement between the two results. A comparison has been carried out between the exposed approach and other conventional approaches such as the penalty method and the Lagrangian method; Figure 3.6 gives the results of the comparison of the different methods used [BAB 00].

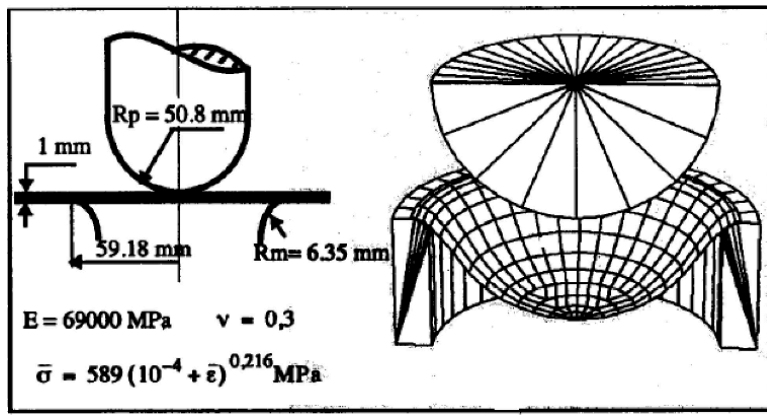

Figure 3.5. *Deformed structure*

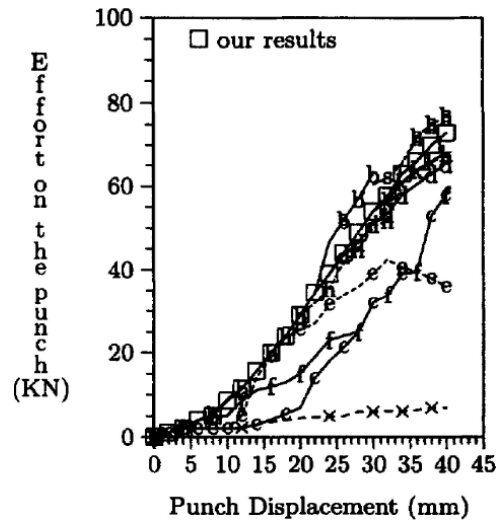

Figure 3.6. *Results of the different methods*

3.6.1. *Sollac test*

This test, proposed by the company Solace's method, is given here. This method is compared with [RAD 98], a comparison of this method can be related with the car manufacturers Renault & PSA to validate the model of behavior of steel sheet [PSA 89]. The sheet is spherical and fixed at the external part, and the punch is hemispheric. A quarter of the sheet is discretized by 331 nodes and 600 triangular elements. The descent of the punch is 50 mm.

The friction coefficient is equal to 0.25. The characteristics of the thin sheet and the results of the finding by the augmented Lagrangian method are given in Figure 3.7.

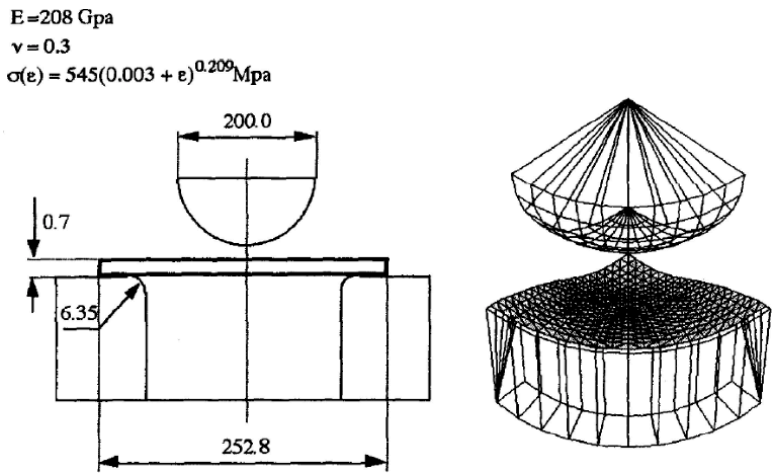

Figure 3.7. *Displacement of the punch (Sollac test)*

Figure 3.8 shows the results of the comparison between the augmented Lagrangian method, the penalty method [KIK 88] and Sollac's experimental results. This figure shows that the augmented Lagrangian method yields results relatively close to the Sollac experimental result at the end of the download. The penalization parameter of the augmented Lagrangian method is equal to 10^4, but it is equal to 10^{11} in the penalty method.

This approach has been applied to the forming of composite materials and the results are satisfactory. We refer to [CHE 09] for more information.

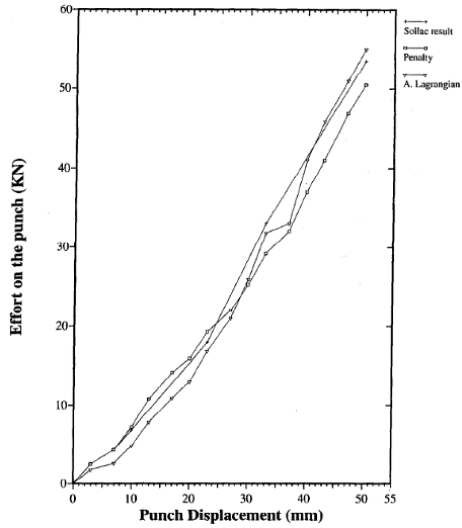

Figure 3.8. *Results of the different methods*

4

Hydroforming

4.1. Introduction

The methods and the technologies of production in the industrial sector have undergone a major review in order to meet new environmental standards and to respond to the increasingly demanding expectations of customers. The hydroforming process, mainly found in advanced industries and in particular in the automotive and the aeronautics sectors, falls within the scope of this concept. Resorting to this process is justified by all of the benefits that it presents relative to conventional processes such as deep-drawing, bending and welding. In effect, the process offers a wider field of formability compared with the conventional forming methods. It presents a less significant residual stress field and better manages the problems of contact and friction due to the use of the pressure exerted by the fluid. The latter also ensures better dimensional accuracy, consequently less springback and less problems in the assembly phase. Figure 4.1 shows a few workpieces manufactured by hydroforming in the automotive industry. Several works have focused on modeling and on optimizing the process in this sector [ASN 03b, OH 06, YUA 06b, LEE 02]. Based on these studies, the authors state that with hydroforming processes the total weight of the car is reduced and as a result so is fuel consumption. The use of the process is becoming widespread in several industrial sectors. Currently, there is interest in hydroforming of composite materials that can make a tremendous contribution to the aviation industry.

Hydroforming is mainly divided into two large families: tube hydroforming and blanks or plates hydroforming. The major difficulty of this process remains in determining the load paths, which depend on the material

Material Forming Processes: Simulation, Drawing, Hydroforming and Additive Manufacturing, First Edition. Bouchaib Radi and Abdelkhalak El Hami.
© ISTE Ltd 2016. Published by ISTE Ltd and John Wiley & Sons, Inc.

properties and the geometry, as well as on other parameters. Numerical simulation only remains insufficient for the development of the process. It is often the case that coupling with an optimization technique is necessary for a good estimation of the operating parameters. The finite element method coupled with a deterministic optimization technique is the approach commonly used in the literature to optimize the process and to obtain a workpiece without defects. This also involves the choice of adequate criteria allowing for the detection of potential plastic instabilities.

Generally, this approach does not take into account the variabilities that may bias certain operating parameters such as material properties, loads and other parameters. A good prediction of the final state of the workpiece essentially depends on the accuracy of these parameters, which often present risks. This begins as soon as the characterization phase of the material, of which several techniques referring thereto have been proposed in the literature. Throughout this chapter, we present the main techniques for the characterization of tubes.

This chapter also highlights the totality of forming techniques by hydroforming, the limitations of the process or the failure modes and also the plasticity criteria that make them possible to detect.

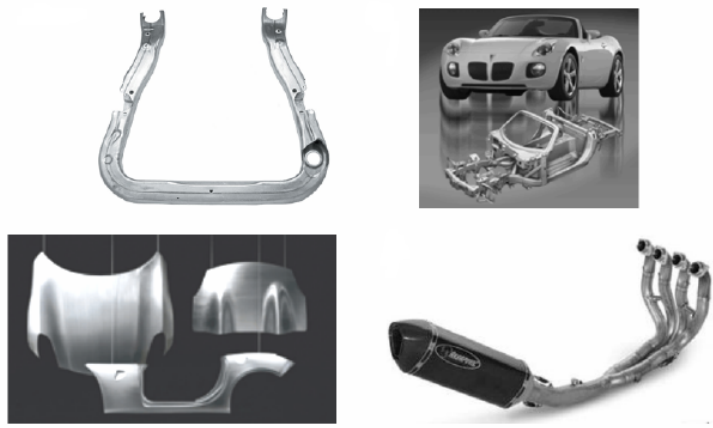

Figure 4.1. *Examples of workpieces obtained by hydroforming [MAK 07]*

4.2. Hydroforming

The first works on hydroforming date back to the 1940s. This method mainly consists of making use of the motive force of a fluid, usually oil or water, to plastically deform sheet metal so that it properly takes the shape of the forming die. The control of the method requires the implementation of criteria for the prediction of the potential plastic instabilities. Among the first works that have contributed to the study and the analytical modeling of the process and notably in tube hydroforming, we cite [ASN 03a], [KIM 02].

In effect, this process is used to manufacture simple or complex tubular shapes and in sheet metal forming as a substitute for deep-drawing technologies. In comparison with the conventional forming processes, the fluid replaces the force exerted by the punch, subsequently resulting in a better management of the contact problems between rigid and deformable bodies. This enables that the piece has good mechanical properties. Among hydroforming processes, we can mainly distinguish tube hydroforming and sheet or plate metal hydroforming.

4.2.1. *Tube hydroforming*

Tube hydroforming has broad applications in the industrial sector, and is particularly encountered in the automotive industry. Among the pieces manufactured by this process, we can find rails, engine exhausts, tailgates, etc. Figure 4.2 summarizes the various stages of the process. In general, this type of process involves two types of loads: an internal pressure generated by a fluid, enabling the tube to be plastically deformed by expansion, and an axial compressive stress, generated by two cylinders that bring material to the expanded area in order to compensate for the thinning of the tube and improve its formability. An appropriate choice of these two types of loads helps to avoid the premature necking of the tube and to ensure a better formability of the piece. The complexity of the method lies in determining the paths of the optimal loads.

This problem intensifies in the case of complex tubular forms and preformed tubes. The choice of loads depends strongly on the geometrical characteristics of the workpiece to manufacture and also on the material being used. The success of the process requires a synchronization between the internal pressure and the axial displacement. A large number of works have focused on the optimization of load paths for simple and complex geometries [AUE 04, IMA 05, FAN 03, MOH 09].

4.2.2. *Sheet metal hydroforming*

Hydroforming of sheet metal is similar to conventional stamping techniques. In effect, the fluid can have the same role as the punch or as the forming die. The use of a fluid under pressure instead of the force exerted by the punch results in a better management of the contact problems between rigid and deformable bodies. This makes it possible to expand the formability domain of the material and to obtain workpieces with a better distribution of the final thickness.

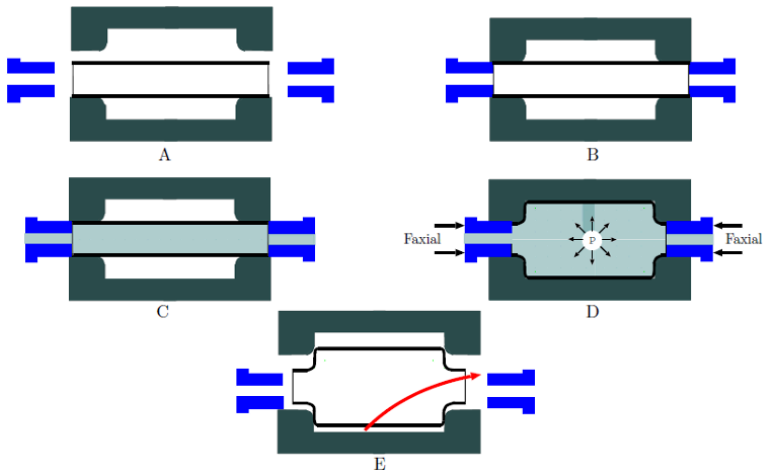

Figure 4.2. *Tube hydroforming*

Blank hydroforming represents a new alternative to the conventional method of stamping, in which the punch or the forming die are replaced by a system that is capable of generating a pressure, which will in turn allow the piece to be formed. The blank hydroforming process is classified into two categories: the first is known as hydromechanical stamping (see Figure 4.3) in which the fluid is replaced by the die while in the second category the fluid plays the role of the punch. The absence of a forming die or punch in the forming of blanks is accompanied by a reduction in costs. However, hydromechanical stamping is characterized by a slow cycle compared to the conventional stamping process. In the case of mass production, this can be a severe handicap.

Kang *et al.* [KAN 04] have conducted a comparative study between a conventional stamping operation and blank hydroforming for the

manufacturing of a gas tank of a car. They conclude that with the hydroforming process the tank presents a better distribution of the thickness due to the use of a hydrostatic pressure. They have found that the thinning rate is equal to 31.6% in the case of hydroforming, whereas it is equal to 41.6% for the same workpiece obtained by deep-drawing, which justifies the interest in the process.

The hydroforming of blanks in its various forms has a large number of applications in the automotive industry. The American constructor "General Motors" uses this process for the manufacturing of several pieces that are part of the bodywork. Unlike the conventional stamping technology, hydromechanical stamping makes use of pressure underneath the sheet metal. This generates compressive stresses that may delay the plastic stress instabilities and decrease the formation of wrinkles due to the friction stresses.

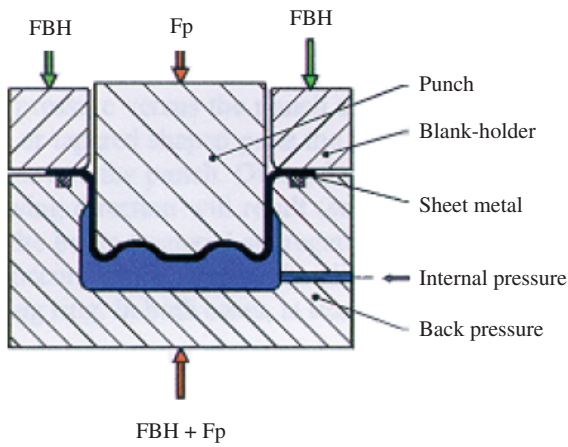

Figure 4.3. *Hydroforming of blanks: hydromechanical stamping*

4.3. Plastic instabilities in hydroforming

During a tube hydroforming operation, we can mainly distinguish three potential failure modes due to strain locations: buckling, wrinkling and necking [KOÇ 02]. The detection of these plastic instabilities requires the use of criteria for the strain localization. These plastic instabilities appear when the stresses and the strains reach critical values and when the steady state is

no longer verified between the external stresses applied and the internal resistance of the material. In order to obtain a workpiece with no defects, a good synchronization is required between the axial displacement and the internal pressure in the case of tubes. Following a similar process as in blank hydroforming, this requires that the force of the punch, back pressure and/or pressure be effectively determined. This compromise is often difficult to find and resorting to the finite-element method coupled with various optimization techniques is inevitable to solve this type of problem and to obtain a workpiece without defects. The following sections detail the different modes of failure that might occur. Subsequently, we present the main criteria for predicting and localizing these instabilities.

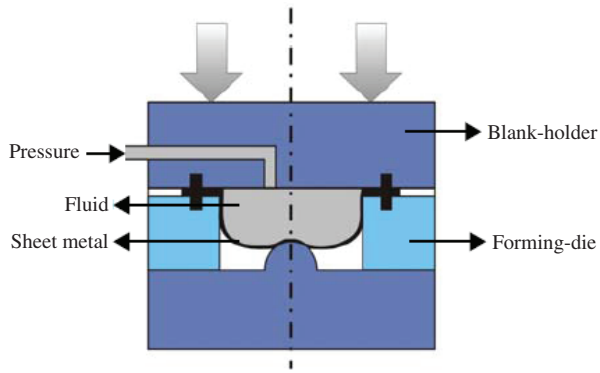

Figure 4.4. *Blank hydroforming*

4.3.1. *Tube buckling*

This type of instability is specific to tube hydroforming. It is generally observed in long tubes with low thickness (i.e. low $\frac{D}{t}$ ratio, where D is the tube diameter and t its thickness). Buckling is the result of excessive axial displacement and appears at the scale of the structure. It occurs most often at the beginning of the process when a strong axial displacement is applied. Geometrically, this type of plastic instability manifests as shown in Figure 4.5. This tendency to buckling increases with the increase in the free length of the tube in the forming die. When this failure mode appears, it is no longer possible to control the process, and the correction of this instability by a variation of the pressure or the axial displacement is no longer possible. A detailed study of this phenomenon has been made by Asnafi [ASN 03a] and shows that it essentially depends on the geometrical parameters of tubes.

Figure 4.5. *Tube buckling*

Figure 4.6. *Tube wrinkling*

4.3.2. *Wrinkling*

Wrinkling is a special case of buckling or a localized buckling. This mode of failure usually occurs at the beginning of the process. Geometrically, it is manifested as ripples or blisters on the membrane of the surface. Figures 4.6 and 4.7 illustrate this plastic instability in the case of tubes and plates forming.

Figure 4.7. *Blank wrinkling [ABD 05]*

This forming defect is mainly due to a strong compressive stress. Unlike buckling, if this mode of failure is detected early in the process it can be corrected by a slight increase in the internal pressure. Wrinkling appears for low- and medium-length tubes (that is with a significant $\frac{D}{t}$ ratio). This type of plastic unstability strongly depends on the geometric characteristics of the forming die. This phenomenon becomes difficult to study in the case of complex tubular shapes, for instance. Ansafi [ASN 03a] has demonstrated the interest of properly controlling the progress of the punch in tube hydroforming, because it is the driving of the piston that has a significant influence on the appearance of wrinkling.

[YUA 06a] carried out a more detailed study on the phenomenon of wrinkling, and have distinguished three kinds of wrinkling in tubes: beneficial wrinkles that improve the formability of the material, dead wrinkles and wrinkles that leads to tube bursting where necking occurs at the level of the ripple.

In blank hydroforming, wrinkling is due to a back pressure or to an insufficient clamping force. In effect, the wrinkling is more significant when

the clamping force is low. Wrinkling emerges at the beginning of the course of the punch when the blank holder stresses are low. Some authors have studied the prediction of the plastic instabilities in the case of blank hydroforming. Abderrabbo *et al.* [ABD 05] were interested in optimizing the pressure and the back pressure paths in blank hydroforming in order to control wrinkling in sheet metal.

4.3.3. *Necking*

Tube bursting or plate fracturing is the result of localized necking. When necking begins, the strains become non-uniform in the workpiece. The strains are subsequently concentrated in a localized area immediately followed by the tube or the plate breaking. This occurs when a strong pressure is applied. The optimal pressure is an important step in the hydroforming process that depends on the material being used as well as on the geometry of the piece to hydroform.

For simple geometries, certain equations have been proposed in the literature allowing the estimation of the level of necessary pressure. These formulations are in general based on the material and the geometrical characteristics of the piece. Altan *et al.* [ALT 01] propose the adequate pressure levels for the forming of an axisymmetric tube based on the geometrical characteristics of the tube and the material properties. In the case of complex geometries, these equations are no longer valid and the use of numerical simulations is essential in order to determine the pressure levels. Necking is a complex phenomenon to predict in the case of hydroforming since the process is new. The criteria that are based on thinning are also often used by tolerating a thinning of 15%, 25% and 30% for aluminum alloys, low carbon steels and stainless steels, respectively.

For localized necking, the Hill criterion is not accurate for short tubes due to biaxial stresses. To overcome this problem, Boumaiza *et al.* [BOU 06] developed a criterion in which they take the geometrical characteristics of tubes into account. For plates, necking occurs at the end of the process when the stresses generated by the blank holder are significant and also in the case of a strong pressure. The study of necking in the case of hydroforming and particularly in the case of sheet metal hydroforming with internal pressure is a sensitive issue for industries; the prediction of necking presents a real problem for the expansion of sheet metal because as there is no privileged direction for the formation of a localization band, the crack often follows any direction. Figures 4.8 and 4.9 show tubes and sheet metal necking.

4.3.4. *Springback*

In hydroforming of complex tubular shapes, we have often to make use of preforming operations with the objective to facilitate tube forming. Figure 4.10 shows the springback in a preforming operation of a tube. It is primarily due to a relaxation of the stresses after removal of the tools. In effect, the material tends to relax and to return to a previous state. Springback poses a serious problem during the assembly operation. Several studies are focusing on the study of the phenomenon of springback in the case of hydroforming technologies. Some have shown that this problem is less significant for this type of process compared, for example, to a conventional process of deep-drawing, notably in plate hydroforming, and which combines the force of the punch and that of back pressure.

Figure 4.8. *Tube necking*

Various works show that springback is sensitive to several parameters that may be related to the process or to the sheet metal. The parameters of the process are, for example, the synchronization between the internal pressure and the clamping force, the displacement velocity of the punch in the case of sheet metal hydroforming, the type of contact between the sheet and the tools as well as the geometrical parameters, such as the radii of curvature of the tools. The sheet metal parameters are the material that it is made up of, in particular its chemical composition, as well as its thickness. Springback is also dependent on the material; materials with very high resistance often present a higher springback in comparison with ductile materials.

4.4. Forming limit curve

The forming limit curve (FLC) has been introduced by Keeler [KEE 63] and Goodwin [GOO 68] to define the upper formability limits of the material before necking. There are four primary approaches that allow the analytic

construction of FLCs: localized necking by Hill [HIL 52], diffuse necking by Swift [SWI 52], bifurcation in [STO 75] and that in [MAR 67] that introduces the non-homogeneity of sheet metal. This curve can be obtained either in an experimental manner or by numerical simulations. Several approaches have been proposed in the literature in order to determine this curve.

Figure 4.9. *Blank necking*

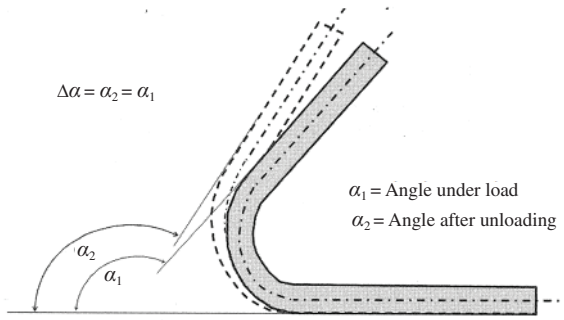

Figure 4.10. *Springback*

The FLC is used in several works as a criterion capable of predicting necking. The use of the FLC in particular in forming is often criticized

because it is valid for proportional load paths, which is not the case for this type of problem. This curve is obtained experimentally and as the operating process is often biased by different types of uncertainties associated with the material, with the machine and with the environment in general. This can affect the prediction of the position of the FLC, which makes it unreliable for a good prediction. Despite these flaws, the FLC is often used as a criterion for the localization of strains. Some authors have also based their works on the FLC in order to define objective functions for the optimization of their forming processes. According to [ASN 00], the tube's FLC should be determined by free expansion trials so that it be usable for the prediction of the necking in the case of metal hydroforming.

In effect, several studies have experimentally shown the dependence of the FLC on the strain path. A nonlinear strain path can change the shape and the position of the FLC in the space of the principal strains. To compensate for this problem, Arrieux [ARR 95] proposes the equivalent of the FLC but in the stress space (forming limit stress diagram) because it is independent of the load path being applied. Shifting from one curve to the other is possible by a formulation of the stresses based on the strains.

4.5. Material characterization for hydroforming

The characterization of the material is a crucial stage in metal forming. This is because the accuracy of a numerical simulation strongly depends on the input parameters. The choice of the most appropriate technique depends on the types of stresses. Several authors have addressed this subject; some cut out their samples in sheet metal to characterize the material destined to hydroform tubular workpieces. This presents a number of major disadvantages since the stress modes are not the same. Song *et al.* [SON 07] have carried out an experimental study for characterizing a material with numerical tensile and inflation tests. They estimate that to obtain a good prediction of the final characteristics, a good characterization is necessary. Through the numerical simulations of an inflation test, they show that the material data originating from an inflation test provide a good prediction compared to the material data obtained from a tensile test. The reliability of the numerical simulations necessarily involves an appropriate choice of the characterization technique, which strongly depends on the types of stresses.

4.5.1. *Tensile testing*

Several tests have been proposed in the literature to characterize the material used in hydroforming of tubes. The simplest is the tensile test: the test pieces are cut according to the longitudinal and the circumferential directions of a tube following the different rolling directions as shown in Figure 4.11. Xing and Makinouchi [XIN 01] compare through an analytical and numerical study the behavior of blanks and tubes, and show that the formability area for a tube is less limited compared to that of the blank. They also demonstrate that the plastic instability for a tube is less important compared to the blank because the anisotropy coefficient is much lower where the value of using samples cut from a tube.

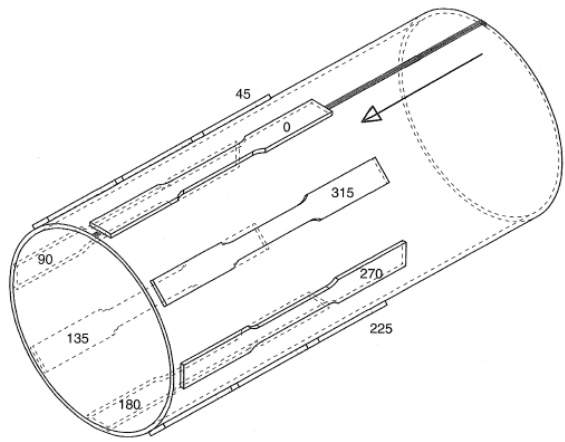

Figure 4.11. *Samples for tensile testing*

4.5.2. *Bulge testing*

The bulge test is designed to determine the behavior of tubes in the longitudinal and circumferential direction. It allows the evaluation of the formability of the tube and also establishing pressure/expansion curves. Others also use it to evaluate the integrity of the welding seam. Several studies have focused on the experimental techniques best adapted to characterize sheet metal, which will be used for hydroforming. Some authors use the information generated from uniaxial tensile testing to simulate their hydroforming processes despite the types of stresses not being the same. To elucidate this issue, some even compare the stress–strain hardening curve for

the same material during a simple tensile test and inflation testing. They clearly highlight the significant difference that may exist between the distributions originating from these two types of characterization. They show that an inflation test is more appropriate in the case of hydroforming. Many researchers [CHE 04, KOÇ 01] consider that bulge testing is more representative when compared to a simple stress–strain test. Figure 4.12 represents the procedure that has to be followed to characterize a material by bulge testing. The burst pressure mainly depends on the material properties and initial thickness. This test can be used to determine the burst pressure and the maximal displacement in the expanded region before the bursting.

Other tests combine internal pressure and axial displacement; this allows going further into radial displacement by changing the axial displacement and the internal pressure ratios. The strain mode may vary from plane strain and approximately into uniaxial tensile stress. The main stresses can be determined based on the axial force, the internal pressure and the geometry of the expanded area. We evaluate the flow stress taking the anisotropy into account [HWA 02]; this approach is based on Hill's theory with orthogonal anisotropy. The internal pressure and the thinning rate are measured during the inflation test. The flow curve obtained with this test can provide reliable and accurate numerical results.

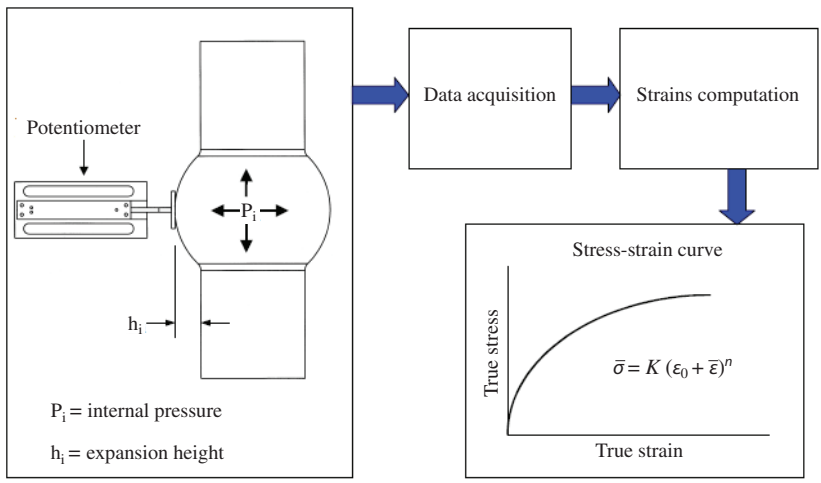

Figure 4.12. *Bulge test*

4.6. Analytical modeling of a inflation test

In the following section, we propose to analyze the circular inflation test while adopting the Hill48 anisotropic plasticity criterion for the description of the behavior of sheet metal.

4.6.1. *Hill48 criterion in planar stresses*

Before starting to analyze the test, we first define an expression of the Hill48 criterion under the plane stress hypothesis, assuming that the main stress reference frame is coinciding with the orthotropic frame. The equivalent stress is then defined in the main reference frame by:

$$\bar{\sigma} = \frac{\sqrt{r_{90}(1+r_0) - 2r_0 r_{90}\Omega + r_0(1+r_{90})\Omega^2}}{\sqrt{r_{90}(1+r_0)}}\sigma_1 \qquad [4.1]$$

with Ω defined by

$$\Omega = \frac{\sigma_2}{\sigma_1} \qquad [4.2]$$

For an associated flow law, the equivalent strain is written as:

$$d\bar{\varepsilon} = \frac{\sqrt{1+r_0}\sqrt{r_0(1+r_{90}) + 2r_0 r_{90}\beta + r_{90}(1+r_0)\beta^2}}{\sqrt{r_0 + r_0 r_{90} + r_0^2}} d\varepsilon_1 \qquad [4.3]$$

with β defined by:

$$\beta = \frac{d\varepsilon_2^p}{d\varepsilon_1^p} \qquad [4.4]$$

On the other hand, it is possible to demonstrate, by using the equation and the normality distribution, that the stresses ratio is connected to the strains ratio by the following relation:

$$\beta = \frac{r_0(1+r_{90})\Omega - r_0 r_{90}}{r_{90}(1+r_0) - r_0 r_{90}\Omega} \qquad [4.5]$$

The equilibrium equation is defined by:

$$\frac{\sigma_1}{R_\theta} + \frac{\sigma_2}{R_\phi} = \frac{P}{e} \qquad [4.6]$$

where σ_1, σ_2 are the principal stresses (superposed to the axes of the material), R_θ and R_ϕ are the radii of curvature, respectively, following the two main directions, P is the inflation pressure and e is the current thickness at the pole of the plate. By introducing the stress ratio Ω and assuming that $R_\theta = R_\phi$, the equilibrium equation is reduced to:

$$\sigma_1 = \frac{P.\rho}{(1+\Omega).e} \qquad [4.7]$$

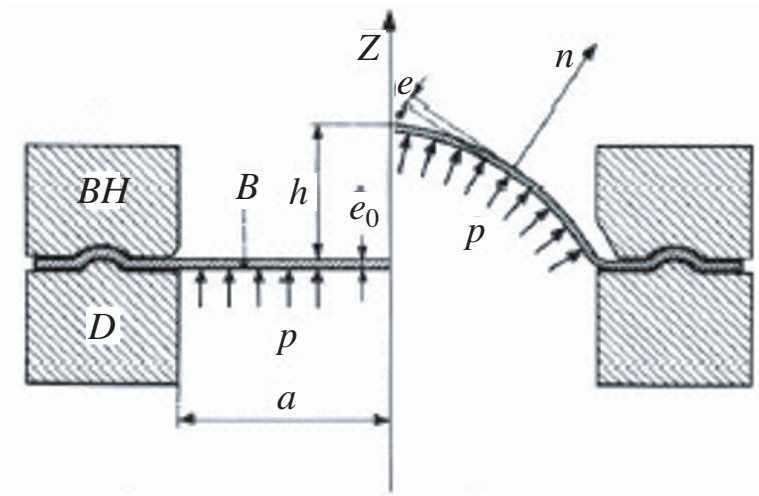

Figure 4.13. *Circular inflation test*

Assuming that the geometry of the deformed sheet metal is of spherical shape, the radius of curvature ρ can be derived from the height of the dome h on a radius a according to the relationship of the spherometer [HIL 50] :

$$\rho = \frac{a^2 + h^2}{2h} \qquad [4.8]$$

It can also been shown that the principal strain is defined by:

$$\varepsilon_1 = \ln\left(1 + \frac{h^2}{a^2}\right) \qquad [4.9]$$

At this stage, we know the stress and the principal strain according to the measurable variables (h, a, e, P). It thus remains to determine the strain ratio W in order to be able to establish a direct relationship between the forces and the strains.

To this end, a state of normal anisotropy is assumed as a first approximation. This reduces the number of anisotropy parameters to the sole parameter r. In this case, the behavior is isotropic in the plate plane, an equi-biaxial stress–strain state is thus derived ($\beta = \Omega = 1$). The equivalent stress and the equivalent strain are then defined by:

$$\bar{\sigma} = k\left(\sqrt{\frac{2}{(1+\bar{r})}}\sigma_1\right), d\bar{\varepsilon} = \sqrt{2(1+\bar{r})}d\varepsilon_1 \qquad [4.10]$$

Using a strain-hardening distribution of the Hollomon type and taking the expression of the equivalent strain into account, the equivalent stress is then defined by:

$$\bar{\sigma} = k\left(\sqrt{2(1+\bar{r})}\ln(1 + \frac{h^2}{a^2})\right)^n \qquad [4.11]$$

Based on the hypothesis of plastic incompressibility, the current thickness at the pole is defined based on the initial thickness e_0 by:

$$e = e_0 \exp\left(2\ln\left(1 + \frac{h^2}{a^2}\right)\right) \qquad [4.12]$$

The final equation connecting the inflation pressure to the height of the dome is derived from the equations, and considering the equivalent strain expression:

$$P = 2\sqrt{2(1+\bar{r})}K\frac{e_0 h}{a^2}\frac{1}{((1+\frac{h^2}{a^2}))^3}\left(\sqrt{2(1+\bar{r})}\ln\left(1+\frac{h^2}{a^2}\right)\right)^n \quad [4.13]$$

NOTE 4.1.–

1) The inflation pressure gradually increases until reaching the maximum pressure, called the burst pressure, beyond which begins a strain phase, known as unstable, reflected by a decrease in the pressure, although the sheet metal continues to inflate.

2) According to the prediction of the model, the burst pressure $P_{\max}$ is very sensitive to the anisotropy coefficient; $P_{\max}$ increases with $\bar{r}$. At the same time, the model shows that the height reached by the material at the burst pressure is independent of the anisotropy coefficient.

4.7. Numerical simulation

This section presents the hydroforming of a homogeneous circular plate under pressure. The mechanical behavior of the material has been simulated at ambient temperature and at low strain rate by the software. The elastic properties of the material, as well as its density, are presented in Tables 4.1 and 4.2.

The finite element method is used to explore the stress and the displacement as well as the influence of strain hardening, anisotropy, and sensitivity of these parameters on the response of sheet metal. A three-dimensional model discretized in finite-elements (3D) is then built with 100811 nodes and 57295 C3D4-type elements, and then solved with Ansys v13©. This is a sheet metal and die assembly of initial dimensions and parameters (see Figure 4.14).

A surface pressure profile of 5 MPa over time is applied on the sheet metal surface. It is inflated under this load by releasing only its ends in the direction of the axis of symmetry of the plate. The behavior is formulated in the context of anisotropic elastoplastic models and with isotropic hardening.

Designation	Density (kgm^{-3})	E (GPa)	Poisson coefficient
DC04	7,800	210	0.3

Table 4.1. *Elastic characteristics and density of the DC04 under study*

Diameter SM (mm)	SM thickness (mm)	Die diameter (mm)	Die radius (mm)
150	1	110	6

Table 4.2. *Geometrical characteristics of sheet metal (SM) and die*

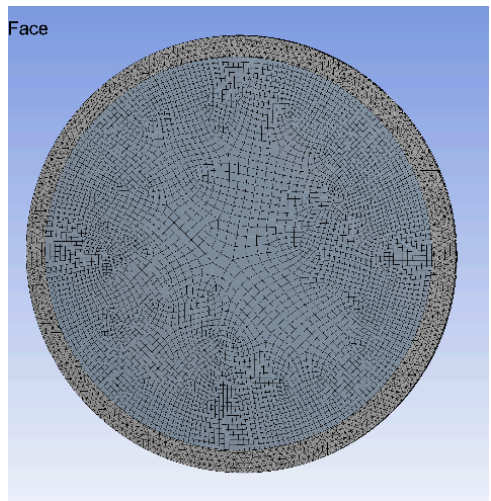

Figure 4.14. *Considered mesh*

4.8. Mechanical characteristic of tube behavior

Taking into account the thickness/diameter ratio of the tube, the radial stress is considerably low compared to the circumferential stresses σ_θ and longitudinal σ_z. In addition, the main axes of the stress tensor and the orthotropic axes are considered to be coaxial. The hypothesis of transversal anisotropy represented by the efficiency criterion can be written as:

$$\bar{\sigma}^2 = F(\sigma_z - \sigma_\theta)^2 + G\sigma_z^2 + H\sigma_\theta^2 \qquad [4.14]$$

with (F, G, H), which are the parameters characterizing the current anisotropy state.

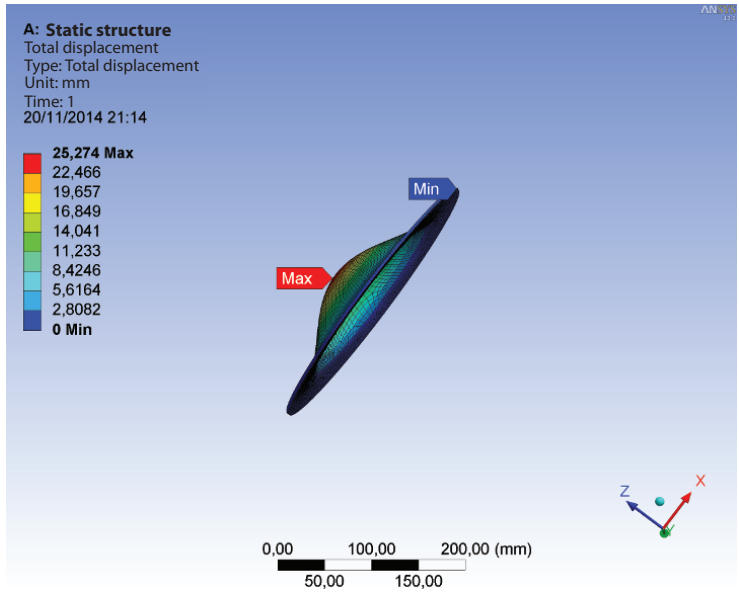

Figure 4.15. *Hydroformed metal sheet. For a color version of this figure, see www.iste.co.uk/radi/material.zip*

When the circumferential direction is considered to be a reference material, the effect of anisotropy can be characterized by a unique coefficient R and equation [4.14] becomes:

$$\bar{\sigma}^2 = \frac{1}{1+R}\left[R(\sigma_z - \sigma_\theta)^2 + \sigma_z^2 + \sigma_\theta^2\right] \qquad [4.15]$$

The normality and consistency assumptions lead to the following equations:

$$\begin{cases} d\varepsilon_\theta = \dfrac{d\bar{\varepsilon}}{\bar{\sigma}}\left(\sigma_\theta - \frac{R}{1+R}\sigma_z\right) \\ d\varepsilon_z = \dfrac{d\bar{\varepsilon}}{\bar{\sigma}}\left(\sigma_z - \frac{R}{1+R}\sigma_\theta\right) \end{cases} \qquad [4.16]$$

where $\bar{\varepsilon}$ is the efficient plastic strain and $(\varepsilon_\theta, \varepsilon_z)$ are the peripheral strains and the axial directions.

The anisotropic material can be derived from an equivalent definition into working plastic, the incompressibility condition and the normality condition:

$$d\bar{\varepsilon} = \frac{\sqrt{1+R}}{\sqrt{1+2R}}\sqrt{d\varepsilon_z^2 + d\varepsilon_\theta^2 + R(d\varepsilon_z - d\varepsilon_\theta)^2}$$
$$= \left(\sqrt{\gamma^2 + \frac{2R}{1+R}\gamma + 1}\right)\frac{1+R}{\sqrt{1+2R}}d\varepsilon_\theta \qquad [4.17]$$

with $\gamma = \frac{d\varepsilon_z}{d\varepsilon_\theta}$.

Considering the relations expressing strain tensor increments, the equivalent stress (equation [4.15]) becomes:

$$\bar{\sigma} = \left(\sqrt{1 + \gamma^2 + \frac{2R}{1+R}\gamma}\right)\frac{\sqrt{1+2R}}{1+R+R\gamma}\sigma_\theta \qquad [4.18]$$

In the studied case, the ends of the tubes are fixed. As a result, the longitudinal strain of the increment $d\varepsilon_z = 0$ and the relations [4.17] and [4.18] become:

$$\bar{\sigma} = \left(\sqrt{\frac{2R^2+3R+1}{(1+R)^3}}\right)\sigma_\theta \quad d\bar{\varepsilon} = \left(\frac{1+R}{\sqrt{1+2R}}\right)d\varepsilon_\theta \qquad [4.19]$$

Knowing the two unknown strains ε_θ and the stress σ_θ requires the implementation of the final geometric data related to the tube (diameter and wall thickness):

$$\varepsilon_\theta = \ln\left(\frac{d}{d_0}\right) \quad \sigma_\theta = \frac{Pd}{2t} \qquad [4.20]$$

where P is the internal pressure, (d, d_0) are, respectively, the average values of the current and initial diameter of the sample and (t) is the current wall thickness based on the following relation:

$$t = t_0 e^{-(1+\gamma)\varepsilon_\theta} \qquad [4.21]$$

Finally, the physical characteristics of the tube (base metal) are expressed by the effective stress and with efficient strain according to the following equation (Swift's model):

$$\bar{\sigma} = K(\varepsilon_0 + \bar{\varepsilon})^n \qquad [4.22]$$

The values of the resistance coefficient at K, the strain hardening n, the initial strain ε_0, and the anisotropic coefficient R in equations [4.15] and [4.22] are numerically identified.

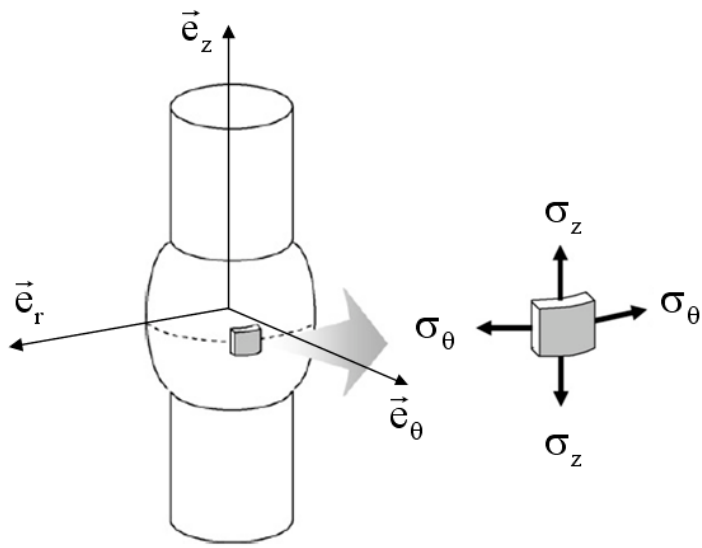

Figure 4.16. *Stress state in the inflated region*

5

Additive Manufacturing

5.1. Introduction

In the current highly competitive environment, manufacturing companies face several problems:

1) a reduction of the time to market of new products;

2) lower production costs;

3) the optimization of their quality.

The use of the tools from computer-based development processes, taking into account simulation and rapid prototyping (RP), allows the optimization of the design, industrialization and production cycles of products by facilitating, systematizing and accelerating the validation of each of the development phases.

Direct manufacturing is a major challenge when moving from the prototype phase to the production phase. The speedup can be considerable if tooling is no longer necessary. This starts with the production of small and medium series; the larger series are discussed for parts of small dimensions. For production, tooling can be partially achieved by additive manufacturing.

The development of new machines, the reliability of existing machinery and the improvement of devices and environments makes possible what was unthinkable in the past. The quality of the parts obtained by additive manufacturing and finishing allows that homologations are made in sectors as demanding as the aeronautics, spatial and medical sectors.

Material Forming Processes: Simulation, Drawing, Hydroforming and Additive Manufacturing, First Edition. Bouchaib Radi and Abdelkhalak El Hami.
© ISTE Ltd 2016. Published by ISTE Ltd and John Wiley & Sons, Inc.

A great novelty is the ultra rapid manufacturing of tooling for the proof of concept. For example, in plastic injection molding the transition from the computer-aided design (CAD) model of the part to be injected to the injection molded piece can be achieved in a few hours, which enables making "real-process" functional prototypes. A large number of research projects are being developed. The piece is designed, tested and optimized in its real configuration and real usage environment. Risks are minimized for the manufacturing of production tooling and when it is put into operation.

In fact, additive manufacturing has a number of environmental advantages:

1) a lower consumption of raw materials;

2) the reduction of energy needs (additive manufacturing would help saving more than 50% of the current energy spent in "subtractive" manufacturing, according to the U.S. Department of Energy);

3) the limited use of hazardous chemicals;

4) the reduction of transport requirements (relocation, production close to the consumer);

5) the possible maintenance of the objects to avoid the accumulation of waste.

The design and manufacturing phases are crucial because during these stages, different requirements (functional, environmental, cost, etc.) must be validated. The conventional mechanical manufacturing methods are facing numerous challenges due, in particular, to the complexity of the parts to be achieved, timing and the cost of production, not to mention the environmental impacts that they generate.

Additive manufacturing constitutes a reliable alternative to address these challenges. Rapid product development is an approach for developing innovations while considering traditional criteria: technical performance, quality, cost and time. The concept of rapid product development has the advantage of a uninterrupted implementation of the tools of computer-based development processes: CAD and digital simulation, prototyping, tooling and rapid manufacturing.

The main five loop iterations are:

1) the loop for the decryption of the specifications of the product from the functional analysis for the elaboration of the requirements chart;

2) the first shift from a virtual concept to a real environment in the form of first-level models;

3) the validation loop with the real characteristics. From this stage, collaborative work is essential for optimizing the technological solutions in regard to stress methods, both of productions and design and tooling manufacture. As in every validation stage, physical prototyping is achieved after all the numerical simulations have been tested. As a result, the errors found after these physical validations are a proof of success. They allow filtering by minimizing the risks and hazards;

4) validation with true processes and true materials. This very important step has the objective of validating the choice of processes and procedures to test them as close as possible to the future production by means of tooling and advanced solutions. This step is the last before the major investments that must be made to initiate the production. Collaborative work plays a predominant role here. At the end of this step, the specifications of the production must be established. Some clarifications will be made later in the study;

5) fabrication with additive manufacturing for production tooling or tooling components.

The use of additive manufacturing techniques allows the substantial reduction of the manufacturing time and therefore the time to market of new products by increasing both their complexity and the number of their functions. Having recourse to rapid manufacturing is a major asset in a market where the lifecycle of products decreases and where the manufacturer has to adapt his products to the new expectations of customers.

5.2. RP and stratoconception

In a conventional IT-based development process relying on RP, the digital model of a part can be generated in different ways: starting from a purely CAD-based digital design or a virtual sculpture, following the digitization of a physical model of the part or even by mixed digitization and digital retouching techniques. The digital model upon which it is common to work is the stereolithography (STL) model (format used in stereolithography software programs), which is provided by a meshing operation of the digital model of the piece. Based on this model, the slicing operations and the generation of manufacturing routes are calculated. These are then translated into a language that enables the controlling of the manufacturing machine (Figure 5.1).

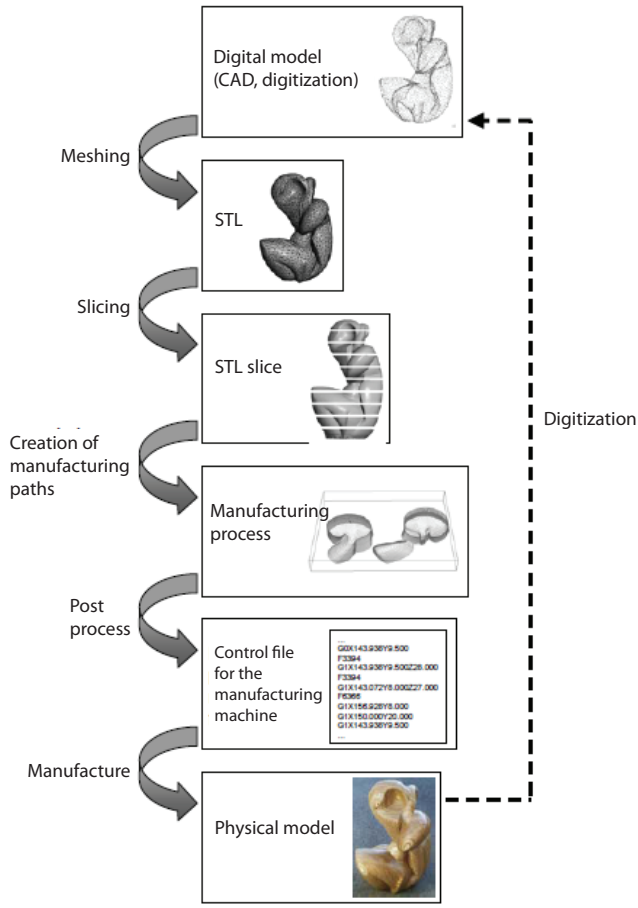

Figure 5.1. *Rapid IT-based prototyping process [LAU 05]*

The physical models produced by RP are used at different times in the development process of a product. At the beginning of the design cycle, RP is used in the validation of the esthetic and ergonomic aspects of the product; this is referred to as a design model. When emphasis is given to the accuracy of the model geometry, a geometric prototype is obtained allowing its use as a model for tooling, for example. If we add the good material characteristics to the obtained prototype, it becomes representative of the basic functions of the product and contributes to their possible optimization. A functional prototype

of the product is then obtained. It is even possible to make use of this kind of prototype in tooling design.

Currently, prototyping processes provide a means to reduce the product development process by the direct creation of tooling elements. This is expected to continue in the years to come due to the direct rapid manufacturing of the final finished product material as a replacement for the conventional sequential manufacturing processes (casting, stamping, injection, etc.) [DOR 03, FEE 03] without tooling.

Stratoconception is a solid/solid RP process initiated in the late 1980s by Professor Barlier [BAR 15], which consists of the automatic decomposition of the object into a series of additional elementary layers called strata, into which positioning inserts are introduced. The conventional creation mode of slices in stratoconception is made by 2.5 axis machining. The tool creates the model according to the opposite direction of the slicing direction. Thus, the so-called draft surfaces are surfaces accessible to the cutting tool and the undercut surfaces are inaccessible to the tool. In stratoconception, the creation of a slice can be achieved in two phases, this is then referred to as turnaround. First of all, the draft areas are worked upon, then after turning the plaque around, the originally undercut areas are machined. For more details on this topic, see [LAU 05].

5.3. Additive manufacturing definitions

Currently, additive manufacturing is the subject of a proposal for a standard, in particular all that relates to the main definitions. We can refer to the French standard NF E 67-001, which gives all definitions necessary to define, characterize and represent the elements that are needed in the whole of the IT-based and technological production chain integrating additive manufacturing. This then referred to as additive manufacturing and as direct additive manufacturing [BAR 15].

At the end of the 1980s and early 1990s, RP started to be adopted whose general principle made it possible to produce a three-dimensional object from an STL file.

Additive manufacturing means a set of forming processes by the addition of material, stacking up layers and contrasting with the forming process by removing material, such as machining. This technique is also commonly called 3D printing (Figure 5.2) according to the standard NF E 67-001 [AFN 11]. These processes are distinguished by:

– how the different layers of materials are layered down (fusion, sintering, polymerization, etc.);

– the materials used in the solid form (metal powders or polymer powders), liquid form (photosensitive resin), or even in the form of semifinished strips or yarn products.

Figure 5.2. *3D printer*

In the 1980s, additive manufacturing, called RP, was supposed to reduce the creation timings of the prototype parts. The technology at the time allowed the manufacture of plastic parts of small dimensions and with limited mechanical properties. These prototypes were non-functional and were only intended to illustrate or validate a concept. However, the technology has advanced very quickly, the dimensions of the machines have increased, the processes have improved and diversified, thereby resulting in a wider choice of materials and improving the mechanical properties of the manufactured

part. Additive techniques currently allow functional prototypes to be achieved, as well as finished or semifinished pieces in small series (rapid manufacturing) or even further the manufacture of molds and tooling for large-scale production (rapid tooling) (see Figure 5.3).

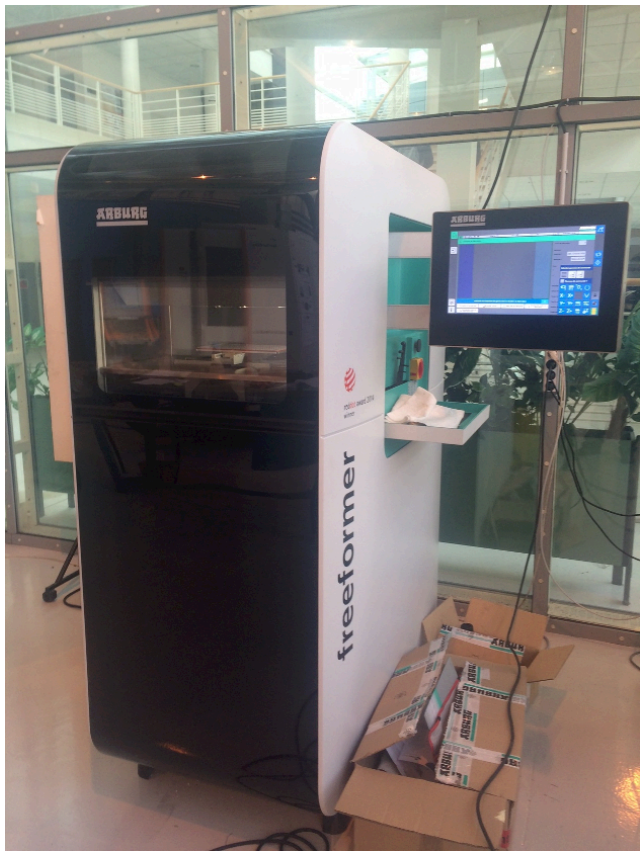

Figure 5.3. *Additive manufacturing machine (INSA Rouen)*

The potential of the additive manufacturing technologies, in terms of customizing the produced objects and reducing the environmental impact (the right amount of material used), is considerable (Figure 5.4):

– at the technology level: we have direct production of small series of complex shaped parts with fast manufacturing, a reduction in the design time, the possibility of implementing geometries that are impossible to achieve with conventional processes and with a lighter structure;

– at the IT level: we have direct manufacturing from a 3D model and a topology optimization can be performed with the objective to lighten, to spend less material and to promote exchanges within the network of enterprises;

– at the economical level: we have direct insertion of means of authentication in the product and a complete customization of “just in time“ deliverable products.

Figure 5.4. *Products from additive manufacturing (CESI Rouen)*

Georges Taillandier [GOE 08], President of the *Association Française de Prototypage Rapide* (AFPR), states that the aim is first to improve the design reactivity with regard to the market fluctuations and the evolution of the needs. It also aims to promote the creativity and the development of new concepts in the ideas and in the design while simplifying the communication between client and provider. The integration of the product is optimized in its environment, the manufacturing, maintenance, control or packaging problems are anticipated, and tests are carried out on the product to verify certain characteristics (ergonomics, aerodynamics, etc.). Finally, sometimes a piece has to be formed that will be used as a model for the fabrication of tooling in a short time or to directly develop a mold for plastic molding injection or casting.

The materials used in additive manufacturing machines can be of different forms (liquid, pastes, powders, granules, yarns), the types and shades of materials available are very limited. It is an area undergoing intense development for metallurgists and chemists. The extent of the dimensions of the parts that can be obtained by additive manufacturing is very broad. This ranges from less than 1 mm to several tens of meters. Some machines allow continuous manufacturing. The characteristics of the parts obtained are improving on a daily basis. Some machines allow the manufacture of parts whose material characteristics vary depending on certain regions chosen by the designer.

Resorting to fused deposition modeling (FDM) technology for the production of pieces, instead of injection molding, enables the design to be modified with a simple update of the file, and therefore leaves more freedom in terms of design and shape. The parts are immediately ready for the production.

The FDM process has been developed by Stratasys (USA). It uses the motion of a three-axis machine to lay down a melted metal filament on the piece during the fabrication. The solidification is instantaneous when the wire comes into contact with the previous section. The materials used for the filament are wax, polyamide, polypropylene, ABS, etc. This method is fast and inexpensive since the emergence of 3D printers. In melting processes, the powder is coaxially melted by a laser beam and amalgamates on the piece to be built.

5.4. Principle

The concept at the basis of the principle of additive manufacturing is layer upon layer manufacturing. It allows a greater freedom to design than traditional

processes. It is in effect possible to create shapes impossible to reproduce in casting or by machining. There are several additive manufacturing processes (stereolithography, melting filament deposition, stratoconception, 3D printing from metallic or non-metallic powders, laser recharging, selective melting by laser electron beam, etc.). They offer several possibilities to designers. The foundation is based on two technologies [BRE 15]:

– laser melting/sintering on a layer of powder (selective laser melting/selective laser sintering) (SLM/SLS) that consists of an electron beam or a laser that melts or sinters a thin layer of powdery material. A second layer is then deposited and then melted/sintered. The materials used are metals, polymers and ceramics in the form of powder;

– laser melting/sintering with projection of powder (laser metal deposition) that consists of a laser that melts the metal surface of the piece upon which a powder spray is simultaneously projected. This powder melts and forms a layer that merges with the substrate. The materials used are powdered metals.

5.4.1. *Principle of powder bed laser sintering/melting*

The principle of powder bed laser melting/sintering consists of melting a thin layer of powder (metal, plastic, ceramic, etc.) using a high-energy laser. These techniques are based on the same steps summarized here below:

1) a thin layer of powder is spread by a roller on a manufacturing piston;

2) this layer is sintered/melted by a high-power laser that traces a 2D section on the surface of the powder. The solidification takes place after the laser is stopped;

3) the piston supporting the 3D model under construction descends from the thickness of the layer carried out while the powder supplying cartridges adjust their level with that of the plateau;

4) a new powder bed is spread out and the process is repeated until the 3D model is completed.

In fact, there is a significant difference between laser melting (SLM) and laser sintering (SLS). Sintering is a process consisting of heating powder without melting it. The only difference between laser sintering and melting is therefore the power of the laser being used. Sintering enables certain properties to be obtained that can be interesting for well-defined applications (for instance high yield strength).

There is another technology very close to laser melting and sintering with powder: laser melting by electron beam (or electron beam melting) (Figure 5.5). The main difference with the processes previously mentioned is the use of a beam of electrons instead of the laser. This electron beam is obtained by heating a tungsten filament in a vacuum. The latter thus releases electrons, which are then accelerated and directed by electromagnets in order to be projected at high-speed on the surface of the powder. The powder is therefore brought to the melting point. The powders used with this technology must be based on conductive materials otherwise no interaction with the electron beam is possible. As a result, metal powders are thus preferred. One of the strengths of this technology is the speed of manufacture; in fact, some manufacturers argue that the electron beam can be separated to heat several places simultaneously.

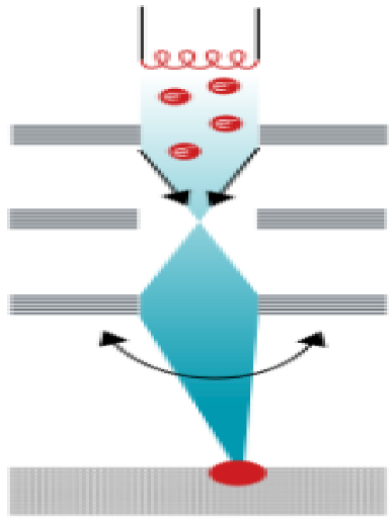

Figure 5.5. *Explanatory diagram of the laser sintering 3D printing process (source: IFTS from the University of Reims)*

Technologies based on laser melting/sintering of a powder bed present the main advantage of enabling the fabrication of parts with extremely complex geometries. In fact, the powder not melted/sintered by the laser can serve as a support for the following layers of material spread by the roller. Thus, this facilitates obtaining undercut forms.

5.4.2. *Principle of laser sintering/melting by projecting powder*

This technique consists of melting the surface of a metal piece with a laser. Simultaneously, a powder spray is projected onto the melting area. This powder melts on the molten area and thus come to form a layer that merges with the substrate (Figure 5.6). Several passes may be necessary to obtain the desired thickness [TRU 12].

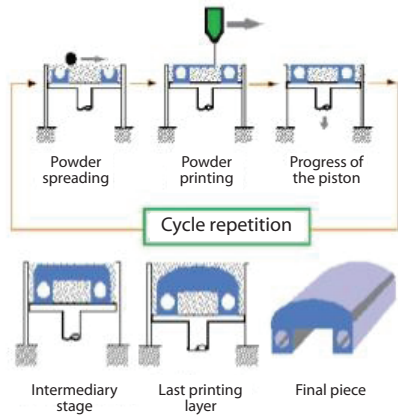

Figure 5.6. *Laser sintering by powder projection*

This technology is also used to create 3D parts. It presents the advantage of getting a good metallurgical cohesion between the coating applied and the substrate. This technique can also be used for applying special surface treatments with the objective to improve the resistance to corrosion or to wear.

The process of projecting powder relies on laser melting (or sintering) based on overlay welding. The powder is injected through a nozzle mounted on a 5-axe machine that when moving, creates weld seams. This offers a great geometric flexibility [HAR 11].

Each process suffers still from the limitation imposing new design constraints. For example [MEU 14], in the case of selective laser melting, the piece will be manufactured on a mounting plate and the first fabrications strata are mounts enabling that heat be removed and that the piece be separated from the plate. This has a negative influence on the time and the cost of manufacturing, in addition the size and the positioning of these mounts require some experience from the end user.

The choice of orientation of the workpiece at the time of manufacture also necessitates a good knowledge of the process and results from a compromise between the size of the tray and the need to limit to the maximum the dimension of the molten pool for each layer. It is also necessary to also provide one or more evacuation path for the residual powders. After production of the piece, a relaxation heat treatment or postmachining operations should eventually be anticipated in order to improve the surface condition of the functional areas.

The lack of knowledge and hindsight regarding the opportunities and the limitations of these new manufacture methods as well as their still significant cost currently limit their industrial development. In fact, design consultants are accustomed to designing parts with geometries that should be simple to manufacture by conventional processes; these are the bases of "design for manufacturing (DFM)". In order to benefit from the full potential of additive manufacturing, it is necessary to develop design supporting tools adapted to these new manufacturing processes ("design for additive manufacturing"). There is at the present time still little methodology of this type [PON 13, ROD 11] and often they do not allow ensuring the manufacturability of the part or do not benefit from the advantages of additive manufacturing.

5.5. Additive manufacturing in the IT-based development process

Additive manufacturing can differentiate and complexify the objects manufactured without significant additional costs during the simultaneous manufacturing of different objects with the same manufacturing machine. These possibilities are related to the principles of modeling and information computer processing that enable rapid and controlled iterations between the real world of physical parts and that of virtual objects that can be derived and customized with no limitations and at the lowest costs.

5.5.1. *Concept "from the object to the object"*

This concept is based on the fact that the dynamics of product development rely on a process located between IT, allowing the definition and the referencing of the models of the products desirable to be obtained, and the real shape of their physical realization (Figure 5.7).

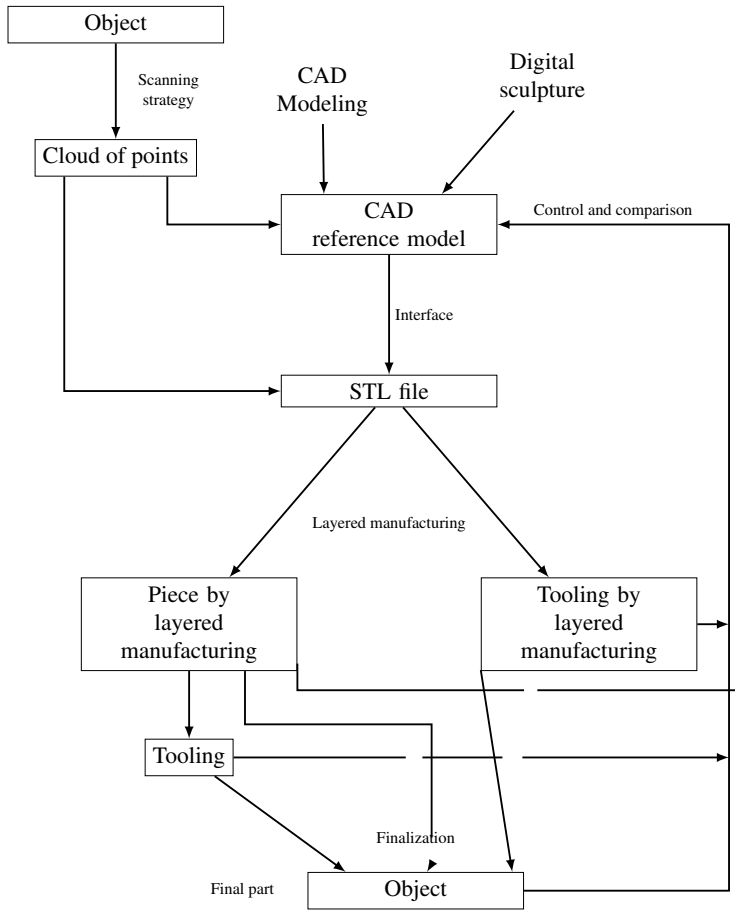

Figure 5.7. *Process from the object to the object*

5.5.2. *Key element of the IT development process*

Additive manufacturing is located at the heart of the IT development process. There is the rapid manufacturing and completion of objects by additive manufacturing. It is possible to advance either by a direct redefinition in CAD, or by an optimization and a validation through simulation or by the digitization of the physical modifications brought to the manufactured object. This possibility of iteration is one of the key performance factors of this

manufacture. Figures 5.8–5.10 show typical computer-aided processes concerning the manufacture of objects.

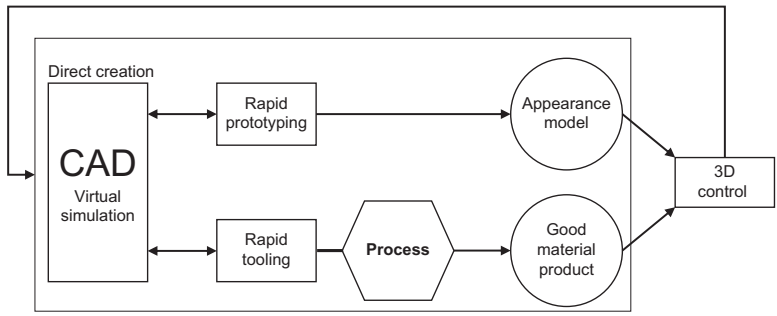

Figure 5.8. *Direct computer-based creation sequence of objects (source: InSIC)*

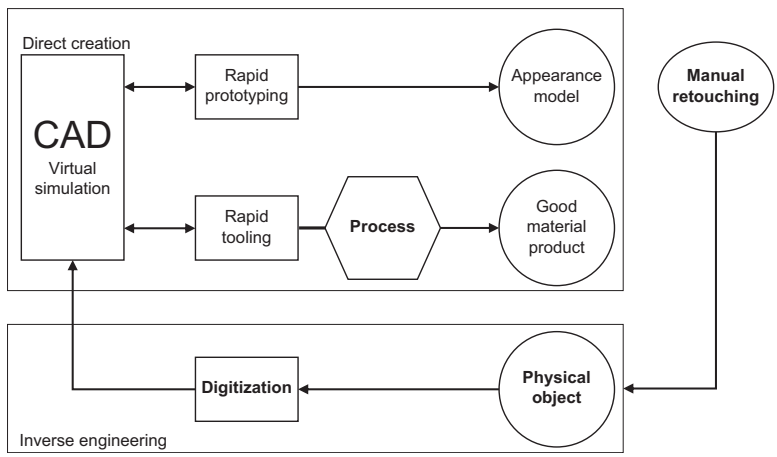

Figure 5.9. *Direct sequence and reverse engineering (source: InSIC)*

The RP industry is maturing; future developments are essentially connected to the available materials and reliability of equipment. The areas of application and the expected impacts are significant, a large number of things remain to be consolidated and to be experimented in a forward-looking and collaborative context.

The existence of numerical models is invariant and constitutes the entry point to the implementation of additive manufacturing processes. This

constraint is also to be regarded as an element of primary importance in the context of the conservation of perennial models and the integration of the various models necessary to the usages of the product during its lifecycle. The robustness of the models and that of the IT development process are therefore paramount in order to streamline the flow of the necessary information to obtain new products.

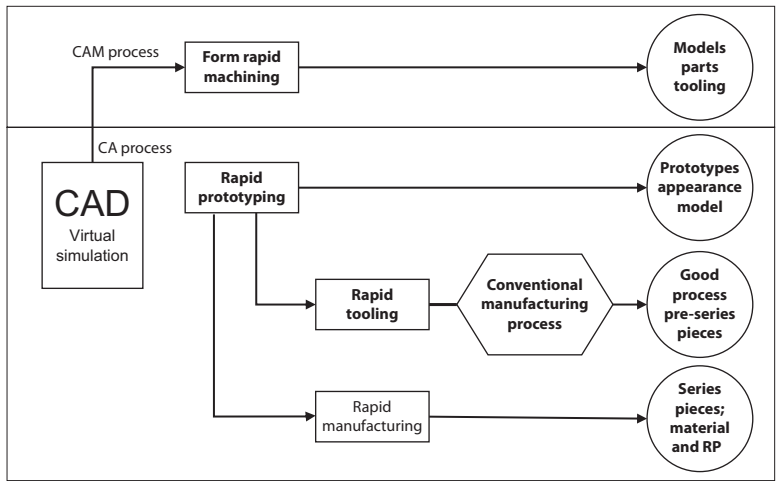

Figure 5.10. *Additive manufacturing and machining computer-based development sequence (source: InSIC)*

6

Optimization and Reliability in Forming

6.1. Introduction

The process of metal forming by hydroforming involves several complex phenomena and presents several types of nonlinearities (geometric, material, etc.). The development of a hydroforming process requires a large number of tests to accurately determine the optimum loads paths and to obtain a workpiece without defects. The progress achieved at the level of the numerical tools has helped industrialists to simulate and optimize their means of production before starting the manufacture with the objective to minimize as much as possible the rate of defective parts. This is justified by the multitude of parameters that have to be controlled and also by the exorbitant cost of real testing. Several techniques or deterministic optimization methods have been proposed over the past decade in order to correctly perform forming operations.

The majority of these techniques combine the finite elements method and optimization techniques. With these resources, companies can simulate their processes virtually, allowing them to provide answers to certain questions, mainly on the feasibility of the workpiece and also on the ability of the load path to properly form the piece. This coupling often allows for noticeable improvement. However, it does not provide any guarantee about the stability of the process and does not exclude that certain types of plastic instabilities may occur during the manufacturing process because there are several sources of uncertainty related to the material, loads, press and also to the operator.

Material Forming Processes: Simulation, Drawing, Hydroforming and Additive Manufacturing, First Edition. Bouchaib Radi and Abdelkhalak El Hami.
© ISTE Ltd 2016. Published by ISTE Ltd and John Wiley & Sons, Inc.

6.2. Different approaches to optimization process

In this section, we establish the state of the art of the main deterministic optimization techniques proposed in the literature that provide solutions to optimize simple and complex tubular shapes and also in the case of blank hydroforming. It brings forward the most interesting works. In [AYD 05], these techniques are classified into four major families:

– *Conventional approach*: in the conventional approaches, the load paths are determined on the basis of certain equations governing material flow. These analytical models are only valid in the case of simple tubular shapes. The limitations of this method are that the equations cannot account for some physical phenomena. Among the first studies that were based on analytical models, we can cite the works of Ansafi [ASN 03a]. He has validated the effectiveness of this approach with finite elements simulations and also by comparing these results to the experimental measurements. However, this approach becomes complicated in the case of complex geometries.

– *"Self-feeding" approach*: this approach is proposed by Starno *et al*. [STR 10]. It consists of performing numerical simulations without taking into account the axial or the friction efforts until the desired shape is obtained. In the second stage, we measure the displacement of the node that is encountered on the edge of the tube and the thinning rate in the expanded area, and we adjust the load path by including the adequate axial displacement. This allows the prevention of the localization of the visualized thinning and subsequently the phenomenon of necking. This approach presents several disadvantages; it consists of performing several simulations in order for the different parameters to properly adjust and consequently results in a significant computational time and high costs. Figure 6.1 illustrates this approach, and as a matter of fact the measured displacement does not take into consideration the friction effects between the die and tube. This value is proportionately increased, after a new simulation is launched including the contact effects between the die and the tube. This approach seems inappropriate in the case of non-symmetrical workpieces such as T or Y shapes since the displacement rate is no longer the same on both sides.

– *Adaptive approach*: the principle of this approach consists of implementing a control algorithm allowing the detection of the types of the potential instabilities and to progressively react in order to refit the input parameters. This approach has the advantage of converging toward the optimal solution in a single simulation. It presents a gain in computational time compared to the other techniques previously mentioned. This technique has been adapted by several authors to optimize simple and complex tubular

forms. The adaptive approach is based on its ability to detect the beginning of adverse situations that appear such as buckling, wrinkling and necking followed by bursting. According to the type of plastic instability detected, the algorithm reacts by an increase or a decrease in the internal pressure or in the axial displacement. Shu-hui *et al.* [SHU 07] have used an adaptive approach combining the latter with a technique based on fuzzy logic in order to predict the optimal load paths. The criteria for each type of plastic instability are implemented for detecting wrinkling and necking. During each increment, the wrinkling and necking values are evaluated and according to the values found they adjust the new pressure and axial displacement parameters. In [AYD 05], an adaptive approach is also used: they are based on other types of criteria for the detection of wrinkling and necking. Regarding wrinkling, they use an energy criterion based on the bifurcation theory, whereas for necking they use the FLC. Based on these two criteria, the parameters are adjusted during the simulation by means of a technique based on fuzzy logic. In [JAN 08], an adaptive optimization method is proposed based on the response surface method. The adaptive approach can be summarized in Figure 6.2.

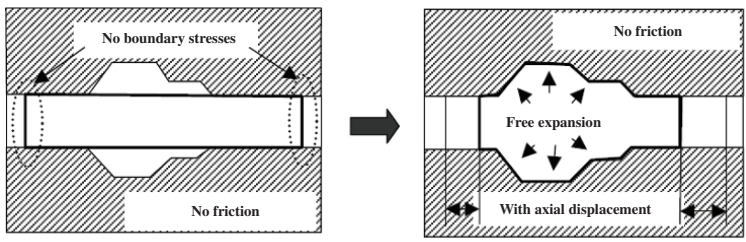

Figure 6.1. *Principle of the "self-feeding" approach*

– *Approach based on an optimization technique*: this consists of defining an objective function to be minimized or maximized with or without stresses. The criterion to be optimized can involve, for example, the distribution of the final thickness, the damage rate or, for example, the level of compliance of the piece with respect to the die. An objective function is defined [IMA 05], that involves the thickness variation by imposing stresses on the final aspect of the piece and also on the equivalent maximal plastic stress permissible. Several authors have adapted the same philosophy through an objective function and the stresses. In [LOU 07], the main focus is about T-shape tubes, they optimize the load path by imposing two objective functions. The first involves a minimization between the volume of the die and the final volume of the tube while the second ensures a uniform distribution of the final thickness. In their problem, they impose a stress that controls the equivalent stress in

each element that must not exceed the ultimate stress of the material. The conjugate gradient method is used to optimize a T-shaped tube [FAN 03]. Other techniques have been proposed such as the one from [ABE 08], which couples the finite element method with an intelligent optimization technique combining a local search technique (response surface or quadratic method) and an overall search technique (genetic algorithm). In recent years, the response surface method has been widely used for forming optimization. This allows the problem of the computation time to be addressed while ensuring the good accuracy of the final result.

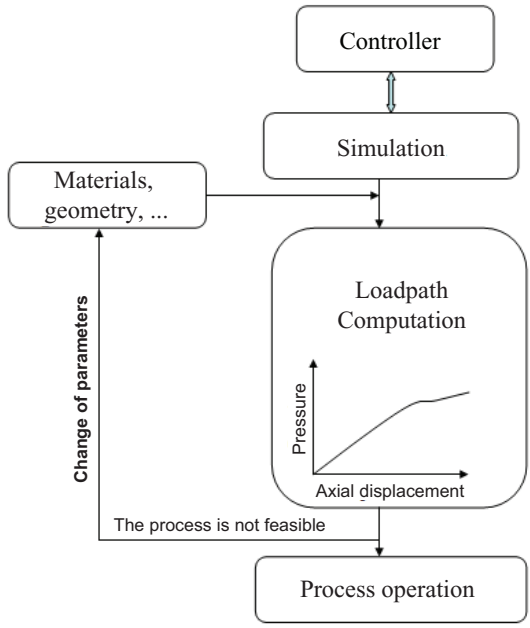

Figure 6.2. *Principle of the adaptive approach*

6.2.1. *Limitations of the deterministic approaches*

Deterministic optimization techniques (see Appendix 1) present a few disadvantages given that they do not take account of the variabilities involved in the process. These variabilities may have their origin in the material parameters, the geometry of the piece, the load parameters, the lubrication conditions, as well as external factors such as temperature or humidity and tool wear and tear effects. Not accounting for these variabilities may cause

some types of plastic instabilities to appear. The deterministic approach does not, therefore, guarantee the stability or the robustness of the process with regard to the modes of failures likely to show up, as it does not include the uncertainties of some of the parameters. Their integration into the optimization process proves to be indispensable in order to ensure an acceptable level of reliability. This makes it possible to considerably decrease the rate of defective parts. In order to take these variabilities into account, new approaches have been proposed that enable the integration of these uncertainties such as the reliability and the robust approaches [ELH 13b].

These approaches appear as promising alternatives that can at the same time optimize the process and also guarantee a level of acceptable reliability. However, the accuracy and the reliability of the finite element method depends on the accuracy on the input parameters. In reality, these parameters must be defined by their statistical moments and their probabilistic distributions. Access to this information is costly and requires a series of tests for characterizing the material or on the variability of the machine. For this reason, our probability distributions as well as the variation coefficients are defined in the form of hypotheses.

6.3. Characterization of forming processes by objective functions

The optimization of forming processes is usually carried out by defining the objective functions and the stress functions. These functions provide control over the process and ensure the good quality of the final product during the process. They also make it possible to avoid the appearance of different modes of failure that might occur. Several works featured in the literature are inspired from the limit forming curve whether it be at the level of the stresses or of the principal strains to define their functions. Some define functions that involve the level of compliance with respect to the die such that the workpiece takes the shape of the die. Other types of functions can be defined that consist of minimizing the damage rate in the piece.

The optimization of forming processes by means of some objective functions with or without deterministic stresses is a widely used approach. Nonetheless, it is often criticized because it does not involve the uncertainties about the parameters despite these hazards being present. Throughout this chapter, we optimize the hydroforming process with different types of objective functions by replacing the deterministic stresses with probabilistic stresses. The coupling between the mechanical and the probabilistic aspects is also presented.

6.4. Deterministic and probabilistic optimization of a T-shaped tube

6.4.1. *Problem description*

This example has been extensively studied in the literature but in a deterministic optimization context. The problem is solved in a deterministic manner and then again with a probabilistic approach in order to compare the two and bring forward the contribution of the probabilistic approach. The same methodology has been presented in [BEN 14] and [BEN 13] for tube hydroforming. The formulation of the optimization problem can be expressed in different ways according to the objectives sought.

A finite element model is defined to perform all of the necessary numerical simulations. This model is composed of a die that is used to give shape to the tube, and of a punch whose function is to bring material to the expanded area so as to avoid the premature necking of the tube. These two bodies are modeled by rigid bodies. The tube has a length of 121 mm, a diameter equal to 45.4 mm and an initial thickness of 1.2 mm. The finite element model and the mesh are given in Figures 6.3 and 6.4. Given the symmetry of the problem, and in order to reduce the computation time, one-fourth of the model is modeled.

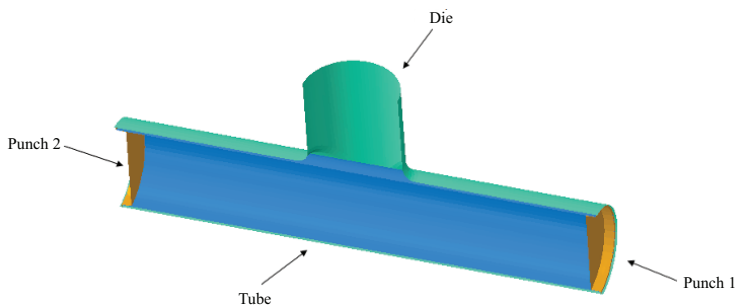

Figure 6.3. *Finite element model: exploded view*

The material used for forming this tube is $DC06$ steel. A Swift strain-hardening model is chosen whose mechanical properties are presented in Table 6.1.

k (MPa)	n	ε_0
527	0.24	0.0024

Table 6.1. *Hardening model coefficients*

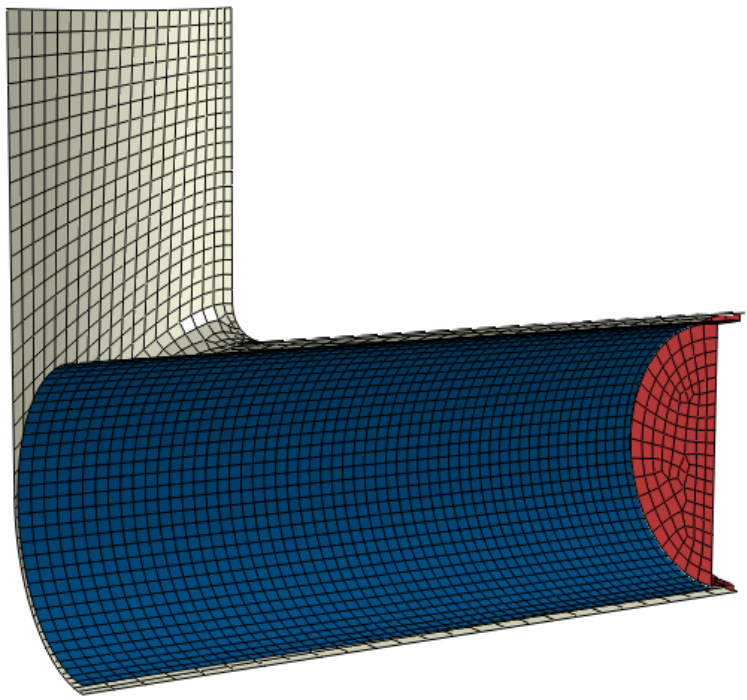

Figure 6.4. *Mesh adapted from the model*

6.4.2. *Choice of the objective function and definition of the stresses*

Solving this type of problem can be formulated in a different manners. We can establish an objective so as to ensure uniformity at the level of the distribution of the final thickness, a minimization of the damage rate or others. Here, we are interested in maximizing the height of the dome, $u_{\max}$ denotes the maximal height reached during the process. The stresses of the problem are defined to avoid the probable failure modes during the process.

Tube hydroforming often presents two types of plastic instabilities to be controlled: wrinkling and necking. To prevent these two modes of failures occurring, two criteria are defined. The evaluation and the control of these two plastic instabilities make it possible to obtain a workpiece without defects. These two criteria are illustrated as follows:

– *Wrinkling criterion*: for the detection of wrinkling, we base ourselves on the critical out-of-plane strain. In fact, the maximal value of this strain is localized at the level of the transition area as shown in Figure 6.5. A high value of this strain is synonymous with wrinkling. This critical strain value is equivalent to $\tilde{\varepsilon}_{hp} = 0.65$ determined by means of a few deterministic simulations.

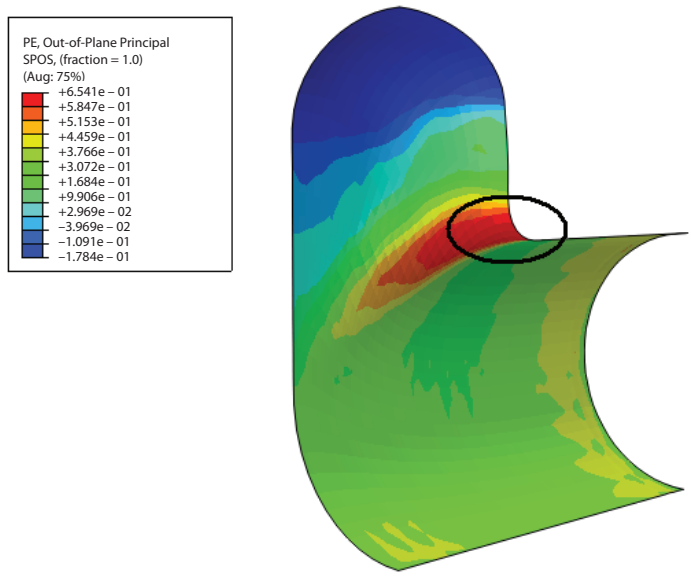

Figure 6.5. *Localization and limit value of the out-of-plane strain. For a color version of this figure, see www.iste.co.uk/radi/material.zip*

– *Necking criterion*: with regard to necking, a simple criterion serves as the basis, which consists of defining a critical thinning rate that must not be exceeded. Here we tolerate a thinning rate of the order of 25%.

6.4.3. *Choice of the uncertain parameters*

The choice of the load parameters as uncertain parameters is justified by the fact that the process presents a certain sensitivity with respect to these parameters. In fact, a slight variation in these parameters around their mean values can result in the failure of the process and plastic instabilities occurring. The success of this type of process requires proper synchronization between the internal pressure and the applied axial displacement. Taking

these uncertainties into account in an optimization context makes it possible to better determine the load paths that cause the process to become unresponsive to the different variations. The material parameters as well as friction coefficient between the forming die and the tube are considered non-deterministic and defined by their nominal values.

The load paths giving the variation of pressure and of the axial displacement with respect to time are shown in Figure 6.6. These load parameters are given according to their mean values. The probabilistic characteristics of these parameters are presented in Table 6.2.

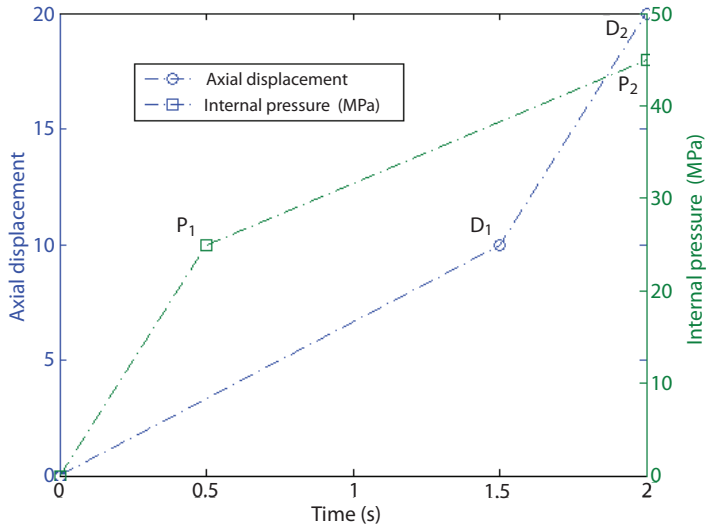

Figure 6.6. *Load paths. For a color version of this figure, see www.iste.co.uk/radi/material.zip*

R. var.	Mean	Std (%)	Distribution
P_1	25	5	Normal
P_2	45	5	Normal
D_1	10	5	Normal
D_2	20	5	Normal

Table 6.2. *Probabilistic characteristics of the load parameters*

6.4.4. *Choice of the objective function and the stresses*

The solution of the optimization problem is based on the construction of metamodels giving the objective function and the stresses according to the uncertain parameters. An experimental design centered of the composite type is chosen to perform all of the necessary numerical simulations. In view of the nonlinearities existing in the problem, one chooses a quadratic model given by equation [7.3] to represent the totality of these responses. Figures 6.7–6.9, respectively, represent the maximal displacement from the dome, the maximal out-of-plane strain and the final thinning at the level of the dome. A statistical analysis on the metamodels correctly shows that the latter ensure a level of accuracy that is quite acceptable to predict the responses. The determination coefficients are presented in Table 6.3.

Response	$u$max	ε_{hp}	Thinning
R^2	0.997	0.9393	0.9954
R^2_{adj}	0.9856	0.7175	0.978

Table 6.3. *Statistical indicators*

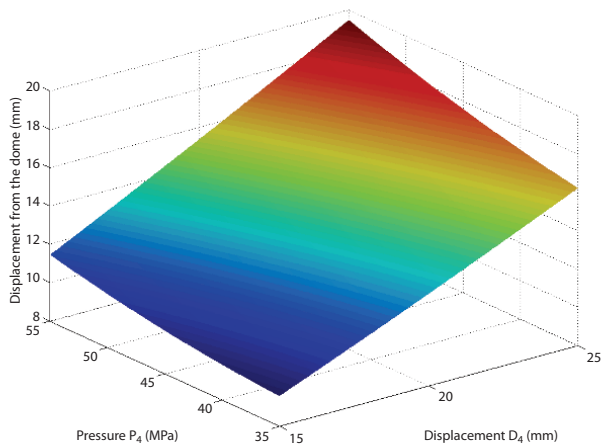

Figure 6.7. *Approximation of the maximal displacement. For a color version of this figure, see www.iste.co.uk/radi/material.zip*

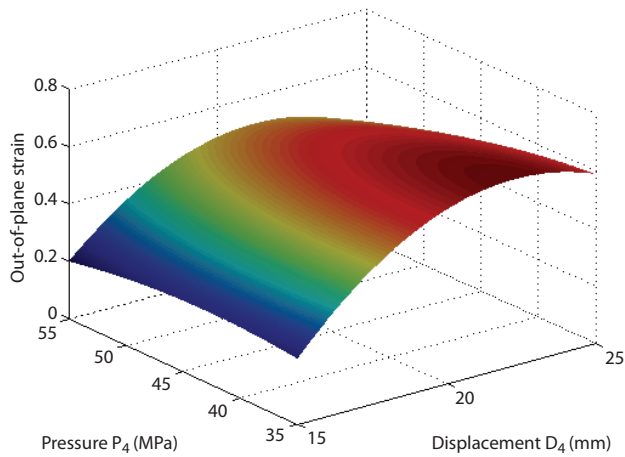

Figure 6.8. *Approximation of the out-of-plane strain. For a color version of this figure, see www.iste.co.uk/radi/material.zip*

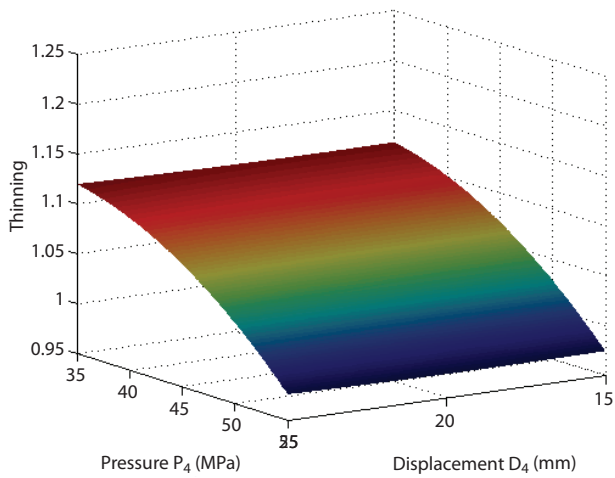

Figure 6.9. *Thinning approximation. For a color version of this figure, see www.iste.co.uk/radi/material.zip*

6.4.5. *Deterministic formulation of the optimization problem*

The problem is first solved in a deterministic manner. Two types of nonlinear optimization algorithms are used in order to determine the deterministic optimum: a gradient-based algorithm and a directional search algorithm "Pattern Search (PS)", which is based on a grid technique for searching the optimum.

Mathematically, the deterministic optimization problem can be formulated as follows:

$$\begin{cases} \max\ u_{\max}(x_i) \\ g_1(x_i) = \tilde{\varepsilon}_{\text{hp}} - 0,65 \leq 0 \\ g_2(x_i) = 0,95 - \tilde{h}_{\min} \leq 0 \\ x_i = \{D_1, D_2, P_1, P_2\} \end{cases} \quad [6.1]$$

The optimization problem consists of maximizing the height of the dome while ensuring that neither necking or wrinkling will appear during forming. In order to control the necking, we tolerate a thinning of the order of 25%.

The solution of the problem with a sequential quadratic programming (SQP) algorithm allows the deterministic optimum to be reached after 19 iterations. The optimum load paths obtained in the deterministic case are compared with the initial paths in Figure 6.10. The maximum height of the dome is also presented in the deterministic case, it reaches a maximum value of 19.457 mm (see Figure 6.11).

With the PS algorithm, the algorithm converges after five iterations and 643 evaluations of the objective function. The convergence path of these two algorithms are given in Figure 6.12.

The optimum load paths obtained with this algorithm are compared with those obtained by the SQP algorithm. The maximal height of the dome obtained with the PS algorithm is smaller than that obtained with the SQP algorithm, it is equal to 19.3227 mm. Figure 6.14 shows the distribution of the displacement for the second case. The use of these two types of algorithms shows that the SQP algorithm converges to a smaller value, which proves its effectiveness compared to PS algorithm. On the other hand, the latter converges more quickly toward the optimal solution.

6.4.6. *Probabilistic formulation of the optimization problem*

In the following, the problem is solved in a reliabilist manner. The deterministic stresses formulated in equation [6.1] are now transformed into probabilistic stresses pertaining to the evaluation of the probability that one of these stresses is not satisfied. It should also be noted that these two modes of failures are assumed to be independent, which means that the occurrence of one does not depend on the other. In a reliability context, the stress is defined by a limit state function or performance function. The two limit state functions are expressed according to the deterministic stresses and they are given by the following system of equations:

$$\begin{cases} G_1 & = -g_1 \\ G_2 & = -g_2 \end{cases} \qquad [6.2]$$

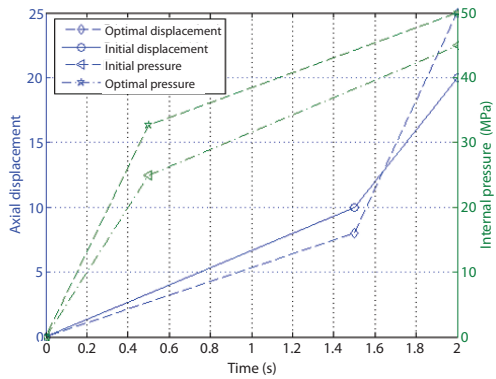

Figure 6.10. *Comparison of the deterministic optimum paths with the initial paths. For a color version of this figure, see www.iste.co.uk/radi/material.zip*

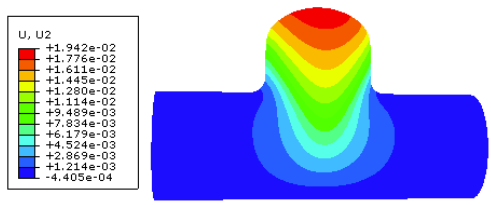

Figure 6.11. *Maximum height at the dome. For a color version of this figure, see www.iste.co.uk/radi/material.zip*

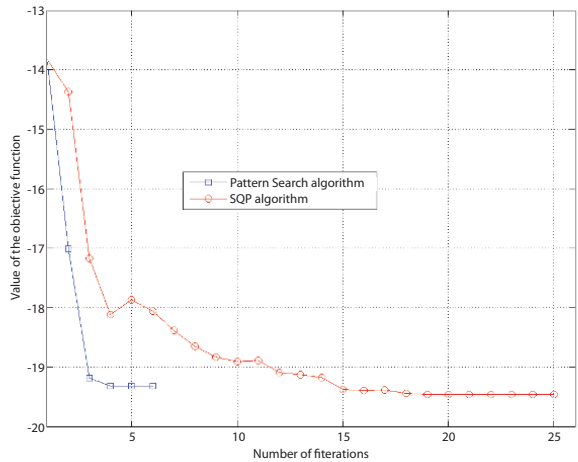

Figure 6.12. *Convergence path for the SQP algorithm and the PS algorithm*

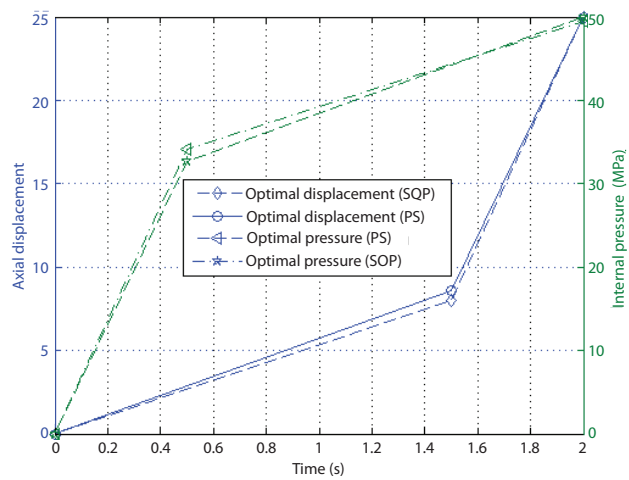

Figure 6.13. *Comparison of the optimum paths obtained with the two algorithms. For a color version of this figure, see www.iste.co.uk/radi/material.zip*

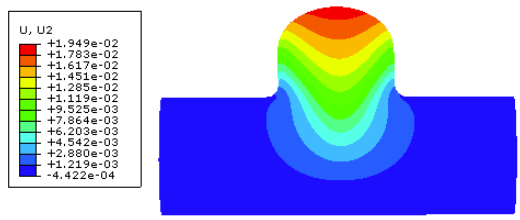

Figure 6.14. *Maximum height at the dome. For a color version of this figure, see www.iste.co.uk/radi/material.zip*

The reliability problem consists of maximizing the average values of the optimization variables given by the vector $\mu = (\mu_{D_1}, \mu_{D_2}, \mu_{P_1}, \mu_{P_2})$.

The optimization-based reliability problem is formulated as follows:

$$\begin{cases} \max\ u_{\max}(\mu_i) \\ P[G_1(x) \leq 0] \leq P_{\text{admissible}} \\ P[G_2(x) \leq 0] \leq P_{\text{admissible}} \\ \mu_i = \{\mu_{D_1}, \mu_{D_2}, \mu_{P_1}, \mu_{P_2}\} \end{cases} \quad [6.3]$$

The optimum load paths are sought for different levels of admissible reliability: $P_f = 2.28\%$, $P_f = 0.62\%$, $P_f = 0.13\%$, and $P_f = 3.1686 \times 10^{-3}\%$, which correspond to the following reliability indices: 2, 2.5, 3 and 4.

The SQP algorithm is used to solve problem [6.3]. The algorithm converges for the different levels of reliability. The convergence of the objective function based on the number of iterations for these different cases is presented in Figure 6.15.

The load paths obtained for the different levels of reliability are compared with the initial paths and the deterministic optimal paths given in Figures 6.16 and 6.17.

The maximal displacement at the level of the dome for the different levels of reliability is given in Figures 6.18–6.21. The more significant the reliability level, the smaller the height of the dome compared to the deterministic case.

The distribution of the thickness for the deterministic optimum and the reliability optima are presented in Figure 6.22.

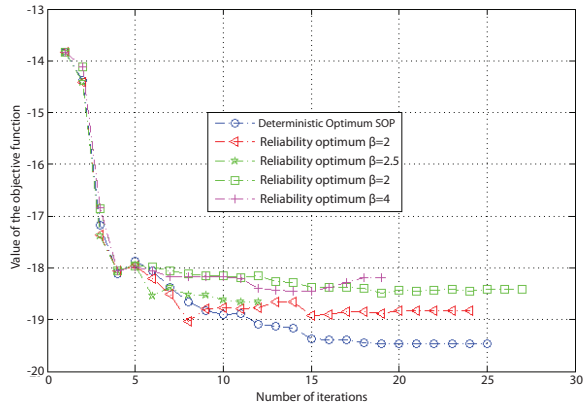

Figure 6.15. *Evolution of the objective function during the iterations. For a color version of this figure, see www.iste.co.uk/radi/material.zip*

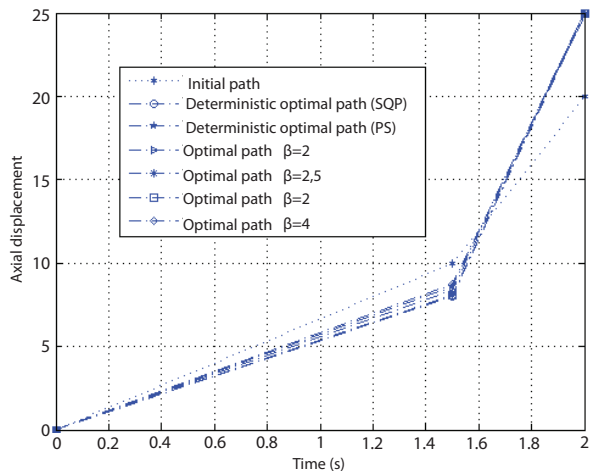

Figure 6.16. *Comparison of the optimum paths: axial displacement (mm) - time (s)*

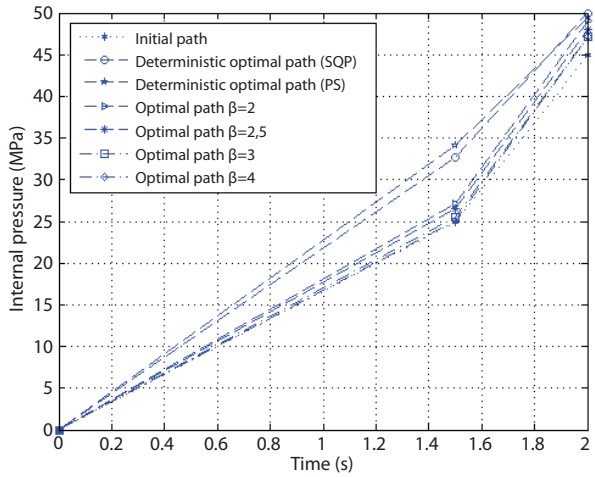

Figure 6.17. *Comparison of the optimum paths: internal pressure (MPa) - time (s)*

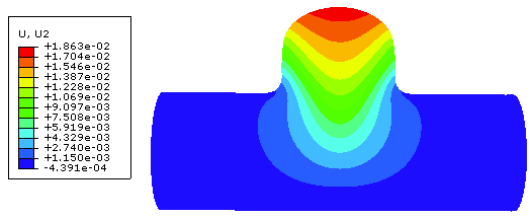

Figure 6.18. *Maximal displacement:* $\beta = 2$

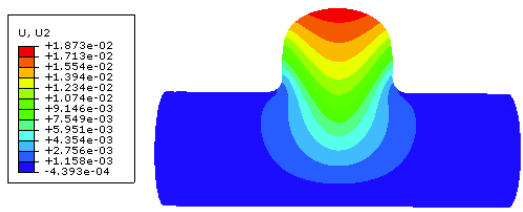

Figure 6.19. *Maximal displacement:* $\beta = 2.5$

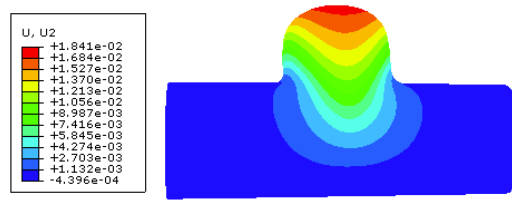

Figure 6.20. *Maximal displacement:* $\beta = 3$

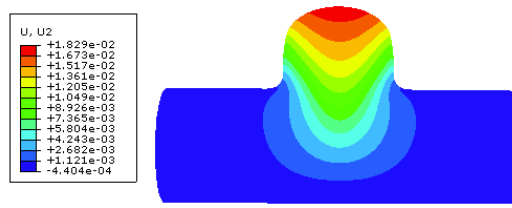

Figure 6.21. *Maximal displacement:* $\beta = 4$

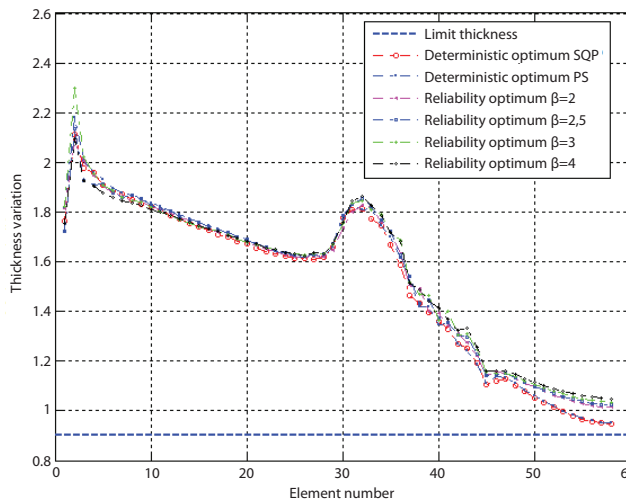

Figure 6.22. *Thickness variation depending on the axial position. For a color version of this figure, see www.iste.co.uk/radi/material.zip*

Figure 6.23 shows the height at the level of the dome. Comparing with the thickness distribution given by Figure 6.22, it can be observed that the more significant the height of the dome is, the more significant the thinning is.

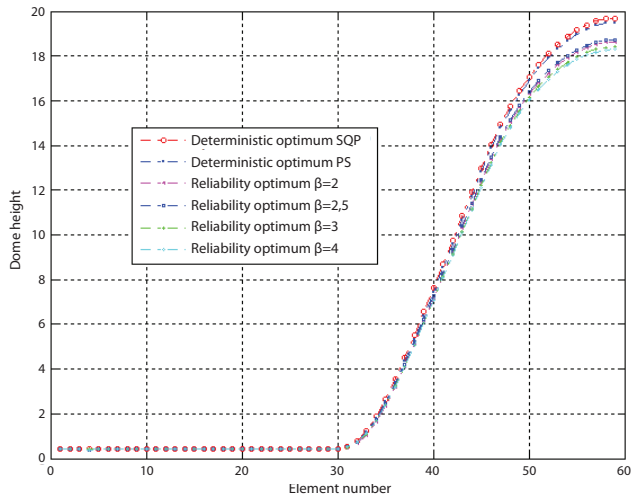

Figure 6.23. *Height at the dome for several optima. For a color version of this figure, see www.iste.co.uk/radi/material.zip*

The localization of the optima is given in the space of the parameters that have a great influence, namely (P_2, D_2) determined with sensitivity analysis. The outline of the objective function and the stresses are plotted in Figure 6.24.

The interest of the optimization-based reliability lies in the search for the optimum that satisfies a target level of reliability. In fact, as shown in Figure 6.24, the deterministic optimum always tends toward the limits of the stresses. Taking into account the uncertainties affecting certain parameters can foster the emergence of plastic instabilities. The interest of optimization-based reliability becomes more obvious in this example as one increases the target reliability index. It should be noted, for instance, that the optimum that guarantees a level of reliability equivalent to a reliability index $\beta = 4$ is clearly further away from the deterministic optimum and from the limits of the stresses. Therefore, with this level of reliability, we are moving away from the risk area that enables ensuring the stability of the process.

In order to make additional investigations about the influence of the initial point on the convergence toward the reliabilistic optimum, we look for

different initial points. There is only interest in the case where the reliability index is established at $\beta = 3$.

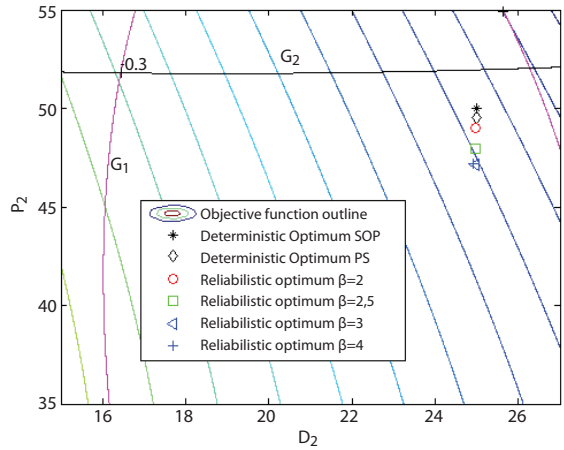

Figure 6.24. *Localization of optima in the search space. For a color version of this figure, see www.iste.co.uk/radi/material.zip*

Table 6.4 summarizes the optima found for six different starting points and also provides the number of iterations as well as the value of the objective function. As a point of fact, the forming problems are strongly nonlinear and converge to various local optima by changing the initial point. In this type of problem, we often try several initial points and from among all these optima, the one that presents the lowest value of the objective function is chosen.

Initial point	Reliabilistic optimum	Number of iterations	Value of f_{obj}
[10 20 25 45]	[8.09 24.95 25.45 47.13]	27	-18.41
[11 18 23 47]	[8.85 24.88 24.04 48.28]	10	-18.29
[9 22 27 43]	[8.18 24.97 27.95 46.20]	20	-18.38
[11 22 24 49]	[8.34 24.97 22.55 48.53]	26	-18.46
[12 20 21 46]	[8.34 24.97 26.33 47.93]	34	-18.58
[9 19 21 47]	[9.46 24.97 22.39 49.85]	20	-18.37

Table 6.4. *Influence of the starting point on the reliabilistic optimum*

6.4.7. *Optima sensitivity to uncertainties*

With the aim to examine the sensitivity of the deterministic and reliabilistic optimum to the uncertainties, these two optima are perturbated so

as to see their variation ranges. With regard to the reliabilistic optimum, the one that corresponds to a reliability index $\beta = 4$ is chosen. In Figure 6.25, it can be seen that the reliability optimum does not exceed the limits imposed by the two stresses denoted in Figure 6.25 by (G_1, G_2) and that, respectively, represent the stress related to the out-of-plane strain and the final thinning. On the contrary, a variation of the deterministic optimum pushes it toward the non-feasibility domain which affects the stability of the process and does not exclude that certain plastic instabilities may occur during the process due to the instant uncertainties. In effect, the mechanical properties, the applied load paths as well as the lubrication conditions can change from one tube to another, which makes the prediction of the final state of the workpiece unpredictable; this fact leaves the deterministic optimum often at risk and does not guarantee the stability of the process. The variation region occupied by the reliability optimum is much more stable compared to that occupied by the deterministic optimum.

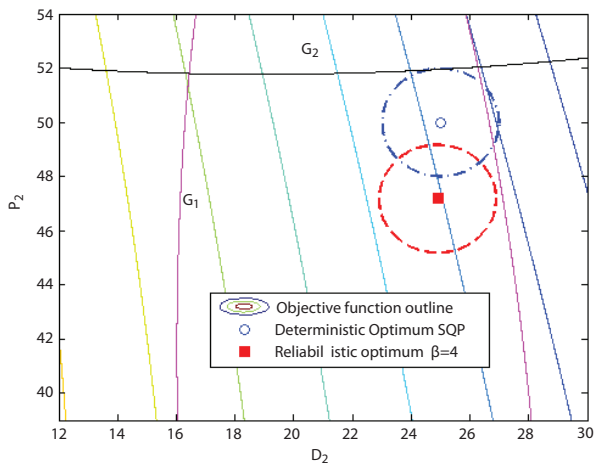

Figure 6.25. *Optima sensitivity to uncertainties. For a color version of this figure, see www.iste.co.uk/radi/material.zip*

For the same purpose, the deterministic and reliabilistic optima are perturbated with a defined variation rate and we observe their variations in the feasibility space. With two different variation levels corresponding to $(\delta = 2\%$ and $\delta = 5\%)$, $1,000$ random realizations are generated with a Monte Carlo method and their distributions are analyzed. Figures 6.26 and 6.27 illustrate the distribution of these realizations in the space (D_2, P_2) and delimiting the feasibility domain denoted by Ω_s of the failure domains

denoted by Ω_f. Concerning the first level of uncertainty, we note that only the realizations originating from a perturbation of the deterministic optimum exceed the boundaries of the feasibilities. An increase in the level of perturbation affects the deterministic optimum much more than the reliabilistic optimum. Most of the realizations originating from a perturbation of the reliabilistic optimum are in the admissible domain.

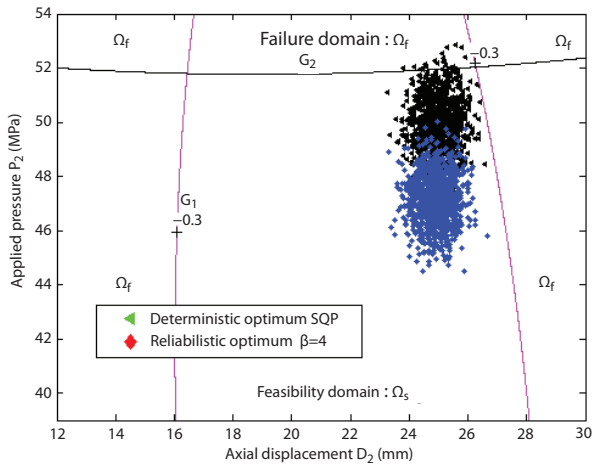

Figure 6.26. *Effect of the perturbation of the optima with a rate $\delta = 2\%$. For a color version of this figure, see www.iste.co.uk/radi/material.zip*

6.5. Deterministic and optimization-based reliability of a tube with two expansion regions

6.5.1. *Problem description*

The second example addressed in this chapter consists of hydroforming a tube with two growing areas of different heights. The problem is solved with a conventional deterministic and probabilistic approach in order to compare them. To simplify the problem, only the load parameters are considered as uncertain.

The finite element model consists of a die with two expansion areas and punches that ensure that material be added to the expanded area modeled by rigid bodies. The tube has a diameter of 45 mm and an initial thickness of 1.5 mm. The finite element model is presented in Figure 6.28.

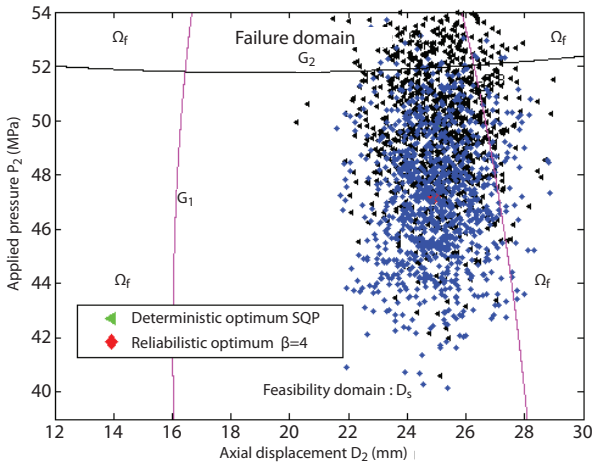

Figure 6.27. *Effect of the perturbation of the optima with a rate $\delta = 5\%$. For a color version of this figure, see www.iste.co.uk/radi/material.zip*

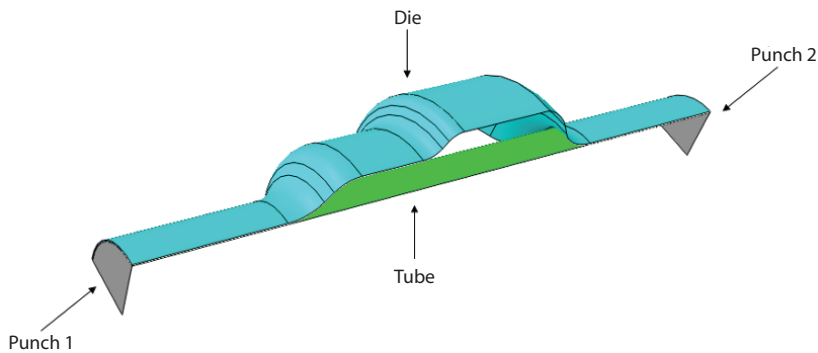

Figure 6.28. *Finite element model*

The dimensions of the die are shown in Figure 6.29, the tube has the same length as the die. The material being used is DC04 steel whose elastoplastic properties are presented in Table 6.1.

The load paths being used are presented in Figures 6.30 and 6.31. The goal of the problem is to optimize load paths in a deterministic and also in a

reliabilist manner. The main objective is to control the displacements of the two punches and the internal pressure. In this problem, the axial displacement is modeled by points D_1 for punch 1 and D_2 for punch 2. The internal pressure is controlled by three levels of pressure denoted by (P_1, P_2, P_3).

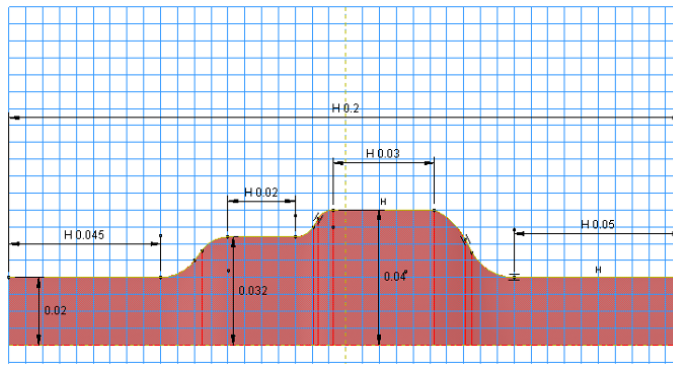

Figure 6.29. *Die dimensions (in meters)*

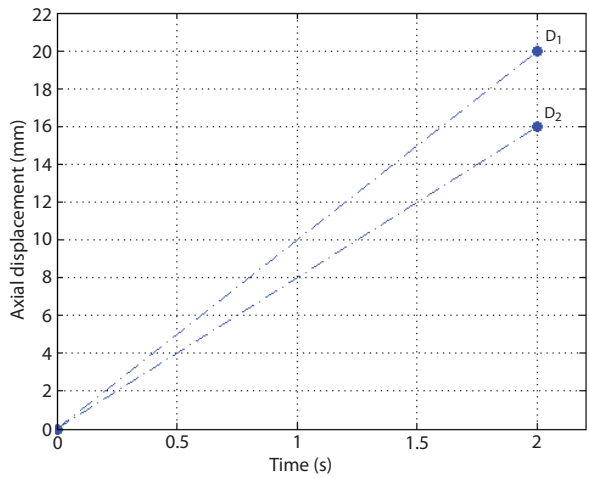

Figure 6.30. *Load path: displacement (mm) - time (s)*

Table 6.5 represents these variables with their probabilistic characteristics. These variables are assumed to be statistically independent.

The defined objective function involves the minimization of the variation of the final thickness (equation [6.4]). It makes it possible to ensure a homogeneous distribution of the final thickness. The first term accounts for the excessive thinning that favors the formation of necking while the second enables one to control the thickening of the tube, which provides a means to control the tendency to wrinkle. In other words, it makes sure that neither thinning nor thickening would assume excessive values. The objective function is formulated in the following manner:

$$f(x) = \frac{1}{N}\left(\sum_{i=1}^{N}\left(\frac{h_0 - h_i}{h_0}\right)^2\right)^2 + \frac{1}{N}\left(\sum_{i=1}^{N}\left(\frac{h_i - h_0}{h_0}\right)^2\right)^2 \qquad [6.4]$$

where $f(.)$ is the objective function, x is the optimization parameters vector, h_i is the thickness of the element i, h_0 is the initial thickness and N is the total number of elements.

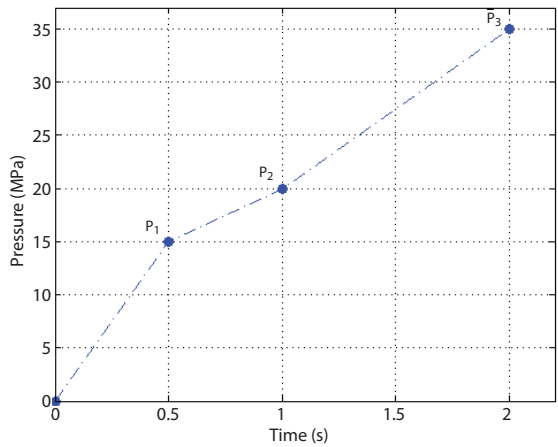

Figure 6.31. *Load path: internal pressure (MPa) - time (s)*

The definition of stresses will focus on the potential plastic instabilities. The wrinkling is taken into account by means of the objective function that enables the control of the tube thickening and also by means of geometric stress. With regard to necking, the CFL of the material serves as a basis in order to define a stress that prevents this instability from occurring. For necking, we rely on the principal critical strains as shown in Figure 6.32.

R. var.	Mean	Std. (%)	Distribution
D_1	20	5	Normal
D_2	16	5	Normal
P_1	15	5	Normal
P_2	20	5	Normal
P_3	35	5	Normal

Table 6.5. *Probabilistic characteristics of the load parameters*

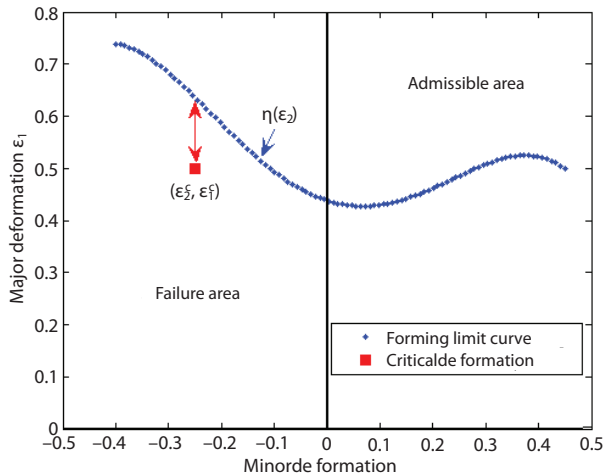

Figure 6.32. *Forming limit curve: necking criterion*

Geometric stresses are also defined that allow the tube to properly assume the shape of the die. These three stresses imply that the distance of the nodes at the level of the three radii is minimal. Figure 6.33 details these types of stresses.

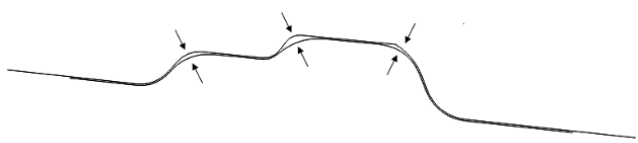

Figure 6.33. *Geometric stresses*

6.5.2. *Deterministic and reliabilist formulation of the optimization problem*

The deterministic optimization problem is written as follows:

$$\begin{cases} \min\ f(x) \\ g_1(x) = \varepsilon_1^c - \eta(\varepsilon_2^c) \\ g_i = d_i - d_m;\ i = \{2,3,4\} \\ x = \{D_1, D_2, P_1, P_2, P_3\} \end{cases} \quad [6.5]$$

in which f represents the objective function, x is the vector of the optimization variables, g_1 is the deterministic stress pertaining to the tube necking, g_i are the geometric stresses, with $i = \{1,2,3\}$ and $\eta(\varepsilon_2)$ is the equation of the forming limit curve.

Concerning the reliabilist formulation of the problem, the stress linked to the tube necking is transformed into a probabilistic stress. The geometric stresses are maintained as deterministic.

The optimization-based reliability problem is defined as follows:

$$\begin{cases} \min\ f(\mu_x) \\ P[G_1(\mu_x) \leq 0] \leq P_{\text{admissible}} \\ g_i = d_i - d_{m_i};\ i = \{2,3,4\} \\ \mu_x = \{\mu_{D_1}, \mu_{D_2}, \mu_{P_1}, \mu_{P_2}, \mu_{P_3}\} \end{cases} \quad [6.6]$$

where $G_1 = -g_1$; $P[\bullet]$ is the likelihood of occurrence of the plastic instability and μ_x is the mean of the uncertain parameters.

The problem is solved with the same approach exposed in the previous example. The convergence for the deterministic and reliabilistic optimum for a $\beta = 3$ is summarized in Figure 6.34.

The optimum load paths are summarized in Figures 6.35–6.36 giving the variation of the pressure and of the axial displacement with respect to time.

The distribution of the final thickness obtained by the conventional deterministic approach and the probabilistic approach are given in Figure 6.37. It can be observed that the reliabilist approach allows a better distribution of the thickness and present less thinning, which minimizes the formation of necking.

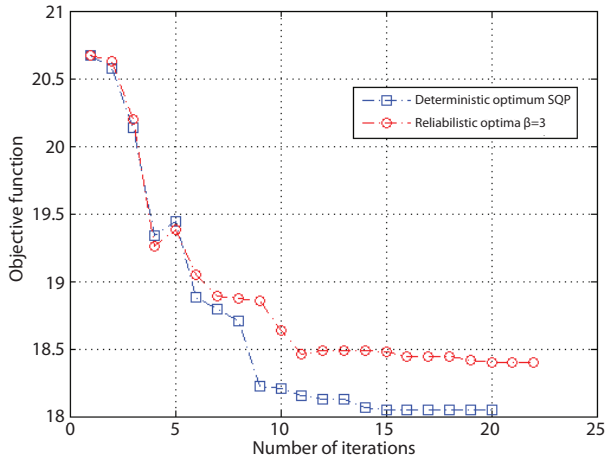

Figure 6.34. *Convergence of the objective function*

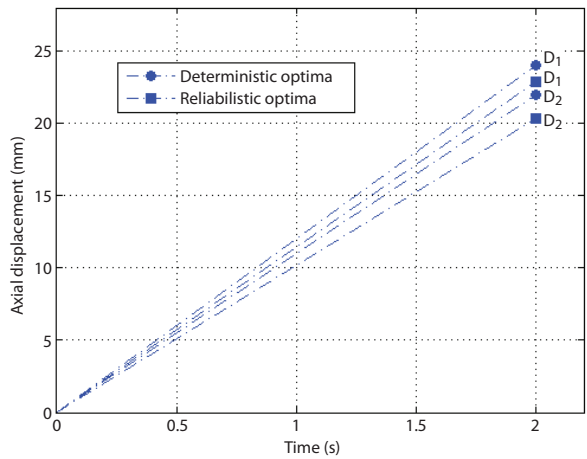

Figure 6.35. *Optimum paths: axial displacement (mm) - time (s)*

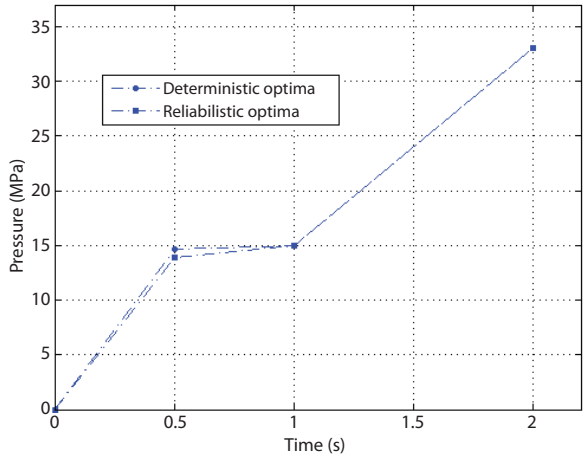

Figure 6.36. *Optimum paths: pressure (MPa) - time (s)*

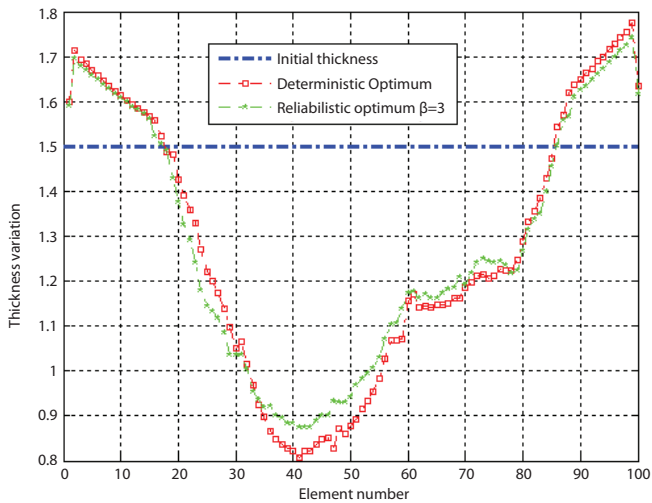

Figure 6.37. *Distribution of the thickness according to the axial position*

6.6. Optimization-based reliability of circular sheet metal hydroforming

6.6.1. *Problem description*

The study of this example has for an objective the deterministic and the optimization-based reliability of circular sheet metal hydroforming. The finite element model representing the die and the plate is given in Figure 6.38.

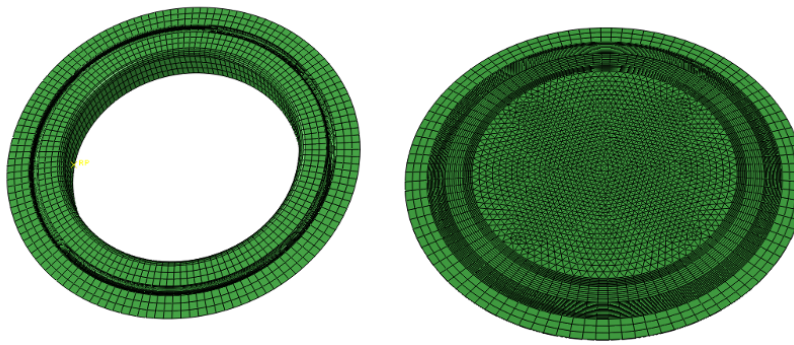

Figure 6.38. *Finite element model*

In this example, we consider the variabilities that may affect the applied pressure, the material parameters as well as the friction coefficient between the die and the plate. It is assumed that the material is isotropic and modeled by Swift law. The friction between the sheet and the die is modeled by Coulomb's law with a coefficient $\mu = 0.15$ that represents its mean value. It is assumed that all of these parameters follow a uniform type of distribution whose upper and lower bounds are summarized in Table 6.6. The vector of the uncertainty parameters is given by $X = \{P, k, n, \mu\}$.

Variable	Lower bound	Upper bound	Distribution
P	4	6	Uniform
k	$1,280$	$1,732$	Uniform
n	0.4965	0.6718	Uniform
μ	0.1	0.2	Uniform

Table 6.6. *Probabilistic characteristics of the optimization parameters*

6.6.2. *Construction of the objective function and of the stresses*

The deterministic- and optimization-based reliability of the process is achieved using metamodels. Quadratic models are used to represent all of these functions. The construction of the objective function and the stress is carried out by means of a numerical experimental design based on Latin hypercubes. Figure 6.39 shows the distribution of these parameters in the variation space.

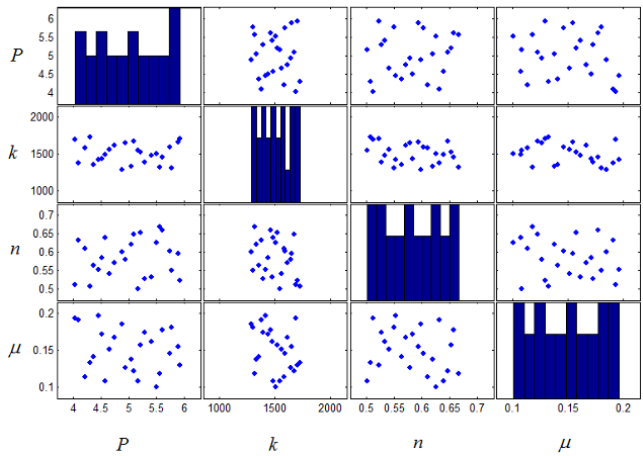

Figure 6.39. *Distribution of the parameters in the search space*

The approximations providing the form of the objective function of the displacement from the axis and the stress on the equivalent plastic strain are presented in Figures 6.40 and 6.41 according to the internal pressure P and the strain-hardening modulus k.

6.6.3. *Effects diagram*

In order to see the influence of each parameter on the process, we plot the diagram of the effects by varying the parameters between the bound values (see Figure 6.45). The main interest is to see the impact on the objective function and the stress.

According to the effects plot, the friction coefficient does not really impact on the objective function nor on the stress. A variation of this coefficient between its two bound values does not produce a significant change in the displacement from the axis or on the equivalent plastic strain. In

the following, this parameter is considered to be deterministic and is represented by its value. The vector of the uncertainty parameters is reduced to $X = \{P, k, n\}$.

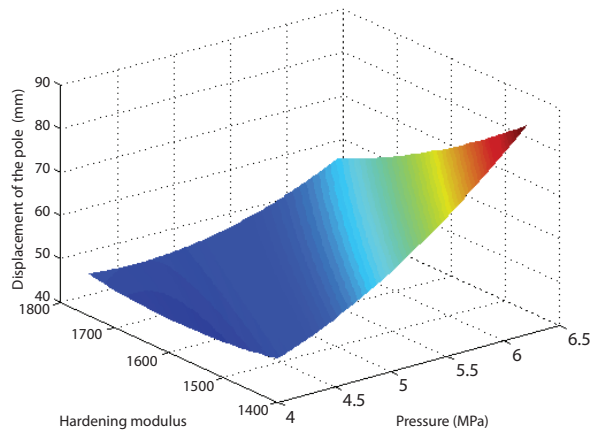

Figure 6.40. *Approximation of the objective function: displacement at the dome. For a color version of this figure, see www.iste.co.uk/radi/material.zip*

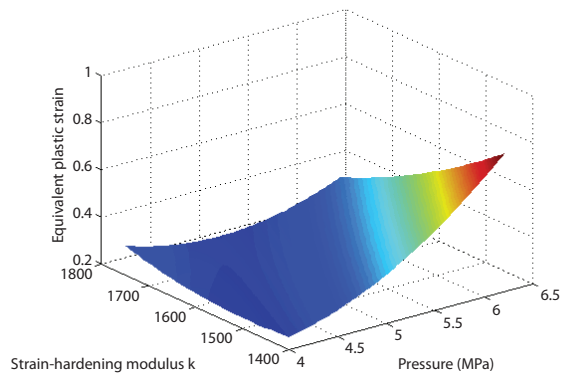

Figure 6.41. *Approximation of the stress function: equivalent plastic strain. For a color version of this figure, see www.iste.co.uk/radi/material.zip*

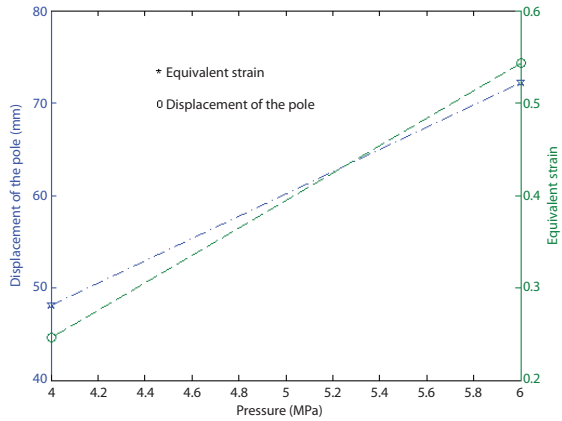

Figure 6.42. *Effect of the pressure on the responses*

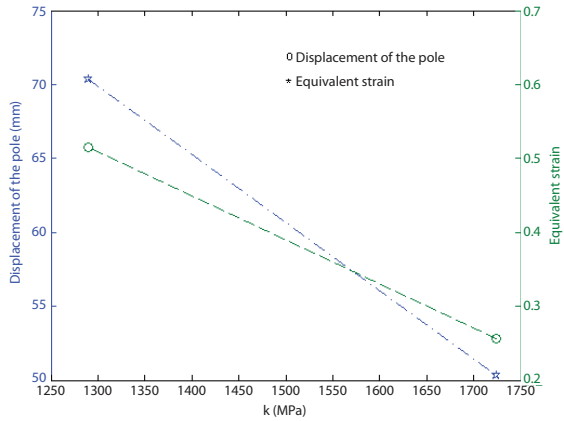

Figure 6.43. *Effect of the hardening modulus on the responses*

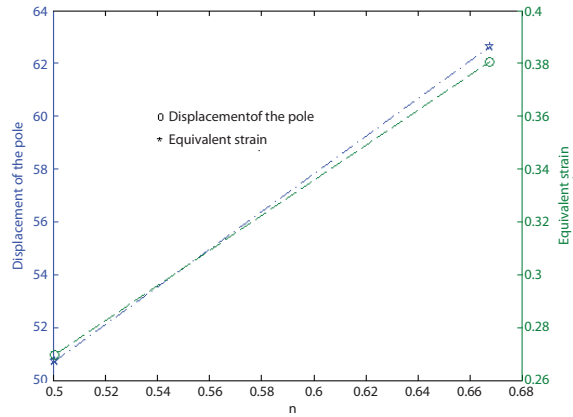

Figure 6.44. *Effect of the hardening coefficient on the responses*

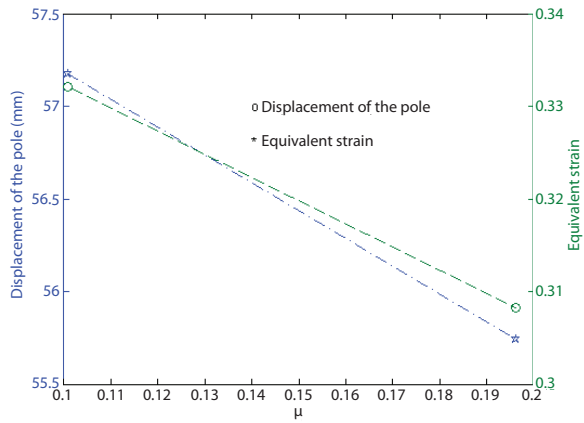

Figure 6.45. *Effect of the friction coefficient on the responses*

The optimization-based reliability with metamodels always requires performing statistical tests in order to ensure their robustness and to observe their ability to accurately predict the levels of responses. Figures 6.46 and 6.47 demonstrate a good correlation between the approximated values and the predicted values. The statistical indicators giving the determination coefficients and the fitted determination coefficients are given in Table 6.7.

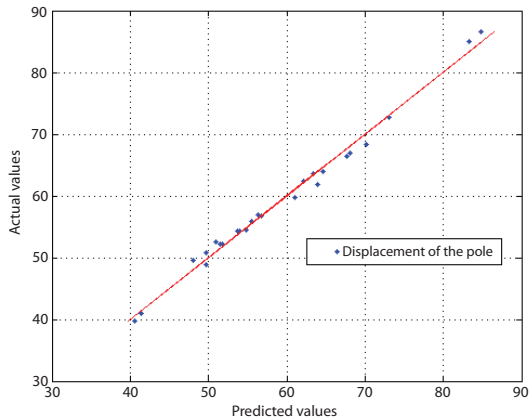

Figure 6.46. *Predicted values–approximate values: displacement from the axis*

Response	R^2	R^2_{adj}
$u_{\max}$	0.9911	0.9573
ε_{eq}	0.9797	0.9035

Table 6.7. *Statistic indicators*

6.6.4. *Deterministic solution of the optimization problem*

In the industrial applications of plate hydroforming, the main concern is often to maximize the height at the level of the axis. The stress often consists of ensuring that the plastic strain, the maximal stress or the maximal thinning do not exceed a critical value. In this application, our optimization problem consists of the definition of an objective function that allows maximizing the displacement from the axis and a stress that ensures that the equivalent plastic

strain does not exceed a critical value set to $\varepsilon_{max}^{eq} = 0.5$. The deterministic optimization problem can be defined as follows:

$$\begin{cases} \max\ u(P,k,n) \\ g = \varepsilon^{eq}(P,k,n) - \varepsilon_{\max}^{eq} \\ x = (P,\ k,\ n); \quad x_{\min}^{i} \leq x \leq x_{\max}^{i} \end{cases} \qquad [6.7]$$

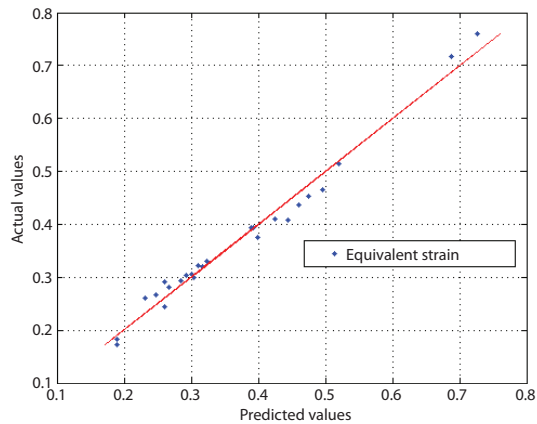

Figure 6.47. *Predicted values–approximate values: equivalent strain*

The problem is solved using the SQP algorithm. The algorithm converges after 44 iterations and the objective function is evaluated 176 times. The non-deterministic optimal variables are given in Table 6.8.

P (MPa)	k (MPa)	n
5.49	1499	0.6674

Table 6.8. *Deterministic optimal variables*

The convergence of the objective function is given in Figure 6.48. The maximal displacement from the axis is 70.0067 mm. The isovalues of the axial displacement and of the equivalent plastic strain are given in Figures 6.49–6.50.

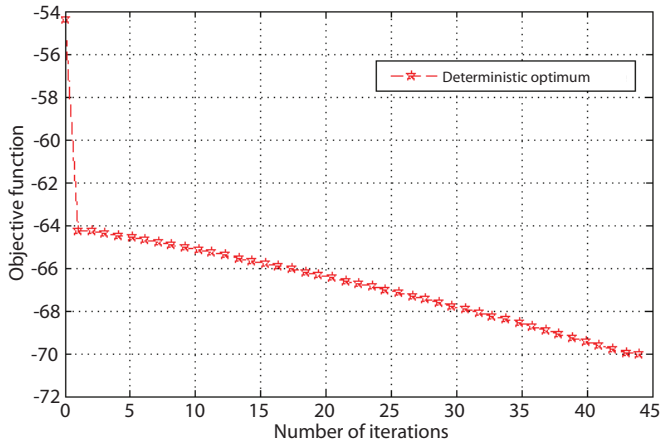

Figure 6.48. *Convergence of the objective function*

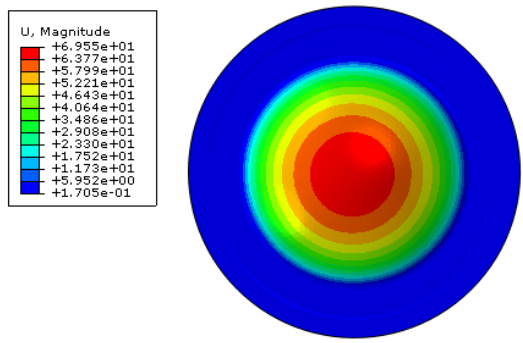

Figure 6.49. *Isovalues of the displacement from the axis. For a color version of this figure, see www.iste.co.uk/radi/material.zip*

6.6.5. *Reliabilist solution of the optimization problem*

The solution of the optimization-based reliability problem consists of converting the deterministic stress into a probabilistic stress. The boundary state function separating the failure domain from the safety domain is given by:

$$G_1(P,k,n) = 0,5 - \tilde{\varepsilon}^{eq}_{\max} \qquad [6.8]$$

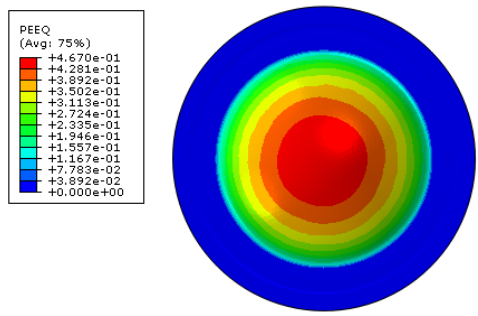

Figure 6.50. *Isovalues of the equivalent plastic strain. For a color version of this figure, see www.iste.co.uk/radi/material.zip*

Taking this boundary state equation into account, the reliability problem can be formulated as follows:

$$\begin{cases} \max\ u(P,k,n) \\ P[G_1(\mu(x)) \leq 0] \leq P_{\text{admissible}} \\ \mu(x) = [\mu(P), \mu(k), \mu(n)] \end{cases} \quad [6.9]$$

The optimization-based reliability problem is solved for two likelihood levels of admissible failure, and $P_f = 2.28 \times 10^{-0,13\%}$, which correspond to the reliability indices: $\beta = 2$ and $\beta = 3$.

For $\beta = 2$, the algorithm converges after 12 iterations to the variables of Table 6.9. For $\beta = 3$, the algorithm diverges.

Reliability index	P (MPa)	k (MPa)	n
$\beta = 2$	5.4758	1605.487	0.667

Table 6.9. *Reliability optimal variables*

The isovalues giving the displacement from the axis as well as the equivalent plastic strain are presented by Figures 6.51 and 6.52. The convergence of the objective function in the reliability case is given in Figure 6.53.

The reliabilistic optimum is reached after six iterations, whereas the deterministic optimum is reached after 44 iterations. However, the number of evaluations of the objective function is much more significant in the reliability

case, as for the computational time. For higher reliability levels, the algorithm does not converge toward a feasible solution. The outline of the objective function, the stress and the two optimal variables are plotted in Figure 6.54.

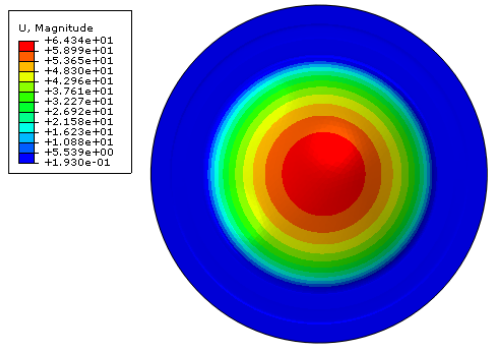

Figure 6.51. *Isovalues of the displacement from the axis. For a color version of this figure, see www.iste.co.uk/radi/material.zip*

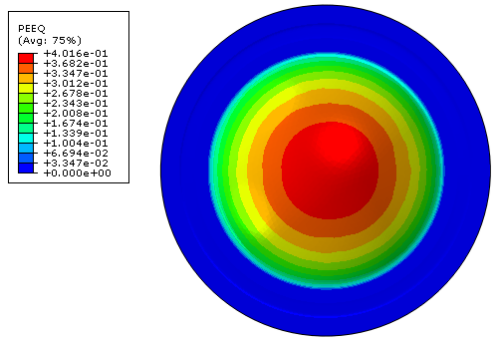

Figure 6.52. *Isovalues of the equivalent plastic strain. For a color version of this figure, see www.iste.co.uk/radi/material.zip*

6.6.6. *Effect of uncertainties on the optimal variables*

The topic of this section is to highlight the deterministic and reliability optimum sensitivity with respect to the uncertainties. By perturbating these optimal variables with two different levels defined as $\delta = 5\%$ and $\delta = 8\%$, then generating with Monte Carlo simulations with $1,000$ realizations, we can observe a clear difference in the percentage of failing realizations

between these two optimal variables. Reliability optimization presents a major interest to ensure the reliability and the stability of the process. Figures 6.55 and 6.56 underline this difference and show the contribution of the optimization-based reliability by comparing it with a conventional deterministic optimization approach. The reliability optimum is considerably less sensitive to the variations that may affect the parameters [RAD 10].

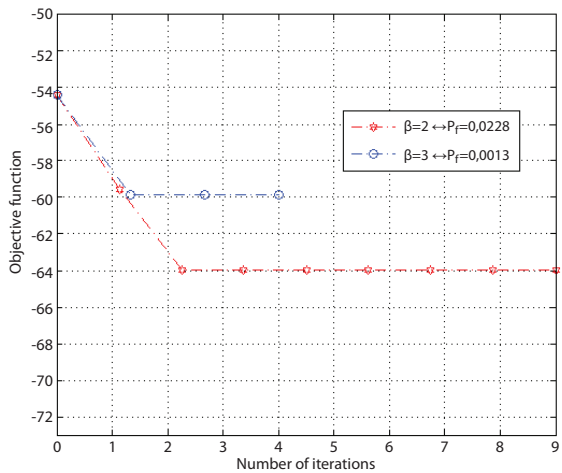

Figure 6.53. *Convergence of the objective function: optimization-based reliability. For a color version of this figure, see www.iste.co.uk/radi/material.zip*

The path giving the displacement with respect to the pressure is illustrated in Figure 6.57 for the deterministic and the reliability optima. It should be noted that these two paths are very similar except that at the end the deterministic optimum allows going further at the level of the final amplitude.

The work-hardening curve obtained for the two optimal variables is given in Figure 6.58.

Distribution of the thickness according to the axial position of the sheet metal is given in Figure 6.59.

6.7. Deterministic and robust optimization of a square plate

In this last example, we solve the optimization problem of forming a square plate with two different methods: a conventional deterministic optimization and a robust optimization in order to compare the two.

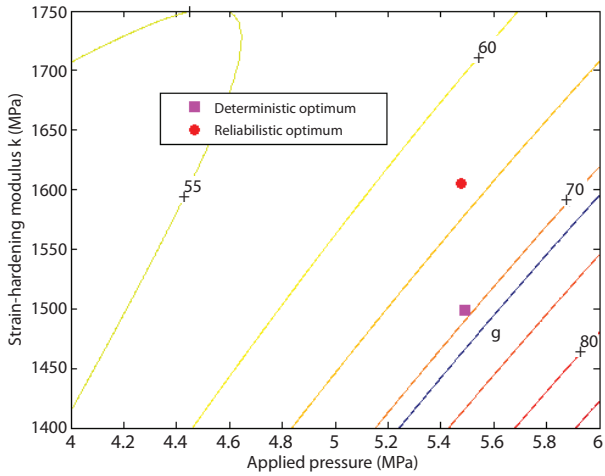

Figure 6.54. *Localization of the optimal variables in the space of the uncertainty parameters*

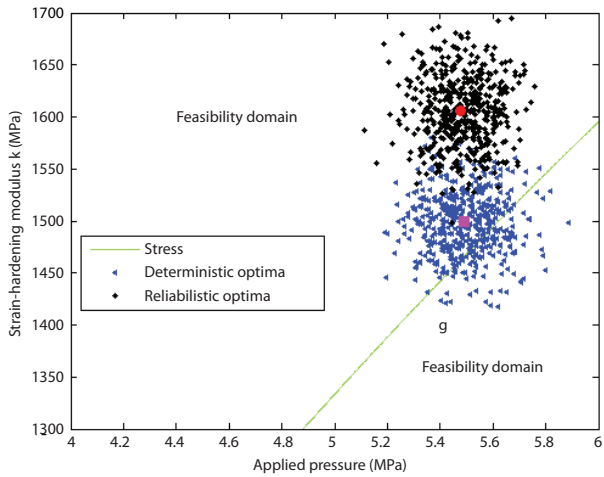

Figure 6.55. *Sensitivity of the optimal variables at a perturbation level with* $\delta = 2\%$

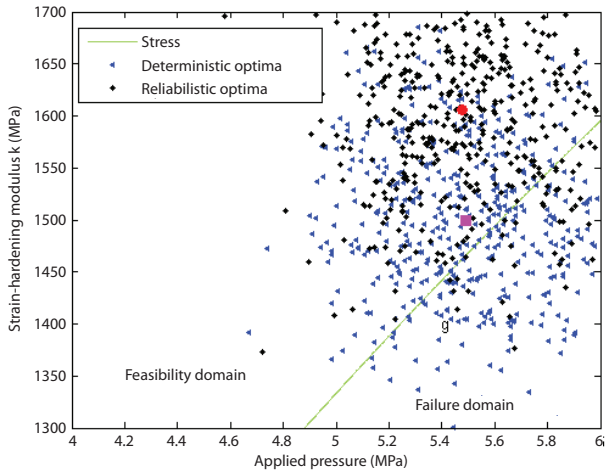

Figure 6.56. *Sensitivity of the optimal variables at a perturbation level with* $\delta = 5\%$

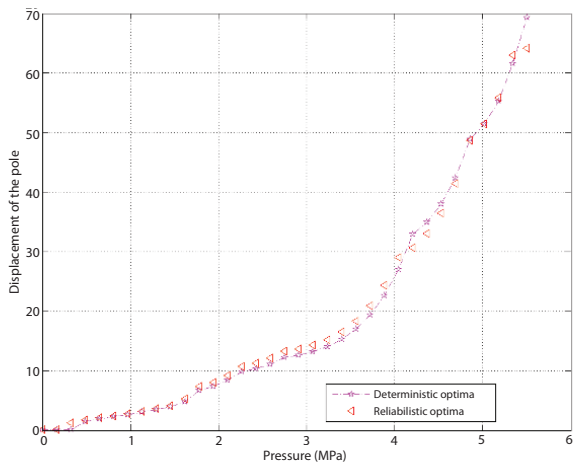

Figure 6.57. *Variation of the displacement from the axis according to the pressure*

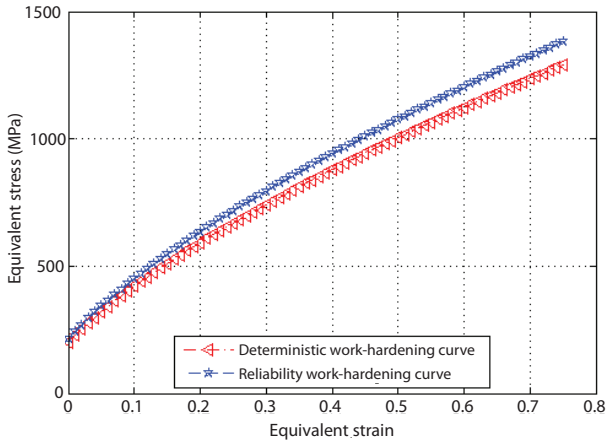

Figure 6.58. *Work-hardening curves obtained for the two optimal variables*

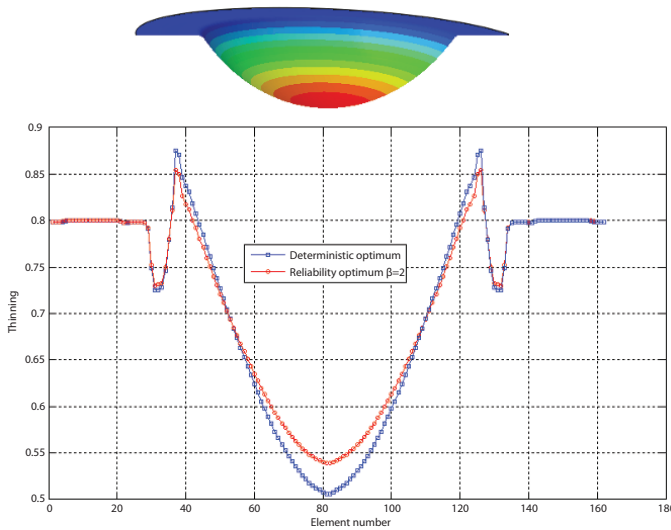

Figure 6.59. *Thickness variation depending on the axial position. For a color version of this figure, see www.iste.co.uk/radi/material.zip*

The practical aspects of the process consist of applying an internal pressure denoted by P and of applying a back pressure that actually represents the clamping force to prevent sheet metal wrinkling. This back pressure is set to 9 MPa and is assumed to be deterministic. This process remains sensitive to the fluctuations affecting the pressure and also to the variations of the material parameters. It is also sensitive to the geometrical parameters of the plate and notably its initial thickness. Taking these variabilities into account during the optimization phase can bring more robustness to the implementation of the process.

These parameters present fairly significant hazards and variations, which affect the stability of the process and create significant differences at the level of the final mechanical characteristics. These can also be at the origin of the rise of plastic instabilities. Controlling the process involves an adjustment of the variation levels of the different parameters that allows the reduction of the spatial and temporal variabilities at the level of the responses be global or local.

The dimensions of the plate are 30×30 mm with an initial thickness of 1 mm. The finite element model of the plate is given by Figure 6.60. The plate is meshed with $1,600$ S4R-type quadrangular elements and $1,608$ triangular elements of the S3R-type from the Abaqus/Explicit© library.

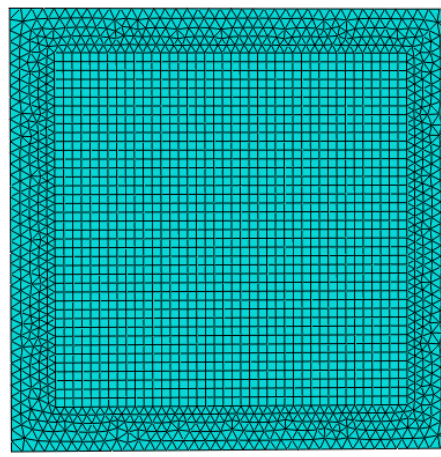

Figure 6.60. *Finite element model of the plate*

The hydroforming process for this plate consists of applying an internal pressure enabling the expansion of the workpiece. The boundary conditions of this problem involve fixing the edges of the plate and applying a back pressure

on the section meshed by triangular elements compelling the plate to remain fixed.

During the forming, an internal pressure is applied to the plate represented by its amplitude D. The localization of the strain is often concentrated at the level of the axis. The second optimization variable is the initial thickness of the plate, the necking phenomenon is directly related to the thickness. The pair (P, h) represents the optimization variables. The probabilistic characteristics of these parameters are summarized in Table 6.10. In addition, it is assumed that the material parameters are uncertain and follow normal distributions (see Table 6.11).

R. var.	Mean	Std. (%)	Distribution
P (MPa)	6	15	Normal
h (mm)	1	10	Normal

Table 6.10. *Probabilistic characteristics of the optimization variables*

Parameters	Mean	Std. (%)	Distribution
k (MPa)	988	5	Normal
n	0.182	5	Normal
σ_y (MPa)	200	5	Normal

Table 6.11. *Probabilistic characteristics of the uncertain parameters*

The objective function used for solving this problem involves a minimization of the variance of the equivalent plastic strain. For this type of problem, three deterministic stresses are defined. The first two make it possible to ensure that the final thinning does not exceed 20% and that the principal maximal stress does not exceed the Von Mises stress. The third is an equality stress to ensure that the amplitude at the axis be equal to 55 mm.

Solving the robust optimization problem requires a large number of evaluations of the objective function and stresses. This seems impractical because the numerical simulations require a significant computation time. Having recourse to metamodels is inevitable in order to solve the problem. The construction of these metamodels requires the selection of a numerical design of experiments and also the collection of the various responses. An experimental design based on Latin hypercubes is chosen with 50 computations by finite element. A quadratic polynomial model is used to represent the different responses given by equation [4.22].

The statistical analysis consists of estimating the determination coefficients for all of the models; it presents an acceptable level of accuracy allowing us to determine with accuracy the deterministic and robust optima.

For the deterministic case, the material parameters are defined by their average values given in Table 6.11. Therefore, the formulation of the deterministic optimization problem can be defined as follows:

$$\begin{cases} \min\ Var(\bar{\varepsilon}_{eq}) = f(x) \\ g_1(x) = \tilde{h}_{\min} - 0.8 \leq 0 \\ g_2(x) = \sigma_{\max} - \sigma_{\text{Von Mises}} \leq 0 \\ h(x) = \tilde{u}_{\max} - 55 \approx 0 \\ x = [P, h] \end{cases} \quad [6.10]$$

The SQP algorithm is used to solve this problem. In the deterministic case, the uncertain parameters are fixed to their mean values. The solution of the deterministic problem has converged toward the optimum given in Table 6.12 after 13 iterations.

P(MPa)	h(mm)
6.212	0.978

Table 6.12. *Deterministic optimal variables*

6.7.1. *Robust resolution of the optimization problem*

The formulation of a robust optimization problem resembles that of a optimization-based reliability problem, except that the objective function consists of minimizing either the variance or the mean of a mechanical quantity. Similarly to optimization-based reliability problems, the deterministic stresses are transformed into probabilistic stresses. The formulation of the robust optimization problem is written as follow:

$$\begin{cases} \min\ Var(\bar{\varepsilon}_{eq}) = f(\mu(x)) \\ P[G_1(\mu(x)) \leq 0] \leq P_{\text{admissible}} \\ P[G_2(\mu(x)) \leq 0] \leq P_{\text{admissible}} \\ h(\mu(x)) = \tilde{u}_{\max} - \tilde{u} \approx 0 \\ \mu(x) = [P, h] \end{cases} \quad [6.11]$$

The estimation of the reliability is carried out with Monte Carlo simulations based on metamodels. In reality, this approach is feasible for a

small number of probabilistic stresses. It presents convergence problems and memory problems when the number of probabilistic stresses increases. In this application, the admissible probability of failure, equal to 2.28%, is equivalent to a reliability index of $\beta = 2$. Table 6.13 recapitulates the best optimal values in the reliabilist case.

P(MPa)	h(mm)
7	1.1082

Table 6.13. *Deterministic optimal variables*

Figure 6.61 shows the variation of the objective function according to the number of iterations. Concerning the robust optimization, the objective function presents a more significant value than the deterministic case, which means that it moves away from the bounds and consequently that it is less sensitive than the deterministic optimum.

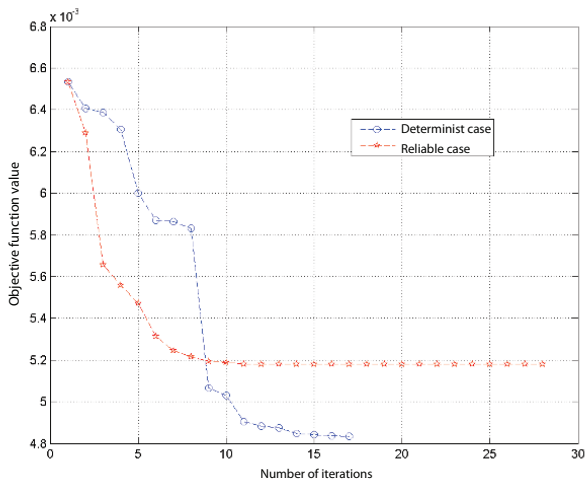

Figure 6.61. *Convergence of the objective function*

The distribution of the equivalent plastic strain for the deterministic case and the robust case is presented in Figures 6.62 and 6.63.

Table 6.14 summarizes the number of iterations, the number of evaluations of the objective function and its final value.

The adapted approach to solve the problem in a probabilistic manner strongly depends on the initial point. For some points, the problem does not

converge and for a more significant level of reliability, $\beta = 3$ for example, the algorithm does not converge.

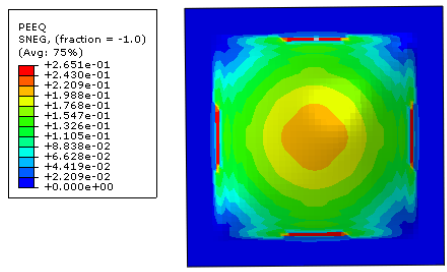

Figure 6.62. *Distribution of the equivalent plastic strain: deterministic case. For a color version of this figure, see www.iste.co.uk/radi/material.zip*

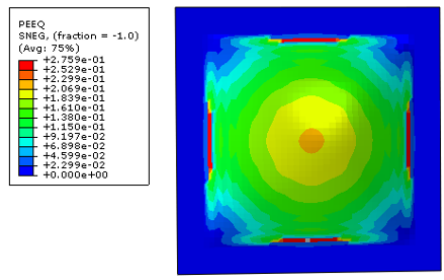

Figure 6.63. *Distribution of the equivalent plastic strain: reliability case. For a color version of this figure, see www.iste.co.uk/radi/material.zip*

	Iteration number	Evaluation of f_{obj}	Value of f_{obj}
Deterministic case	17	63	0.0048
Robust case	28	93	0.0052

Table 6.14. *Characteristic of the convergence*

6.8. Optimization of thin sheet metal

Optimization is the action of obtaining the preferable results during the design of the workpiece. In the application of the computer-aided design based optimization of the finite elements computational software program Abaqus©, several situations can give rise to numerical noise (wrinkling). When there is numerical noise in the design analysis loop, it will create many local artificial

minima. In this case, the minimization of the local thinning state in the sheet metal blank has been tested with a cost function of the optimization system that has been chosen to minimize the thinning rate by 20%:

$$f(t) = \sum_{i=1}^{n} \left\| \frac{t - t_0}{t_0} \right\|^2 \qquad [6.12]$$

In this case, a design variable significant for the formability of the blank during the hydroforming process and the design (D and d) and the stresses have been defined: $50 \leq D \leq 250$ mm and $20 \leq d \leq 100$ mm.

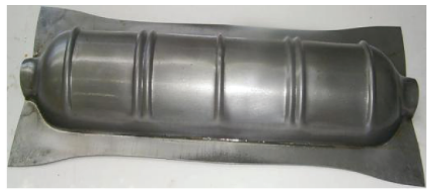

a) Experimental Tests

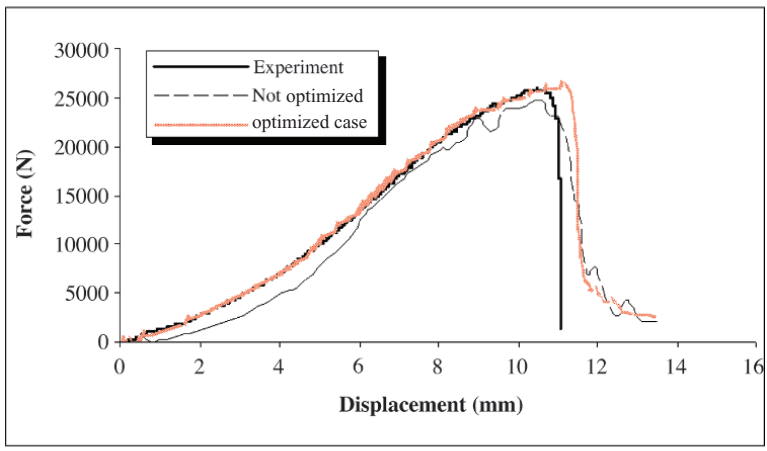

b) Counter-displacement force (optimized and non-optimized cases)

Figure 6.64. *Optimized and non-optimized case*

The final form is experimental as shown in Figure 6.64(a). The comparison of the force with respect to the maximal displacement with the

initial and optimized blank form is shown in Figure 6.64(b). Good agreement between the shape and the optimization of the experimental values. Figures 6.65(a) and (b) compare the first and the optimal blank shape. We achieve a reduction of the cost function (dilution ratio) from 50 to 20%, which is obtained without wrinkling (Figure 6.65(c) and (d)) [AYA 11].

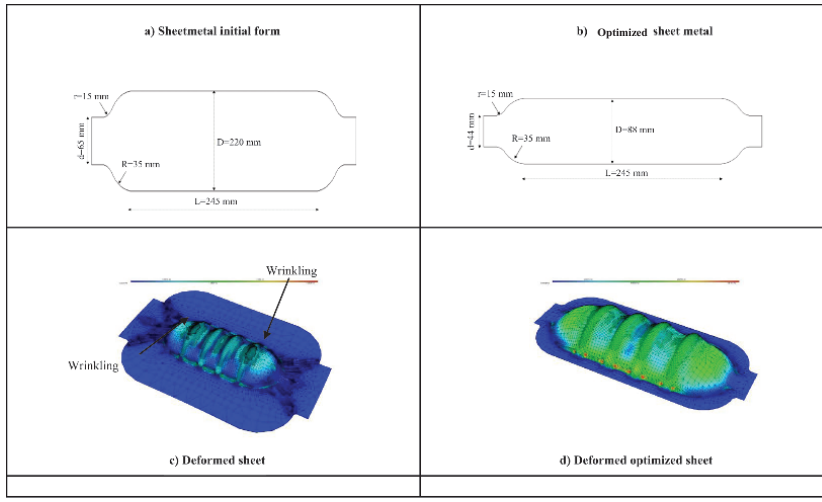

Figure 6.65. *Thin sheet before and after optimization*

7

Application of Metamodels to Hydroforming

7.1. Introduction

The conventional reliability methods (Monte Carlo, first-order reliability method, second-order reliability method, etc.) provide a means for estimating with good accuracy the level of reliability as soon as a probabilistic characterization of the uncertain parameters and the identification of the limit states are provided. The field of application of these methods is restricted when the problem presents nonlinearities (materials, geometric, etc.) and also in the case where the limit state function is implicitly defined according to uncertain parameters. These two problems are present in the case of forming, which makes it complex and requires a reflection on the methods that can be applied and that can evaluate in an accurate manner the probability of failure. For this type of problem, approximation techniques have often been used to replace the actual model by an approximated model or metamodel that allows the quick evaluation of the response. Several approximation techniques have been used for reliability problems, the most commonly used being the response surface method. Other techniques such as kriging or neural networks have also been successfully utilized.

This chapter presents an approach for accurately evaluating the failure probability in a hydroforming operation applied to the case of a simple tube. Some approaches have been proposed in the literature for the evaluation of reliability in sheet forming [BEN 14, ELH 12, KLE 02, RAD 07].

The approach consists of determining the probability of spatial failure for each element of the critical region. The latter is defined by identifying the

Material Forming Processes: Simulation, Drawing, Hydroforming and Additive Manufacturing, First Edition. Bouchaib Radi and Abdelkhalak El Hami.
© ISTE Ltd 2016. Published by ISTE Ltd and John Wiley & Sons, Inc.

critical element, then a path around this element is proposed that represents the most likely failure region. The identification of the critical element for each failure mode is achieved by plotting the deformation state on the material forming limit curve (FLC). The access to the probability of spatial failures can provide insight on the stability of the process and also enables the effective prediction of the area where the plastic instability can most likely appear.

The estimation of the failure's probability is based on a probabilistic characterization of the principal strains (major and minor) for each mode of failure and each element. Access to this likelihood of failures in a direct manner is impossible given the complexity of the problem and the huge number of necessary finite elements computations. To compensate for this problem, we can rely on Monte Carlo simulations coupled with response surfaces. The evaluation of the likelihood of failure allows us to have an idea about the stability of the process. This approach presents several advantages compared to the techniques found in the literature: it can be applied to any forming process, can be integrated with any finite element code and the calculation time remains within reasonable limits. It also provides access to the failure's probability since sometimes the localization of the plastic instability can be random in the region of the likely failure.

7.2. Sources of uncertainty in forming

Several parameters are involved in forming [RAD 07]. Often, these parameters are affected by uncertainties that may affect the stability of the process if they are not taken into account as early as the design phase. These fluctuations may originate from material parameters, from geometric parameters and also the parameters related to the process as the loads, the contact and friction problems [BAB 00, ELH 08, RAD 98]. Other types of variability may also exist; they are relative to the environment such as temperature and humidity, and also the errors induced by the operator.

Several studies have highlighted the random character of a forming operation. According to [COL 03], these uncertainties may originate from the variabilities associated with the material, the roughness of the surface and the initial thickness of the sheet. They can also originate from the tools likely to undergo geometric changes due to wear phenomena, and changes in mechanical properties and in the variation of the temperature. All these phenomena affect the final quality of the workpiece, not to mention the changes that may affect the loads, such as the blank-holder force or the progress of the punch as well as the applied pressure. Lubrication also plays a

significant part in metal forming. This phenomenon is difficult to control; as a matter of fact, the lubrication conditions may change in a global or local manner because of the roughness of the surface or of the distribution of temperature. For this reason, taking these condition into account and modeling them are often addressed in a comprehensive manner at the scale of the structure. Other types of variability may also exist such as an incorrect setting of the machine or an incorrect positioning of the workpiece or the tools.

Some authors have carried out real tests to quantify the level of variation in certain parameters. In [KAR 02], more than 45 samples of the same material have been taken and show that the variability at the level of strain-hardening coefficient has reached 14%. This can greatly affect the final thinning rate, and also the final springback, after forming. It is shown that in a forming operation, there are 12 parameters for which the process can present high sensitivity [GAN 02]. These parameters include the strain-hardening coefficients, the flow stress, the anisotropy coefficients, the initial thickness of the blank and the friction coefficients. In [CAO 03], it is shown that during a bending operation, the strain-hardening modulus k can vary by more than 20%. This is a variation of 16% for the strain-hardening coefficient n and reaches up to 65% in the case of the friction coefficient. In a single manufacturing process (that is the same forming die and the same modeling parameter), the rate of change in the geometric properties from one piece to the other can reach 21% [MAJ 03]. This is especially manifested in the case of complex parts and thin plates.

Taking into account the random aspects or the spatial variability of the parameters, we are able to better give an opinion on the probability of failure of the process and its stability. A probability study of the process can be used to validate the input parameters and obtain an idea about its stability. In general, a forming process is considered stable when, even in the presence of the different fluctuations, the variance remains low at the level of the final characteristics of the piece, either, for example, on the distribution of the final thickness, the damage rate or even on the final form of the piece. Some consider the forming process as stable when the rate of faulty parts does not exceed 1%.

7.3. Failure criteria

Various defects can appear during the forming of tubes or plates. The prediction of these defects requires the implementation of adequate criteria for each plastic unstability. Despite the progress made at the level of software

for the computation of finite elements, the process remains poorly controlled due to the instabilities that can emerge. The majority of the current codes for finite elements do not integrate adequate criteria to faithfully detect or predict the occurrence of these types of instabilities. The success of a forming operation by hydroforming requires the implementation of the appropriate criteria allowing the detection of these plastic instabilities. This makes it possible to react and correct the loading trajectory either by an increase or by a decrease in pressure or in the axial displacement. The two following sections illustrate the main criteria employed for the detection of these modes of failures in the case of tubes and plates.

7.3.1. *Failure criteria for necking*

Some works have focused on the prediction of necking in the case of hydroforming based on the criteria used for plates. This seems unreliable because deformation modes or stresses are not the same. In [BOU 06], the Swift criterion, used in the case of sheets, is adapted in order to make it usable in the case of tubes. The prediction of the location of thinning can be carried out with several techniques. Among these criteria and as an example, Considère's or Swift's can be distinguished. Some have used the FLC in the strains or the stresses space to detect the location. Particular attention is given to the FLCs. Besides the methods previously presented, other approaches based on damage mechanics [CHE 02] or fracture mechanics have also been used in the literature.

7.3.2. *Failure criteria for wrinkling*

Several criteria have been developed in the literature allowing the detection of wrinkling. There are mainly geometric criteria, energy criteria and criteria based on the bifurcation theory. The estimation of stresses in the bifurcation theory involves boundary conditions as well as imposed displacements that may induce wrinkling. This type of criterion presents some limitations due to its complexity at the formulation level and also sometimes requires access to the source code.

Several authors [CAO 03, THO 99, SHE 04, JIR 04] have successfully made use of geometric criteria in detecting wrinkling in the case of stamping or hydroforming of tube and blanks. Concerning the geometric criteria, the evaluation of wrinkling is measured by comparing the present state of the workpiece with respect to the position of the supposedly rigid tools. The geometric criteria are often used because of their simplicity at the formulation

level and also in the implementation that is based on the measurement of ripple with respect to the reference level of the metal sheet. Several works cited in the literature impose in their optimization problems that the difference in terms of strain does not undergo an abrupt change, because this is synonymous with the presence of wrinkling. Other criteria that are based on energy approaches are used in the literature, the major drawback of these criteria is the complexity in their formulation and their implementation.

The FLC also allows detection if there is or no wrinkling in the plate. By superimposing the levels of the principal strains at the end of the process on the FLC, the presence of the strains under the pure shear line (in the plane of the principal strains) is representative of a significant tendency for wrinkling or thickening in the forming process. Several authors have used this criteria in their optimization problems.

7.4. Evaluation strategy of the probability of failure

The estimation of the probability of failure of the hydroforming process remains a difficult task. In effect, the problem presents several types of nonlinearities, a large number of uncertain parameters, no explicit limit states and also a prohibitive computational time associated with finite element computations. All these elements sum up and delegate the estimation of the probability of failures as a difficult task to solve with conventional reliability methods. To overcome this problem, a strategy is implemented allowing the estimation of precision of the likelihood of failures. The example studied in this chapter focuses on the hydroforming of a tube with a simple geometrical shape. This approach has been presented by Ben Abdessalem and El Hami [BEN 15] for the evaluation of the probability of failures in a tube.

The estimation of the probability of failures requires the identification of uncertain parameters and their probabilistic characteristics, which describe their variations (statistical moments, probability density, etc.) and also a failure criterion. In this work, we make use of the FLC of the provided material in the space of the principal strains. By using the FLC, we have been able to identify the critical regions for each failure mode, namely necking and wrinkling, based on the critical element. This approach consists of subsequently determining the probability densities of the main critical strains associated with each mode of failure and for each element. The quantification of uncertainties in the main strains subsequently allows us to easily access the probability of failure with Monte Carlo simulations. The accuracy of the

result depends strongly on the analysis of the metamodels and their ability to accurately predict the responses. Statistical analyses are made to validate all these metamodels.

The advantage of this approach lies in its accessibility, its simplicity of implementation and also in its application that can be generalized to any forming operation. In addition, the routine can be implemented independently of the finite element code. The choice of this approach will facilitate the problem and presents an effective tool for the evaluation of the reliability of the process.

This strategy is summarized through the following steps:

– identification and selection of the uncertainty parameters;

– identification of the critical elements for potential failure modes through deterministic calculations;

– definition of the size of the region;

– parsing of the search space and choice of the numerical experience plan;

– evaluation of the output indicators or failure criteria;

– construction of the local approximations;

– evaluation of the robustness of the metamodels and their accuracy;

– evaluation of the probability of failure.

7.4.1. *Finite element model and choice of uncertainty parameters*

The geometric model as well as the dimensions of the tube are given by Figures 7.1 and 7.2. This model is composed of a matrix presenting the desired final shape, a punch that allows adding material to the expanded area and a tube with the initial thickness of 1.5 mm.

The die and the punch are modeled by rigid bodies and are meshed with R3D4-type elements. The tube is modeled by a deformable body meshed with shell elements of the S4R-type with five integration points in the thickness. With regard to the symmetry of the problem, a quarter of the model is studied. The tube is meshed with $2,480$ elements. The Abaqus finite element code is used with the aim of carrying the full numerical simulations. The dimensions of the die and the tube are given in Table 7.1.

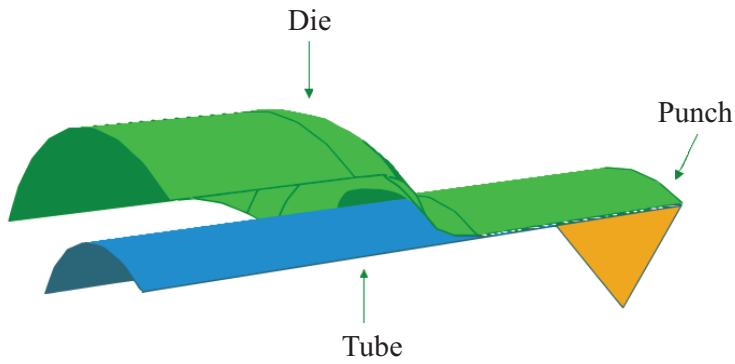

Figure 7.1. *Finite elements model*

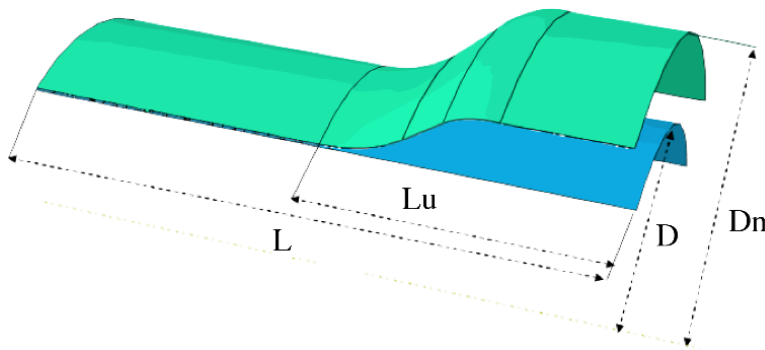

Figure 7.2. *Tube and die dimensions*

L	Lu	D	Dm
80 mm	35 mm	20 mm	33 mm

Table 7.1. *Tube and die dimensions*

During a forming operation, several parameters become involved. Most of these parameters have an uncertain character. In this chapter, we will only address the parameters that relate to the properties of materials, the loads and

the friction coefficient between the die and the tube. The material is modeled by a Swift law given by the following expression:

$$\sigma = k \times (\epsilon + \epsilon_0)^n \qquad [7.1]$$

The strain-hardening parameters (k, n) are considered as being random. They are obtained from a free bulging test [BEN 05]. It is assumed that these parameters present a variation coefficient of 10% and that they follow normal laws. The probabilistic characteristics of these parameters are given in Table 7.2.

Random variable	Mean	Std. (%)	Distribution type
k(MPa)	494	10	Normal
n	0.234	10	Normal

Table 7.2. *Probabilistic characteristics of the hardening parameters*

The other material parameters of DC04 steel are given in Table 7.3. Young's modulus, Poisson's ratio and the density are considered to be deterministic.

Material	E(MPa)	ν	ρ(kg/m^3)
DC04	$210,000$	0.3	$7,800$

Table 7.3. *Material parameters for DC04 steel*

Regarding the geometric parameters, we only consider the initial thickness of the tube, assumed to be uncertain. The contact and friction problem also play a significant role in the implementation of hydroforming. In this study, the friction is modeled by a Coulomb's law. The latter depends strongly on temperature as well as on the contact pressure and its variability must be taken into account.

Table 7.4 includes all of these parameters with their means, their variation coefficients as well as their respective probabilistic laws. Tube hydroforming involves in general two types of loads: an internal pressure and an axial displacement. Several studies have shown the sensitivity of the method with regard to load parameters. A variation of these parameters can affect the stability of the process and cause some plastic instabilities to appear. Taking these variabilities into account enables us to better evaluate the reliability of the process.

Random variable	Average value	Var. coef. (%)	Distribution type
h (mm)	1.5	8	Normal
μ	0.1	15	Normal

Table 7.4. *Probabilistic characteristics of the thickness and the friction coefficient*

The load trajectory giving the axial displacement according to time is modeled by a linear line (Figure 7.3). The variation on the axial displacement is taken into account through the amplitude D. The load trajectory giving the variation of the internal pressure according to time is modeled by three points P_1, P_2 and P_3. The uncertainty in the loading trajectory is taken into account by considering these three parameters as uncertain.

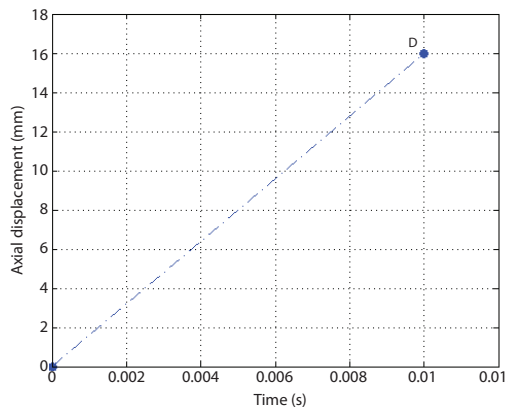

Figure 7.3. *Loading trajectory: displacement (mm) - time (s)*

The probabilistic characteristics of these parameters are summarized in Table 7.5.

Random variable	Average value	Var. coef. (%)	Distribution type
D	16	10	Normal
P_1	10	10	Normal
P_2	20	10	Normal
P_3	35	10	Normal

Table 7.5. *Probabilistic characteristics of the loading parameters*

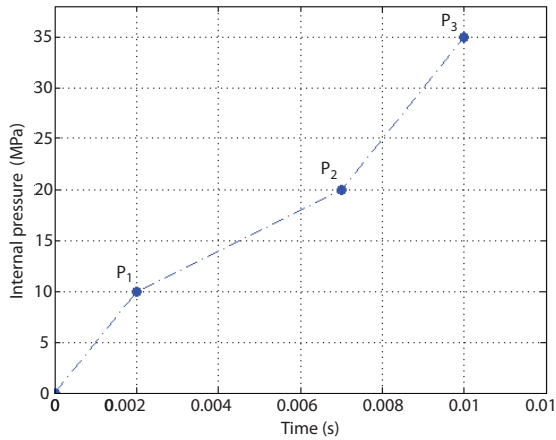

Figure 7.4. *Loading trajectory: pressure (MPa) - time (s)*

7.4.2. *Identification of failure modes and definition of boundary states*

Two types of plastic instabilities are likely to occur in a tube hydroforming operation. An excessive displacement can cause tube wrinkling, whereas a significant pressure may cause the tube to burst. In order for a workpiece to be obtained without defects, these parameters have to be controlled. The evaluation and the control of these instabilities require the implementation of adequate criteria allowing their prediction and evaluation.

The FLC (strain) in the main strain plane is chosen as the failure criterion for the evaluation of the likelihood of failures for both failure modes. The choice of the FLC is also justified by its simplicity and its generalization regardless of the method and the type of stress with regard to other criteria that require additional development. Although it can be argued, its usage is very widespread in industrial circles and even in research works as a criterion allowing for the control of forming operations and especially in hydroforming.

In reality, despite its recurring utilization in the optimization and the development of certain forming processes, this curve mainly presents two major drawbacks: the first is its dependence with regard to the trajectories of the strains. In effect, it is effective for proportional trajectories, which is not

the case in forming where there are several types of nonlinearities (material and geometric nonlinearities). The second disadvantage originates from the nature of the FLC, this curve is determined experimentally, which justifies its uncertain character. In our study, the variability that the FLC may present is taken into consideration assuming that it follows a probability distribution.

In the forming limit diagram (FLD), two curves or limit state functions are defined: the first represents the limit curve of the necking and the second the wrinkling limit curve (see Figure 7.5).

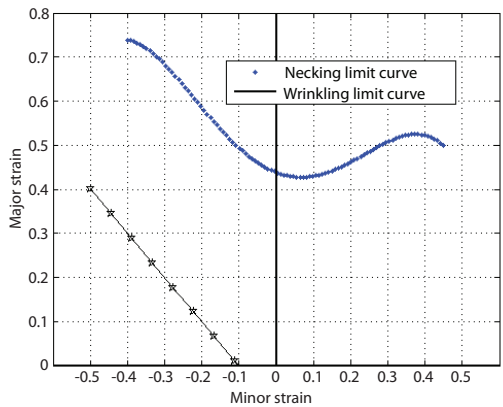

Figure 7.5. *Failure criteria: forming limit curves*

7.4.3. *Identification of elements and critical areas*

The estimation of the probability of failure requires in reality the estimation of the probability of failure for each structure element. For complex problems such as forming this seems impractical and requires enormous computation resources. In order to overcome this problem, we propose an approach that is based on the most critical element of the structure when all the parameters are set to their nominal values.

The identification of the critical element allows us to subsequently define a critical region around this element and represents a localization area where the principal strains can reach critical values. Subsequently, this region presents a significant risk of potential failure that means that the probability of failure reaches its maximal values in this area. This technique allows a drastic simplification of the problem by focusing only on the critical area and at the

same time makes it possible to get an idea about the spatial distribution of the probability of failure.

By plotting the strains state predicted at the end of the simulation on the FLC (Figure 7.6), we can identify the critical elements that are the nearest with respect to these limit curves for each failure mode. The main major and minor strains are shown in Figures 7.7 and 7.9, respectively.

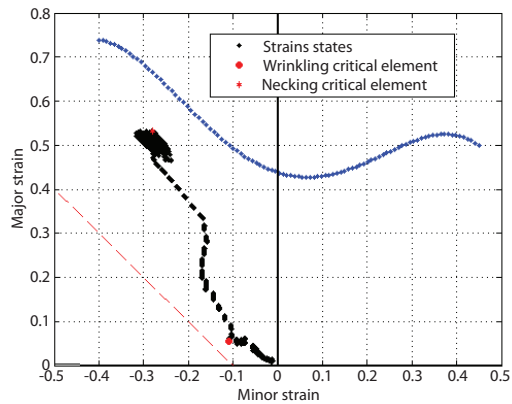

Figure 7.6. *Identification of the critical elements*

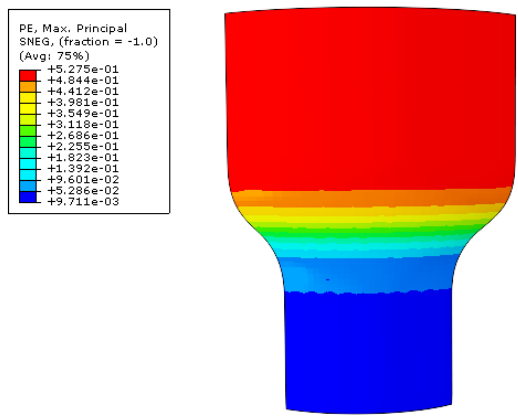

Figure 7.7. *Distribution of the main major strain. For a color version of this figure, see www.iste.co.uk/radi/material.zip*

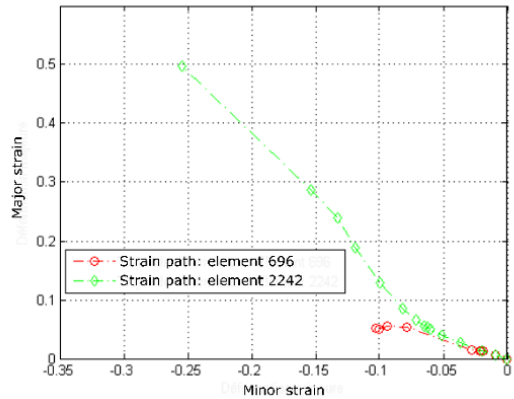

Figure 7.8. *Strain trajectory of the critical elements. For a color version of this figure, see www.iste.co.uk/radi/material.zip*

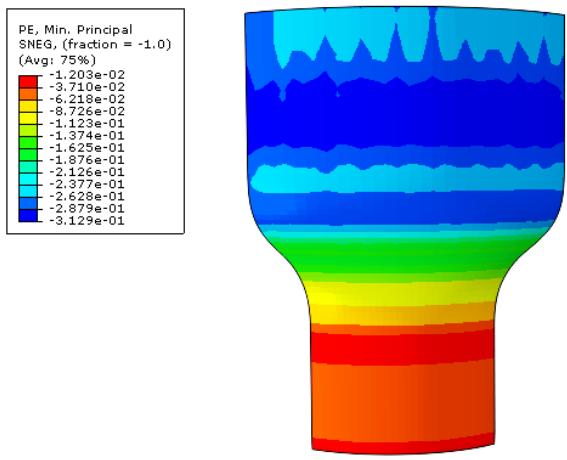

Figure 7.9. *Distribution of the main minor strain*

Figure 7.10 shows the location of these two elements on the structure. The wrinkling is located at the level of the element 696, whereas the necking is localized at the level of the element $2,242$. The critical region where the probability of failure is maximal is defined by all of the elements that surround the critical element for each failure mode. The extent of this area covers the 25 elements, closest to the critical element. The designer has to

make this choice. The spatial determination of the failure probability around the critical element is a more rational criterion for the evaluation of the failure probability in forming and allows us to have an idea on the level of reliability in a local manner.

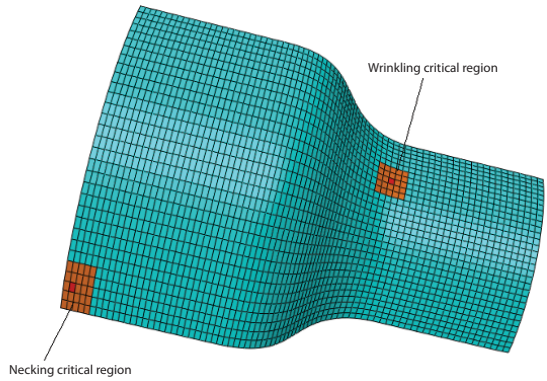

Figure 7.10. *Location of the critical elements*

The strain trajectories of the critical elements are represented in Figure 7.8. The proposed approach is based on the probabilistic characterization of the major and minor critical strains for necking and wrinkling in order to access the probability of failure. These critical elements are characterized by their major strains and their minor strains denoted by $(\varepsilon_1^s, \varepsilon_2^s)$ for necking and $(\varepsilon_1^w, \varepsilon_2^w)$ for wrinkling.

By superimposing the minor and the major strains of each element on the FLC, it can be seen that the strains are on the left side of the FLC. Thus, these two limit curves will be modeled by first-order linear equations. Analytically, the limit state functions are expressed according to the critical strains and are given by the following equations:

$$\begin{cases} G_w &= \varepsilon_1^w + \varepsilon_2^w - s \\ G_s &= G_1^s + \alpha\varepsilon_2^s - \gamma \end{cases} \qquad [7.2]$$

where $\varepsilon_1^w, \varepsilon_2^w$, respectively, represent the main major strain and minor wrinkling; $(\epsilon_1^s, \epsilon_2^s)$, respectively, represent the main major and minor strain of the necking; γ is the value at the origin of the necking FLC; α is the slope of the limit curve of necking and s is the factor of safety for the wrinkling curve boundary.

The variability related to the FLC is taken into account by means of the parameter α. It is assumed that this parameter follows a normal distribution whose statistical parameters are given in Table 7.6.

Random variable	Average value	Var. coef. (%)	Distribution type
α	0.8241	10	Normal

Table 7.6. *Variabilities associated with the FLC*

In the case in which it is assumed that the parameter α randomly varies, the impact of these fluctuations on the position and on the shape of the FLC with respect to the reference FLC can be observed in Figure 7.11, hence the interest in introducing a term that takes this variability into account.

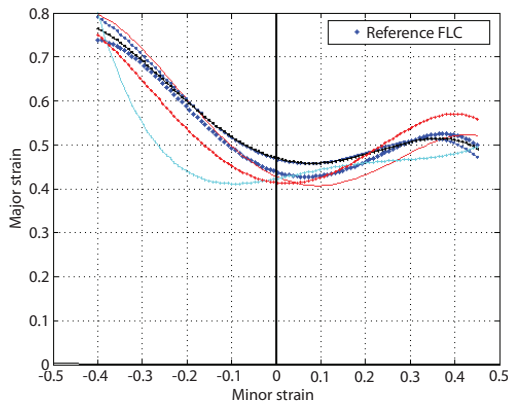

Figure 7.11. *Effect of the uncertainties on the FLC*

7.5. Critical strains probabilistic characterization

The probabilistic characterization of the principal major and minor strains allows us to decide about the probability of failure, taking into account the previously defined limit states. The objective of the next step is to determine the probability distributions that these strains can follow. At the basis of these probabilistic characteristics, the access to the probability of failures becomes direct when using Monte Carlo simulations.

7.5.1. *Choice of numerical experimental design*

Acknowledging the large number of uncertain parameters, the choice of adequate experimental design requires an in-depth study allowing for the choice of a plan that allows an optimal distribution of the different achievements in the variation space. The Latin hypercube planes seem to be very effective in the case where multiple parameters are involved. Three properties are often desirable during the construction of a Latin hypercube plane: the space must be filled up that amounts to covering the maximum definition space, the second points consists of securing the independence of the factors, and the last point consists of ensuring an uniform distribution of the different points. In the end, the choice of an optimal plan is tantamount to solving an optimization problem following a criterion that has to be minimized or maximized. The approach adapted in this study consists of generating several Latin hypercube planes and choosing the best according to the chosen optimality criterion defined by the first point. For this type of plane, the number of achievements is set to 100. After $5,000$ iterations, the algorithm converges to the experimental design given in Figure 7.12.

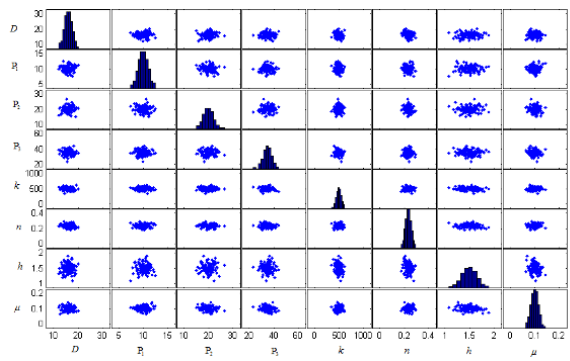

Figure 7.12. *Variation levels of the uncertain parameters*

7.5.2. *Construction of metamodels*

The choice of the model is a crucial step for modeling the responses, especially for strongly nonlinear problems. This step requires additional investigations in order to determine the model that can predict the responses with an acceptable confidence level. Keeping in mind the nonlinearities associated with this problem, we opt for a quadratic polynomial giving the

responses according to the uncertainty parameters. This model is given by equation [7.3]:

$$y = \beta + \sum_{i=1}^{n} \beta_i x_i + \sum_{i=1, j \geq 1}^{n} \beta_{ij} x_i x_j + \varepsilon \qquad [7.3]$$

where y represents the principal critical strains, β is the model coefficient, n is the number of parameters, ε is the error associated with the model and x is the parameters of the model [ELH 15].

7.5.3. *Validation and statistical analysis of metamodels*

In this section, we strive to ensure the robustness of metamodels by means of statistical indicators, which enable the evaluation of the robustness of these approximations. This step is crucial because the accuracy of the probability of failure depends on the accuracy of the metamodels and on their ability to faithfully predict the level of responses. The first test consists of pointing out the trend of the exact values calculated by finite element and the predicted values. This allows us to accept or reject the metamodels. In the event that the latter fails to be accurate, a first alternative is to increase the number of points in the variation space. This proposal does not guarantee the best prediction, but minimizes the error. An analysis of variance is made from all of the predicted metamodels. This makes the robustness of these approximations meet the expectations to predict with an acceptable level of confidence the level of the critical strains.

7.5.4. *Fitting of distributions*

The fitting of the distributions is a rather delicate stage in the probabilistic approaches, especially in the case of low failure probabilities. The objective behind this step is to approximate the usual probability distributions (normal, lognormal, Weibull, etc.) to all of the principal strains by specifying their statistical moments (mean, standard deviation, etc.). Figures 7.13–7.16 represent the histograms of the critical wrinkling and necking strains. Here, we will just detail the fitting step solely for two critical elements. The same approach is applied to all of the elements. According to the obtained histograms, it should be noted that even if the initially defined uncertainty parameters follow normal distributions, the outputs involving the principal strains are all of probability densities differing from these input distributions; this is due to the nonlinearity of the problem.

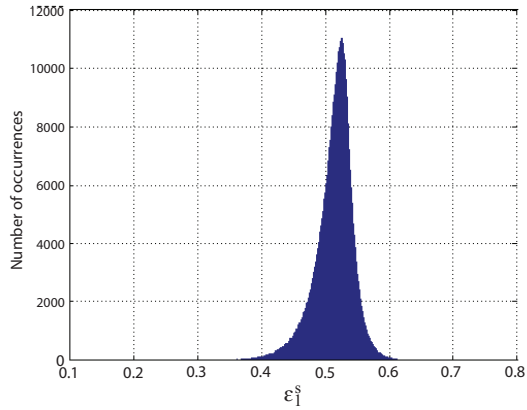

Figure 7.13. *Histogram of the major necking strain*

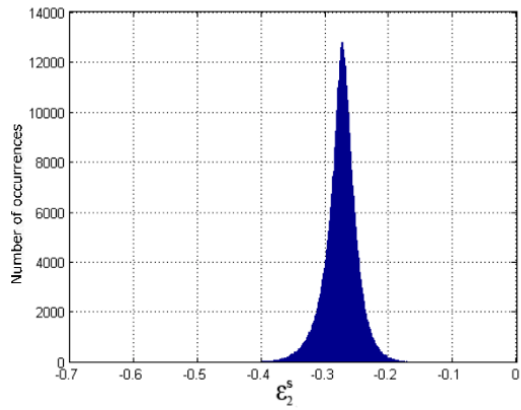

Figure 7.14. *Histogram of the minor necking strain*

Based on these histograms, the first thing to do is a visual comparison with the usual probability laws. This must be subsequently confirmed by statistical tools. The main methods that make it possible to test whether a probability density correctly describes the data set include the chi-square test, the Kolmogorov–Smirnoff (K–S) test and the estimation of the maximum likelihood. The estimation of low probabilities of failures requires a proper fit

of the probability densities, mainly at the level of the distribution tails in order to make a rather accurate opinion on the probability of failure.

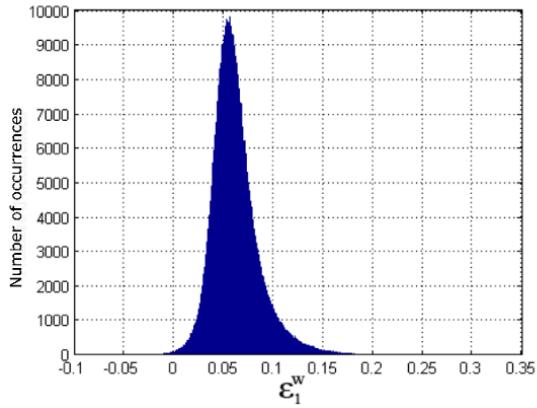

Figure 7.15. *Histogram of the major wrinkling strain*

7.5.4.1. *Distribution fitting of the major necking strain*

A maximum likelihood test shows that the major necking strain can be adequately approximated by a Weibull distribution generally characterized by three parameters. In our case, this distribution is characterized by two parameters (k, λ). The first term is a shape parameter and the second is a scale parameter. The probability density as well as the distribution function are given by equations [7.4] and [7.5]:

$$f(x,k,\lambda) = \frac{k}{\lambda}\frac{x}{\lambda}\exp\left(-\frac{x^k}{\lambda}\right) \qquad [7.4]$$

$$F(x,k,\lambda) = 1 - \exp\left(-\frac{x^k}{\lambda}\right) \qquad [7.5]$$

An estimation of the parameters (k, λ) by maximum likelihood is made. Figure 7.17, giving the probability density, shows that a Weibull distribution with these parameters properly describes the major necking strain. The parameters of this distribution are given in Table 7.7.

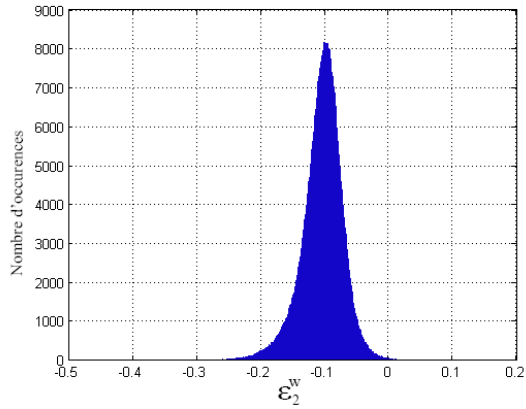

Figure 7.16. *Histogram of the minor wrinkling strain*

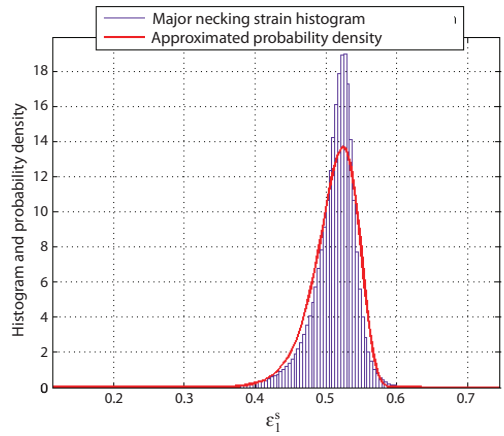

Figure 7.17. *Histogram and probability density of the major necking strain*

Distribution type	k	λ
Weibull	0.5255	18.2584

Table 7.7. *Weibull distribution parameters*

Distribution type	μ	σ	ν
Student	-0.274294	0.0038	4.01315

Table 7.8. *Student's distribution parameters*

7.5.4.2. *Distribution fitting of the minor necking strain*

A maximum likelihood test proves that the minor necking strains originate from a Student's distribution. This distribution is characterized by three parameters: a localization parameter where the distribution is centered, a scaling parameter and a forming parameter. The values of these parameters are shown in Table 7.9.

Figure 7.18 shows that a Student's distribution with the parameters given above correctly describes the data obtained by the Monte Carlo simulations.

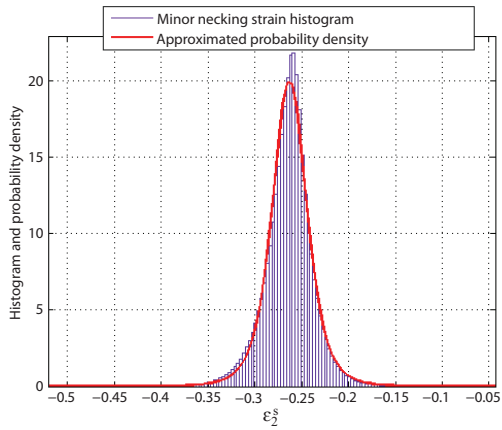

Figure 7.18. *Histogram and probability density of the minor necking strain*

7.5.4.3. *Distribution fitting of the major wrinkling strain*

Statistical analyses have showed that the major wrinkling strain follows a three-parameter gamma distribution. This distribution is tested for two and three parameters; the probability density with three parameters better approximates the strains histogram. The parameters characterizing this distribution are given in Table 7.9. The histogram and the probability density of the major wrinkling strain are represented in Figure 7.19. It should be

noted that this distribution allows an acceptable approximation when comparing with the data obtained by Monte Carlo simulations, especially at the level of the distribution tails.

Distribution type	a	b	c
Gamma	40.1444	0.0038	−0.0904

Table 7.9. *Gamma distribution parameters*

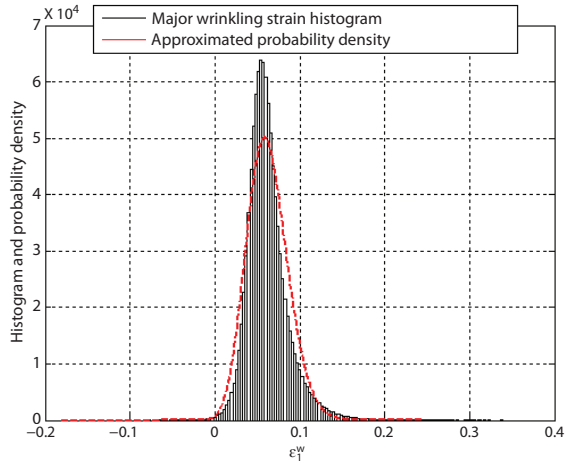

Figure 7.19. *Histogram and probability density of the major wrinkling strain*

7.5.4.4. *Distribution fitting of the minor wrinkling strain*

Based on the histogram drawn for these strains, the first two moments of the distribution are estimated by the likelihood method. An approximation with a Gumbel distribution properly describes the data obtained with Monte Carlo simulations based on the metamodel. The characteristics of the Gumbel distribution are provided in Table 7.10. These parameters (a, b), respectively, represent the scaling parameter and shape parameter.

Distribution type	a	b
Gumbel	−0.089	0.0321

Table 7.10. *Gumbel distribution parameters*

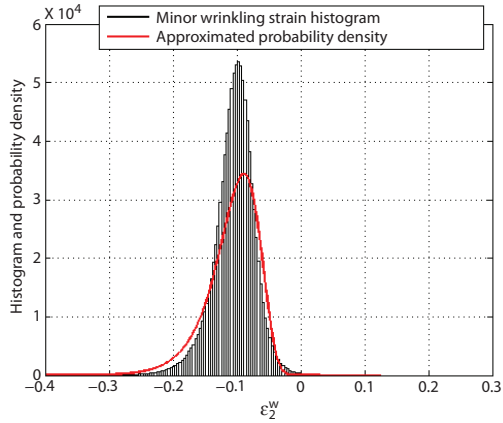

Figure 7.20. *Histogram and probability density distribution of the minor wrinkling strain*

7.6. Necking and wrinkling probabilistic study

The limit state function that separates the failure region from the safety region is given by the following equation:

$$G(\varepsilon_2^s, \varepsilon_1^s) = \varepsilon_1^s + \alpha \times \varepsilon_2^s - \gamma \qquad [7.6]$$

where ε_1^s is the major necking strain, ε_1^s is the minor necking strain, α is the slope of the necking limit curve and γ is the value at the origin of the necking limit curve.

The estimation of the probability of failure is actually tantamount to numerically estimating the integral given by equation [7.7]. This is now possible since the principal strains are characterized with probability distributions:

$$P_f(G > 0) = P_f(\varepsilon_1^c + \alpha\varepsilon_1^c > \gamma) = 1 - P_f(\varepsilon_1^c + \alpha\varepsilon_1^c \leq 0) \qquad [7.7]$$

the major and minor strains being characterized in a probabilistic manner. It is now possible to determine the failure probability of necking and wrinkling in a direct manner. It is assumed that the principal strains are statistically independent.

The limit state function that separates the failure region from the eligible or feasibility region is given by equation [7.6]. Monte Carlo simulations have allowed us to determine the probability density of the first limit state function. The probability density actually seems to follow a Student's distribution whose parameters are summarized in Table 7.11.

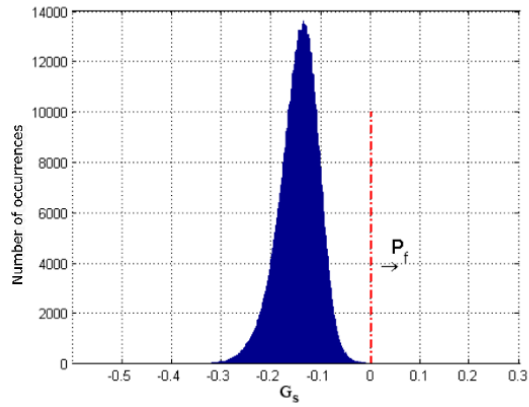

Figure 7.21. *Limit state function: necking*

Distribution type	Mean μ	Standard deviation σ	ν
Student	-0.143291	0.03554	8.16939

Table 7.11. *Probabilistic characteristics of the first limit state function*

Access to the probability of failure now becomes direct. Firstly, it is considered that the FLC is deterministic, which is not true. Also, we often define, both in the industry and in works published in the literature, a safety region that consists of offsetting the FLC with respect to its reference position. Known as the FLD, this curve is most of the positioned from 5 to 10% with respect to the reference curve. Then, it is assumed that the FLC varies according to a normal distribution that can give us an idea about the variation of this probability in the case where the location and the shape of the FLC are affected.

Based on the results in Table 7.12, a clear difference can be observed in the failure probabilities for each case. If these probabilities are translated in terms of numbers of faulty workpieces in a production cycle, this gives us a rate of $1,000$ pieces: 0.849 pieces for the deterministic case, 1.7 workpieces for a FLC offset by 5%, 4.2 defective pieces for a FLC offset by 10% and 0.961

pieces in the case where the FLC follows a normal distribution. The definition of a safety margin does not rely on any basis and is not justified.

Failure mode: necking	P_f	β
Deterministic FLC	8.49×10^{-4}	3.1388
FLC ($s = 5\%$)	0.0017	2.9329
FLC ($s = 10\%$)	0.0042	2.6387
FLC (random)	9.61×10^{-4}	3.1023

Table 7.12. *Probability of failure and associated reliability index*

It can be observed that the difference in the failure probability between the deterministic case and the case where the FLC is random is only of 1.16%. We can conclude that the definition of the FLDs does not actually make it possible to affect the probability of failure and that minimizing the extent of the eligible formability area has no reliabilistic meaning. With this approach, it has been possible to decide on the reliability of the process, but also on the reliability of the reference FLC to ensure an acceptable reliability level, which allows us to improve the admissible or feasibility area. Figure 7.22 presents the distribution of the principal strains generated according to their probability distributions in the case where the limit curve is considered deterministic.

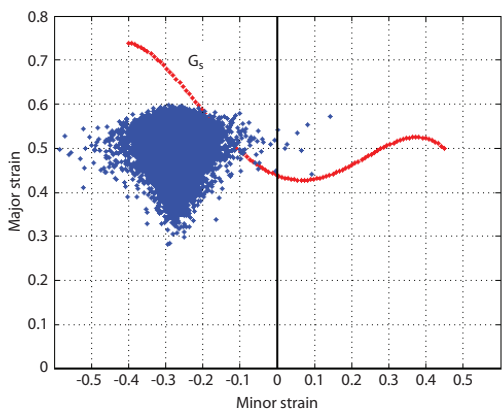

Figure 7.22. *Minor wrinkling strain*

The estimation of the wrinkling probability of failures is based on the wrinkling-limit curve offset from the pure shear curve [BEN 14]. This latter is analytically expressed according to the following equation:

$$G(\varepsilon_2^w, \varepsilon_1^w) = \varepsilon_1^w + \tan(45 + \theta) \times \varepsilon_2^w - \zeta \quad [7.8]$$

where ε_1^w is the major wrinkling strain, ε_2^w is the minor wrinkling strain, θ is the angle of inclination with respect to the limit wrinkling curve and ζ is the safety factor.

In the case where θ is zero, this equation is reduced to:

$$G(\varepsilon_2^w, \varepsilon_1^w) = \varepsilon_1^w + \varepsilon_2^w - \zeta \quad [7.9]$$

Based on the probabilistic characteristics of the previously determined main strains, we can plot the probability density of this limit state. The probability of failure is also calculated for certain values of the angle θ. In fact, the angle θ is to be determined by the user, its value is defined on the basis of the level of quality desired by the end user. This can be reflected by the quality of the surface. The more θ increases, the better the quality of the final piecework becomes and the less ripples can be seen on the membrane.

The reliability levels for a number of values of θ are given in Table 7.13.

Failure mode: wrinkling	P_f	β
$\theta = 0$	0.0012	3.029
$\theta = 5$	0.0060	2.5152
$\theta = 10$	0.0272	1.9233

Table 7.13. *Probability of failure and reliability index*

7.7. Effects of the correlations on the probability of failure

In this section, we are studying the case where it is assumed that the principal critical necking and wrinkling strains are correlated. Table 7.14 presents the evolution of the probability of failure for various values of the correlation coefficient. Based on these results, we note that the correlation coefficient considerably affects the probability of failures, which increases correlation coefficient between the principal strains.

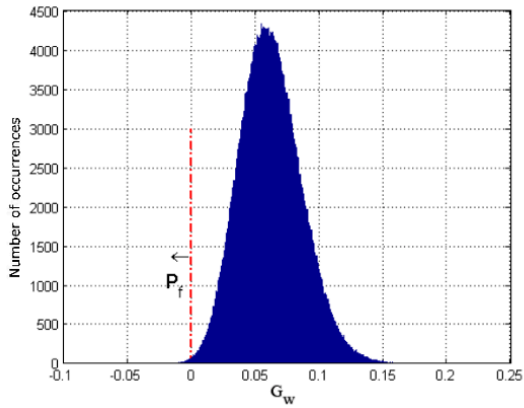

Figure 7.23. *Limit state function: wrinkling*

Correlation coefficient	P_f	β
$\rho = 0$	8.49×10^{-4}	3.1388
$\rho = 0.2$	1.4×10^{-3}	2.9859
$\rho = 0.4$	2.1×10^{-3}	2.8558
$\rho = 0.6$	3.1×10^{-3}	2.7415
$\rho = 0.8$	4.2×10^{-3}	2.6325
$\rho = 1$	6.2×10^{-3}	2.5018

Table 7.14. *Effect of a correlation between the strains on the probability of failure of necking*

Similarly for wrinkling, the correlation coefficient is varied between the principal strains and the probabilities of failure are reevaluated. Table 7.15 summarizes the evolution of the probability of failures.

7.7.1. *Spatial estimation of the probability of failures*

In this section, we are interested in the spatial variation of the probability of failure for the two modes of failure. In effect, due to the uncertainties that may affect certain parameters, the localization of the strain or the stress may change from one element to another. This is confirmed by visualizing the variation of the reliability index in all the elements. Figures 7.24 and 7.25 correctly show that the reliability index randomly varies for both failure modes. This variation

is more significant in wrinkling than in necking. This can be explained by the fact that the wrinkling phenomenon is more sensitive to variations that may affect the course of a hydroforming operation. It appears that tube necking is less sensitive to the variations of these parameters, given that the index does not vary significantly.

Correlation coefficient ρ	P_f	β
$\rho = 0$	1.2×10^{-3}	3.029
$\rho = 0.2$	1.8×10^{-3}	2.9144
$\rho = 0.4$	2.6×10^{-3}	2.8009
$\rho = 0.6$	3.3×10^{-3}	2.7216
$\rho = 0.8$	3.8×10^{-3}	2.6681
$\rho = 1$	3.9×10^{-3}	2.66

Table 7.15. *Effect of a correlation between the strains on the probability of failures in wrinkling*

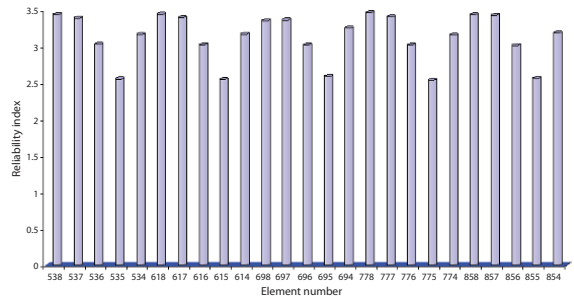

Figure 7.24. *Spatial evolution of the reliability index in wrinkling*

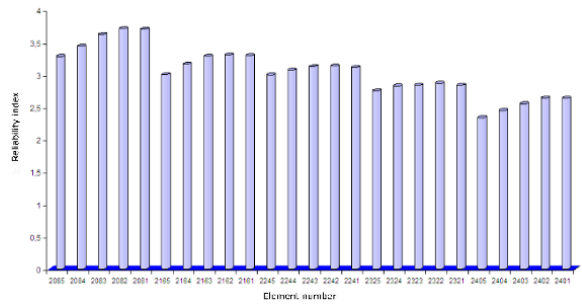

Figure 7.25. *Spatial evolution of the reliability index in necking*

8

Parameters Identification in Metal Forming

8.1. Introduction

This chapter first presents a calculation approach on the basis of a numerical and experimental methodology to adequately study and simulate the formability of hydroforming in welded tubes and sheet metal. The experimental study is dedicated to the identification of the strain-hardening parameters of the concerned material with an optimization approach based on the use of a software platform (Abaqus, Matlab, etc.) based on the overall displacement expansion and pressure measures.

Secondly, the analysis of the reliability of the hydroforming process of the tube is presented and the numerical results are given to validate the approach and show the significance of this analysis.

8.2. Identification methods

Assuming a purely isotropic sheet metal hardening, only one scalar parameter is required to describe the evolution of the surface flow. This is the equivalent plastic strain that has been calculated as being the integral time of the equivalent plastic strain rate:

$$\varepsilon = \int_0^T \dot{\varepsilon} dt \qquad [8.1]$$

Material Forming Processes: Simulation, Drawing, Hydroforming and Additive Manufacturing, First Edition. Bouchaib Radi and Abdelkhalak El Hami.
© ISTE Ltd 2016. Published by ISTE Ltd and John Wiley & Sons, Inc.

The evolution at the level of the surface of the pair $(\sigma_y, \bar{\varepsilon}^p)$ is taken into account by means of the swift hardening distribution:

$$\sigma_y = k(\varepsilon_0 + \bar{\varepsilon}^p)^n$$

where k is the strain-hardening coefficient, ε_0 is the plastic reference strain and n is the hardening coefficient.

These three parameters are the characteristics of the material. Three other parameters are not represented by the strain-hardening model, but affecting the characteristics of the strain. They are the anisotropy parameters of the material, the friction coefficient between the tools and the sheet metal and the thickness t of the sheet.

The parameters (k, ε_0, n) are calculated such that the constitutive equations associated with the plastification surface best reproduce the forming characteristics of the material. The problem that remains to be resolved consists of finding the best damage combination from parameters that minimize the difference between the numerical predictions and the experimental results.

This minimization is related to differences between the experimental measurements of the tensions and their numerical prediction performed on stress specimens. Due to the complexity of the formulas, a numerical minimization strategy has been developed based on the Nelder–Mead simplex method [FLE 87].

The technique for the identification of the material parameters is based on the coupling between the Nelder–Mead simplex method (Matlab code) and the numerical simulation according to the finite elements method via Abaqus/Explicit of hydroforming [RAD 11]. In order to obtain information from the output file of Abaqus/Explicit, we use advanced Python code (see Figure 8.1).

8.2.1. *Validation test*

A three-dimensional finite element analysis has been made, using the finite element code from Abaqus/Explicit to study the hydroforming process.

Rectangular samples with the following geometrical characteristics: thickness $= 1.0$ mm, width $= 12.52$ mm and initial length = 100 mm, have been made using stainless steel (Figure 8.2).

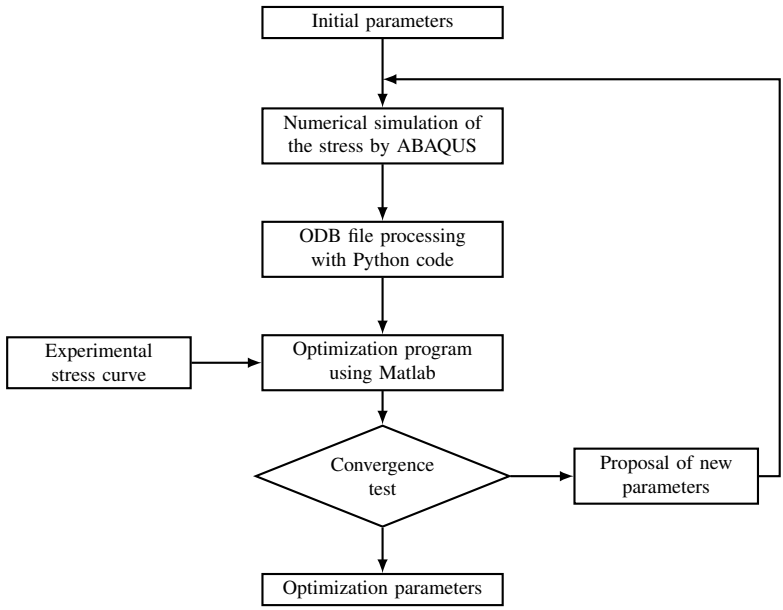

Figure 8.1. *Identification process*

All numerical simulations have been carried out in controlled displacement conditions with constant velocity $v = 0.1$ mm/s. The predicted force with respect to the displacement curves compared with the experimental results for the three orientations under study are indicated in Figure 8.2. With a small ductility (step 1), the maximal stress is about 360 MPa and reaches 25% of the plastic strain and the final fracture is obtained for 45% of plastic strain. With the moderate ductility (step 3), the maximal stress is approximately 394 MPa and reaches 37.2% of the plastic strain and the final fracture is obtained for 53% of plastic strain.

The best values of the parameters of the material using the optimization process are summarized in Table 8.1. Within these coefficients of the response (stress versus plastic strain), there is a nonlinear isotropic hardening with a maximal stress reached for the plastic strains and the final fracture is obtained for 22% of plastic strain. The map of the plastic strain of the optimal case is presented in Figure 8.2.

Phase	Critical plastic strain (%)	k [MPa]	ε_0	n
1	25.8	381.3	0.0100	0.2400
2	29.8	395.5	0.0120	0.2415
3	37.2	415.2	0.0150	0.2450
Optimal	36.8	416.1	0.0198	0.2498

Table 8.1. *Used material properties*

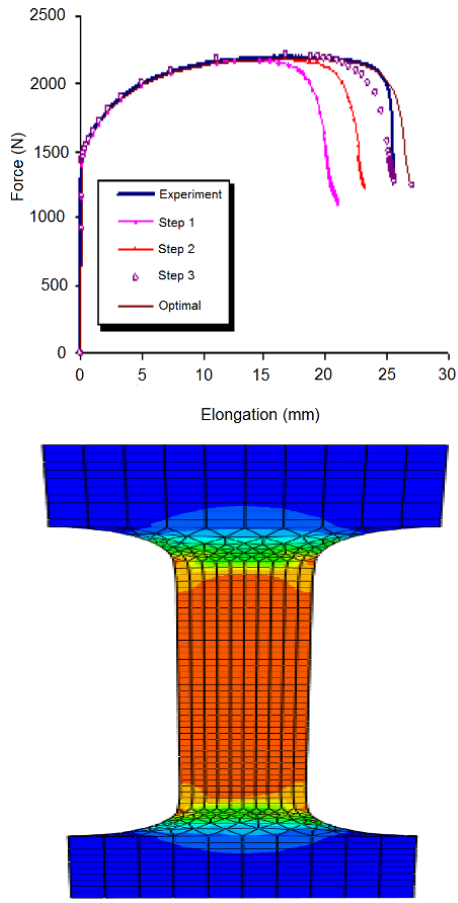

Figure 8.2. *Force/stretching for different optimization stages and plastic strain map. For a color version of this figure, see www.iste.co.uk/radi/material.zip*

8.3. Welded tube hydroforming

In this case, the strain with geometric singularities found in the welded tube is assumed as transversely orthotropic, while its behavior is represented by the Swift model. The observation with the optical microscope on the cross-section of the wall is used to construct the geometric profile of the notch produced by the welded junction [AYA 11].

Taking into account hypotheses relative to isotropic thin shells ($R = 1$) with uniform thickness, the previously established relations, [4.19], [4.20] and [4.22], allow us to build the first experimental model of hardening making use of the measures of the radial displacements/internal pressure. This model is then proposed as an initial solution to solve the inverse problem of the necessary hardening distribution that minimizes the following objective function:

$$\xi_F = \frac{1}{m_p}\sqrt{\sum_{i=1}^{m_p}\left(\frac{F^i_{\exp} - F^i_{num}}{F^i_{\exp}}\right)^2} \qquad [8.2]$$

where $F^i_{\exp}$ is the experimental value of the thrust force corresponding to its nth nanoindentation depth; F^i_{num} is the corresponding simulated thrust force and m_p is the total number of experimental points.

Various evolutions of the flow stress of the isotropic hardening (initial, intermediate and optimal) are proposed in order to estimate the best behavior of the strain with geometrical singularities encountered in tube hydroforming.

Figures 8.3 and 8.4 represent the effective stress according to the plastic strain curves and the associated radial displacement/pressure for these three cases. As can be seen, there is a good correlation between the optimal hardening evolution and the experimental results. Table 8.2 summarizes the parameters of these models.

The anisotropic factor R is determined only for the optimal hardening evolution. In the problem to be solved, there is only a single parameter that exists in the initial solution, which corresponds to the case of an isotropic material ($R = 1$). The numerical iterations have been carried out on the tube hydroforming with a non-uniform thickness, and the results obtained are presented in Figure 8.5. A good improvement of the quality of the predicted results can be noted when R corresponds to the value 0.976.

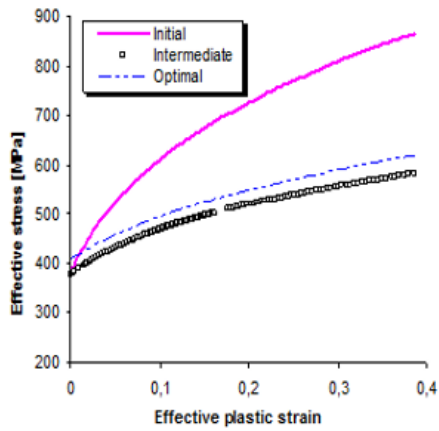

Figure 8.3. *Evolution of the stress–strain for the various hardening distributions*

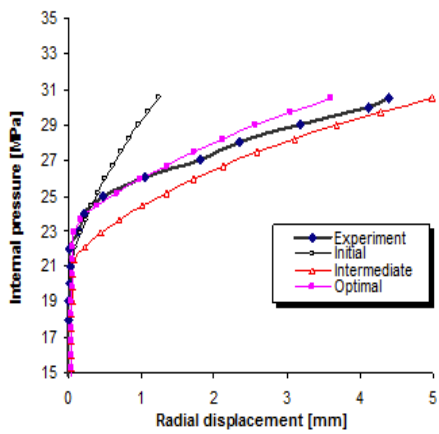

Figure 8.4. *Internal pressure according to the radial displacement*

Model	ϵ_0	k (MPa)	n
Initial	0.025	1,124.6	0.2941
Intermediate	0.055	692.30	0.2101
Optimal	0.080	742.50	0.2359

Table 8.2. *Swift parameters of the various evolutions of the hardening*

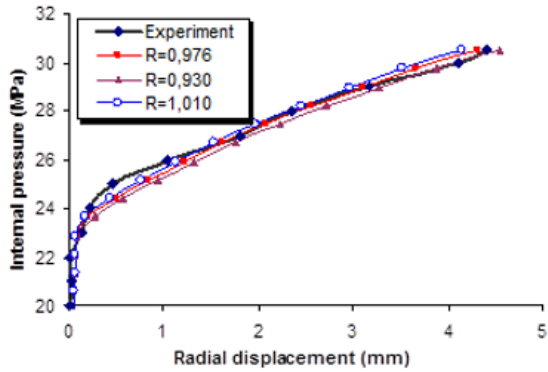

Figure 8.5. *Radial displacement for different values of the anisotropy coefficient R*

8.3.1. *Thin sheet metal hydroforming*

Examples of sheet metal will be presented in order to test the ability of the proposed methodology to simulate the operation of thin plate hydroforming using the entirely isotropic model concerning the elasticity and the plasticity [CHE 02]. These results are obtained from a circular area with a diameter of 300 mm and a thickness of 0.6 mm.

During the hydroforming of the blank, the forming die continues in contact with empty space, which prevents the deformed area of additional deformation and makes the strain area moving outward. The shutter flange is sucked into the female die, which decreases the thinning strain of the deformed area and facilitates the deformation of the contact with the female forming die and the uniformity of the strain.

Compared to experiments performed previously, the limit deep-drawing ratio of the blank is remarkably improved. Taking into account hypotheses relative to isotropic thin shells with uniform thickness, the relations previously established allow for building the first experimental hardening model using force/dislocation measures. This model is then proposed as an initial solution to solve the inverse problem of the necessary hardening distribution that minimizes the following objective function:

$$E_{error} = \frac{i=1}{m} \sqrt{\sum_{1}^{m} \left(\frac{P^i_{\exp} - P^i_{num}}{P^i_{\exp}} \right)^2} \qquad [8.3]$$

where $P^i_{\exp}$ is the experimental value of the thrust pressure corresponding to the ith displacement, $P^i_{num}\delta_i$ is the corresponding predicted pressure and m is the total number of experimental points.

The process parameters are controlled at the internal fluid pressure applied to the sheet as a uniformly distributed load on the inner surface of the sheet and is introduced as an increasing linear function of time with a constant flow of about 10 mL/min. A comparator is used to measure the axial displacement. The effect of three industrial cavities (D1, D2 and D3, see Figure 8.6) on the localization of the flows and of the plastic damages is studied during the hydroforming of the sheet metal. These forming die cavities consist of a succession revolution surfaces (conical, plane, concave, convex and spherical). The evolution of the pole's displacement as a function of the internal pressure during the test and the sheet's thicknesses are studied experimentally. The displacement profiles are obtained from the deformations of the sheet before bursting.

These are restored by using the 3D Dr. PICZA Roland-type scanner with a precision of 5 μm with a contact stage regulated at 5 mm. In addition, both measurement techniques have been used to evaluate sheet thinning after forming, namely a non-destructive technique using an ultrasound source of the brand Sofranel (model 26 MG) and a destructive technique using a digital caliper micrometer from the brand Mitiyuta with a precision of 10 μm (Figure 8.7).

Experimental results with circular sheet hydroforming are represented in Figure 8.8 (Die D1), Figure 8.9 (Die D2) and Figure 8.10 (Die D3). For the cavities of the dies D1 and D3, fracturing has appeared in the round corner (near the border areas between the conical and the hemispherical die surfaces).

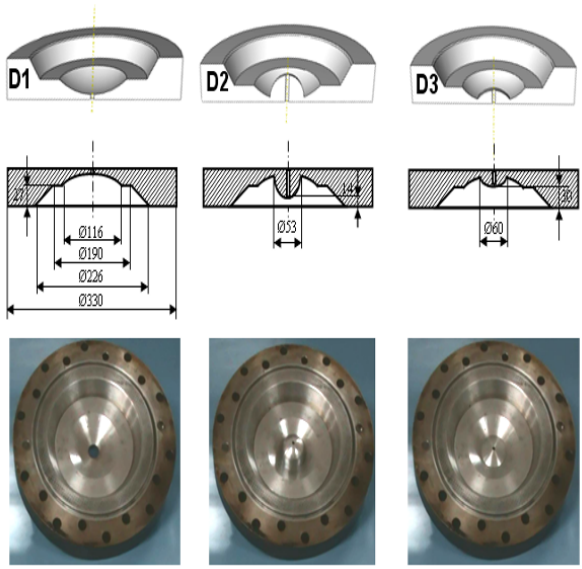

Figure 8.6. *Geometry of the cavities (D1, D2 and D3)*

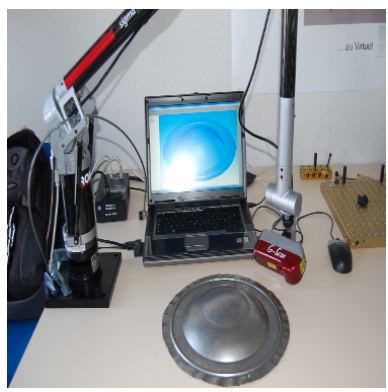

Figure 8.7. *3D scanner G scan for reconstitution*

Regarding the cavity of the die D2, a fracture occurs at the center of the blank when the pressure is excessive. This shows that the critical strain occurs in these regions. It should be noted that the fracture area depends on the fluid under pressure overflowing the die from the cavity under pressure, and the effect of inverse curvature at the shoulder of the die is not observed in the experiment. In this section, we are interested in the comparison between the experimental observations of the regions where the damages occur and the numerical predictions of the domains covered by the plastic instability and the damages. Figures 8.8–8.10 present the main results of the simulations of all applications addressed in this study. The predicted results with the cavity dies show that the equivalent von Mises stress has reached high critical values and then suffered a significant decrease in the damaged areas. This decrease is estimated for the three cavities of the dies D1, D2 and D3, respectively, at29, 14 and 36%.

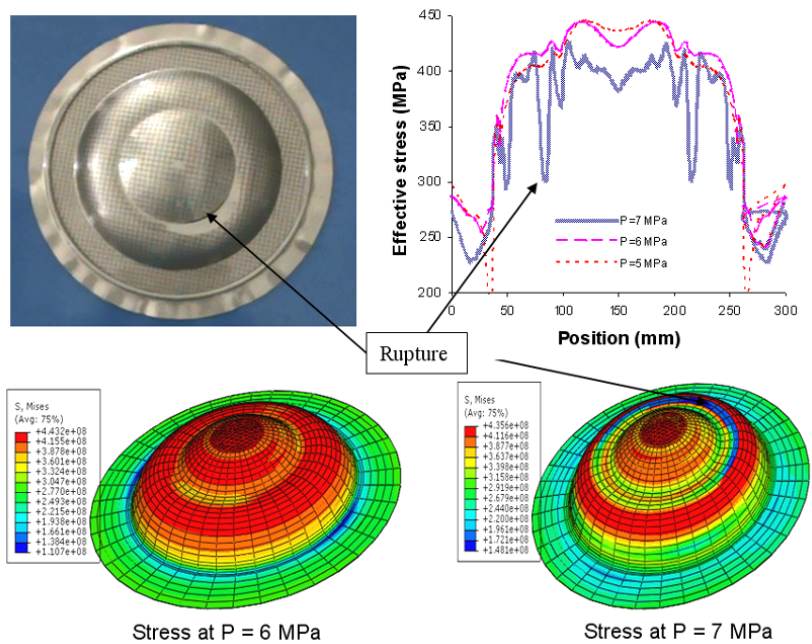

Figure 8.8. *Hydroforming experimental and numerical results using the cavity of die D1. For a color version of this figure, see www.iste.co.uk/radi/material.zip*

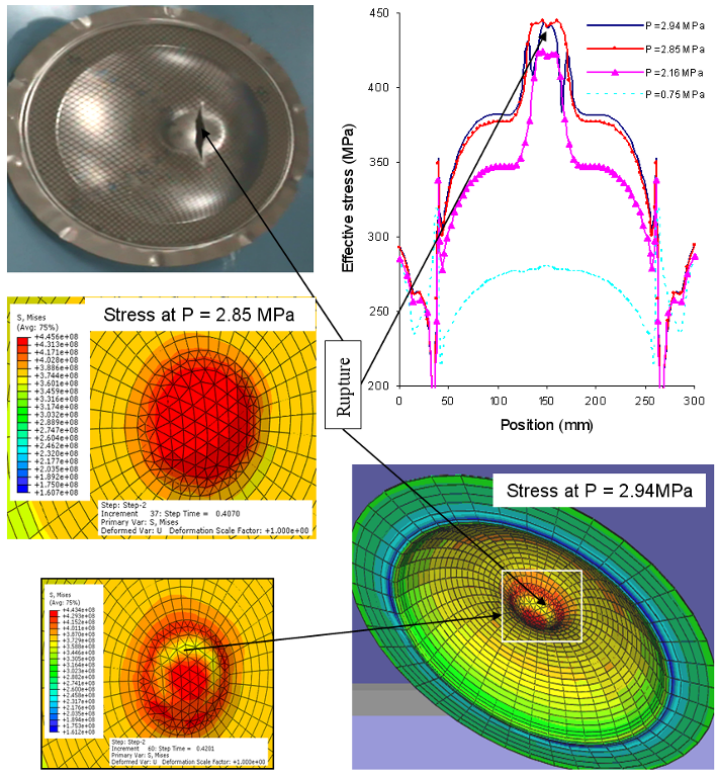

Figure 8.9. *Hydroforming experimental and numerical results using the cavity of die D2. For a color version of this figure, see www.iste.co.uk/radi/material.zip*

The comparisons between the numerical predictions of the damaged regions and the experimental observations of the fracture zones have led us to the following conclusions:

1) The numerical computations show that by increasing the pressure, the regions increasingly more pronounced by an increase in the equivalent stress followed by a sudden decrease can be correlated with the experimentally observed damaged areas. In this context, the results of the first cavity of die D1 show that the instabilities are located in the central area of the blank, delimited by a circular contour with a 72 mm radius. The largest decrease in stress is located within the area bounded by two edges with radii of 51 and 64 mm, respectively, whereas the fracture took place on the boundary of the flat surface with a spherical surface located on a circle with 60 mm of radius. With the

cavity of die D2, the highest decrease is located between two contours of radii equal to 10 and 19 mm, the break is observed at a distance of 17 mm from the axis of rotation of the deformed blank. Finally, with the cavity of die D3, the computations show that the damaged area is located in a region delimited by two edges of radii equal to 54 and 73 mm, respectively; the fracture occurred at the junction of the flat surface with a spherical surface.

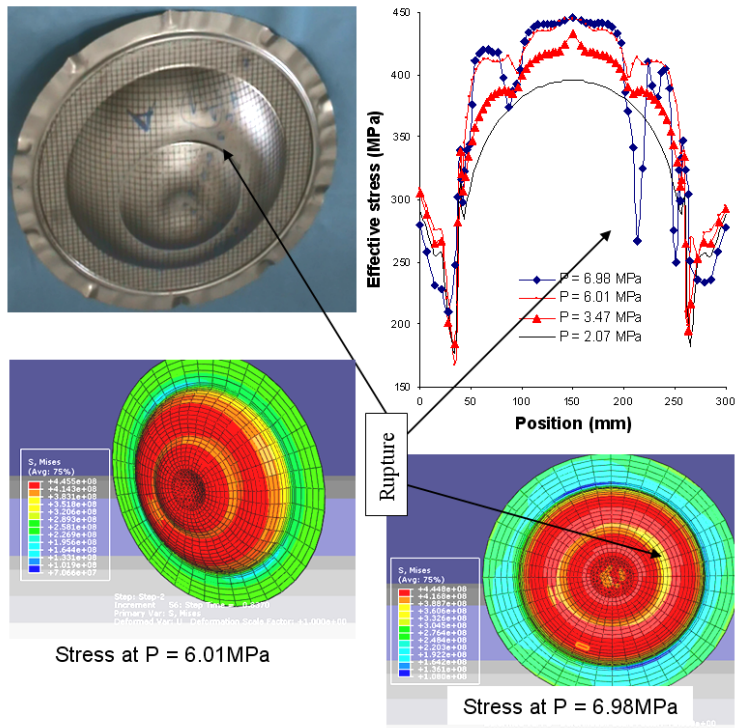

Figure 8.10. *Hydroforming experimental and numerical results using the cavity of die D3. For a color version of this figure, see www.iste.co.uk/radi/material.zip*

2) The pressures that characterize the beginning of the instabilities are, respectively, in the order of 4.90 (for D1), 2.85 (for D2) and 5.1 MPa (D3). For the applications with cavities of dies D1 and D3, the regions where the instability starts have been identified (see Table 8.3).

The results presented in Figure 8.11 show that the relative differences between the expected results and the experiments of the displacement axis are

within the 7% limits while the pressure levels are below a threshold characterizing the type of application.

Cavity of die	Instability start (MPa)	Critical (MPa)	Experimental (MPa)
D1	4.90	6.74	5.2
D2	2.85	2.85	3.0
D3	5.10	6.86	5.3

Table 8.3. *Pressure levels for various cavities*

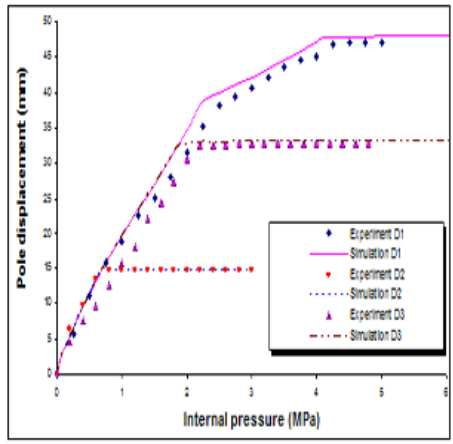

Figure 8.11. *Displacement of the axis according to the internal pressure*

Appendices

Appendix 1

Optimization in Mechanics

A1.1. Introduction

Optimal design of structures has raised interest for more than 20 years. Still rarely applied to conventional engineering techniques, it is being gradually integrated as its reliability increases. Started in response to the simplest problems, the field of application of structural optimization now reaches more interesting new challenges [ELH 11].

Numerical simulation in the field of computational structural mechanics has seen many changes during the past years due to the progress of scientific computation in the development of computers, and their improvement both in processing speed and quality of the managed information. The engineer thus has access to a wide range of methods supported by computer-based tools, notably the finite element method and optimization methods, which constitute valuable tools for optimal structure design while abiding to certain rules or standards [ELH 10].

The finite element method has appeared with the need to solve complex and general computational problems, in a context where the massive development of computers has allowed the automation of processes for solving large systems of equations. Numerous industrial software programs for computer-aided design based on the finite elements method have therefore been developed, including Ansys, Abaqus and Nastran. Today, the numerical methods used for solving PDFs have reached a maturity that allows them to participate in processes supporting engineering design. At the same time, the field of optimization has considerably developed alongside computing infrastructures. Currently, a number of algorithms are available for solving

Material Forming Processes: Simulation, Drawing, Hydroforming and Additive Manufacturing, First Edition. Bouchaib Radi and Abdelkhalak El Hami.
© ISTE Ltd 2016. Published by ISTE Ltd and John Wiley & Sons, Inc.

nonlinear programming, deterministic (descent methods, simplex) or stochastic approaches (simulated annealing, evolutionary algorithms, particle swarm algorithms, etc.). It thus seems natural to combine these two areas in order to provide automatic strategies to aid design based on optimization.

A1.2. Classification of structural optimization problems

Determining the appropriate form of structural components is a problem of primary importance for engineers. In all fields of structural mechanics, the impact of good design of a part is significant for its resistance, its life duration and its use in operation. Optimization appears as paramount in increasing the performance and in minimizing the mass of the structures, therefore resulting in substantial material savings. This research area has been so intensely the focus of attention for researchers that a resurgence of publications in this area can be observed. Among the optimization problems of structures, three major categories can be distinguished according to the nature of the design variables:

– design optimization: the variables are the cross-sections, thicknesses, all quantities that can evolve without requiring modification of the finite element mesh, and the form is fixed;

– shape optimization: admits modifications in shape compatible with a topology fixed in advance;

– topological optimization: allows for more fundamental modifications of the nature of the structure.

A1.2.1. *Design optimization*

Design optimization (also known as sizing optimization) does allow the modification of the cross-section or the transversal thickness only of the components of a structure whose shape and topology are fixed. No modification of the geometry model is possible, which severely limits the variety of the possible shapes. This is referred to as homeomorphic transformation. In mathematics, the objective of design optimization is to find the design parameters that minimize an objective function. The general formulation is written as:

$$\begin{array}{ll} \min_d & G_I(d) \\ \text{u.c.} & \left\{ \begin{array}{ll} G_i(d, X) \geq 0 & i = 1, \ldots, m \\ h_j \geq 0 & j = m+1, \ldots, n_h \end{array} \right. \end{array} \qquad [A1.1]$$

where d is the vector of the variables to be optimized, also called decision variables, X is the deterministic parameters vector, G_i is the performance functions, h_j is the geometric and physical feasibility function and G_I is the objective function.

EXAMPLE A.1.– Given a homogeneous beam P_1 with a circular cross-section having a diameter $2a$. The beam is a cantilever, with a load on the free end. We are looking to obtain the dimensions of a beam P_2 with rectangular cross-section (by slicing the circular cross-section of the beam P_1) to support the maximal load at its free end.

Let M the bending moment, I the moment of inertia and σ the stress at a distance y. It is assumed that the width of the beam P_2 is $2x$ and its length is $2y$. We get $\frac{\sigma}{y} = \frac{M}{I}$, then $\sigma_{max} = \frac{M}{I}y = \frac{3M}{4xy^2}$. The problem is tantamount to minimizing the quantity $\frac{k}{xy^2}$ under the stress $x^2 + y^2 = a^2$, which we write in the form:

$$\begin{array}{ll} \min & f(x,y) = kx^{-1}y^{-2} \\ \text{u.c.} & g(x,y) = x^2 + y^2 - a^2 = 0 \end{array} \qquad [A1.2]$$

The computation of the various gradients gives:

$$\frac{\partial f}{\partial x} = -kx^{-2}y^{-2} \quad \frac{\partial f}{\partial y} = -kx^{-1}y^{-3}$$

$$\frac{\partial g}{\partial x} = 2x \qquad \frac{\partial g}{\partial y} = 2y$$

We then find:

$$\left(\frac{\partial f}{\partial x}.\frac{\partial g}{\partial y} - \frac{\partial f}{\partial y}.\frac{\partial g}{\partial x}\right)_{x^*,y^*} = 0$$

where $-2x^{-2}y^{-2}(2y) + 2kx^{-1}y^{-3}(2x) = 0$. Consequently, it yields: $y^* = \sqrt{2}x^*$, which results in:

$$\left\{ \begin{array}{lcl} x^* & = & \frac{a}{\sqrt{3}} \\ y^* & = & \frac{b}{\sqrt{3}} \end{array} \right.$$

A1.2.2. *Shape optimization*

This approach optimizes the value of the fitness function by changing the contours of the object while the topology remains the same. In other words, the unknown is a contour (2D) or a surface (3D). The border is parameterized by control nodes and the gradient of the fitness function is calculated relatively to the position of these nodes, which is displaced repeatedly in the direction of the gradient.

Shape optimization consists of searching for the best possible shape for a given problem. Shape optimization problems often originate in industry (for example to find the best aircraft wing or the best design for a vehicle). The general approach to a shape optimization problem is the following:

– search for an existing optimal solution, especially the uniqueness of this optimal solution (but this is a very difficult question in general);

– study the optimality conditions that characterize the optimal shapes;

– calculate the optimal solution or, at least satisfactory approximated solutions.

Regarding problems of an industrial nature, the approach is often rather different. Industrialists have before them an initial form that they wish to improve. The scientist must then propose a method for modifying the shape of the initial shape according to the specifications.

A1.2.3. *Topology optimization*

Finally, topological optimization allows more fundamental modification of the nature of the structure. This time, the geometry of the piece is considered without any *a priori* knowledge about the connectivity of the areas or of the structural members present in the solution. We search for, without any explicit or implicit restriction, the best shape possible even if it implies changing the topology. Optimizing the topology naturally leads to determining in a certain manner the shape or the optimal cross-sectional dimensions of the structure, such that some authors also refer to it by the name of generalized shape optimization [MAK 08].

It is obvious that the gains in performance are an increasing freedom function that is available to perform the optimization. Thus, the flexibility available with a variable topology allows very significant performance gains which are significantly higher than those obtained by a shape or a dimension optimization method.

A1.2.4. *Multiobjective structural optimization*

This is a multiobjective optimization problem proposed by [STA 92] (see Figure A1.1). The objective is to find an optimal structure for the wire frame by simultaneously minimizing the total mass and the static displacement at point C. The minimization of the weight of a mechanical structure always remains practically an indispensable objective in mechanical technology. Both criteria are in conflict because minimizing the mass of a structure results in a tendency for the displacement to increase. Therefore, the best solution is to find a compromise between the two criteria. To do this, we consider two cost functions to minimize the total volume $f_1(\text{cm}^3)$ and the displacement $f_2(\text{cm})$.

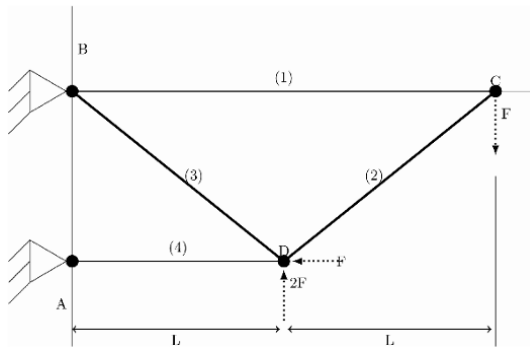

Figure A1.1. *4-bar wire-frame*

Analytically, the problem can be presented by the following system:

$$\begin{cases} \min\left(f_1(x), f_2(x)\right) \text{ such that} \\ f_1(x) = L\left(2x_1 + \sqrt{2}x_2 + \sqrt{x}_3 + x_4\right) \\ f_2(x) = \frac{FL}{E}\left(\frac{2}{x_1} + \frac{2\sqrt{2}}{x_2} - \frac{2\sqrt{2}}{x_3} + \frac{2}{x_4}\right) \\ \text{s.t. } (F/\sigma) \leq x_1, x_4 \leq 3(F/\sigma) \\ \quad \sqrt{2}(F/\sigma) \leq x_2, x_3 \leq 3(F/\sigma) \end{cases} \qquad [A1.3]$$

With regard to the design parameters, four variables are selected for the optimization, namely the four cross-sections of the wire-frame bars, such that: $F = 10\ kN$, $E = 2 \times 10^5\ kN/\text{cm}^2$, $L = 200$ cm and $\sigma = 10\ kN/\text{cm}^2$.

The overall Pareto border for this problem can be obtained by enumeration. The process consists of a reiteration phase on the four design variables (with a reasonable step) to obtain a set of points representing the space of the objectives functions (Figure A1.2(a)). The result of this process is a Pareto front consisting of 200 solutions, whereas the NSGA Pareto front is composed of 750 solutions (Figure A1.2(b)).

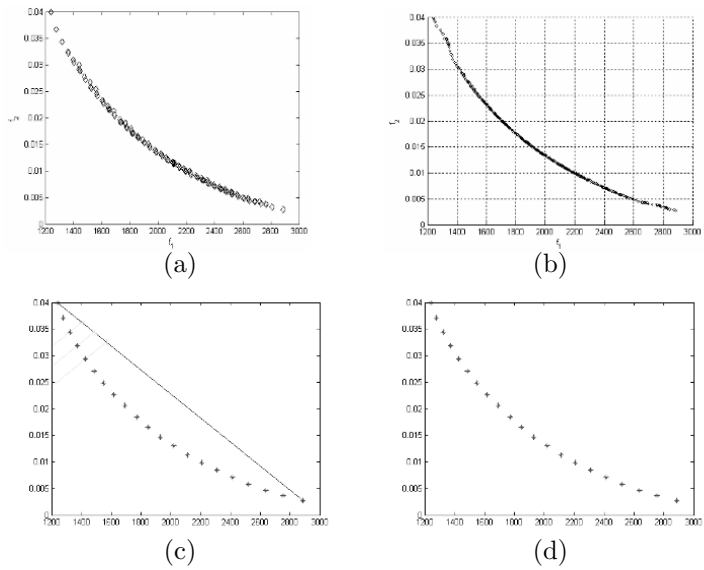

Figure A1.2. *Comparison of the optimal Pareto borders in the objective space*

The optimal Pareto border obtained by a variant of the first method is given by the graph (Figure A1.2(d)). This example clearly shows the great potential of this method; it can be observed that the optimal solutions are uniformly distributed over the Pareto frontier with a very small number of points compared with the NSGA method. We have intentionally chosen a small number of points but that is at the same time representative to precisely point out the effectiveness of this method. It is shown that the NSGA method uses 750 points to plot the Pareto border, whereas this method uses 21 points only to reduce the number of solutions on the Pareto border; one can use a Datamining tool. The basic concepts upon which this method relies make it flexible and effective (see Figure A1.2(c)). It should also be noted that there are portions on the optimal Pareto border obtained by NSGA that do not give

a good approximation of the border. Namely, the left side where $1200 \leq f_2 \leq 1400$ and the right side where $2600 \leq f_2 \leq 2900$; on these sections the NSGA has failed to find the optimal solutions.

A1.2.5. *Robust optimization*

Robust optimization has the same characteristics as deterministic optimization at the data processing level but with uncertainties in the design variables and in the objective functions as well as in manipulating the stresses. In mechanical engineering, these uncertainties are inherent to modeling defects, the mechanical properties of the materials (Young's modulus, density, etc.) and the manufacturing and assembly processes (sheet metal thickness, junction, etc.). In a preliminary design phase, these uncertainties are introduced to take into account the lack of knowledge of some design variables. We introduce the following definitions:

– *uncertain parameter*: a non-deterministic parameter characterized by a nominal value and by uncertainty;

– *nominal model*: the model in which the parameters are set to their nominal values;

– *random model*: the model in which the values of the parameters are randomly chosen.

Appendix 2

Reliability in Mechanics

A2.1. Introduction

The reliability of mechanical and mechatronic systems is based on the competitiveness of French and global companies in the automotive, aeronautics, space, civil engineering and defense fields, among others. For example, in the field of mechatronic systems, which combines mechanics and electronics, failure phenomena have emerged that have not been addressed in depth and that are thereby not sufficiently well understood.

In aeronautical and automotive applications in particular, the reliability of embedded systems depends on several parameters. In the case of electronic circuit boards, excessive stresses can lead to failures such as weld or terminal block fracturing or even to signal and information loss. These can significantly impact the functioning and the security of the systems.

Systems reliability is therefore, more than ever, a major challenge for industrial factories. They must respond to the increasingly growing demands of contractors, and non-compliance with them results in penalties or warranty extensions, and in significant costs due to poor quality when defects have to be corrected. Furthermore, it can even lead to the dissatisfaction of the customers that can reach international notoriety, thus compromising future markets. This is an indicator that the significance of embedded electronics in vehicles and in systems is becoming increasingly predominant in the industry [ELH 13a].

Material Forming Processes: Simulation, Drawing, Hydroforming and Additive Manufacturing, First Edition. Bouchaib Radi and Abdelkhalak El Hami.
© ISTE Ltd 2016. Published by ISTE Ltd and John Wiley & Sons, Inc.

A2.2. Structural reliability

A structure is built to respond to a clearly identified set of requirements. Structural reliability aims to evaluate the probability that a structure subjected to hazards (temperature, vibrations, shock and fatigue, etc.) is able to address the totality of these needs for a given lifetime. However, the calculation of this probability imposes a rigorous study methodology of four steps:

– define a deterministic mechanical model adapted to the problem being addressed;

– identify the random parameters of this model and model them with adequate probabilistic tools;

– define the modes and the scenarios of failure of the problem;

– evaluate the probability of occurrence of these failure modes.

The precision, the accuracy of the result and the probability of failure of the structure are thus conditioned by a number of expert, experimental, mathematical, numerical and practical factors intervening at each stage of the reliability study.

A2.3. Modeling a structural reliability problem

A2.3.1. *Deterministic mechanical model*

The first step of a reliability study is to identify the mechanical problem being addressed. An adapted deterministic mechanical model is then defined. It integrates the geometry of the structure, the mechanical properties of the materials and the boundary conditions.

A2.3.2. *Uncertainty and probabilistic modeling*

Among the various parameters involved in this model, some are known only in a random manner. The uncertainties involving the physical properties of materials and the geometric characteristics of the workpieces of the structure are called internal uncertainties. These uncertainties depend on the quality and on the accuracy of manufacturing, the characterization of materials and the structural elements. The uncertainties relating to the actions exerted on the structure are called external uncertainties. The origin of these uncertainties is often found in the difficulty of precisely evaluating the value of uncontrolled stresses, the action of the swell, the wind or car traffic on a bridge, for example.

An identification of the parameters is carried out and statistical adequacy tests validate the hypotheses formulated. When the problem has m random variables X_i, the random vector is defined as:

$$X = (X_1, X_2, \ldots, X_m)^T \qquad [A2.1]$$

Note that certain actions, notably accidental or catastrophic ones, hardly pertain to a probabilistic model. A ship colliding with a bridge pier or a plane crashing into a building do not occur by mere coincidence. Nevertheless, this type of extremely rare events cannot be taken into account in a realistic manner in the design of a structure.

A2.3.3. *Structural modes of failure*

To ensure the integrity of the structure in the face of potential risks, rules of good functioning are established. Non-compliance with one of these criteria can cause the elementary mode of failure of the structure. The succession of events originating failure represents a scenario of failure. The modes or failure scenarios are established according to the potential risks: the presence of stresses or excessive strain in a structural element, the fracture of a workpiece, etc.

Several physical phenomena may be at the origin of a failure: lamination, fatigue, creep, the presence of cracks, large strains, etc. Each phenomenon or the combination of these results in a scenario or a mode of failure. To simplify the notation, we are considering now the case of a structure having only one single mode of failure. The probabilistic modeling of a mode of failure is carried out through the definition of a function $G(X)$ called the limit state function or performance function. It can be noted that the construction of the function $G(X)$ itself is a random variable. Thus:

– $G(X) > 0$ defines the structural safety domain;

– $G(X) < 0$ defines the structural failure domain;

– $G(X) = 0$ defines the limit state surface.

The structure therefore has two possible states: a good functioning state and a failure state, separated by a border known as limit state. Nevertheless, it should be noted that the reality is often more complex than this binary modeling.

A2.3.4. *Structural failure probability*

DEFINITION A2.1.– *The probability of failure of the structure is then equal to:*

$$P_f = P(G(X) \leq 0) \qquad [A2.2]$$

Let

$$P_f = \int_{G(X)\leq 0} f_X(x)dx \qquad [A2.3]$$

where f_X is the joint probability density of the random vector X.

DEFINITION A2.2.– *The reliability of the structure is defined by:*

$$P_s = 1 - P_f \qquad [A2.4]$$

Although the formulation of P_f is simple, its calculation can prove to be extremely complex. The difficulty in explicitly knowing f_X and the often nonlinear expression of the border of D_f in general make this analytical computation impossible.

A2.3.5. *Computation of the structural failure probability*

Currently, there are two major categories of methods for the evaluation of the probability of failure of a structure. The objective of the first is to evaluate P_f over the entire domain of failure D_f and resorts to simulations based on the Monte Carlo method. The second consists of an idealization of domain D_f allowing the calculation of an approximate value of P_f from a reliability index β.

A2.3.6. *Computation of the failure probability based on a reliability index*

Several authors have proposed indices or reliability indexes. The best known are Rjanitzyne–Cornell's and Hasofer–Lind's.

A2.3.6.1. *Rjanitzyne–Cornell's index*

The Rjanitzyne–Cornell index β_c is obtained from the mean μ_G, and the standard deviation σ_G of the performance function G:

$$\beta_c = \frac{\mu_G}{\sigma_G} \qquad [A2.5]$$

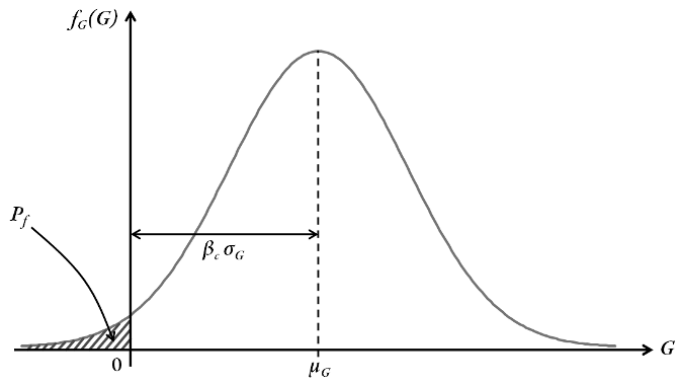

Figure A2.1. *Graphical representation of the Rjanitzyne–Cornell index*

It can be seen in Figure A2.1 that this index multiplied by the standard deviation σ_G represents the difference between the mean point μ_G and the limit state ($G = 0$). The major drawback of this index is that it gives different values for various expressions of the limit state function.

EXAMPLE A2.1.– Given the following limit state function $G(r, s) = r - s \leq 0$, we have:

$$\beta = \frac{m_r - m_s}{\sqrt{\sigma_s^2 + \sigma_r^2}}$$

If we rewrite the limit state function in a different manner, that is in the form $G(r, s) = \frac{r}{s} - 1 \leq 0$, then in this case, after linearization it yields:

$$\begin{aligned} G(r,s) &= G(m_r, m_s) + \frac{\partial G}{\partial r}|_{m_r,m_s}(r - m_s) + \frac{\partial G}{\partial s}|_{m_r,m_s}(s - m_s) \\ &= \frac{m_r}{m_s} - 1 + \frac{1}{m_s}(r - m_s) + \frac{1}{m_r}(s - m_s) \end{aligned}$$

where

$$\beta = \frac{m_G}{\sigma_G} = \frac{m_s}{\sqrt{\frac{\sigma_r^2}{m_s^2} + \sigma_s^2 \frac{m_r^2}{m_s^2}}}$$

Two different indices for the same limit state function are therefore obtained. To overcome this difficulty, we introduce the Hasofer and Lind reliability index.

A2.3.6.2. *Hasofer and Lind index*

To remove the risk of dependence of the reliability index on the limit state, Hasofer and Lind have proposed to perform the calculation of β in the space of the standard normal random and statistically independent variables. To do this, the random vector X is transformed into a random vector U, with:

$$U_i = T(X_i) \qquad \text{[A2.6]}$$

The random variables follow a standard normal distribution and $\forall i \neq j$, U_i and U_j are mutually independent variables. This probabilistic processing T requires knowing the statistical distributions of each of the random variables. The limit state function becomes after transformation:

$$H(U) = G[X(U)] \qquad \text{[A2.7]}$$

The probability of failure is then equal to:

$$P_f = P(H(U) \leq 0) \qquad \text{[A2.8]}$$

that is

$$P_f = \int_{H(u)\leq 0} \Phi_m(u)du \qquad \text{[A2.9]}$$

Φ_m is the density function of the multivariate normal distribution. The reliability index β_{HL} is defined as being the Euclidean distance from the origin of the normal standard space to the limit state surface $H(u) = 0$ (Figure A2.2). u is a realization of the random vector U, that is $u = (u_1, u_2, \ldots, u_m)^T$. $H(u)$ is a realization of the random variable $H(U)$.

It is therefore necessary to solve the following constrained minimization problem:

$$\begin{cases} \beta_{HL} = \min \sqrt{u^T.u} \\ u \in \mathbb{R}^m, \text{ verifying:} \\ H(u) = 0 \end{cases} \quad [A2.10]$$

This problem is equivalent to:

$$\begin{cases} \beta_{HL} = \min f(u) \\ u \in \mathbb{R}^m, \text{ verifying:} \\ H(u) = 0 \end{cases} \quad [A2.11]$$

with

$$f(u) = \frac{1}{2} u^T.u \quad [A2.12]$$

The reliability index is therefore the minimum of the function f under the stress $H(u) = 0$. The analytical calculation of β_{HL} is achievable only in a limited number of special cases and a numerical solution is usually necessary. The objective function f is a quadratic, and convex form, twice continuously differentiable with respect to the variables u_i. On the other hand, the stress function $H(u)$ is rarely convex. In addition, the function $H(u)$ is sometimes complex, implicit and non-continuously differentiable with respect to the variables u_i.

Let u^* the solution vector of problem (A2.11) and P^* the point on the limit state such that $OP^* = u^*$. P^* is called design point or the most probable point (MPP) of failure (see Figure A2.3). In addition:

$$u^* = -\beta_{HL}\alpha \quad [A2.13]$$

α is the vector normal to the surface $H(u) = 0$ at point u^*, that is its normalized gradient. The objective is then to link β_{HL} to the probability of failure of the structure. Several methods exist and provide a more or less finer value of P_f.

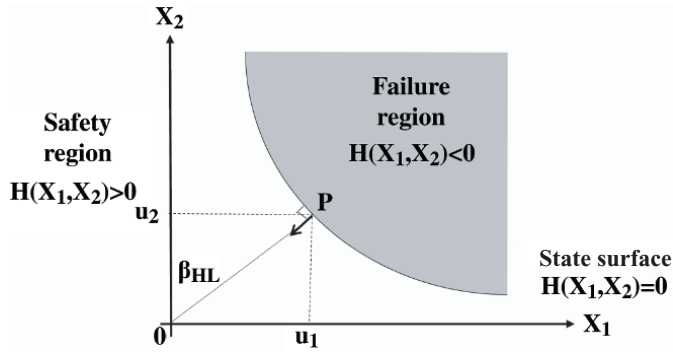

Figure A2.2. *Geometric representation of β_{HL} for a bivariate problem*

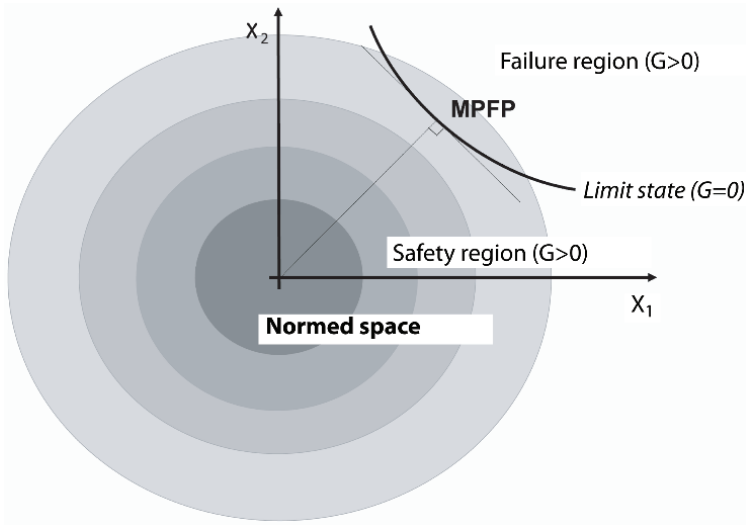

Figure A2.3. *The most probable point (MPP) in the physical space*

A2.3.7. *First order reliability method*

The first order reliability method (FORM) consists of replacing the limit-state surface by the hyperplane tangent at the MPP P^*, $Z(u) = 0$, linear approximation of $H(u) = 0$. The general principle of the FORM is as follows:

– *Step 1*: definition of the probabilistic transformation T between the initial physical space and the standard Gaussian space;

– *Step 2*: transformation of the surface of failure $G(u) = 0$ in the initial space into the failure surface $H(u) = 0$ in the standard Gaussian space;

– *Step 3*: computation of the reliability index β_{HL} the solution of problem (A2.11);

– *Step 4*: calculation of P_f^*, approximate value of P_f, defined by:

$$P_f^* = \int_{Z(u)\leq 0} \Phi_m(u)du \qquad [A2.14]$$

that is

$$P_f^* = \Phi(-\beta_{HL}) \qquad [A2.15]$$

Φ is the distribution function of the standard normal distribution and D_f^* is the domain of $\mathbb{R}^m$ such that $Z(u) \leq 0$ with:

$$Z(u) = \alpha^T.u + \beta_{HL} \qquad [A2.16]$$

If the limit-state surface is convex, then $P_f^* > P_f$; concave, then $P_f^* < P_f$; and a hyperplane, then $P_f^* = P_f$.

The accuracy of the FORM approximation strongly depends on the curvature of the limit-state surface at the MPP and therefore the nonlinearity of the function $H(u) = 0$. One of the major disadvantages of the FORM is the difficulty in estimating the computational error of the probability of failure. A validation solution is then to make use of Monte Carlo simulations. The number of computations directly depends on the number of random variables in the problem.

A2.3.8. *Second-order reliability method*

If the limit-state function is strongly nonlinear, the approximation of the limit-state surface by a hyperplane can lead to a wrong probability of failures. *Second-order reliability method* (SORM) consists of replacing the limit-state surface at the MPP of failure by a quadratic surface. Therefore, the limit-state function is approximated at the point u^* by an order-two Taylor expansion.

Under the hypotheses that the point u^* is unique, the limit-state function admits second derivatives at the point u^* and the principal curvatures κ_i, $i = 1$ at $m - 1$, of the limit-state surface at point u^* verify

$\kappa_i \beta_{HL} \geq -1$, with $\beta_{HL} \to +\infty$, the probability of failure of the structure is equal to:

$$P_f = \Phi(-\beta_{HL}) \prod_{i=1}^{m-1} \frac{1}{\sqrt{1+\kappa_i \beta_{HL}}} \qquad [A2.17]$$

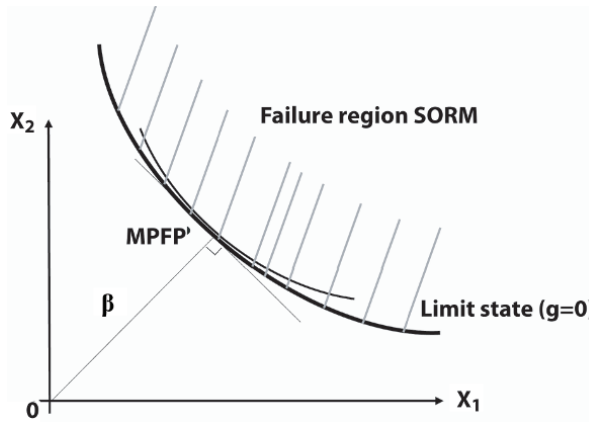

Figure A2.4. *Principle of the SORM for a bivariate problem*

The principal curvatures κ_i, $i = 1, \ldots, m-1$ at the point u^* are the eigenvalues of matrix A of dimensions $(m-1) \times (m-1)$ whose components are defined by:

$$a_{ij} = -\frac{(Q.\nabla_u^2 H(u^*).Q^T)_{ij}}{\|\nabla_u H(u^*)\|}, \quad i,j = 1, \ldots, m-1 \qquad [A2.18]$$

Q is the orthogonal rotation matrix in the Gaussian space such that in the new reference frame, the point u^* belongs to the first coordinate axis and $\nabla_u^2 H(u^*)$ is the Hessian matrix of the limit-state function $H(u)$ at the point u^*.

Appendix 3

Metamodels

A3.1. Introduction

In the design of complex products such as aircrafts, detailed simulation models are needed to evaluate and improve design during development. These detailed simulation models often take a long time to execute. In addition, it may happen that information originating from the simulation models may be unavailable or wrong. In these cases, metamodel-based design optimization can be seen as an alternative. Metamodels are simplified models of detailed simulation models with smooth gradients. The evaluations based on metamodels are fast compared to the evaluations using detailed models. Metamodels are developed according to a comprehensive set of principles concerning simulation models. One of the advantages of using metamodels in multidisciplinary optimization is that the people responsible for the different disciplines can work in parallel during the development of metamodels and verify their accuracy before the process of optimization begins. Since metamodels are approximations of detailed simulation models, an additional source of error is introduced and the challenge is to keep this error at an acceptable level for the problem to be addressed.

A3.2. Definition

A metamodel is a mathematical approximation of a detailed and generally large-sized model. Metamodels can be used when a large number of evaluations are needed, as in optimization, and in the evaluation of the reliability of structures.

Material Forming Processes: Simulation, Drawing, Hydroforming and Additive Manufacturing, First Edition. Bouchaib Radi and Abdelkhalak El Hami.
© ISTE Ltd 2016. Published by ISTE Ltd and John Wiley & Sons, Inc.

Let x be an input vector (values of design variables), transformed into an output vector y (response values). The detailed model can be considered as a function $f\colon \mathbb{R} \rightarrow \mathbb{R}$, meaning that the function f transforms the set of real numbers of k (design variables) into another set of real numbers of l (responses):

$$y = f(x) \qquad \text{[A3.1]}$$

For each scalar response y, a metamodel can be constructed to approximate the real response as:

$$\hat{y} = s(x) \qquad \text{[A3.2]}$$

where $s(x)$ is the mathematical function defining the metamodel and that combines the design variables x to the expected answer $\hat{y}$. In general, this approximation is not accurate and the predicted response $\hat{y}$ will differ from y the reaction observed with the detailed model, that is:

$$y = \hat{y} + \epsilon = s(x) + \epsilon \qquad \text{[A3.3]}$$

where ϵ represents the approximation error.

A metamodel for a unique response is built from an input x_i and an output data set y_i corresponding to $y_i = f(x_i)$, where $i = 1, \ldots, n$ and n are the number of models used to fit the model. Consequently, n evaluations of the detailed model with various variable parameters $x = (x_1, x_2, \ldots, x_k)^T$ design variables k necessary to assemble the metamodel.

Several mathematical formulas can be used for metamodels. Some of them are suitable for global approximations, that is to say that they can be used to represent the complete design space, while others are rather suited for local approximations of part of the design space. Metamodels can interpolate the responses of the detailed simulations or those approximating the responses according to the formulation. In the case of deterministic simulations, interpolation metamodels can be considered, if the numerical noise is negligible. However, an interpolation metamodel is not necessarily better than an approximation to the prediction of the reaction between the fixation points.

Different approaches are used to build the metamodels:

– parametric techniques rely on a relation between design variables and the response of the system under study. The metamodel is constructed from the design variables data set, and the corresponding responses from the initial model by determining the coefficients of the selected function. Polynomial and Kriging models are examples of metamodels built this way;

– non-parametric techniques are used to create different types of neural network models. These techniques do not have an *a priori* functional form; instead, they make use of an *a priori* method for the construction of an approximation function based on the available data. This is done by using different types of simple models in different areas, which are then combined to build a global model.

In the following sections, we present a number of different metamodels, known and often used, and their main characteristics as well as the basic idea behind their derivations.

A3.3. Main metamodels

The objective is to replace the uncertainty loop inside the optimization loop by the construction of a metamodel. Thus, at each optimization step x_i, a metamodel was built for the functions:

$$u \mapsto f(x_i, u) \qquad [A3.4]$$

$$u \mapsto g_j(x_i, u) \quad j = 1, \ldots, q \qquad [A3.5]$$

The cost of this approach is still $N \times n$, where n is the number of points required for the estimation of metamodels. However, n is much smaller than for the Monte Carlo methods.

A3.3.1. *Experimental design and response surfaces*

To create a metamodel, a matrix X containing a set of experimental points and the vector of outputs Y corresponding are necessary. The matrix X constitutes the experimental design. The n observations are sufficiently well distributed over the definition set of the variables in order to create a good metamodel.

The principle of response surface methods (RSM) is to construct a mathematical function, a simplified modeling of the response of the

mechanical system, based on a limited number of experiments. This function or response surface (RS) is said to be:

– global when it simulates the mechanical phenomenon over the whole of the variation space of the parameters involved in the process; these are called factors;

– local if it is constructed in a particular subspace.

In general, the iterative generation of several local surfaces in the experimental space provides a faithful representation of the mechanical problem. Nonetheless, as with any approximation method, the validity of the RSs must be carefully studied. The RSM also give an answer to the following questions:

– what is the influence of one or more factors on the response of the system in a given subdomain?

– what is the geometry of the RS in the neighborhood of certain points?

In mechanical reliability, the response of the structure is the value of the limit-state function. The random variables of the problem assume the role of factors. An experiment is a numerical finite elements computation. The finite element computational code allows for the construction of the RS of the structure. This simple mathematical function replaces the limit-state surface as the border between the safety and the failure domains and then serves as a basis to the conventional reliability methods. The decoupling term of the mechanical calculations and the RSs reliability calculations is thus commonly used to describe these methods.

RS coupling is decomposed into four fundamental stages that ensure the good fit of the approximation model and the mechanical phenomenon [MOR 02]:

– the first step consists of choosing a sensible approximation function. It must have the simplest mathematical form possible. The Monte Carlo method imposes any continuity and differentiability constraints on the approximation function. However, the RS must be global to simulate the behavior of the system in the whole experimental domain. The FORM method is based on the calculation of the index, the solution of the minimization problem under stress (see Appendix 2). Global optimality conditions impose a twice-differentiable stress function in the neighborhood of the solution. The RS is therefore a simple function, twice-differentiable and whose gradient computation is easily achievable;

– the second step defines the set of points of the experimental domain necessary to the approximation. The theory of the design of experiments (DOE) offers several solutions depending on the chosen RS. Advanced mathematical studies allow the definition of D-optimal experimental designs, ensuring a maximal fit of the approximation function and the actual response. However, these designs are often difficult to implement and simpler approaches are preferred at the cost of lower accuracy. In the following, m represents the number of variables of the problem:

- axial or star polytope design comprises $(2m+1)$ points distributed on the axes of the space (see Figure A3.1). Each variable takes three values $-a$, 0 and a if the central point is the point of origin. The quadratic behavior along the axes can be studied. On the other hand, the interaction between variables is not taken into account. The distance between the central point and the farthest point of a DOE is equal to a,

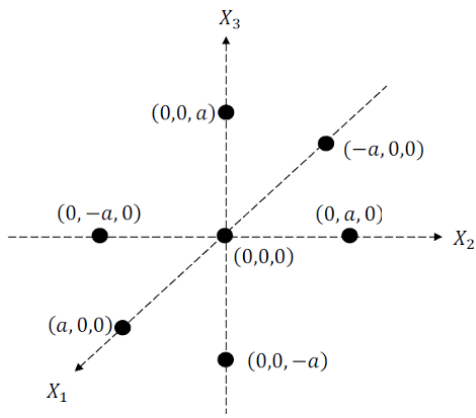

Figure A3.1. *Representation of a three-variable axial polytope design*

- two-level factorial-based designs or 2^m is composed of a set of points of the form $(\pm d, \pm d, \ldots, \pm d)$ (see Figure A3.2). The number of generated points is 2^m, a number that quickly becomes prohibitive if the problem has several factors. The quadratic behavior of the variables along the axes and their interaction can be accessed here. The distance between the focal point and the furthest point of a factorial experimental design 2^m is equal to $\sqrt{m}d$. In practice, fractional factorial designs are used to limit the number of points,

- centered composite experimental designs are among the most representative designs of an experimental space. By the combination of a star experimental design and a factorial DOE 2^m, they comprise $(2^m + 2m + 1)$

points (see Figure A3.3). Nonetheless, the greater m is, the higher the number of generated points, which proves the use of a central composite experimental design ill-advised. The distance between the central point and the furthest in a central composite experimental design is generally of a (if $a > \sqrt{m}d$).

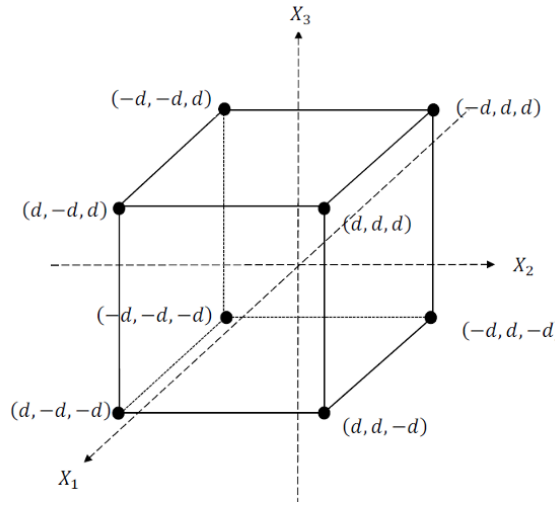

Figure A3.2. *Representation of a three-variable factorial design* 2^m

These three types of designs are the most common in structural reliability;

– the third step consists of choosing the approximation method. This choice is dictated by the available number of points in the domain. If the number of points is exactly equal to the number of polynomial coefficients, a direct polynomial interpolation is used. When a higher number of points is available, the least-squares method is preferred [LEM 09]. In fact, the accuracy of the approximation is in this case much better than that obtained through direct interpolation but the number of calls to the limit-state function and therefore of finite elements calculations grows significantly.

At the end of these first three steps, the RS is constructed and then substitutes the actual limit-state function of the problem for the reliability analysis of the structure;

– the fourth step of RSs coupling is designed to calculate the structural probability of failure. To evaluate this probability, some authors propose a coupling of the RSM and advanced Monte Carlo methods [MOR 02].

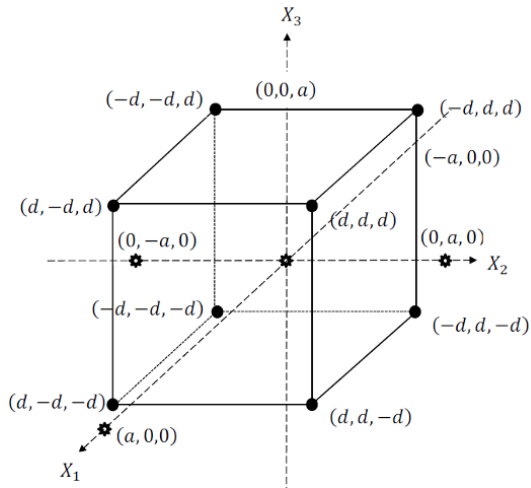

Figure A3.3. *Representation of a three-variable central composite design*

Note that in a reliability analysis, two options are available to the mechanic:

– build the DOE and the RS inside the physical space;

– build the DOE and the RS in the standard normal space.

The first solution ensures a certain physical reality to the RS. The basic variables appear explicitly in the approximated limit-state function. The relation input variables/response variables of the system thus provide an expert judgment on the validity of the generated surface. Furthermore, the experiment shows that the limit-state function is much less perturbated in the physical space than in the Gaussian space, therefore enforcing a better fit between the real response and the RS [ELM 10]. The construction of the experimental design and the response in the standard normal space surface offers the main advantage of obtaining stress functions directly usable for calculating β_{HL}. However, the mechanical calculations are, on their part, performed in the physical space, using a computational finite-element code. Moreover, the probabilistic transformation between these two spaces is in general nonlinear and the following issues appear:

– is the structure of the DOE built in the standard space kept in the physical space after an inverse probabilistic transformation of the points?

– do the points obtained after inverse probabilistic transformation have a physical significance in the mechanical problem?

– a necessary condition to obtain a good representation of the space is that two points are sufficiently distant in the standard space: are they not equal or too close in the physical space?

A3.3.2. *Global metamodel*

This approach is quite similar to the previous since it consists of building a comprehensive DOE on the space of points (x, u), a design from which one (or more) metamodels are estimated. However, it differs in how to build the experimental design and the metamodel:

– the DOE is no longer crossed but simple:

$$P = (x_i, u_i)_{i=1,\ldots,n} \qquad [A3.6]$$

– metamodels do not directly model the criteria to be optimized, but functions:

$$u \mapsto f(x_i, u) \qquad [A3.7]$$

$$u \mapsto g_j(x_i, u) \quad j = 1, \ldots, q \qquad [A3.8]$$

The optimization is then achieved by replacing the function f and g_j by the estimated metamodels. The probabilistic criteria (mean, variance, etc.) are estimated from the metamodel either by Monte Carlo methods [LEE 01] or analytically [CHE 08a]. Metamodels will improve if they are reestimated throughout the optimization with adaptive planning techniques.

A3.3.3. *Kriging model*

The term Kriging comes from the name of the South African geologist C.D. Krige. This method has been used to create metamodels in numerous engineering applications. Computer-based design and analysis of experiments is a statistical framework to process Kriging approximations of complex or costly computational models, presented in [KHO 11, KLE 09]. A function $y(x)$ sought to be modeled is considered.

A3.3.4. *Polynomial regression*

Polynomials-based metamodels are often called RS models and are used in external response methodology (RSM). RSM [MYE 11] is a set of statistical and mathematical methods for developing, improving and optimizing processes and products. The models are developed based on regression, which is the process of fitting a regression model $y = s(x, \beta) + \epsilon$ for a database of x, n variable parameters and y corresponding response.

The least-squares method chooses the regression coefficient β allowing the quadratic error to be minimized, that is solving the regression of the problem:

$$\min \sum_{i=1}^{n} \epsilon_i^2 = \min_{\beta} \sum_{i=1}^{n} (y_i - s(x_i, \beta))^2 \qquad [A3.9]$$

A3.3.5. *Least squares*

Polynomial metamodels can generate errors when the response of the system is highly nonlinear, but may yield good approximations in small regions where the response is less complex. According to [HAM 14], the mathematical description of a metamodel MLS can be formulated as:

$$\hat{y}(x) = \sum_{i=1}^{p} f_i(x) b_i(x) = f^T(x) b(x) \qquad [A3.10]$$

where f is a vector of the basic functions (polynomials) for the metamodel and b is a coefficients vector. The number of coefficients p depends on the order of the approximation.

Bibliography

[ABD 05] ABDERRABBO N., ZAMPALONI M.A., POURBOGHRAT F., "Wrinkling control in aluminum sheet hydroforming", *International Journal of Mechanical Sciences*, vol. 47, pp. 333–358, 2005.

[ABE 08] ABEDRABBO N., WORSWICK M., MAYER R. *et al.*, "Optimization methods for the tube hydroforming process applied to advanced high-strength steels with experimental verification", *Journal of Materials Processing Technology*, vol. 209, pp. 110–123, 2008.

[AFN 11] AFNOR, *Fabrication Additive - Vocabulaire*, Nf E67-001, 2011.

[ALT 01] ALTAN T., JIRATHEARANAT M., STRANO M., SHR S.G., "Adaptative FEM process simulations for hydroforming tubes", *Proceeding of the International Conference on Hydroforming*, 2001.

[ARR 81] ARRIEUX A., Contribution à la détermination des courbes limites de formage du titane et de l'aluminium. Proposition d'un critère intrinsèque, Thesis, University of Lyon I and INSA de Lyon, 1981.

[ARR 95] ARRIEUX R., "Determination of the forming limit stress diagrams in sheet metal forming", *Journal of Material Processing Technology*, vol. 53, pp. 47–56, 1995.

[ASN 00] ASNAFI N., SKOGSGARDH A., "Theoretical and experimental analysis of stroke-controlled tube hydroforming", *Journal of Materials Sciences and Engineering*, vol. 279, pp. 95–110, 2000.

[ASN 03a] ASNAFI N., "Analytical modelling of tube hydroforming", *Thin-Walled Structures*, vol. 34, pp. 295–330, 2003.

[ASN 03b] ASNAFI N., NILSSON T., LASSI G., "Tubular hydroforming of automotive side members with extruded aluminium profiles", *Journal of Materials Processing Technology*, vol. 142, pp. 93–101, 2003.

Material Forming Processes: Simulation, Drawing, Hydroforming and Additive Manufacturing, First Edition. Bouchaib Radi and Abdelkhalak El Hami.
© ISTE Ltd 2016. Published by ISTE Ltd and John Wiley & Sons, Inc.

[AUE 04] AUE-U-LAN Y., NGAILE G., ALTAN T., "Optimizing tube hydroforming using process simulation and experimental verification", *Journal of Materials Processing Technology*, vol. 146, pp. 137–143, 2004.

[AYA 11] AYADI A., RADI B., CHEROUAT, A. *et al.*, "Optimization and identification of the characteristics of an Hydroformed Structures", *Applied Mechanics and Materials*, pp. 11–20, 2011.

[AYD 05] AYDEMIR A., VREE J.H. P.D., BREKELMANS W.A.M. *et al.*, "An adaptive simulation approach designed for tube hydroforming processes", *Journal of Material Processing Technology*, vol. 159, pp. 303–310, 2005.

[BAB 00] BABA O.A.R.B., GELIN J.-C., "An augmented lagrangian treatment of the metal forming process", *Mathematical and Computer Modelling*, vol. 32, pp. 1171–1179, 2000.

[BAR 05] BARLAT F., ARETZ H., YOON J., KARABIN M. *et al.*, "Linear transfomation-based anisotropic yield functions", *International Journal of Plasticity*, vol. 21, no. 5, pp. 1009–1039, 2005.

[BAR 15] BARLIER C., BERNARD A., *Fabrication additive: du prototypage rapide à l'impression 3D*, Dunod, 2015.

[BEN 05] BEN-TAHER M., Contributions à l'étude et la simulation du procédé d'hydroformage, PhD thesis, Ecole des Mines de Paris, 2005.

[BEN 13] BEN ABDESSALEM A., PAGNACCO E., EL HAMI A., "Increasing the stability of T-shape tube hydroforming process under stochastic framework", *International Journal of Advanced Manufacturing Technology*, vol. 69, pp. 1343–1357, 2013.

[BEN 14] BEN ABDESSALEM A., EL HAMI A., "Global sensitivity analysis and multi-objective optimisation of loading path in tube hydroforming process based on metamodelling techniques", *International Journal of Advanced Manufacturing Technology*, vol. 71, nos. 5-8, pp. 753–773, 2014.

[BEN 15] BEN ABDESSALEM A., EL HAMI A., "A probabilistic approach for optimising hydroformed structures using local surrogate models to control failures", *International Journal of Mechanical Sciences*, vol. 96, no. 97, pp. 143–162, 2015.

[BOI 94] BOISSE P.D.J., GELIN J., "Eléments fini de coque à trois nuds pour le calcul des structures minces en grandes déformations", *Revue Européenne des Eléments finis*, vol. 2, no. 2, pp. 139–190, 1994.

[BOU 06] BOUMAIZA S., CORDEBOIS J.B., NEFUSSI G., "Analytical and numerical study on plastic instabilities for axisymmetric tube bulging", *International Journal of Mechanical Sciences*, vol. 48, pp. 674–682, 2006.

[BRE 15] BRETEAU T.B.F., Fabrication Additive Métallique Technologies et Opportunités, report, INSA Rouen, France, 2015.

[BUC 99] BUCZKOWSKI R.K.M., "A stochastic model of rough surfaces for finite element contact analysis", *Computer Methods in Applied Mechanics and Engineering*, vol. 16, no. 9, pp. 43–59, 1999.

[CAO 03] CAO J., KRISHNAN N., "Estimation of optimal blank holder force trajectories in segmented binders using ARMA model", *Journal of Manufacturing Science and Engineering*, vol. 125, pp. 763–770, 2003.

[CHA 98] CHABRAND P., DUBORIS F., RAOUS M., "Various numerical methods for solving unilateral contact problems with friction", *Mathematical and Computer Modelling*, vol. 28, no. 4/8, pp. 97–108, 1998.

[CHE 02] CHEROUAT A., SAANOUNI K., HAMMI Y., "Numerical improvement of thin tubes hydroforming with respect to ductile damage", *International Journal of Mechanical Sciences*, vol. 44, pp. 2427–2446, 2002.

[CHE 04] CHEN K.K., SOLDAAT R., MOSES R.M., "Free expansion bulge testing of tubes for automotive hydroform applications", *SAE Technical Paper No. 2004-01-0832.*, vol. 41, pp. 761–772, 2004.

[CHE 08a] CHEN X., DU W., LIU D., "Response surface optimization of biocatalytic biodiesel production with acid oil", *Biochemical Engineering*, vol. 40, 2008.

[CHE 08b] CHEROUAT A., RADI B., EL HAMI A., "The frictional contact of the composite fabric's shaping", *Acta Mechanica*, vol. 100, pp. 111–121, 2008.

[CHE 09] CHEROUAT A., RADI B., EL HAMI A., "The study of the composite fabric shaping using an augmented Lagrangian approach", *International Journal of Multidiscipline Modeling in Materials and Structures*, vol. 5, no. 2, pp. 185–198, 2009.

[COL 02] COL A., *Emboutissage des tôles, Importance des modes de déformations*, Techniques de l'ingénieur, M 318, 2002, .

[COL 03] COL A., "Investigation on press forming scatter origin", *Proceeding on the Sixth International ESAFORM Conference on Material Forming*, 2003.

[DOR 03] DORMAL T., Du prototypage rapide à la fabrication rapide, Rencontres Internationales du Développement Rapide de Produit VirtuReal, CIRTES, Saint Dié, 2003.

[DUV 72] DUVAUT G., LIONS J., *Les inéquations en mécanique et en physique*, Dunod, Paris, 1972.

[ELH 08] EL HAMI A., RADI B., SBAA M., "RBDO analysis of the dynamic contact inside the piezoelectric motor", *Applied Mathematical Sciences*, vol. 2, no. 41, pp. 2029–2045, 2008.

[ELH 10] EL HAMI A., *Multidisciplinary*, *Design Optimization in Computational Mechanics*, ISTE, London and John Wiley & Sons, New York, 2010.

[ELH 11] EL HAMI A., RADI B., *Fiabilité et optimisation des systèmes*, Ellipses, Paris, 2011.

[ELH 12] EL HAMI A., RADI B., CHEROUAT A., *Metal Forming: Process, Tools, Design*, InTech, 2012.

[ELH 13a] EL HAMI A., RADI B., *Incertitudes, optimisation et fiabilité des structures*, Hermes-Lavoisier, 2013.

[ELH 13b] EL HAMI A., RADI B., *Uncertainty and Optimization in Structural Mechanics*, ISTE Ltd, London and John Wiley & Sons, New York, 2013.

[ELH 15] EL HAMI A., RADI B., "Analysis of the hydroforming process using metamodels", *Advanced Materials Research*, vol. 1099, pp. 52–61, 2015.

[FAN 03] FANN K.J., HSIAO P.Y., "Optimization of loading conditions for tube hydroforming", *Journal of Materials Processing Technology*, vol. 140, pp. 520–524, 2003.

[FEE 03] FEENSTRA F.F., How fast is rapid tooling and what will rapid manufacturing bring us?, Rencontres Internationales du Développement Rapide de Produit Virtu-Real, CIRTES, Saint Dié, 2003.

[FLE 87] FLETCHER R., *Practical Methods of Optimization*, John Wiley & Sons, Chichester, 1987.

[GAN 02] GANTAR G., PEPELNJAK T., KUZMAN K., "Optimization of sheet metal forming processes by the use of numerical simulations", *Materials Processing Technology*, vol. 131, pp. 54–59, 2002.

[GEL 92] GELIN J.-C., LOCHEGNIES, *Simulations numériques en grandes déformations plastiques, Physique et mécanique de la mise en forme des métaux*, Presse du CNRS, 1992.

[GOE 08] GOETZ M., "Fabrication additive: du prototypage rapide à la pièce bonne matière", *Micronora Informations*, no. 112, pp. 2–7, 2008.

[GOO 68] GOODWIN G.M., "Application of strain analysis to sheet metal forming in the press shop", *SAE Technical Paper No. 680093*, vol. 56, pp. 25–48, 1968.

[HAR 11] HARDENNE T., Application du laser cladding au rechargement et à la fabrication de pièces, Report, University of Liège, 2011.

[HIL 50] HILL R., "A theory of the plastic bulging of a metal diaphragm by lateral pressure", *Philosphical Magazine*, vol. 7, pp. 1133–1142, 1950.

[HIL 52] HILL R., "On discontinuous plastic states with special reference to localized necking in thin sheets", *Journal of the Mechanics and Physics of Solids,* vol. 1, pp. 19–30, 1952.

[HOS 79] HOSFORD W., "On yield loci of anisotropic cubic metals", *Proceedings of the Seventh North American Metalworking Research Conference*, Dearborn, pp. 191–197, 1979.

[HWA 02] HWANG Y.M., LIN Y.K., "Analysis and finite element simulations of the tube bulge hydroforming process", *Journal of Material Processing Technology*, vol. 1, pp. 821–825, 2002.

[IMA 05] IMANINEJAD M., SUBHASH G., LOUKUS A., "Loading path optimization of tube hydroforming process", *International Journal of Machine Tools and Manufacture*, vol. 45, pp. 1504–1515, 2005.

[JAN 08] JANSSON T., NILSSON L., MOSHFEGH R., "Reliability analysis of a sheet metal forming process using Monte Carlo analysis and metamodels", *Materials Processing Technology*, vol. 22, no. 1, pp. 255–268, 2008.

[JIR 04] JIRATHEARANA S., Advanced methods for finite element simulation for process design in tube hydroforming, PhD thesis, Ohio State University, 2004.

[KAN 04] KANG B.S., SON B.M., KIM J., "A comparative study of stamping hydroforming processes for an automobile fuel tank using FEM", *International Journal of Machine Tools and Manufacture*, vol. 44, pp. 87–94, 2004.

[KAR 02] KARTHIK V., COMSTOCK R.J., HERSHBERGER D.L. *et al.*, "Variability of sheet formability and formability testing", *Journal of Materials Processing Technology*, vol. 121, pp. 350–362, 2002.

[KEE 63] KEELER S.P., "Forming limit curve", *Trans ASME*, vol. 56, pp. 25–48, 1963.

[KEE 65] KEELER J., "Determining of forming limits in automotive stamping", *SAE Technical Paper 650535*, 1965.

[KHO 11] KHODAPARAST H.H., MOTTERSHEAD J.E., BADCOCK K.J., "Interval model updating with irreducible uncertainty using the kriging predictor", *Mechanical Systems and Applied Processing*, vol. 25, pp. 1204–1226, 2011.

[KIK 88] KIKUCHI N.O.J., *Contact Problems in Elasticity. A Study of Variational Inequalities and Finite Element Methods*, SIAM, 1988.

[KIM 02] KIM S., KIM Y., "Analytical study for tube hydroforming", *Journal of Materials Processing Technology*, vol. 128, pp. 232–239, 2002.

[KLE 09] KLEIJNEN J.P.C., "Kriging metamodeling in simulation: a review", *European Journal of Operational Research*, vol. 192, pp. 707–716, 2009.

[KLE 02] KLEIBER M., ROJEK J., STOCKI R., "Reliability assessment for sheet metal forming operations", *Computer Methods in Applied Mechanics and Engineering*, vol. 191, no. 39-40, pp. 4511–4532, 2002.

[KOÇ 01] KOÇ M., AUE-U-IAN Y., ALTAN T., "On the characteristics of tubular materials for hydroforming experimentation and analysis", *International Journal of Machine Tools and Manufacture*, vol. 41, pp. 761–772, 2001.

[KOÇ 02] KOÇ M., ALTAN T., "Prediction of forming limits and parameter in the tube hydroforming process", *International Journal of Machine Tools and Manufacture*, vol. 42, pp. 123–138, 2002.

[KOS 94] KOSS S., Ecrouissage isotrope et anisotrope des aciers laminés soumis à des grandes déformations, PhD thesis, University Joseph Fourier, Grenoble, France, 1994.

[KUR 00] KURODA M., TVERGAARD V., "Forming limit diagrams for anisotropic metal sheets with different yield criteria", *International Journal of Solids and Structures*, vol. 37, no. 37, pp. 5037–5059, 2000.

[LAC 69] LACOMBE A., "Méthode d'utilisation des grilles susceptibles d'aider l'interprétation des emboutis", *Colloque GAMI ISMCN*, 1969.

[LAU 05] LAUVAUX G., La réalisation d'oeuvres d'art par prototypage rapide avec le procédé de Stratoconception, PhD thesis, IFTS, University of Champagne Ardenne, Reims, 2005.

[LEE 90] LEE J.K.W.K.-N.E., A benchmark test sheet forming analysis, Report no. ERC/NSM-5-90 22, National Service Foundation, Engineering Research Center for Net Shape Manufacturing, Ohio State University, 1990.

[LEE 01] LEE K.-H., PARK G.-J., "Robust optimization considering tolerances of design variables", *Computers & Structures*, vol. 79, pp. 77–86, 2001.

[LEE 02] LEE M.H., SOHN S.M., KANG C.Y. *et al.*, "Study on the hydroforming process for automobile radiator support members", *Journal of Materials Processing Technology*, vol. 130-131, pp. 115–120, 2002.

[LEM 09] LEMAIRE M., *Structural Reliability*, ISTE Ltd, London and John Wiley & Sons, New York, 2009.

[LI 97] LI M.S.D.-T.K., "Linear complementary formulations involving frictional contact for elastoplastic deformable bodies", *Journal of Applied Mechanics Transactions ASME*, vol. 64, pp. 80–89, 1997.

[LOU 07] LOUKUS A., SUBHASH G., IMANINEJAD M., "An optimization of material properties and process parameters for tube hydroforming of aluminum extrusions", *Journal of Engineering Materials and Technology*, vol. 129, pp. 233–241, 2007.

[MAJ 03] MAJESKE K.D., HAMMETT P.C., "Identifying sources of variation in sheet metal stamping", *Interntional Journal of Flexible Manufacturing Systems*, vol. 15, pp. 5–18, 2003.

[MAK 07] MAKI T., WALTER C., "Liquid curves Sheet hydroforming helps the sporty Solstice standout", *Stamping Journal*, pp. 32–37, 2007.

[MAK 08] MAKRIZI A.R.B.-E.H.A., "Solution of the topolgy optimization problem based subdomain method", *Applied Mathematical Sciences*, vol. 2, no. 42, pp. 2047–2062, 2008.

[MAR 67] MARCINIAK Z., KUCZYNSKI K., "Limit strains in the processes of stretch-forming sheet steel", *Journal of Mechanics and Physics of Solids*, vol. 1, pp. 609–620, 1967.

[MEU 14] MEUNIER B., Perspectives de développement pour le couplage optimisation topologique et fabrication additive de composants mécaniques, Master thesis, University of Liège, 2014.

[MOH 09] MOHAMMADI F., MASHADI M.M., "Determination of the loading path for tube hydroforming process of a copper joint using a fuzzy controller", *International Journal of Advanced Manufacturing Techno*logy, vol. 43, pp. 1–10, 2009.

[MOR 02] MORO T., EL HAMI A., EL MOUDNI A., "Reliability analysis of a mechanical contact between deformable solids", *International Journal of Probabilistic Engineering Mechanics*, vol. 17, no. 3, pp. 227–232, 2002.

[MOR 10] MOROVVATI M., MOLLAEI-DARIANI B., ASADIAN-ARDAKANI M., "A theoretical, numerical, and experimental investigation of plastic wrinkling of circular two-layer sheet metal in the deep drawing", *Journal of Materials Processing Technology*, vol. 210, no. 13, pp. 1738–1747, 2010.

[MYE 11] MYERS R.H., MONTGOMERY D.C., ANDERSON-COOK C.M., *Response Surface Methodology: Process and Product Optimization Using Designed Experiments*, John Wiley and Sons, 2011.

[ODE 83] ODEN J., PIRES E., "Non local and linear friction laws and variational principles for contact problems in elasticity", *Journal of Applied Mec*hanics, vol. 50, pp. 421–432, 1983.

[OH 06] OH S.I., JEON B.H., KIM H.Y. *et al.*, "Applications of hydroforming processes to automobile parts", *Journal of Materials Processing Technology*, vol. 174, pp. 42–55, 2006.

[PON 13] PONCHE R., Méthodologie de conception pour la fabrication additive, application à la projection de poudres, PhD Thesis, Ecole Centrale Nantes, 2013.

[PSA 89] PSA-RENAULT-SOLLAC, Simulation numérique de l'emboutissage des tables en acier extra doux, progress report no. F3.86-7210-KC/309, 5, contrat CECA, 1989.

[RAD 94] RADI B., PERRIOT A., "Subdomain methods in structural mechanics", *International Journal for Numerical Methods in Eng*ineering, vol. 37, pp. 3309–3322, 1994.

[RAD 98] RADI B., GELIN J.-C., "Treatment of the frictional contact via a Lagrangian formulation", *Mathematical and Computer Modelling*, vol. 28, no. 4-8, pp. 407–412, 1998.

[RAD 07] RADI B., EL HAMI A., "Reliability analysis of the metal forming process", *International Journal of Mathematical and Computer Modelling*, vol. 45, pp. 431–439, 2007.

[RAD 10] RADI B., MAKHLOUFI A., EL HAMI A. *et al.*, "Reliability-based design optimization of an ultrasonic motor by new approach", *Simulation and Multidisciplinary Design Optimization*, EDP Sciences, 2010.

[RAD 11] RADI B., AYADI A., CHEROUAT A., GIRAUD-MOREAU L., EL HAMI A., "Identification of the characteristics of hydroformed structures using optimization methods", *Journal Key Engineering Materials*, vol. 473, no. 62, pp. 723–730, 2011.

[REF 98] REFAAT M.M.-S., "A new strategy for the solution of frictional contact problems", *International Journal of Numerical Methods & Engineering*, vol. 43, pp. 1053-1068, 1998.

[ROD 11] RODRIGUE H., RIVETTE M., CALATORU V., RICHIR S., "Une méthodologie de conception pour la fabrication additive", *Actes du 9e Congrès International de Génie Industriel*, Canada, 2011.

[SHE 04] SHENG Z.Q., JIRATHEARANAT S., ALTAN T., "Adaptive FEM simulation for prediction of variable blank holder force in conical cup drawing", *International Journal of Machine Tools and Manufacture*, vol. 44, pp. 487–494, 2004.

[SHU 07] SHU-HUI L., BING Y., WEI-GANG Z. *et al.*, "Loading path prediction for tube hydroforming process using a fuzzy control strategy", *Materials and Design*, vol. 29, pp. 1110–1116, 2007.

[SIM 92] SIMO J.C.L.-T., "An augmented Lagrangian treatment of contact involving friction", *Computers & Structures*, vol. 42, pp. 97–116, 1992.

[SON 07] SONG W.J., KIM J., KANG B.S., "Experimental and analytical evaluation on flow stress of tubular material for tube hydroforming simulation", *Journal of Material Processing Technology*, vol. 191, pp. 368–371, 2007.

[STA 92] STADLER W., DUER J., "Multicriteria optimization in engineering: a tutorial and survy", *Structural Optimization: Status and Future,* American institute of Aeronautics and Astronautics, pp. 209–249, 1992.

[STO 75] STOREN S., RICE J.R., "Application of strain analysis to sheet metal forming in the press shop", *Journal of Mechanics and Physics of Solids*, vol. 23, pp. 421–441, 1975.

[STR 10] STRANO M., "Reliability based economical optimization of sheet metal forming processes", *European Scientific Association For Material Forming (ESAFORM) Conference*, 2010.

[SWI 52] SWIFT H.W., "Plastic instability under plane stress", *Journal of Mechanics and Physics of Solids,* vol. 1, pp. 1–18, 1952.

[THO 99] THOMAS W., Product, tool and process design methodology for deep drawing and stamping of sheet materials, PhD Thesis, Ohio State University, 1999.

[TRU 12] TRUMPF A., "Industrial applications of laser cladding and the equipment required", *Manufacturing Innovations in Laser Additive Manufacture*, June 2012.

[XIN 01] XING H.L., MAKINOUCHI A., "Numerical analysis and design for tubular hydroforming", *International Journal of Mechanical Sciences*, vol. 43, pp. 1009–1026, 2001.

[YUA 06a] YUAN S., YUAN W., WANG X., "Effect of wrinkling behavior on formability and thickness distribution in tube hydroforming", *Journal of Materials Processing Technology*, vol. 177, pp. 668–671, 2006.

[YUA 06b] YUAN S.J., HAN C., WANG X.S., "Hydroforming of automotive structural components with rectangular-sections", *International Journal of Machine Tools and Manufacture*, vol. 46, pp. 1201–1206, 2006.

Index

A, B

Almansi, 26, 31
basis
  material, 28
Bernstein, 67
  polynomial, 67
Bezier patches, 65

C

casting, 2
Cauchy, 26, 35, 49, 51, 67, 74
convective transport, 30
Cristoffel, 32
criteria forming, 16
criterion
  anisotropic plasticity, 97
  necking, 128
  Tresca's, 22
  Von Mises, 21
  wrinkling, 128
curve forming limit, 92

D

deep-drawing hydromechanical, 87
deformation
  elastic, 19, 36
  plastic, 36
  viscous, 20
derivative convective, 30
design of experiments, 165, 236

E, F

Euler, 26
forging, 9
forming
  by plastic deformation, 7
  cold, 8
  hot, 8
friction coefficient, 55
function
  limit-state, 225
  performance, 225

G, H

Green, 26
Hasofer, 228
Hooke, 46
  operator, 46
hydroforming, 12
  fixed-die, 13
  high-pressure, 13
  low-pressure, 13
  sheet metal, 86
  tubes, 85

Material Forming Processes: Simulation, Drawing, Hydroforming and Additive Manufacturing, First Edition. Bouchaib Radi and Abdelkhalak El Hami.
© ISTE Ltd 2016. Published by ISTE Ltd and John Wiley & Sons, Inc.

I, K, L

index
    Hasofer and Lind, 228
    reliability, 227
    Rjanitzyne-Cornell, 227
Kirchhoff, 35, 44
Lagrange, 26
law
    Coulomb, 54
    elastoplastic behavior, 36
    friction, 54
    Tresca, 55

M, N, O

machining, 3
metallurgy, 5
mode of failure, 225
Monte Carlo, 141
necking, 91
optimization
    design, 216
    robust, 221
    shape, 216
    topological, 216

P

Piola, 35
point
    design, 229
    most probable point of failure, 229
probabilistic modeling, 224
probability of failure, 226

R, S

region
    adherence, 54
    slip, 54
rolling, 9
small perturbations hypothesis, 27, 36, 46
smelting, 2
SORM method, 231
spinning, 9
springback, 19, 92
stamping, 9
strain hardening, 21
    isotropic, 38

T

tensor
    Cauchy stress, 35
    Euler-Almansi, 26
    Green-Lagrange, 26
    Piola-Kirchhoff, 35
    rate, 27
    right Cauchy-Green, 26
    strain, 31
    stress, 35
    transformation, 29
tube buckling, 88

U, V, W

uncertainty, 224
unilateral contact, 53
Von Mises perfect plasticity, 37
wrinkling, 90

Other titles from

in

Information Systems, Web and Pervasive Computing

2016

BEN CHOUIKHA Mona
Organizational Design for Knowledge Management

BÉRANGER Jérôme
Big Data and Ethics: The Medical Datasphere

BERTOLO David
Interactions on Digital Tablets in the Context of 3D Geometry Learning (Human-Machine Interaction Set – Volume 2)

EL FALLAH SEGHROUCHNI Amal, ISHIKAWA Fuyuki, HÉRAULT Laurent, TOKUDA Hideyuki
Enablers for Smart Cities

KITAJIMA Munéo
Memory and Action Selection in Human–Machine Interaction (Human–Machine Interaction Set – Volume 1)

LAGRAÑA Fernando
E-mail and Behavioral Changes: Uses and Misuses of Electronic Communications

MONINO Jean-Louis, SEDKAOUI Soraya
Big Data, Open Data and Data Development

SALGUES Bruno
Health Industrialization

VENTRE Daniel
Information Warfare – 2nd edition

2015

ARDUIN Pierre-Emmanuel, GRUNDSTEIN Michel,
ROSENTHAL-SABROUX Camille
Information and Knowledge System
(Advances in Information Systems Set – Volume 2)

BÉRANGER Jérôme
Medical Information Systems Ethics

BRONNER Gérald
Belief and Misbelief Asymmetry on the Internet

IAFRATE Fernando
From Big Data to Smart Data
(Advances in Information Systems Set – Volume 1)

KRICHEN Saoussen, BEN JOUIDA Sihem
Supply Chain Management and its Applications in Computer Science

NEGRE Elsa
Information and Recommender Systems
(Advances in Information Systems Set – Volume 4)

POMEROL Jean-Charles, EPELBOIN Yves, THOURY Claire
MOOCs

SALLES Maryse
Decision-Making and the Information System (Advances in Information Systems Set – Volume 3)

SAMARA Tarek
ERP and Information Systems: Integration or Disintegration (Advances in Information Systems Set – Volume 5)

2014

DINET Jérôme
Information Retrieval in Digital Environments

HÉNO Raphaële, CHANDELIER Laure
3D Modeling of Buildings: Outstanding Sites

KEMBELLEC Gérald, CHARTRON Ghislaine, SALEH Imad
Recommender Systems

MATHIAN Hélène, SANDERS Lena
Spatio-temporal Approaches: Geographic Objects and Change Process

PLANTIN Jean-Christophe
Participatory Mapping

VENTRE Daniel
Chinese Cybersecurity and Defense

2013

BERNIK Igor
Cybercrime and Cyberwarfare

CAPET Philippe, DELAVALLADE Thomas
Information Evaluation

LEBRATY Jean-Fabrice, LOBRE-LEBRATY Katia
Crowdsourcing: One Step Beyond

SALLABERRY Christian
Geographical Information Retrieval in Textual Corpora

2012

BUCHER Bénédicte, LE BER Florence
Innovative Software Development in GIS

GAUSSIER Eric, YVON François
Textual Information Access

STOCKINGER Peter
Audiovisual Archives: Digital Text and Discourse Analysis

VENTRE Daniel
Cyber Conflict

2011

BANOS Arnaud, THÉVENIN Thomas
Geographical Information and Urban Transport Systems

DAUPHINÉ André
Fractal Geography

LEMBERGER Pirmin, MOREL Mederic
Managing Complexity of Information Systems

STOCKINGER Peter
Introduction to Audiovisual Archives

STOCKINGER Peter
Digital Audiovisual Archives

VENTRE Daniel
Cyberwar and Information Warfare

2010

BONNET Pierre
Enterprise Data Governance

BRUNET Roger
Sustainable Geography

CARREGA Pierre
Geographical Information and Climatology

CAUVIN Colette, ESCOBAR Francisco, SERRADJ Aziz
Thematic Cartography – 3-volume series
Thematic Cartography and Transformations – volume 1
Cartography and the Impact of the Quantitative Revolution – volume 2
New Approaches in Thematic Cartography – volume 3

LANGLOIS Patrice
Simulation of Complex Systems in GIS

MATHIS Philippe
Graphs and Networks – 2nd edition

THERIAULT Marius, DES ROSIERS François
Modeling Urban Dynamics

2009

BONNET Pierre, DETAVERNIER Jean-Michel, VAUQUIER Dominique
Sustainable IT Architecture: the Progressive Way of Overhauling Information Systems with SOA

PAPY Fabrice
Information Science

RIVARD François, ABOU HARB Georges, MERET Philippe
The Transverse Information System

ROCHE Stéphane, CARON Claude
Organizational Facets of GIS

2008

BRUGNOT Gérard
Spatial Management of Risks

FINKE Gerd
Operations Research and Networks

GUERMOND Yves
Modeling Process in Geography

KANEVSKI Michael
Advanced Mapping of Environmental Data

MANOUVRIER Bernard, LAURENT Ménard
Application Integration: EAI, B2B, BPM and SOA

PAPY Fabrice
Digital Libraries

2007

DOBESCH Hartwig, DUMOLARD Pierre, DYRAS Izabela
Spatial Interpolation for Climate Data

SANDERS Lena
Models in Spatial Analysis

2006

CLIQUET Gérard
Geomarketing

CORNIOU Jean-Pierre
Looking Back and Going Forward in IT

DEVILLERS Rodolphe, JEANSOULIN Robert
Fundamentals of Spatial Data Quality